# New Fuels, Flame Quenching and DDT

By

Moustafa Mohamed Attya Okily Shehata

BEng, MSc (Eng)

Submitted in accordance with the requirements for the degree of

Doctor of Philosophy

The University of Leeds

School of Mechanical Engineering

Institute of Thermo-fluids

March 2019

# Intellectual Property and Publications Statements

The candidate confirms that the work submitted is his own, except where work which has formed part of jointly-authored publications has been included. The contribution of the candidate and the other authors to this work has been explicitly indicated below. The candidate confirms that appropriate credit has been given within the thesis where reference has been made to the work of others.

1- Bradley, D., & Shehata, M. (2018). "Acceleration of laminar hydrogen/oxygen flames in a tube and the possible onset of detonation''. International Journal of Hydrogen Energy, 43(13), 6734-6744. *The Author of the present thesis provided the numerical data. Other Author of this publication provided the technical discussions and guidance.*

2- Shehata, M. (2017). "Acceleration of laminar hydrogen/oxygen flames in a tube and the possible onset of detonation''. H2FC Supergen Research Conference. The Hydrogen and Fuel Cell Research Hub, University of St Andrews.

3- Bradley, D., Shehata, M., Lawes, M., & Ahmed, P. (2019). Flame Extinctions: Critical Stretch Rates and Sizes. (Submitted to Journal of Combustion and Flame journal, CNF-D-19-00127). *The Author of the present thesis provided the experimental data. Other Authors of this publication provided the swinging sheet data, the technical discussions and guidance.*

*In memory of my beloved sister*

*Mai*

# Acknowledgements

# Abstract

Two limiting conditions of burning rate are considered, culminating in either flame extinction, or transition to a detonation. A 2D schlieren technique, for flame imaging of quenching kernels has been employed, supported by 3D swinging sheet measurements. The study was able, for the first time, to determine the kernel mean diameters at the point of quench. It was found that the burning regime on the $U/K$ diagram covered higher values of $K$ and strain rate Markstein numbers,$Ma_{sr}$ than previously reported.

Hydrogen, methane, *n*-butanol and *i*-octane air mixtures were studied at different pressures and temperatures, up to 1 MPa and 365 K. Kernel mean diameters are normalised with laminar flame thicknesses, and correlated, through measurement of turbulent length scales, with $K$ and $Ma_{sr}$. It is also shown how the quenching, through blow-off, of jet flames is closely related to that of single kernel quenching of premixed flames. Just as excessive air entrainment causes quenching of jet flames, entrainment of pilot flame gases by a highly turbulent mixture, can ensure its survival.

As a part of the assessment of $H_2$ as a fuel, its autoignition and transition to detonation were studied, with emphasis on laminar flow. This necessitated micro-tubes for flame acceleration. Stoichiometric $H_2/O_2$ mixtures were studied at pressures where autoignition delay times are short.

The probability of a purely laminar propagation leading to a detonation is marginal only when the initial temperature is raised to 375 K, do purely laminar detonations become possible, in tubes of between about 0.5 and 1.35 mm diameter. The tendency of mildly turbulent mixtures to auto-ignite, for an initial temperature of 300 K is greater than with laminar flames on the same initial conditions and tube sizes. A further related study demonstrates a proposed detonation engine for the laminar transition to detonation, but this reveals practical design limitations.

# Table of Contents

# List of Figures

# List of Tables

# Nomenclature

| | | |
|---|---|---|
| $A$ | Flame surface area associated with $u_t$ | m$^2$ |
| $a$ | Cross section area of tube, sound speed | m$^2$, m/s |
| $a_1$ | Acoustic velocity ahead of the shock | m/s |
| $c$ | A defining parameter for $M_1$ | - |
| $c_p$ | Specific heat at constant pressure | J/kg.K |
| $c_{pb}$ | Specific heat at constant pressure of the burner reactants | J/kg.K |
| $c_{pp}$ | Specific heat at constant pressure of pilot flame gases | J/kg.K |
| $D$ | Thermal diffusivity, flame average diameter, pipe diameter | m$^2$/s, m |
| $D_b$ | Limiting jet flame diameter | m |
| $D_c$ | Critical tube diameter for laminar flow | m |
| $d_k$ | Maximum mean quenching diameter of flame kernel | m |
| $E$ | Activation energy | J. mol$^{-1}$ |
| $\bar{E}$ | Detonation stability dimensionless group | - |
| $f$ | Focal length, mass fraction of burned gas | m, - |
| $K, K_s$ | Karlovitz stretch factor | - |
| $Ka$ | Karlovitz number $\cong 15^{0.5} K$ | - |
| $K_{ql}, K_{ql+}$ | Laminar flame extinction stretch factor $= \alpha_q \, \delta_l / u_l$. | - |
| $k$ | Thermal conductivity | W/m.K |
| $\bar{k}_\eta$ | Dimensionless wave number | - |
| $L_b$ | Burned gas Markstein length | m |

| | | |
|---|---|---|
| $L_s$ | Markstein length for strain | m |
| $L_{sr}$ | Strain rate Markstein length | m |
| $l, L$ | Integral length scale | m |
| $l_G$ | Gibson scale | m |
| $Le$ | Lewis number | - |
| $M_1$ | Mach number of shock wave | - |
| $Ma_{sr}$ | Markstein number for strain rate | - |
| $m_b$ | mass of burned gas | kg |
| $\dot{m}_u, m_u$ | Flow rate of reactants to the burner, mass of unburned gas | kg/s, kg |
| $\dot{m}_p$ | Flow rate of pilot flame gases | kg/s |
| $N_{stage}$ | Number of the stages for impulse turbine | - |
| $N_f$ | Fan speed | rpm |
| $P$ | Turbine power | W |
| $P_0$ | Reference pressure | MPa |
| $P_1$ | Shock wave upstream pressure | MPa |
| $P_2$ | Shock wave downstream pressure | MPa |
| $p_b$ | Probability of burning | - |
| $p_{0.8}$ | 80% probability of burning | - |
| $p_{0.2}$ | 20% probability of burning | - |
| $P_i/P_a$ | Pressure ratio of initial stagnation to atmospheric pressure | - |
| $r$ | Tube radius, turbine moving blade radius | m |
| $r_{sch}$ | Flame radius measured by schlieren technique | m |
| $r_o$ | Hot spot radius | m |

| | | |
|---|---|---|
| $\bar{r}$ | Normalised hot spot radius | - |
| $R_j$ | Spherical general radius | m |
| $R_l$ | Turbulent Reynolds number based on turbulent integral length scale | - |
| $R_r$ | Flame root radius | m |
| $R_t$ | Flame tip radius | m |
| $R_v$ | Flame radius for equal volumes | m |
| $R_\lambda$ | Turbulent Reynolds number based on Taylor microscale | - |
| $Re_c$ | Limiting Reynolds number for laminar auto ignition | - |
| $S_f$ | Flame speed along a tube | m/s |
| $S_g$ | Mean gas velocity ahead of flame | m/s |
| $S_h$ | Shock wave speed along the tube | m/s |
| $S_n$ | Stretched laminar flame speed | m/s |
| $s_{q+}$ | Flame extinction positive stretch rate | s$^{-1}$ |
| $s_{q-}$ | Flame extinction negative stretch rate | s$^{-1}$ |
| $\bar{S}(\bar{k}_\eta)$ | Non-dimensional power spectral density | - |
| $T_0$ | Reference temperature | K |
| $T_1$ | Shock wave upstream temperature | K |
| $T_2$ | Shock wave downstream temperature | K |
| $T_b$ | Adiabatic flame temperature, Temperature of the burner reactants | K |
| $T_m, T_u$ | Mixed gas temperature | K |
| $T_u, T_o$ | Unburned gas temperature | K |
| $T_p$ | Adiabatic temperature of the pilot flame gases | K |

| | | |
|---|---|---|
| $T^o$ | Inner layer temperature | K |
| $U_m$ | Rotational speed of the turbine moving blades | m/s |
| $U_b^*$ | Dimensionless flow number for flame blow-off in jets | - |
| $u$ | Mean velocity in burner, fuel flow mean velocity at the pipe exit for subsonic flow. | m/s |
| $u_a$ | Autoignition propagation velocity | m/s |
| $u_g$ | Gas velocity ahead of spherical flame front | m/s |
| $u_\ell$ | Laminar burning velocity | m/s |
| $u_{\ell m}$ | Maximum laminar burning velocity | m/s |
| $u_n$ | Stretched laminar burning velocity | m/s |
| $u_t, u_{tr}$ | Turbulent burning velocity | m/s |
| $u_\eta$ | Kolmogorov velocity | m/s |
| $u'$ | rms velocity | m/s |
| $u'_k$ | Effective rms velocity | m/s |
| $w$ | Specific workout from turbine | kJ/kg |

## Greek

| | | |
|---|---|---|
| $\alpha$ | Mass diffusivity of the deficient reactant, stretch rate, numerical constant | m²/s, s⁻¹, - |
| $\alpha_c$ | Stretch rate for curvature | s⁻¹ |
| $\alpha_q$ | Laminar extinction stretch rate | s⁻¹ |
| $\alpha_s$ | Stretch rate for strain | s⁻¹ |

| | | |
|---|---|---|
| $\beta$ | Numerical constant | - |
| $\gamma$ | Ratio of specific heats | - |
| $\delta_l$ | Laminar flame thickness | m |
| $\delta_k$ | Preheat zone flame thickness | m |
| $\varepsilon$ | Residence time of pressure wave in hot spot normalised by excitation time, dissipation rate | - , $m^2/s^3$ |
| $\eta$ | Kolmogorov length scale, turbine efficiency | m, - |
| $\lambda$ | Taylor length scale, detonation cell width | m |
| $\nu$ | Kinematic viscosity | $m^2/s$ |
| $\xi$ | $a/u_a$ | - |
| $\rho_b$ | Burned gas density | $kg/m^3$ |
| $\rho_u$ | Unburned gas density | $kg/m^3$ |
| $\sigma$ | Density ratio $\rho_u/\rho_b$ | - |
| $\tau_c$ | Chemical time scale | s |
| $\tau_e$ | Excitation time | s |
| $\tau_i$ | Ignition delay time | s |
| $\tau_k$ | Eddy lifetime | s |
| $\tau_\eta$ | Kolmogorov time scale | s |
| $\varphi$ | Equivalence ratio | - |
| $\psi$ | Stage loading coefficient | - |
| $\omega$ | Angular velocity of the turbine moving blade | rad/s |

# Subscripts and superscripts

| | |
|---|---|
| $b$ | Burner |
| $c$ | Critical value |
| $g$ | Gas, Ignition |
| $isen$ | Isentropic |
| $l, \ell$ | Laminar |
| $m$ | Maximum value, mixing |
| $n$ | Stretched |
| $p$ | Pilot, products |
| $sch$ | Schlieren |
| $s$ | Unstretched |
| $t$ | Turbulent, total |
| $u$ | Unburned, mixing |

# Acronyms

| | |
|---|---|
| ADC | Analogue to Digital Converter |
| CCS | Carbon Capture and Storage |
| DDT | Deflagration to Detonation Transition |
| DNS | Direct Numerical Simulation |
| HHO | Oxy hydrogen |
| MIE | Minimum Ignition Energy |
| PDE | Pulse Detonation Engine |
| pdf | probability density function |
| ppm | parts per million |
| RCM | Rapid Compression Machine |
| RM | Rotating Mirror |
| UNEP | United Nations Environment Programme |
| YAG | Yttrium Aluminium Garnet |

# Chapter 1 - Introduction

## 1.1  Foreword and Motivation

In 2015, United Nations Environment Programme (UNEP), sought a worldwide agreement to apply the framework towards negative values of greenhouse gas emissions from fossil fuels consumption by 2100 (UNEP, 2018). Despite many developed countries dependence on coal as a cheap fuel, which is the main source of emissions and pollution, increasing the efficiency related to carbon capture and storage (CCS) and control of conventional power generation has become one of the core challenges concerning increased uptake.

To address the challenges of power generation and the future environmental demand, alternative fuels have been used, such as biofuels, synthetic liquids and hydrogen. Hydrogen is environmentally supporting the reduction in fossil fuels energy and increase the thermal efficiency when employed in engines. Recently, the production of NOx from lean-burn hydrogen operated engines was reported as nominal (Ravi et al., 2016).

Producing hydrogen can be achieved using renewable resources, such as solar (Jericha et al., 2010) and wind energy (Alabbadi, 2012). The electrolysis of water separates stoichiometric hydrogen and oxygen. This method can lead to zero greenhouse gas emissions. The produced hydrogen is fed into the fuel cell which converts the chemical into an electrical energy. This process would only utilise the hydrogen resulted from the electrolysis and the oxygen would vented out and wasted or used in a propulsion systems (de Groot et al., 1997). Instead this mixture of hydrogen and oxygen (HHO) can be used as an alternative to fossil fuels to generate steam at a very high temperature and serves as a feed to a steam turbine so as to generate electricity (Alabbadi, 2012).

Although fuel cells give high thermal efficiency, it is expensive in power generation compared to conventional power generation cycles, Jericha et al. (2010) proposed a hybrid plant with steam and use twelve fuel cells give 2.5

MW each integrated with a combined cycle give 110 MW. The overall net efficiency of the plant was very high 73.8%.

As an effect of this clean fuel on the performance of a gasoline spark ignition engine, Musmar and Al-Rousan (2011) showed that improvement on the brake thermal efficiency at different engine speeds as seen in Fig. 1.1.
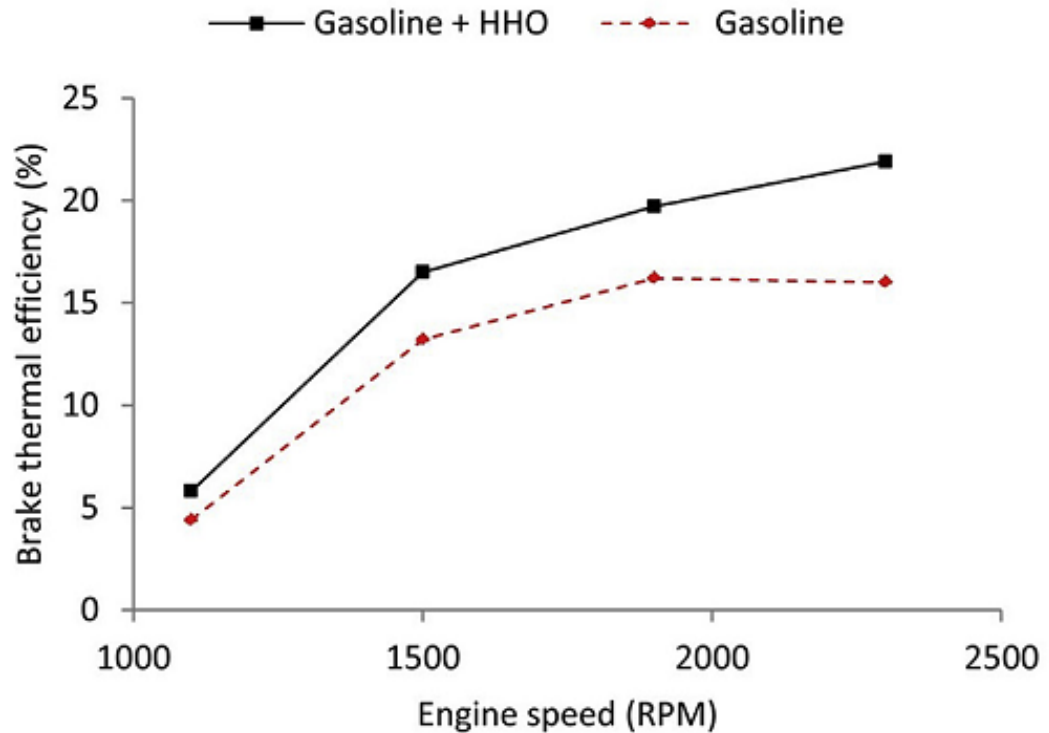


**Figure 1.1** Effect of HHO on Brake thermal efficiency of Spark ignition engine (Musmar & Al-Rousan, 2011).

Biofuels, such as ethanol and *n*-butanol, are produced from renewable sources and represent a viable alternative fuel for conventional engines. *N*-butanol is considered the second generation alcohol fuel as its vapor pressure is lower than gasoline, thus making it safer to use by producing fewer organic emissions (Wu et al., 2008). In terms of future sources of viable energy, this is a promising fuel as it has a higher energy density and a higher calorific value (Xue et al., 2013).

As it is attractive, hydrogen can be produced from butanol using steam and dry reforming thermochemical techniques due to the higher hydrogen content of butanol (13.51 wt.%) compared to methanol and ethanol (Cai et al., 2012). Such fuels like hydrogen and *n*-butanol are investigated in the present work including the burning rates.

Because of its growing importance, $H_2$ plays a key role in the thesis. This thesis examines two aspects of the use of $H_2$. Electrolysis produces $H_2/O_2$ in its stoichiometric proportions and the burning velocity and autoignition delay times are reviewed in a study of whether it is possible for the mixture to detonate in a laminar flow. This leads to the study of the detonation characteristics of such mixtures. Also, because of the good efficiency and low noxious emissions of lean burn hydrogen engines, values of the lean burn flammability limit, as well as this limit for other fuels, are explored experimentally in the Leeds fan-stirred vessel. Quenching limits to flame propagation are studied in terms of limiting stretch rates and limiting flame kernel sizes. All these parameters will be discussed in the following sections.

## 1.2  Deflagration

A deflagration wave is a subsonic combustion wave in which the flame front is dominated by the chemical reactions with propagation aided by molecular transport of energy and species. Deflagration wave can be laminar or turbulent. Laminar deflagration is initiated by the ignition of fresh mixture. The burning rate is controlled by the chemical kinetics of the chain reactions, diffusion coefficients of species and thermal conductivity. Fuel type is also determinant factor. The pressure and density decrease across the deflagration wave.

### 1.2.1   Laminar Deflagration and Flame Structure

The basic structure of laminar deflagration has been summarised by Griffiths and Barnard (1995) as the temperature and concentration profiles for a one dimensional premixed adiabatic flame, as shown in Fig. 1.2. Four zones are

presented, comprising cold reactants, preheated (pre-flame zone), reaction and products zone.
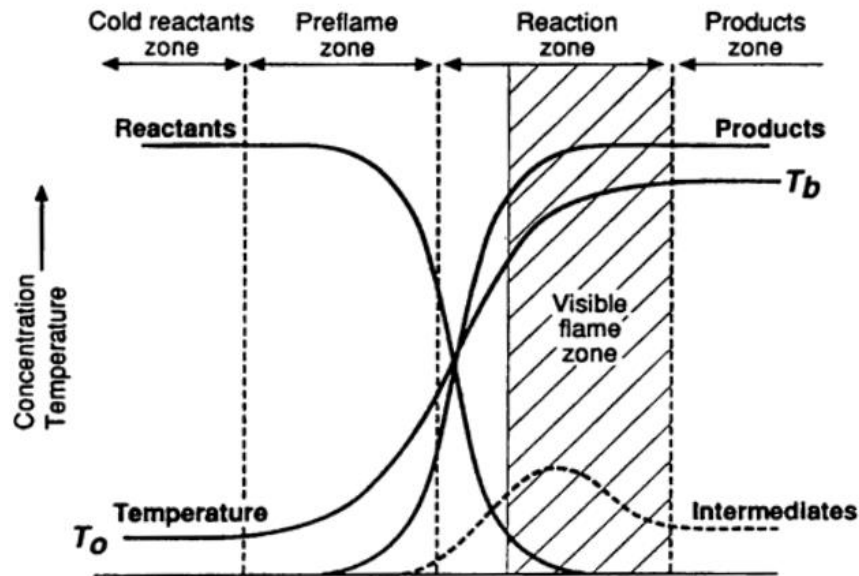


**Figure 1.2** Concentration and temperature profiles associated with one-dimensional, premixed adiabatic flame (Griffiths & Barnard, 1995).

The reactants are preheated from the unburned temperature, $T_o$ in the pre-flame zone where heat conduction increases the temperature of the reactants. A density gradient forms across the flame. Mass diffusion is also involved in this zone. The enthalpy and Gibbs free energy for reactions control the chemical reactions in the reaction zone. In this zone, the temperature increases further, and the chemical reaction rate rapidly increases due to the chain reactions. Finally, the products reach the adiabatic flame temperature, $T_b$.

### 1.2.1.1 Laminar Flame Thickness

Griffiths and Barnard (1995) define the laminar flame thickness (denoted by $\delta_l$ ) as the reaction zone depth where the release of the bulk heat occurs. Essentially, within the flame thickness, the temperature changes from $T_o$ of the cold reactants to $T_b$ of the products.

There are different definitions for the laminar flame thickness; based on the temperature gradient defined as thermal flame thickness involving the diffusion based upon the species production and consumption with (Ciccarelli & Dorofeev, 2008; Clavin, 1985; Matalon & Matkowsky, 1982; Tamadonfar & Gülder, 2014) and based on the hydrodynamic length given by (Abdel-Gayed et al., 1989; Bradley et al., 1998c; Shy et al., 2000) as follows:

$$\delta_l = \nu/u_l \,, \tag{1.1}$$

where $\nu$ is the kinematic viscosity of the cold reactants and $u_l$ is the laminar burning velocity. This definition is used in Sections 3.2 and 3.3, and it is also suitable in the turbulent combustion flow parameters as it linked with the transport coefficient represents in the kinematic viscosity. Generally, it is an important property of the flame because its value is indicative of how much turbulence is interacting with the flame front.

### 1.2.1.2 Laminar Burning Velocity

Both laminar and turbulent burning velocities are relevant to quenching in the present work. The laminar flame speed, $s_n$, in a spherical explosion is defined as the rate of the increase of the flame radius, $dr/dt$. It is the summation of laminar burning velocity, $u_l$, and gas velocity ahead of flame front, $u_g$, due to the volume increase from the gas expansion. Laminar burning velocity is an important physico-chemical parameter. It is the flame velocity relative to the unburned gas and it travels normal to a one-dimensional planar flame surface (unburned gas velocity normal to the reaction zone). This velocity is expressed by:

$$u_l = s_s - u_g. \tag{1.2}$$

Laminar burning velocity, $u_l$, can be also expressed as a function of the un-stretched laminar flame speed, $S_s$, and burned to unburned gas density, $\rho_b/\rho_u$ (Bradley et al., 1998c):

$$u_l = S_s \, \rho_b/\rho_u \,. \tag{1.3}$$

The variations of burning velocity of different fuel/air mixtures with the equivalence ratio, $\varphi$, at atmospheric conditions, are shown in Fig. 1.3.

Hydrogen, ethylene and acetylene are highly reactive gases due to the higher molecular diffusivity and chemical kinetics.

It is clearly shown in the figure how high the laminar burning velocity is for hydrogen, ethylene, and acetylene-air mixtures compared to other fuel/air mixtures.
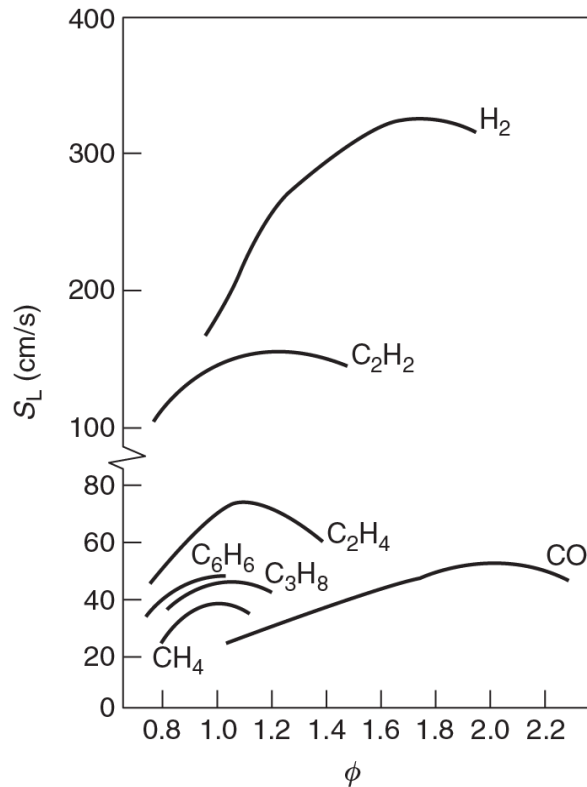


**Figure 1.3** Laminar burning velocity, $S_L$, for various fuels/air at 1 atm, 298 K from (Gibbs & Calcote, 1959; Zabetakis, 1965). In the notation of the present work $S_L$ is $u_l$.

### 1.2.1.3 Flame Stretch Rate

A flame is generally exposed to strain and curvature that change its frontal area, $A$. The stretching rate of the flame was studied by Karlovitz et al. (1953) and the flame stretch and curvature relationship by Markstein (1964). The effects of stretch rate on laminar burning velocity have been interpreted by Candel and Poinsot (1990).

An aerodynamic material surface of area, $A$, experiences a total stretch rate given by:

$$\alpha = \frac{1}{A}\frac{dA}{dt}.$$ (1.4)

In combustion $A$ is the flame surface area, and $\frac{dA}{dt}$ is the rate of change in element area $A$ of the total surface area (Williams, 1985). Consquently, in spherical symmetrical flames with $A = 4\pi r^2$, the flame stretch is a function of the stretched flame speed, $S_n = \frac{dr}{dt}$,

$$\alpha = \frac{2}{r}S_n.$$ (1.5)

The effect of strain rate and curvature on the flame front gives the total stretch rate, $\alpha$:

$$\alpha = \alpha_s + \alpha_c,$$ (1.6)

where $\alpha_s, \alpha_c$, are the flame stretch due to aerodynamic strain and curvature, respectively.

The stretch rate components were defined in (Bradley et al., 1998c) as follow:

$$\alpha_s = \frac{2u_n}{r}$$ (1.7)

$$\alpha_c = \frac{2u_g}{r}$$ (1.8)

To characterise the effect of stretch on the burning rate, a characteristic length defined as burned gas Markstein length, $L_b$, represents the flame speed's sensitivity to stretch rate, and is conveniently measurable. It is the length which shows a near - linear relation between the flame speed and the flame stretch rate (Clavin, 1985) :

$$S_s - S_n = L_b\alpha.$$ (1.9)

This length is found from the slope of the plot of laminar flame speed against flame stretch rate. Its value can be positive or negative. The un-stretched flame speed, $S_s$, is found from the linear extrapolation of the same plot at zero $\alpha$.

Stretching of the flame front has an effect on the burning rate, expressed by the dimensionless Markstein number for strain rate, $Ma_{sr}$ , as:

$$Ma_{sr} = L_{sr}/\delta_l. \tag{1.10}$$

Markstein length for strain rate denoted by $L_{sr}$ and the value of this length was calculated from multiple regression equations described in (Bradley et al., 1996) as a function of $L_s$ and $L_b$ as :

$$L_{sr} = \frac{L_b - L_s}{(\rho_u/\rho_b) - 1} \tag{1.11}$$

where $L_s$ is Markstein lengths for strain and it is a function of $\alpha_s$.

A positive Markstein number, decelerates the burning rate and tends to stabilise the flame. In contrast, negative values accelerate the flame. As flames develop, so do flame surface instabilities wrinkling the flame. This is more marked with a negative Markstein number.

### 1.2.2   Turbulent Deflagration

The key parameter affecting the turbulence is the heat release and the interaction between it and the flame. Simply, the bounded acceleration of a laminar deflagration leads to the generation of turbulence. Different sources used to accelerate the flame with turbulence generators. In spherical vessels, stirring of the fans generates near isotropic turbulence. In burners, are the slotted plates (Bédat & Cheng, 1995; Skiba et al., 2015; Wabel et al., 2017). In closed end-tubes, spiral coil (Shchelkin, 1940) and obstacles (Ciccarelli et al., 2005) are the source of turbulence or turbulence induced due to the high reactivity of the mixture and the formation of a turbulent boundary layer ahead of the flame in smooth tubes (Kuznetsov et al., 2005b; Wu et al., 2007).

Large turbulent eddies wrinkle the flame front causing an increase in flame surface area and the burning rate. As the turbulent flame is more complex than the laminar flame, it can be characterised by different parameters; the root mean square of the fluctuation velocity, $u'$, and integral length scale, $l$, and there are a variety of length scales as the turbulent kinetic energy is dissipated due to molecular viscosity.

The turbulence scales, the turbulent combustion regimes and the correlations of the turbulent burning velocity are discussed in the next section.

**1.2.2.1 Turbulence Parameters and Scales**

The near largest scale is the integral length scale, $l$, and the smallest is the Kolmogorov scale, $\eta$, (Kolmogorov, 1941) where the turbulent kinetic energy is dissipated as heat by molecular viscosity. This is defined by Kolmogorov (1991):

$$\eta = (v^3/\varepsilon)^{0.25}, \tag{1.12}$$

where, $\varepsilon$ , is the dissipation rate and ,$v$, is the kinematic viscosity.

Another length scale, associated with mean strain rate, $u'/\lambda$, is the Taylor length scale $\lambda$. This scale lies between the integral and the Kolmogorov scale. It is related to the Kolmogorov scale by:

$$\lambda = 15^{1/4} R_\lambda^{1/2} \eta, \tag{1.13}$$

where $R_\lambda$ is the Taylor scale Reynolds number, given by:

$$R_\lambda = u' \lambda / v. \tag{1.14}$$

Another important dimensionless group is the turbulent Reynolds number, $R_l$, defined by:

$$R_l = u' l / v . \tag{1.15}$$

A chemical time can be considered as the laminar flame thickness, divided by the laminar burning velocity, $\delta_l/u_l$, while a turbulent eddy lifetime is $\lambda/u'$. The ratio of chemical to eddy lifetime is known as the Karlovitz number, $K$, and is expressed by:

$$K = (\delta_l/u_l)/( \lambda/u'). \tag{1.16}$$

There is a range of length scales and when $K$ is small, the chemical reaction occurs within the eddy, and when it is large, it is not completed during the eddy lifetime. Flame quenching as discussed in Chapter 3 is associated with high $K$, namely high ratio of chemical to eddy lifetime. Eddy lifetime is the reciprocal of strain rate. Sometimes, the turbulent length and velocity scale are chosen to be $\eta$ and $u_\eta$ , respectively, and are expressed as the Karlovitz number, $Ka$ (Bray, 1996; Peters, 2000):

$$Ka = \frac{\delta_l/u_l}{\eta/u_\eta}, \tag{1.17}$$

where $u_\eta$ is the turnover velocity on the Kolmgorov scale, given by:

$$u_\eta = u' \, 15^{1/4}/R_\lambda^{1/2}. \tag{1.18}$$

Peters (2000) defined turbulent Karlovitz number as a function of Kolmogorov length scale as:

$$Ka = \frac{\tau_c}{\tau_\eta} \tag{1.19}$$

The mean strain rate, $u'/\lambda$, is defined by Taylor (1935) as a function of the energy dissipation rate, $\varepsilon$, as follows :

$$(u'/\lambda)^2 = \varepsilon/15\nu \tag{1.20}$$

For isotropic turbulence, $l$, and $\lambda$ are related by:

$$R_\lambda^2 = AR_l, \tag{1.21}$$

where $A$ is a numerical constant and equal to 16 (McComb, 1990) and Eq. (1.21) is expressed by:

$$R_\lambda = 4R_l^{0.5}. \tag{1.22}$$

For isotropic turbulence, integral length scale and taylor microscale can be related as followed:

$$\frac{\lambda^2}{L} = \frac{A\nu}{\acute{u}} \tag{1.23}$$

With $\delta_l$ expressed by $\nu/u_l$, and $A =16$, it follows (Bradley et al., 2005):

$$K = 0.25 \left(\frac{u'}{u_l}\right)^2 R_l^{-0.5}. \tag{1.24}$$

These dimensionless groups are employed in many correlations of turbulent combustion. Equations for $K$ and $Ka$ where employed in Table 3.8 and 3.9.

### 1.2.2.2 Turbulent Burning Velocity

Turbulent burning velocity does not have a specific defintion (Driscoll, 2008). It has been defined differently according to the mass rate of engulfment of unburned gas, or the mass rate of production of burned gas where the

pressure pulse is increasing and this enhances the heat release rate (Abdel-Gayed et al., 1988; Gillespie et al., 2000). It is complex to give a precise definition to the turbulent burning velocity because, generally the mass burning rate is a function of the density, burning rate and the flame area, therefore, any variation in these parameters causes a change in its value (Bradley et al., 2003b). Many correlations based upon experimental work helped to evaluate the turbulent burning velocity based on assumptions and length scales.

It is well established that an increase in the rms turbulent velocity, $u'$, can lead to an increase in turbulent burning velocity, $u_t$, as shown in Fig. 1.4 from (Abdel-Gayed et al., 1985). These values were obtained in a Leeds fan-stirred bomb, in which $u'$ increases linearly with fan speed. The turbulent burning velocity, $u_t$, increases with $u'$, attains a maximum value, then decreases in what is called the bending phenomenon (Abdel-Gayed et al., 1984).
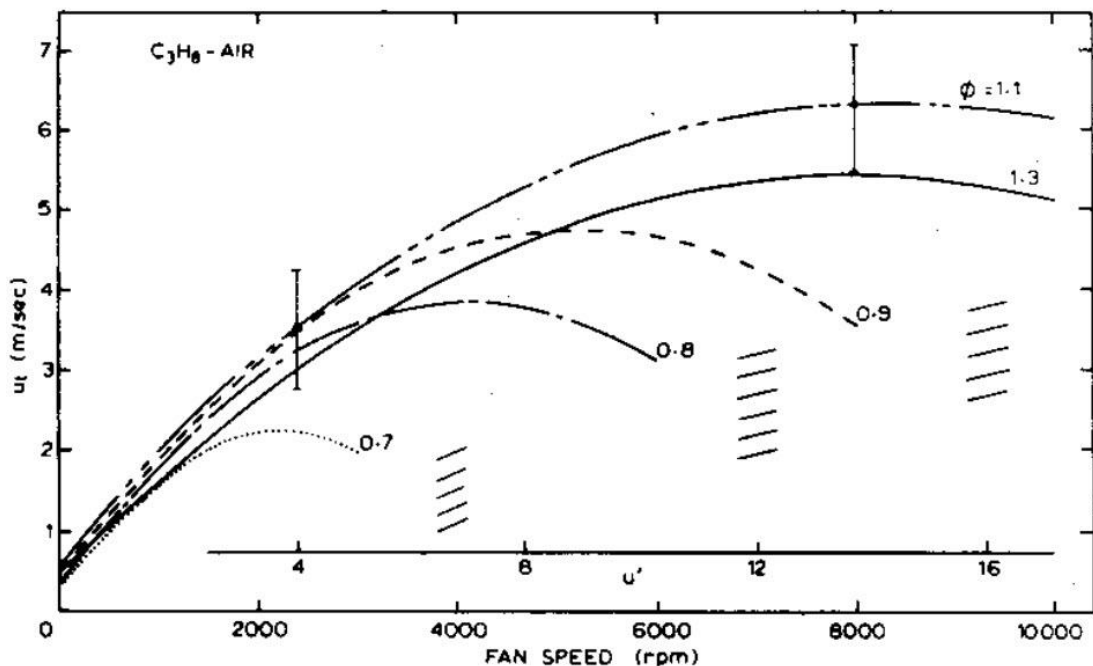


**Figure 1.4** Turbulent burning velocity for propane-air mixture at different equivalence ratio against rms velocity (Abdel-Gayed et al., 1985).

Ultimately the flame is extinguished by the high stretch rate. This occurs when the ratio of chemical to eddy life time becomes too large. With a different explanation, the flame diffuses due to turbulence quicker than the generation of new products via chemical reactions. The decline in $u_t$ may reduce the pressure generated at any shock wave ahead of the flame propagated in a duct, which is sufficient to prevent auto-ignition, and any detonation (Abdel-Gayed et al., 1985).

In the early stages of spherical explosive flame propagation, the flame can only be wrinkled by eddies with a length scale less than the size of the flame kernel. The effective rms velocity is $u'_k$, less than $u'$. The smallest scales of turbulence spectrum, $u'_k$, start to wrinkle the flame front. The flame continues to develop until it exposes to the full spectrum of turbulence when $u'_k$ equals to $u'$, the rms velocity at the full spectrum.

Evaluation of $u'_k/u'$ is by integrating the non-dimensional power spectral density, given in (Bradley et al., 2009b, 2011), over the relevant range of wavelengths, as follows:

$$u'_k = u' \left[ \frac{\sqrt{15}}{R_\lambda} \int_{\bar{k}_{\eta 1}}^{\bar{k}_{\eta 2}} \bar{S}(\bar{k}_\eta) d\bar{k}_\eta \right]^{0.5} \tag{1.25}$$

where $\bar{k}_\eta$ is a dimensionless wave number, $R_\lambda$ is the turbulent Reynolds number based on Taylor microscale and it equals to $(u'\lambda/v)$. The lower limit, $\bar{k}_{\eta 1} = \frac{2\pi\eta}{nL}$, is the maximum wavelength for wrinkling the flame and it is close to the diameter of the flame while the upper limit corresponds to the minimum wave length defined in Gibson scale, $l_G$, as $\bar{k}_{\eta 2} = \frac{2\pi\eta}{l_G}$.

where $n$ is the number of integral length scales and :

$$l_G = 0.133L(\frac{u'}{u_l})^{-3} \tag{1.26}$$

$\bar{S}(\bar{k}_\eta)$ is a non-dimensional power spectral density from (Scott, 1992) to a measured spectra of a wide ranges of $R_\lambda$ as :

$$\bar{S}(\bar{k}_\eta) = \frac{0.01668R_\lambda^{2.5}+3.74R_\lambda^{0.9}-70R_\lambda^{-0.1}}{1+(0.127R_\lambda^{1.5}\bar{k}_\eta)^{5/3}+(1.15R_\lambda^{0.622}\bar{k}_\eta)^4+(1.27R_\lambda^{0.37}\bar{k}_\eta)^7} \tag{1.27}$$

### 1.2.2.3 Turbulent Combustion Diagrams

Turbulence wrinkles the flame causing a change in the surface area. At the same time, there are interactions between the flame and the eddies. These interactions are addressed in a combustion diagram. Many diagrams have been introduced to show various combustion regimes (Abdel-Gayed et al., 1989; Borghi, 1985; Peters, 1988; Poinsot et al., 1991; Williams, 1985) as a function of some dimensionless groups represented in length, velocity, time scales involving dimensionless groups.

Laminar flame thickness, $\delta_l$, and chemical lifetime, $\tau_c$, are the length and time scales participated by the flame in the combustion regimes. Integral, $l$, Taylor, $\lambda$ and Kolmogorov, $\eta$, length scales and eddylife time, $\tau_K$ are introduced by turbulence in the regimes as well.

In the beginning, there was an attempt by Barrere (1974) to establish the difference between flame types. This study was a step to classify the turbulent flames and relate it with same types of dimensionless groups as well. These groups link the turbulent flame parameters to some physical-chemical parameters for laminar flame. Barrere (1974) evidenced four different regimes: pseudo laminar flames; wrinkled flames; volumetric combustion; and pocket flames. However, the turbulent combustion nature then well-discussed in (Borghi, 1985) and (Abdel-Gayed et al., 1989).

For the development to the regime, Peters (1988) studied the entering of laminar flamelets through turbulent flow field for premixed and non-premixed combustion: showing how the length scale and flame thickness play an important role for composing thin layers of embedded flamelets. Combustion regime developed by Peters (2000), is shown in Fig. 1.5.
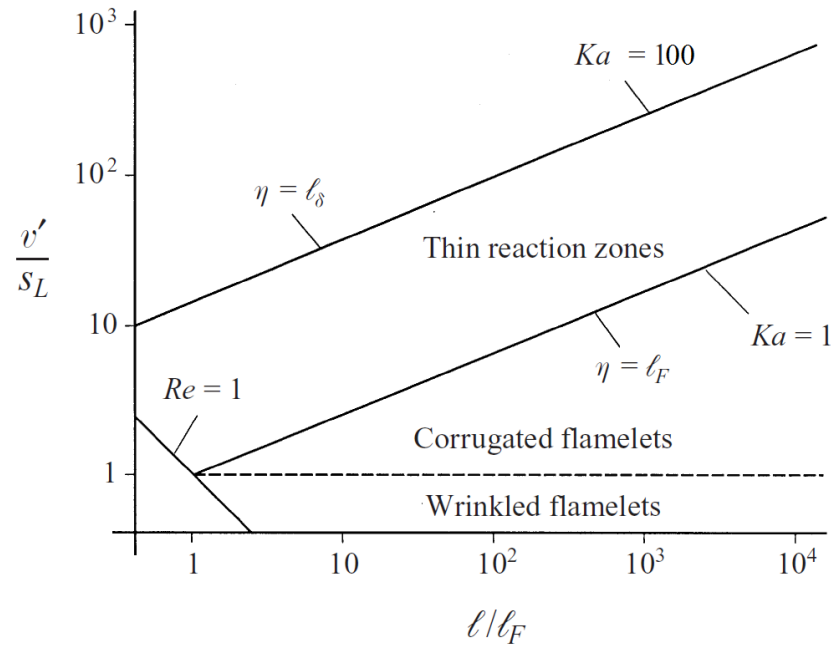
**Figure 1.5** Turbulent combustion regime from (Peters, 1999), In the notation of the present work, the y axis is $u'/u_l$ and the x axis is $l/\delta_l$.

Several regimes have been identified:

- **Laminar flame regime**

Where the Reynolds number, $Re$, is low, i.e. the flow is laminar. The line denoted by $Re=1$, is the border between the laminar and turbulent flames.

- **Flamelet regime**

In this regime, laminar flamelets starts to introduce into the turbulent environment, and it consists of two sub-domains: wrinkled and corrugated flamelets, characterised by $\frac{u'}{u_l}$.

$Ka$ in this regime is lower than 1 and this means that the chemical time scale $\tau_c$ is smaller than the eddy time scale $\tau_k$, and there is no effect on flame inner structure, and flame seems to be still laminar-like with little wrinkling. The flame thickness is smaller than the smallest turbulent scale $\eta$.

➤ **Wrinkled flamelet regime**

When $\frac{u'}{u_l} < 1$, so turbulence intensity is small, and the flame structure is slightly wrinkled because the large eddies are not big enough to stop the chemical reaction represented in $u_l$ which is dominating in this regime.

➤ **Corrugated flamelet regime**

This occurs when $\frac{u'}{u_l} > 1$ and $Re > 1$ also, thus the wrinkling in the flame structure starts to be more credible. Nevertheless, $Ka$ is still lower than unity.

• **Thin reaction zone**

The boundary between the flamelets regime and the thin reaction regime is characterised by $Ka = 1$, Klimov-williams criterion (Williams, 1985) where the flame thickness is equal to $\eta$.

At $Re > 1$, $Ka > 1$, flames is said to be in the thin reaction zone. The smallest eddies of turbulence can penetrate the preheat zone thickness and some pockets of fresh and burnt gases are formed. The flame structure is convoluted.

• **Broken reaction regime**

In this regime, $Ka > 100$, Chemical reaction time scale, $\tau_c$, is longer than turbulent characteristic time scale. Mixing in this regime is enhanced. Thus, Kolmogorov eddies can penetrate the reaction zone and fragments of flame occur and the flame extinguish.

The thin reaction and broken reaction regimes are of the interest in the present work.

### 1.2.2.4 Turbulent Burning Velocity Correlations

Due to such variations in turbulent burning velocity, it is important to know how to evaluate it. There are many correlations and empirical formulas to estimate the turbulent burning velocity. Some of these correlations have been presented for specific fuels hydrocarbons and hydrogen or specific conditions low or high pressure in different applications: burners or constant volume

vessels (Abdel-Gayed & Bradley, 1981; Bradley et al., 1992; Bray, 1990; Koroll et al., 1993; Muppala et al., 2005; Shy et al., 2000; Tamadonfar & Gülder, 2014).

Damköhler (1940) early model relates the burning velocity to the surface area, showing that the turbulence effect on burning rate is due to the wrinkling of the thin reaction layer. The velocity ratio, $u_t/u_l$ is proportional to the area ratio for turbulent and laminar flame, $A_t/A_l$.

Kobayashi et al. (2005) derived a correlation for the turbulent burning velocity of methane-air mixtures for a wide range of initial pressures, $P_o$ of 0.1: 1 MPa, in a high pressure cylindrical burner. It was found that as the pressure increases, the turbulent burning velocity also increases. The correlation shows the effect of pressure on the turbulent burning velocity:

$$\frac{u_t}{u_l} = 5.04 \left[ \left( \frac{P}{P_o} \right) \left( \frac{u'}{u_l} \right) \right]^{0.38} \tag{1.28}$$

The correlation of (Gülder, 1991) was developed for wrinkled flamelets experimentally as a function of $R_l$ as follows:

$$(u_t/u_l) - 1 = 0.6(u'/u_l)^{1/2} R_l^{1/4}. \tag{1.29}$$

Zimont (2000) developed a similar correlation from his experimental and theoretical study, but employed a different constant instead of 0.6 in the Gülder formula. This adjustable constant was in the range of 0.5-0.7 for $H_2$ and 0.5 for all hydrocarbons. Bradley et al. (2003b) employed simultaneous laser sheet Mie-scattering experiments with propane and methane air mixtures explosion in a spherical vessel to study the radial distribution of burned and unburned gas in a spherical turbulent flame, as shown in Fig. 1.6.

An important aspect is what $u_t$ means. In particular terms, it is required to express the mean rate of burning.
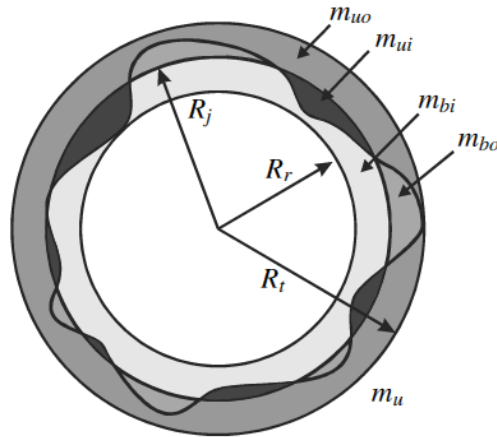
**Figure 1.6** Spherical explosive propagation at instant showing the reference radii and masses of burned and unburned gas (Bradley et al., 2003b).

Different radii were defined, in terms of the associated burned and unburned gas boundaries. Three radii are shown in the figure. The outermost radius is that of the spherical tip radius, $R_t$, and the innermost radius is the root radius, $R_r$. Any general radius is defined as $R_j$. This general radius can be defined in different ways, related to volume and mass. The problem is to decide upon the most appropriate radius to define the area associated with $u_t$. Masses shown in the figure are the masses of burned gas inside, $m_{bi}$ and outside, $m_{bo}$, of the sphere of radius, $R_j$. Also, the masses of unburned gas inside, $m_{ui}$ and outside, $m_{uo}$ of the same sphere.

There is a large difference between engulfment and mass burned turbulent burning velocities. It is shown in (Bradley et al., 2003b) that when the general radius $R_J$ is equal to a radius, $R_v$, at which the total volume of burned gas outside the sphere is equal to total volume of unburned gas inside it, the mass burned turbulent burning velocity is given by:

$$u_t(R_v) = \frac{\rho_b}{\rho_u} \cdot \frac{dR_v}{dt}. \tag{1.30}$$

However, schlieren measurements are more convenient than sheet measurements, it is shown that there is a linear relationship between, $(\rho_b/\rho_u)(dR_{sch}/dt)$ from schlieren experiments and $u_t(R_v)$ from Mie

scattering, as shown in Fig. 1.7 from (Bradley et al., 2003b). The gradient of this line demonstrates that the mass burned turbulent burning velocity is equal to:

$$u_{tr} = \frac{1}{1.11} \frac{\rho_b}{\rho_u} \frac{dr_{sch}}{dt}, \qquad (1.31)$$

where $r_{sch}$, is the flame radius measured by schlieren technique. Equation (1.31) is employed in Section 3.4.
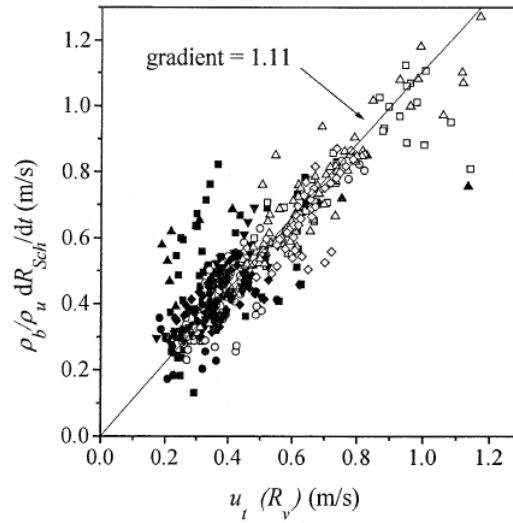


**Figure 1.7** Linear relationship between Mie-scattering, $u_t(R_v)$ and schlieren images $(\rho_b/\rho_u)(dr_{sch}/dt)$. Filled symbols for lean mixtures and open symbols for rich mixtures (Bradley et al., 2003b).

A comprehensive correlation of normalized value of $u_t$, in terms of $K$ and $Ma_{sr}$ up to a pressure of 3.5 MPa is given in (Bradley et al., 2013). Relationships are expressed in the form:

$$U = \frac{u_t}{u_k'} = \alpha \, K^\beta, \qquad (1.32)$$

as $\alpha, \beta$ are constants, defined according to $Ma_{sr}$, in (Bagdanavicius et al., 2015) with :

$$\alpha = \begin{cases} 0.09(7 - Ma_{sr}) & for \ Ma_{sr} < 0 \\ 0.023(30 - Ma_{sr}) & for \ Ma_{sr} > 0 \end{cases} \qquad (1.33)$$

$$\beta = \begin{cases} 0.0103(Ma_{sr} - 30) & for\ Ma_{sr} > 0 \\ -0.008(Ma_{sr} + 30) & for\ Ma_{sr} < 0 \end{cases} \tag{1.34}$$

These relations cover different combustion phases, based upon a wide range of experimental data for different fuels.

These workers related the turbulent burning velocity to the wrinkled surface area of the flame, $A$, to the area, $a$, associated with $u_t$ and the probability of flame propagation, $P_b^{0.5}$ in:

$$u_t/u_l = \frac{A}{a} P_b^{0.5}. \tag{1.35}$$

This work used experimental data from the Leeds spherical bomb and a Cardiff high speed burner. It showed the effect of Markstein number on the probability of burning and the value of turbulent burning velocity. A positive Markstein number revealed the decrease in probability of flame growth and, in turn, the turbulent burning velocity.

Tamadonfar and Gülder (2014) developed two correlations for turbulent burning velocity at the leading edge of a Bunsen burner and at half-burned gas region of methane/air mixture, at different equivalence ratios, giving a highest turbulence intensity $u'/u_l$=24.

$$(u_t/u_l)_{Leading\ edge} = 1 + 7.6\ \varphi^{-1.87}(u'/u_l)^{0.62}(u/u_l)^{-0.52}(l/\delta_l)^{-0.52}\ , \tag{1.36}$$

$$(u_t/u_l)_{half\ burned} = 1 + 0.018\ \varphi^{-4.03}(u'/u_l)^{0.62}(u/u_l)^{-0.36}(l/\delta_l)^{1.35}, \tag{1.37}$$

where $u$ is the main flow velocity in the burner.

## 1.3  Flame Quenching

In orthodox engines, lean burn of $H_2$ is a possible strategy, and in a domestic heating $CH_4$ might be replaced by $H_2$. In both these instances, lean burn flame quenching is an important consideration and these gases rise to a comprehensive study of quenching limits for both premixed and jet flames in the present work.

Flame quenching and extinction of a flammable mixture usually occurs as a result of compositional change, high aerodynamic strain rate, or heat loss: all of which make the mixture less reactive.

Flame quenching has been studied under varied experimental conditions, in burner (Ji et al., 2010; Law et al., 1988; Law et al., 1981; Yang & Shy, 2002),test tubes (Chomiak & Jarosiński, 1982), orifices (Kuznetsov et al., 1999; Thibault et al., 1982) and closed vessels (Abdel-Gayed et al., 1987; Al-Khishali et al., 1983; Bradley et al., 1996; Bradley et al., 2007b).

Figure 1.8 reproduces a sketch from (Abdel-Gayed et al., 1989). Burning stages are shown, followed by extinction. Fragments from the flame front are seen as small parts, indicative of intermittent burning. The flame shown finally disintegrates.
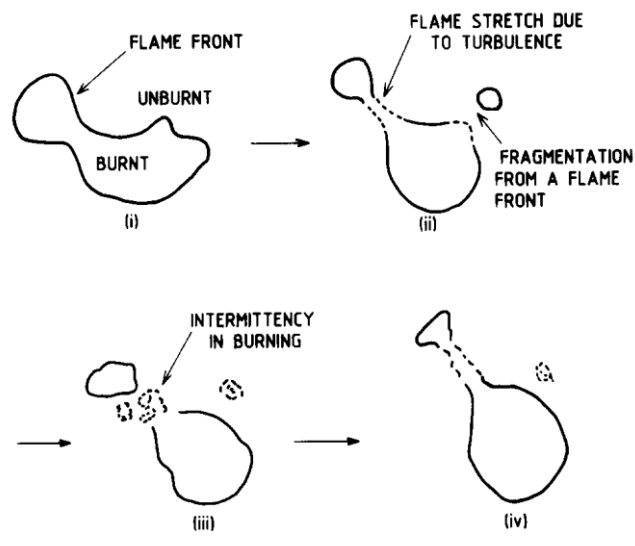


**Figure 1.8** Flame front disintegration and quenching (Abdel-Gayed et al., 1989).

### 1.3.1 Extinction Stretch Rates

Flames exposed to a local quench when the flame stretch approaches the extinction stretch (Poinsot et al., 1991). Flames near to stoichiometry are difficult to quench (Law et al., 1988) and this means that the extinction stretch is higher for those flames. Extinction stretch rates are divided into laminar and turbulent extinction stretch rates.

**1.3.1.1 Laminar Extinction Stretch Rates**

Flame quenching is usually associated with high values of the stretch rate, with a dependence on Markstein number. Whilst extinction stretch rates, $\alpha_q$, have been measured under steady state conditions, these can be exceeded in short time transients, without ensuing extinctions (Donbar et al., 2001). In practical combustion, extinctions limit the volumetric heat release rates that can be obtained.

Extinction stretch rates, in laminar flows have been measured by Law et al. (1988), over wide ranges of stretch rates, fuels and equivalence ratios in symmetrical counter-flow, twin- flame configurations. In (Law et al., 1981) the roles of diffusion, conductivity and Lewis number, $Le$, were emphasised in the extinction of laminar flames.

Here the key parameter is the Lewis number, $Le$, which relates the thermal to mass diffusivity across the flame front by:

$$Le = k/(\rho C_p D),\qquad\qquad(1.38)$$

where, $D$, is the diffusion coefficient for the deficient reactant.

More generally, Lewis and Markstein numbers, in combination with flame stretch rate, also influence burning velocities (Bradley et al., 1992; Dixon-Lewis, 1988)

In (Bradley et al., 1992), the experimental extinction stretch rates (Law et al., 1988) were compared with the chemical kinetic computed values of(Dixon-Lewis, 1988; Kee et al., 1989; Stahl & Warnatz, 1991; Stahl, 1988). For $CH_4$ and $C_3H_8$ these numerical results tended to over-predict $\alpha_q$. It is thus convenient to generalise extinction in terms of a Karlovitz laminar flame extinction stretch factor, $K_{ql}$, equal to:

$$K_{ql} = \alpha_q\,\delta_l/u_l.\qquad\qquad(1.39)$$

Egolfopoulos and co-workers have studied extinctions of both premixed and diffusion counter-flow flames. Values of $\alpha_q$ were measured (Dong et al., 2005; Holley et al., 2006; Ji et al., 2010; Park et al., 2011; Veloo et al., 2010; Wang

et al., 2009; Wang et al., 2011), and modelled through chemical kinetics (Egolfopoulos, 1994; Egolfopoulos & Campbell, 1996; Kee et al., 1989). Experimentally in (Holley et al., 2006), it was found that lean *i*-octane and *n*-heptane was more readily quenched than lean alcohol flames. In (Veloo et al., 2010), quench stretch rates of *n*-butanol are predicted, based upon mathematical modelling, in (Sarathy et al., 2009; Westbrook et al., 2009), and also in experiments. Comparisons are also made between ethanol and *n*-butanol/ air mixtures. These showed similar extinction trends for both fuels. Experimental studies of non-premixed flames (Holley et al., 2007) with single component hydrocarbons, surrogates, and jet fuels, found the higher carbon fuels to be less resistant to quench. A comparative study (Bradley, 2008), showed $H_2$/air mixtures (Dong et al., 2005) to be the most resistant to quench, in comparison with *i*-octane (Holley et al., 2006), $CH_4$ and $C_3H_8$ (Law et al., 1988).

Extinction stretch rates of aromatic hydrocarbon and jet fuel mixtures, have been measured at elevated temperatures, and atmospheric pressures, in the counter flow twin-flame configuration (Hui et al., 2012; Kumar & Sung, 2007), and compared with the formulation of Kee et al. (1989).

### 1.3.1.2  Turbulent Extinction Stretch Rates

Kuznetsov (1982) employed a chemical to the eddy lifetime criterion , but with the latter given by $l/u'$, whilst Abdel-Gayed et al. (1989) employed $\lambda/u'$ for this parameter as discussed in Section 1.2.2.1.

This demonstrated the nature of turbulent flame quenching through schlieren images of fragmenting and quenching flame kernels in a cylindrical explosion vessel, with fan-generated turbulence. Their correlation of available experimental flame quench data showed a dependence upon $Le$ in one of the two quench regimes:

$$u'/u_l \geq 0.71 R_l^{0.5} \qquad\qquad for\ R_l < 300, \qquad\qquad (1.40)$$

$$u'/u_l \geq 3.1(R_l\ /\ Le^2) \qquad\qquad for\ R_l > 300. \qquad\qquad (1.41)$$

Meneveau and Poinsot (1991) evaluated the stretch rate of flamelets using detailed numerical simulations of vortex-flame interaction and a model of intermittent turbulence. The onset of flame quenching was expressed in plots of $u'/u_l$ against $l/\delta$, with high values of $u'/u_l$, being required or $l/\delta \leq 10$. They sensibly cautioned that quenching is a strong function of heat losses and that these are difficult to estimate in experiments. Both Abdel-Gayed et al. (1989) and Poinsot et al. (1991) show the Klimov-Williams criterion overestimates the flame quenching.

A probability density function, (pdf), of strain rates was derived from direct numerical simulations by Yeung et al. (1990). This enabled pdfs of flame stretch rate to be generated (Bradley et al., 2003a). With the lower (negative) and upper (positive) stretch rate limits, these could yield theoretical values of flame propagation probabilities.

Bradley et al. (1998b) reproduced the upper and the lower limits of quenching on extended Borghi diagram as seen in Fig. 1.9. The upper limit is resulted from DNS work of Poinsot et al. (1991) and the lower limit is Klimov-Williams theory (Bray, 1980; Williams, 1985). The constant $K$ lines are extracted from (Abdel-Gayed et al., 1989). This diagram is discussed in the present work for the quenching limits for the comparison of the premixed and jet flames in Section 5.5.
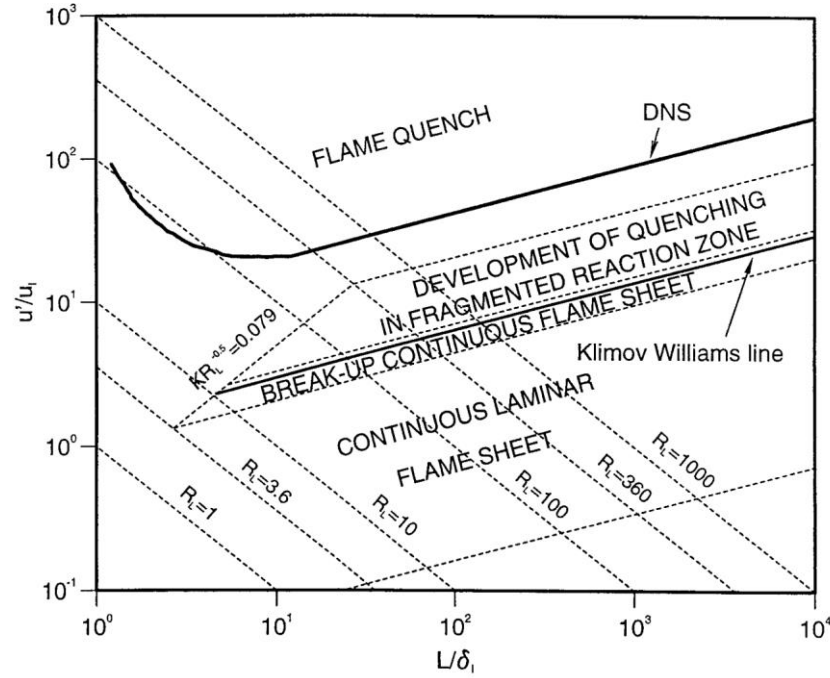
**Figure 1.9** Extended Borghi diagram showing the upper limit of quenching reproduced from (Bradley et al., 1998b).

Further details of flame extinctions were obtained experimentally in (Bradley et al., 2007b) from the Leeds fan-stirred explosion vessel with values of $u'$ up to 7 m/s, with different fuel air mixtures at pressures up to 1.5 MPa measured probabilities of flame propagation, as distinct from extinction. Both pressure and $\varphi$ had probabilities of 80% ($p_{0.8}$) and 20% ($p_{0.2}$) for flame propagation were expressed as a function of $K$ and $Ma_{sr}$ by:

$$K(Ma_{sr} + 4)^{1.4} = 37.1 \quad at \quad -3 \le Ma_{sr} \le 11 \quad (for\ p_{0.2}) \tag{1.42}$$

$$K(Ma_{sr} + 4)^{1.8} = 34.4 \quad at \quad -3 \le Ma_{sr} \le 11 \quad (for\ p_{0.8}) \tag{1.43}$$

Experimental values of the probability of flame propagation are presented and compared with theoretical flame propagation probabilities in (Bradley et al., 2007b), derived by integrating the flame stretch rate probabilities between the appropriate limits. However, theoretical limitations arise from uncertainties in the positive and negative flame extinction stretch rates, whilst optical

diagnostics have shown flame extinctions do not necessarily occur when localised stretch rates briefly exceed the extinction stretch rates (Donbar et al., 2001). Following the earlier quenching laws for the two regimes (Abdel-Gayed & Bradley, 1985), and according to the results as the flame propagation probability is 80%, then at $R_l \geq 300$, the flame would quench if $KLe > 2.4$, although predictions based on $Ma_{sr}$ were preferred.

Turbulent combustion diagram shown in Fig. 1.10 has been reproduced from (Bagdanavicius et al., 2015) and composed of three regimes: regime (A), regime , (B) and regime (C).
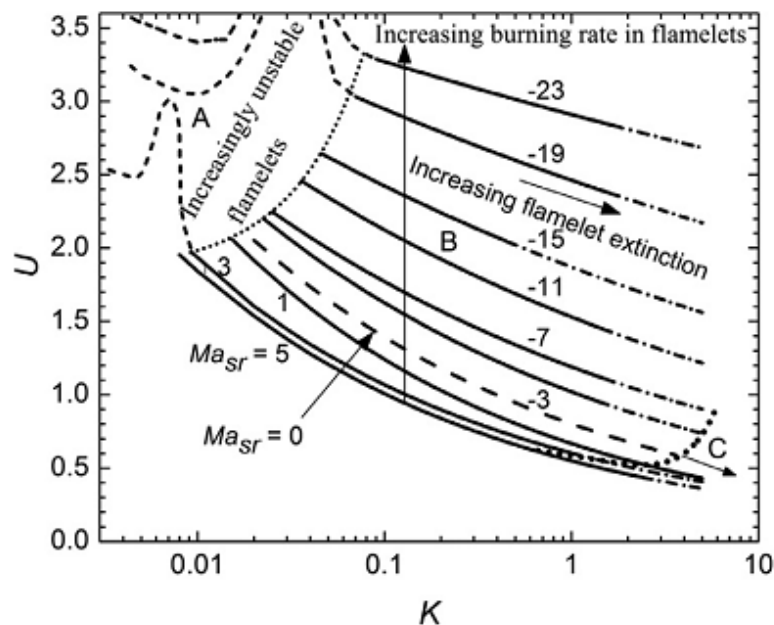


**Figure 1.10** Turbulent combustion regime (*U/K*) diagram (Bagdanavicius et al., 2015).

The turbulent burning velocity, $u_t$, is normalised by $u_k'$, to give $U$. The strain rate influences upon $U$ are expressed by $K$, and those of the strain rate Markstein number, $Ma_{sr}$, are shown in Fig. 1.10, from (Bradley et al., 2013), with $Ma_{sr} = 0$ added from (Bagdanavicius et al., 2015). The different regimes of premixed turbulent burning are also indicated. Regime (B) covers both positive and negative $Ma_{sr}$. It is one of normal turbulent flame propagation, whilst regime (C) is one in which flames are extinguished by excessive stretch rate. The present study re-examines the extent of the latter in Section 3.6.

## 1.4 Auto-ignition and Detonation

A plentiful economic supply of $H_2/O_2$ from water in stoichiometric proportions could lead to those gases being used auto-ignitively in units that include burning and auto-ignition.

### 1.4.1 Auto-ignition

Auto ignition is a spontaneous combustion without any external source of ignition (Lefebvre et al., 1986). It is a self-sustained reaction of the flammable mixture. The time for its occurrence is the autoignition delay time, $\tau_i$. If $P$ and $T$ are rapidly generated in this time, autoignition occurs. Examples of values of $\tau_i$ are given in Fig. 1.11.

Spadaccini and Colket Iii (1994) defined it as the interval time between the mixture shock heating and the start of the quick reaction phase. Induction, or auto-ignition delay time, is tabulated for homogeneous mixtures for different temperatures, $T$ and pressures, $P$ as shown in Fig. 1.11 whereas the variations in $\tau_i$ for different mixtures with $P$ and $T$.
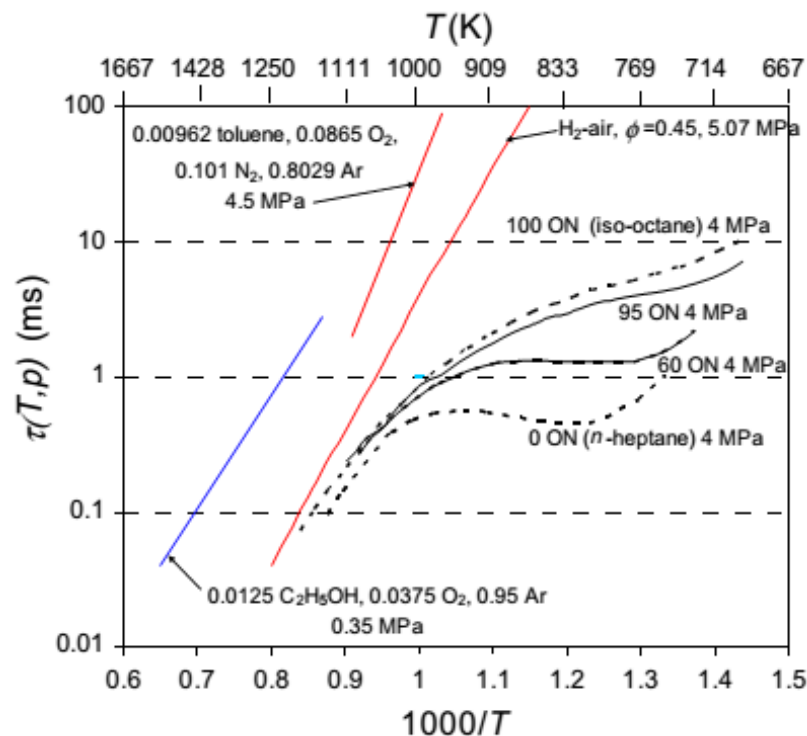


**Figure 1.11** Auto-ignition delay time for different mixture against $1000/T$ (Bradley & Kalghatgi, 2009).

When the heat released by the auto-ignition, on a short enough excitation time scale, $\tau_e$, is fed into the associated pressure pulse a damaging detonation wave can be created. Ignition delay times in the present work are discussed in Section 4.3 on stoichiometric $H_2/O_2$ mixtures.

Ignition delay time is measured predominately in either shock tubes (Ciezki & Adomeit, 1993; Lifshitz et al., 1971; Pang et al., 2009; Zhang et al., 2012) or Rapid Compression Machines (RCMs) (Griffiths et al., 1993; Mittal et al., 2006; Strozzi et al., 2012).

In shock tubes, a transmitted shock waves produce in a tube with two sections as shown in Fig. 1.12, one section is at high pressure and works as a driver to the high-pressure gas through the tube and the other section is the driven section which contains the test gas at low pressure. These sections are separated by a diaphragm (barrier).

The shockwaves form once the diaphragm removed or ruptured as the high-pressure gas moves into the lower pressure gas section. The strength of this shockwave depends on the differential pressure increase. This strengthened shock wave initiates the auto-ignition of the test gas in the driven section.



**Figure 1.12** Shock tube basic concept.

### 1.4.2   Detonation

Detonation occurs when a shock wave and chemical reaction are coupled. Unlike deflagration discussed in Section 1.2, detonation waves are dependent upon the propagation of shock waves and the elevations of temperature and pressure they produce. Consequently, they are more dangerous than deflagration waves. The detonation propagation velocity is approximately two kilometres per second for hydrocarbons and roughly less than three kilometres per second for highly reactive mixtures such as stoichiometric

hydrogen-oxygen, ethylene-oxygen and acetylene-oxygen mixtures. The present study is of the conditions that can give rise to a detonation, rather than of detonation interactions. Nevertheless, it is useful briefly to review the structure and interactions of detonation waves.

Detonations often have a three-dimensional structure, a train of shock waves and reaction zones that move with a supersonic speed. The structure of a detonation wave is shown in Fig. 1.13. The detonation wave consists of incident shock, transverse waves and Mach stems. The Mach stem is created by the intersection of the incident shock and the transverse wave and it shows higher post-shock temperature and pressure than the incident shock. The three waves intersect at a point called the triple point.

The detonation can be single headed or multi-headed, depending on the number of transverse waves. The resulting cellular structure of a detonation, shown in the figure, refers to the trajectory of the triple point created. Increasing the number of cells means that the detonation is more destructive. The detonation cell size is termed the detonation width, $\lambda$.

Because the Mach shock is much stronger than the incident shock, the induction time behind it is low compared to that of the incident shock. As depicted in the figure, there is a layer called the shear layer. This layer separates the gas behind the Mach and incident shock and it is formed due to the difference in gas velocity between both shocks. At the triple point, the Mach stem is coupled with the chemical reaction zone, which in turn reduces the induction time and as the Mach stem moves, it decays and decouples from the chemical reaction zone, decreasing its strength and transforming it into an incident shock.
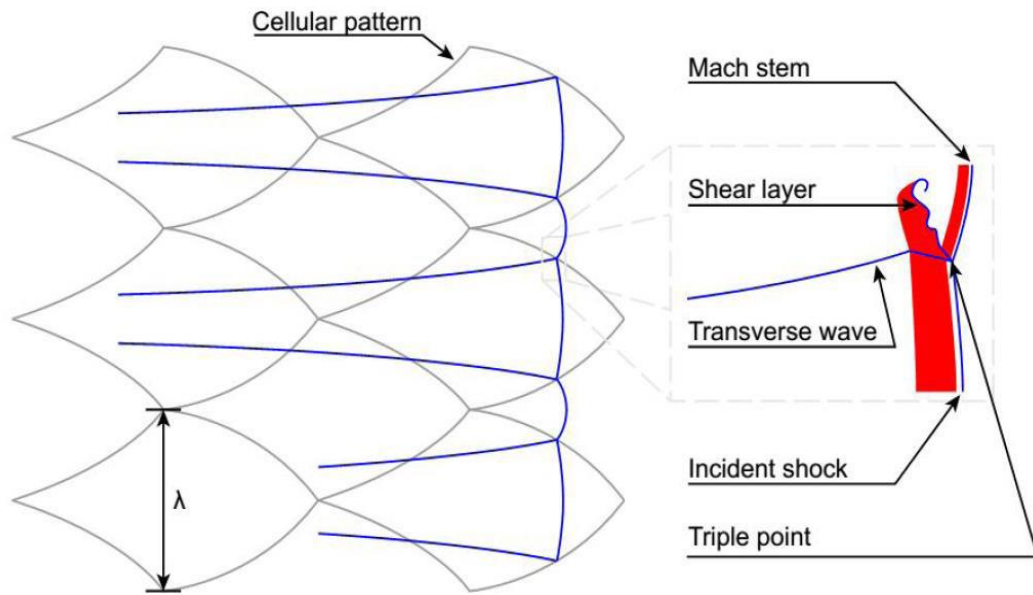
**Figure 1.13** Detonation pattern composed of Mach stem, incident shock and transverse shock (J. Lee, 2008).

### 1.4.3   Autoigntion Velocity and ε- ξ Detonation Peninsula

Autoignition triggered by hot spots. These hot spots form a cause of flammable gas inhomogeneity or temperature gradients. Reactivity gradient mechanism by Zel'dovich et al. (1970), developed at hot spots in the unreacted mixture ahead of the flame, showed that this gradient, increases what is called autoignition velocity, $u_a$. Detonation triggers when the pressure pulse, resulted from the autoignition, is high enough. This occurs when the autoigntion velocity is close to the speed of sound, $a$. At that time the heat release rate is suffiicent to induce a detontion.

The autoignitive velocity, is given by (Bates et al., 2016; Bradley, 2012; Bradley & Kalghatgi, 2009; Bradley et al., 2012):

$$u_a = (dr/d\tau_i) = (dr/dT)(dT/d\tau_i) = (dr/dT)(\tau_i E/RT^2)^{-1} \qquad (1.44)$$

where $r$ is the distance along the temperature gradient, $dr/dT$ is the reciprocal of the reactivity gradient in (mm/K) and $E$ is the activation energy. Low values of autoignition delay times, $\tau_i$, causes an increase in $u_a$ values.

A critical value of the temperature gradient, $(dT/dr)_c$ is attained when $u_a$ is equal to the acoustic velocity, $a$, and:

$$a = (dr/dT)_c(\tau_i E/RT^2)^{-1} , \tag{1.45}$$

To see the interaction between the speed sound and autoignition velocity , a dimensionless group, $\xi$, (Bates et al., 2016; Bradley, 2012; Bradley & Kalghatgi, 2009; Bradley et al., 2012) was found as:

$$\xi = a/u_a = (dr/dT)/(dr/dT)_c \tag{1.46}$$

This group is a function of ignition delay time, $\tau_i$, and expresses the pressure pulses effect on the ignition. Thereofore, if $\xi$ is close to unity, the ignition is strong and a developing detonation induces. Low values of $\xi$ occur at high auto-ignition velocity, $u_a$.

If the radius of the hot spot is $r_o$ and the excitation time for heat release is $\tau_e$ then:

$$\varepsilon = (r_o/a\tau_e). \tag{1.47}$$

This is the ratio of the residence time within the hot spot of the pressure pulse that is generated by the rate of change of the heat release rate, to the duration for the heat release, the excitation, time, $\tau_e$, (Bates et al., 2016; Gu et al., 2003) and it expresses the energy transferred into the acoustic wave moves through the hot spot.

In a detonation, reaction might decouple from the shock and it has been found that the coherence and stability of a detonation are enhanced by low values of $(\tau_i/\tau_e)(E/RT) = \bar{E}$ (Liang et al., 2007; Short & Sharpe, 2003; Sirmas & Radulescu, 2017).

To this product can be added $lnT/d\bar{r}$ (Bradley, 2012), the dimensionless gradient at a hot spot, and it follows that:

$$\xi\varepsilon = \bar{E}(dlnT/d\bar{r}). \tag{1.48}$$

where $\bar{r} = r/r_o$ , $E$ is the local global activation energy in (J/mol), $R$ is the gas constant in (J/mol.K).

Detonation peninsula plots the ratio of acoustic to autoignitive velocity, $\xi$, against $\varepsilon$ as shown in Fig. 1.14. This plot shows the upper and lower limits, $\xi_u, \xi_l$, for detonation. This peninsula is employed in Section 5.1 in the discussion of auto-ignition of $H_2/O_2$ mixtures.

In general, the figure shows that the developing detonation peninsula is associated with low values of $\xi$ (close to unity) and high values of $\varepsilon$.

When $\xi$ is lower than unity, thermal explosion induces where the reaction wave is supersonic but at the same time it is not coupled with pressure waves. Deflgration occurs at higher $\xi$ than the upper limit, $\xi_u$, outside the detonation peninsula. Subsonic autoignition regime located where $\xi$ equals or a bit higher than the upper limits. Lower values of $\xi\varepsilon$ indicate a developing detonation where $\bar{E}(dlnT/d\bar{r})$ is low. This means a stable and strong detonation.
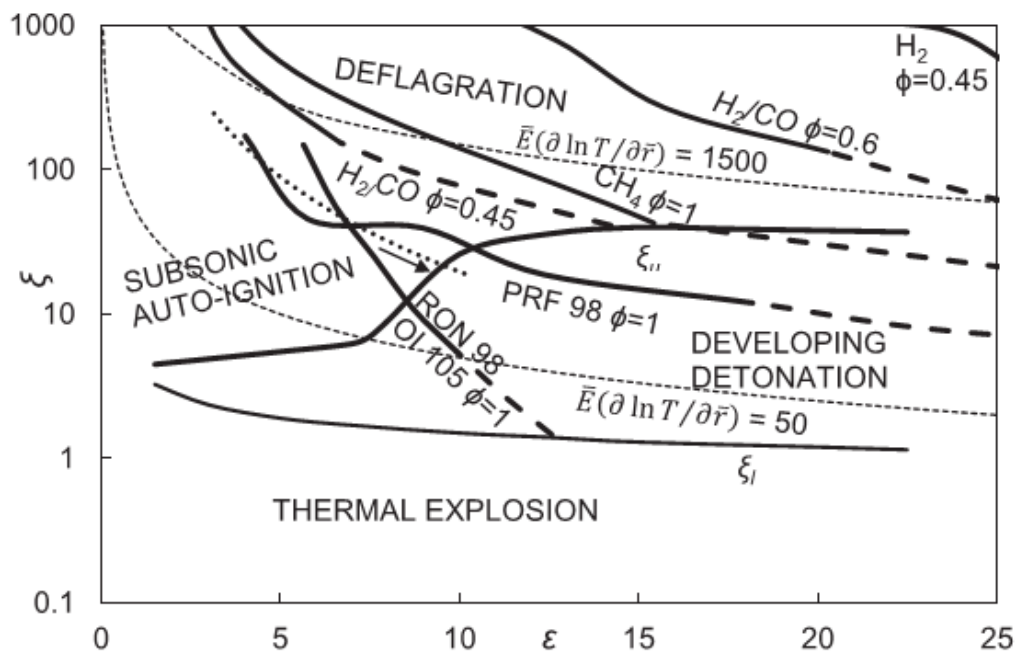


**Figure 1.14** Detonation Peninsula reproduced from (Bates et al., 2017a).

## 1.5  Deflagration to Detonation Transition (DDT)

Full understanding of the deflagration to detonation transition (DDT) is still incomplete, this is one of the main problems facing combustion theory. It can occur in different combustion applications such as coal mines, gaseous

explosions in pipes; and engines. It indicates an abrupt change of a deflagrating wave into a supersonic detonation wave. It is one of the key factors of the present work as discussed in Section 4.6.

When a combustible mixture ignites at one end of a tube, a laminar flame can initially be observed which accelerates and changes into a turbulent structure generating a shockwave, and ultimately DDT can occur, this features as a violent explosion, as seen in Fig. 1.15.
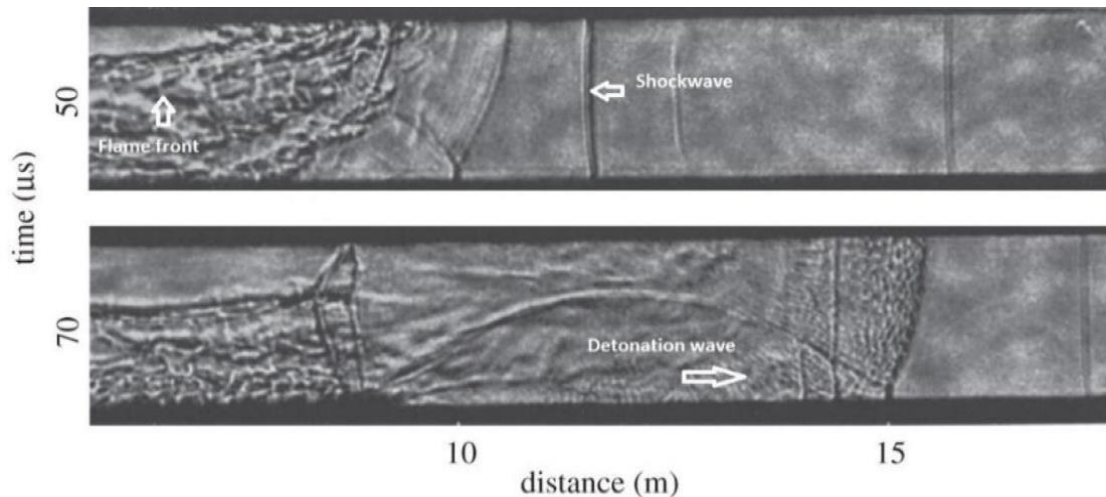


**Figure 1.15** Detonation initiation in stoichiometric hydrogen/oxygen mixture in the early study of Urtiew and Oppenheim (1966).

The deflagration to detonation transition arises from a flame propagating in a duct when the burning velocity is sufficiently high to create a shock wave strong enough to trigger autoignition discussed in Section 4.1. The heat release from this which feeds into the pressure wave created by the originating rate of change of heat release rate, may be sufficient to create a detonation.

A precursor for the onset a detonation is the flame acceleration process (FA). This process will lead to a fast deflagration which eventually gives an enough pressure rise to trigger a detonation. This fast deflagration can lead to the formation of hot spot (Khokhlov et al., 1999; Lee, 1977) discussed in Section 1.4.3. With more flame acceleration, this would induce a detonation. This process is called deflagration to detonation transition (DDT).

### 1.5.1    Pulse Detonation Engines (PDEs)

An application to DDT is the pulse detonation engines. It is going to be an effective approach for propulsion systems as it offers a higher thrust to weight ratio, low cost and higher thermal efficiency.

The difference between the pulse detonation engines and pulse jet engines is the combustion wave. Pulse jet engines produce deflagration wave as a subsonic wave unlike pulse detonation engine which produce detonation wave (supersonic).

Simply, pulse detonation engine is a tube closed at one end filled with a fuel-air mixture and ignite similarly to the model proposed by Bradley et al. (2008). Detonation wave produces and the combustion products leave out the tube's open end resulting in a thrust. The operating cycle is shown in Fig. 1.16. In the first stage, all reactants must have been purged from the previous cycle before the entrainment of the fresh mixture.
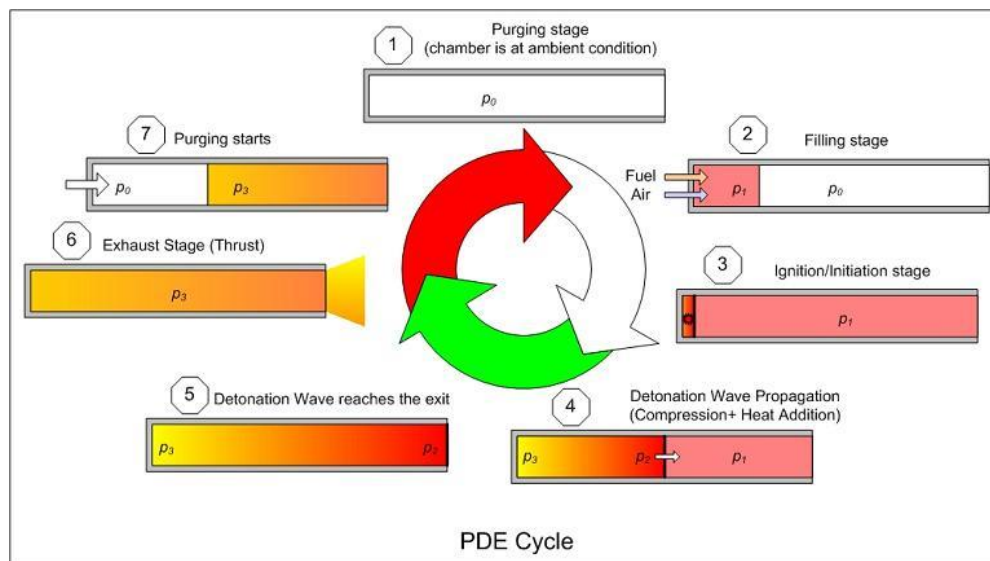


**Figure 1.16** Stages of pulse detonation cycle (PDE) reprrduced from (UTA, 2011).

A fuel is mixed with air in the PDE in the second stage until the tube is filled with the required amount of the mixture then, the mixture is ignited at the closed end. The flame acceleration initiates and the flame travels in a

subsonic wave till the flame speed becomes higher than acoustic velocity and shock waves form.

The interaction of the shockwave and flame front is the key process of DDT. A detonation wave is produced with a speed exceeding 1 km/s and high pressure ratio. The final stage is the purging of the products before repeating the cycle and this produces the thrust. Purging occurs by injection air without fuel to ensure the full burning of the fresh mixture. A proposed detonation engine of the present DDT results in Chapter 4 is discussed in Section 5.2.

## 1.6 Review on Possible Laminar Deflagration to Detonation Transition

The present work involves numerical studies of the probability of a laminar deflagration to detonation transition of a stoichiometric $H_2/O_2$ mixture. This requires a detailed knowledge of laminar burning velocities of the mixture, as well as of the auto-ignition delay times at high temperatures and pressures.

Interestingly, evidence as to whether such a laminar transition is possible has not been clearly demonstrated experimentally. It is unclear whether both the burning velocity of stoichiometric $H_2/O_2$ and the flame front area can be sufficiently high, whilst the tube diameter might have to be so small to maintain laminar flow that the associated stretch rate and heat loss would extinguish the flame. Quantitatively, study of this possibility is not assisted by the confusing spread, over orders of magnitude, of both measured and chemical kinetically modelled values of ignition delay times, $\tau_i$, at different pressures and temperatures, and, to a lesser extent, the values of laminar burning velocity, $u_l$.

Usually laminar burning velocities are insufficient to generate a shock wave strong enough to autoignite the mixture ahead of the flame, and DDTs occur more readily with turbulent flames. To generate a rapid DDT, turbulence has been created by roughened tubes which have an enhancing effect on flame propagation, due to the induced flame wrinkling (Dorofeev et al., 1996; Lee et al., 1985; Obara et al., 1996; Schmidt et al., 1953). In addition, the use of

restrictive obstacles was pioneered by Chapman and Wheeler (1926) who increased the flame speed by inserting rings. Subsequently, (Shchelkin, 1940; Shchelkin, 1947), introduced a spiral coil inside the tube, which effectively shortened the run-up distance to DDT, a particularly important consideration in detonation engines. Such coils develop vortices and generate turbulence, with more rapid acceleration of the flame.

In contrast, many experimental (Kuznetsov et al., 2005b; Kuznetsov et al., 2010; Liberman et al., 2010a; Liberman et al., 2010b; Meyer & Oppenheim, 1971; Nagai et al., 2009; Urtiew & Oppenheim, 1966; Wu et al., 2007) and numerical studies (Han et al., 2017; Ivanov et al., 2011a; Ivanov et al., 2011b; Ivanov et al., 2013; Liberman et al., 2010b; Liberman et al., 2012) have analysed DDT in a smooth duct. Urtiew and Oppenheim (1966) conducted DDT studies with reactive mixture, of equi-molar and stoichiometric $H_2/O_2$ in a rectangular smooth duct, 3.81 x 2.54 cm, closed at one end. They photographically recorded the "explosion within the explosion", attributed to the interaction of the flame with the walls of the tube. A train of compression waves created from this interaction indicated a DDT, developing between the turbulent flame front and shock wave. A "strong ignition" was characterised by low values of $\partial \tau_i / \partial T$ by Meyer and Oppenheim (1971).

Kuznetsov et al. (2005b) exploded stoichiometric $H_2/O_2$ mixtures in a smooth tube, at different initial pressures ranging from 0.02 to 0.8 MPa, and suggested that a growing turbulent boundary layer controlled the turbulence and the onset of DDT. The numerical simulations of Fukuda et al. (2013) revealed the role of the boundary layer in smooth tubes on the transition to detonation of stoichiometric $H_2/O_2$. High shear rates can be generated in viscous sub-layers, which might initiate autoignition, aided by weak transverse waves from hot spots (Sivashinsky, 2002).

Liberman and co-workers suggested that in such highly reactive mixtures; as stoichiometric $H_2/O_2$, ethylene/oxygen and acetylene/oxygen, the DDT could be triggered by laminar combustion (Ivanov et al., 2013; Kuznetsov et al., 2010; Liberman et al., 2010a; Liberman et al., 2010b), while for less reactive

mixtures, such as those of  methane-air, turbulence was necessary (Kessler et al., 2010). In their experimental studies  of stoichiometric $H_2/O_2$,. Kuznetsov et al. (2010) and Liberman et al. (2010a) suggested it was uncertain whether a DDT followed the Zel'dovich reactivity gradient mechanism, developing at hot spots in the unreacted mixture ahead of the flame.

Liberman et al. (2010a), in their studies of DDTs of stoichiometric $H_2/O_2$ and ethylene/oxygen, mixtures considered the upstream flow to remain laminar up to the transition to detonation. In experiments with stoichiometric $H_2/O_2$, in a duct of 50 x 50 mm cross section, Kuznetsov et al. (2010)  reported the flow ahead of the flame remained laminar in the bulk. Furthermore, in their 3D computational study of the DDT of stoichiometric $H_2/O_2$  at 298K and 0.1 MPa, in a duct of 10 x 10 mm cross-section, Ivanov et al. (2013) wrote that "the flow remains laminar everywhere in the channel ahead of the flame all the time till the transition to detonation.'' Optical imaging suggested the onset of a turbulent flame pattern at the transition. Here the problem is whether a configuration that requires a high flow velocity to create strong enough shock waves, can maintain laminar flow with practical duct sizes.

The high reactivity of such mixtures, particularly at low pressure, suggests transitions to detonation may not require significant turbulence to accelerate the flame. In their experimental study with stoichiometric ethylene/oxygen in micro tubes of 0.5, 1 and 2 mm diameter at 0.1 MPa, Wu et al. (2007) observed, for the first time, transition to detonation in micro-tubes. Laminar flame accelerations were very rapid, but values of Reynolds number suggested that the initial flame became turbulent.

A key factor in the flame acceleration, in the absence of flame wrinkling due to turbulence, is the elongated parabolic gas velocity distribution ahead of a laminar flame. This increases the ratio of flame area, $A$, to that of the cross-sectional area of flow, $a$. In a numerical study of laminar flame propagation in stoichiometric acetylene-oxygen mixtures in a narrow channel  with adiabatic walls, Gamezo and Oran (2006) showed that high values of $A/a$ were rapidly attained, in the absence of strong shock. The relatively rapid attainment of

high velocities ahead of the flame is a valuable characteristic for micro-propulsion devices. Even with intense turbulence, the generation of DDTs with $CH_4$/air can only be achieved with large diameter tubes (Kuznetsov et al., 2002; Zipf et al., 2013).

## 1.7  Aims of the Present Work

The present work aims to study the mechanism of the propagation of $H_2/O_2$ mixture to know whether the gas flow created by stoichiometric $H_2/O_2$ laminar flames can create sufficiently strong shock wave to auto-ignite the mixture. The analysis based on a one-dimensional DDT model, and the work relies on collecting comprehensive data on ignition delay times, $\tau_i$, and laminar burning velocities, $u_l$, at different pressures and temperatures.

Using chemical kinetics to simulate the ignition delay times of stoichiometric $H_2/O_2$ at different pressures and temperatures and applying empirical correlations to predict the laminar burning velocities at high pressures is one of the aims that couples with the discussion of the data collected. The study discusses the possible sizes of the tubes to induce a laminar DDT.

The present work aims to discover the other behaviour of the flames expressed in quenching via an experimental investigation to the effect of higher stretch rate on the turbulent flame and the probabilities of quenching. Interestingly the critical size for flame quenching and the length scales associated with it for different mixtures including hydrogen and *n*-butanol mixtures and the limits for the flame propagation have been discovered.

## 1.8  Structure of the Thesis

The thesis consists of six chapters, this first chapter has presented an introduction on the background and motivation of the study, introducing all the main aspects of it.

Chapter 2 describes the experimental test rig and the measurement techniques employed in the present work. Normal safety procedures and the techniques for processing the data are discussed as well.

Chapter 3 presents the experimental results for laminar and turbulent burning velocity of $H_2/O_2/N_2$ mixtures and the results of flame quenching for different fuel mixtures including hydrogen, *n*-butanol, methane, *i*-octane mixtures at different conditions.

Chapter 4 describes a modified one-dimensional DDT model integrated with substantial range of laminar burning velocity and ignition delay times of stoichiometric $H_2/O_2$ mixture obtained from the literature and via modelling to study the laminar and turbulent DDT of stoichiometric $H_2/O_2$ in a closed end tube.

Chapter 5 offers a discussion for the results obtained in Chapter 3 and 4. Ultimately, Chapter 6 presents the summary of the present work and the future work recommendations.

# Chapter 2 - Experimental Apparatus and Measurement systems

## 2.1 Introduction

All experiments for laminar, turbulent and quenching flames were conducted in a fan-stirred constant volume spherical vessel. Such vessels have the merits of being able to generate turbulence that is close to isotropic and homogeneous; and have no difficulties of flame stabilisation. Global and partial flame quenching for different fuel-air mixtures under different initial pressures, temperatures and equivalence ratios are possible when facilitated by the large vessel with optical windows.

## 2.2 Leeds MKII Combustion Vessel

Leeds spherical explosion, fan-stirred vessel (MKII). It is manufactured from stainless steel (SAE316) (Bradley et al., 2009a; Vancoillie et al., 2014) shown in Fig. 2.1. The internal diameter is 380 mm with a volume of 0.03037 m$^3$ which is capable of sustaining pressures and temperatures resulting from combusted mixtures at initial pressures and temperatures of up to 1.5 MPa and 600 K.

Three orthogonal pairs of quartz, windows of 150 mm diameter and 100 mm thickness are mounted in the bomb. These provided excellent optical access for the measurement techniques.

Turbulence was generated by four identical steel eight bladed fans, driven by four 8 kW controllable speed induction motors (Vancoillie et al., 2014). Speeds range from 250 to 10,000 rpm. This allows values of $u'$ between 0.25 and 11 m/s.
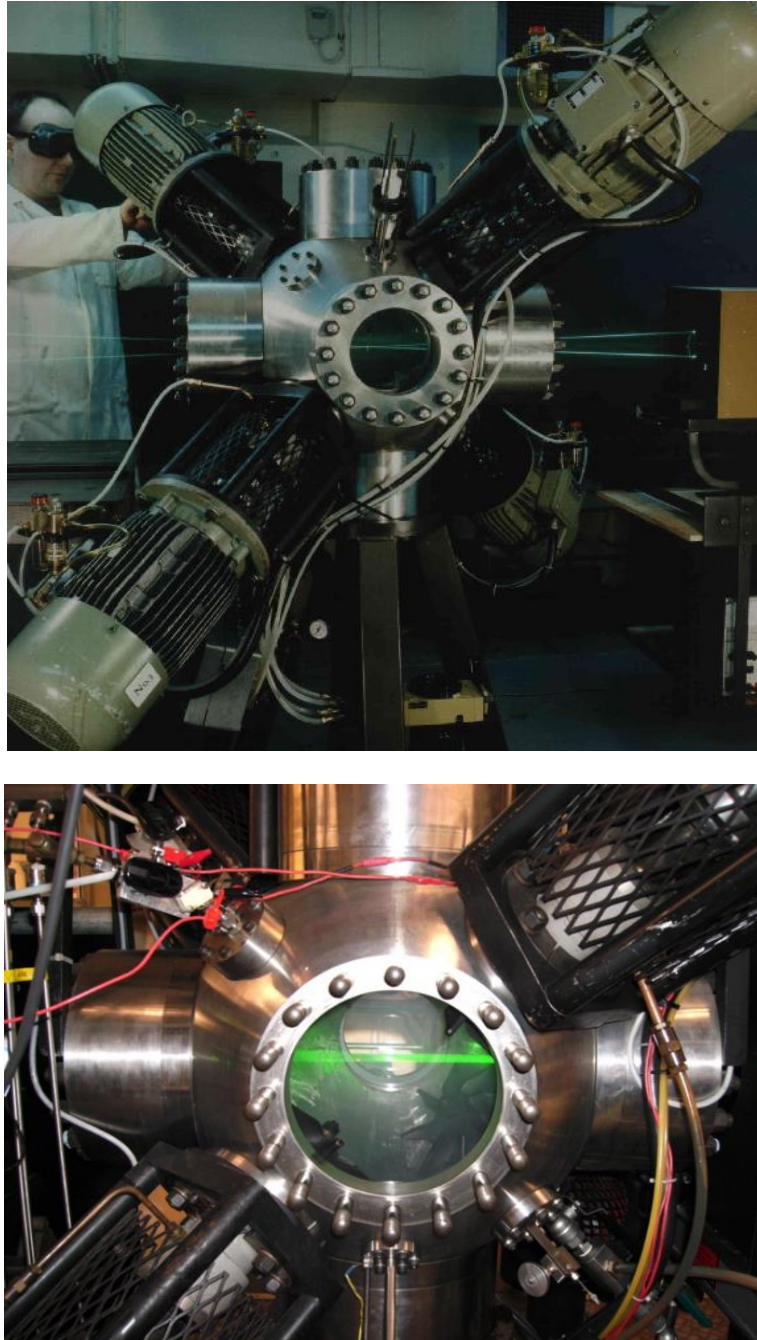
**Figure 2.1** Leeds MKII fan-stirred bomb, top frame is reproduced from Tripathi (2012).

The rms turbulence velocity, $u'$, is related to the fan speed by:

$$u' \text{ (m/s)} = 0.00119 \, N_f \quad , \tag{2.1}$$

where $N_f$ is the fan speed in rpm. The integral length scale of the bomb had been found by two point correlation (Nwagwe et al., 2000) as 20 ± 1 mm. Some turbulence properties from Lawes et al. (2012) are given in Table 2.1. These turbulence macro and micro length scales were measured at different pressures and rms velocity. It can be seen that these scales reduce with pressure and rms velocity except the integral length scale, $l$, which is independent of speeds from 1000 to 10,000 rpm.

**Table 2.1** Experimental turbulence properties in the study of Lawes et al. (2012).

| $u'$ (m/s) | P (MPa) | $l$ (mm) | $\lambda$(mm) | $\eta$ (mm) |
|---|---|---|---|---|
| 1 | 0.1 | 20 | 2.6 | 0.12 |
| 4 | 0.1 | 20 | 1.3 | 0.042 |
| 0.5 | 0.5 | 24 | 1.6 | 0.06 |
| 1 | 0.5 | 20 | 1.2 | 0.035 |
| 2 | 0.5 | 20 | 0.82 | 0.021 |
| 4 | 0.5 | 20 | 0.58 | 0.012 |
| 6 | 0.5 | 20 | 0.47 | 0.0092 |
| 1 | 1 | 20 | 0.82 | 0.021 |
| 4 | 1 | 20 | 0.41 | 0.0074 |

## 2.3  The Auxiliary Systems

The bomb is equipped with auxiliary systems for pressure and temperature measurements in addition to the ignition and triggering systems. These auxiliary systems are used in the mixture preparation.

### 2.3.1   Ignition System

The variable energy ignition unit was designed to generate a spark energy of 23 mJ (Bradley et al., 1998b). Spark electrodes are shown in Fig. 2.2 composed of centrally 1.5 mm diameter steel electrode represents the anode in the circuit. This anode was sheathed by a ceramic insulation within a stainless-steel sleeve comprising the cathode. Both anode and cathode are contained within a 6.35 mm stainless-steel tube. The ignition circuit was

earthed via a cable connection between cathode and the anode. This system was mounted centrally through the wall of the vessel to ensure that no uncontrolled ignition resulted from residual ignition energy (Kondo et al. 1997).

All the mixtures that schlieren system observed were ignited centrally with this unit with a minimum ignition energy (MIE) as a function of initial pressures, fuel and equivalence ratio.

By adjusting the spark plug gap using a feeler gauges, it was feasible to set the minimum ignition energy for different pressures. Therefore, low pressure experiments at 0.1 MPa, the spark plug gap was 0.7 mm and at higher pressure up to 1 MPa, it was 0.3 mm throughout all the experiments.
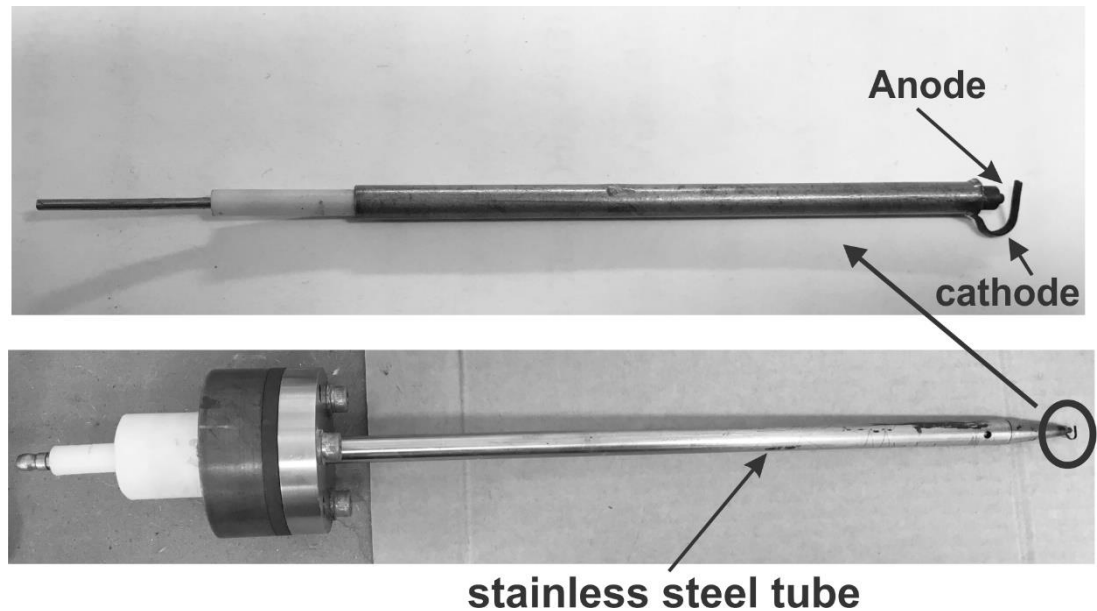


**Figure 2.2** Spark tip and plug used in the experimental work

### 2.3.2　Temperature Measurements and Controls

Heating the mixtures inside the vessel was achieved by two 2 kW electric heating coils placed at opposite faces of the vessel's plates to provide uniform heating.

Prior to ignition, the temperature inside the vessel was adjusted and monitored using a (CAL320) PID temperature controller on a control panel in the protected area in the laboratory. A K-type thermocouple, 25 µm Chrome-

Alumel wire, encased in a 1.5 mm diameter stainless steel was placed diagonally 75 mm from the inner surface wall of the vessel.

In order to carry out experiments requiring high initial temperature, the temperature controller was set on a temperature that is quite higher than the desired to enhance the heating rate and therefore, reduce the time for heating up the vessel.

The fan maintained a uniform temperature within a few degrees higher than the desired temperature prior to mixture preparation and ignition process.

### 2.3.3   Pressure Measurements

A static pressure transducer (Druck PDCR 911) connected to a display in the protected area of the laboratory, monitored the pressure changes during partial pressure mixture preparations. A swage lock ball valve protected this transducer prior to combustion. Ensuring an accurate equivalence ratio for any mixture, a calibrating process to this transducer was performed on a weekly basis against a mercury barometer located in the vessel's room at atmospheric pressure.

Another pressure transducer (Kistler 701A) for dynamic pressures was positioned on the inner surface of the vessel as shown in Fig. 2.3. This transducer was connected to charge amplifier (Kistler 5007) to amplify the charge into an analogue voltage signal. Digitising the signal was via a NI6361 DAQ analogue to digital converter (ADC), connected to the charge amplifier. Interpreting the signal was achieved using a virtual instrument (VI) simulation created using LabVIEW from National Instruments at 50 kHz frequency for 250,000 samples in each experiment. A pressure trace was then recorded to give the peak pressure values for each explosion.10 Volts output from the charge amplifier with a 0.1 MPa/Volt, 0.5 MPa/Volt and 1 MPa/Volt for initial pressures of 0.1, 0.5 and 1 MPa, respectively.

Flush-mounted on the inner surface
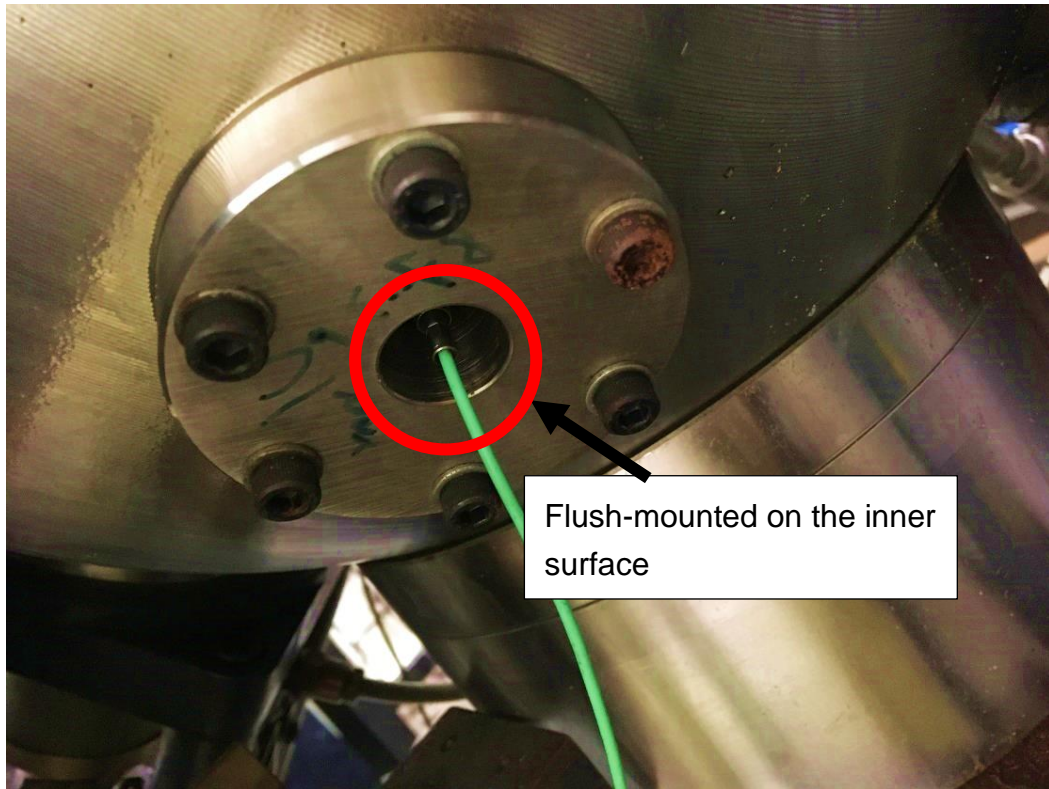
**Figure 2.3** Kistler 701A dynamic pressure transducer ranges from 0:25 MPa.

## 2.4  Imaging Techniques

Schlieren (Bradley et al., 2013) and Mie scattering techniques were employed in the experimental work. The first technique is schlieren system and it depends upon density difference between burned and unburned gases. The second technique gives Mie-scattered images of flames using a high repetition rate laser.

### 2.4.1  Schlieren System

The Schlieren image depends upon the density gradient. Basically, collimating a light source on the area of interest causes a refraction to this light in different angles, due to the density gradient in the area of interest. This refracted light is amplified and received on a pinhole, or knife-edge, and directly onto a camera for recording the high and low density regions.

A high speed Phantom Miro M310 camera was used for the schlieren system and an 80 mm Nikon lens recorded the maximum field of view field of a 150 mm, optical window diameter, with a resolution of 768 x 768 pixels and

sampling rate of 5400 Hz. This resulted in a recorded square view of 159 x 159 mm with a pixel size of 0.20708 mm/pixel. The exposure time was adjusted to 6µs. The light source was a 20 mW class 3B diode laser with centre wavelength of ($\lambda$= 635 nm).

Two plano-convex lens of ($f$ =1000 mm) were used in the system. The first expanded the laser light beam, collimating 150 mm beam through the bomb, and the other lens focused the laser beam through a knife-edge of 0.5 mm directly onto the high-speed camera (see Fig. 2.4). The flame images are saved in (.bmp) format.
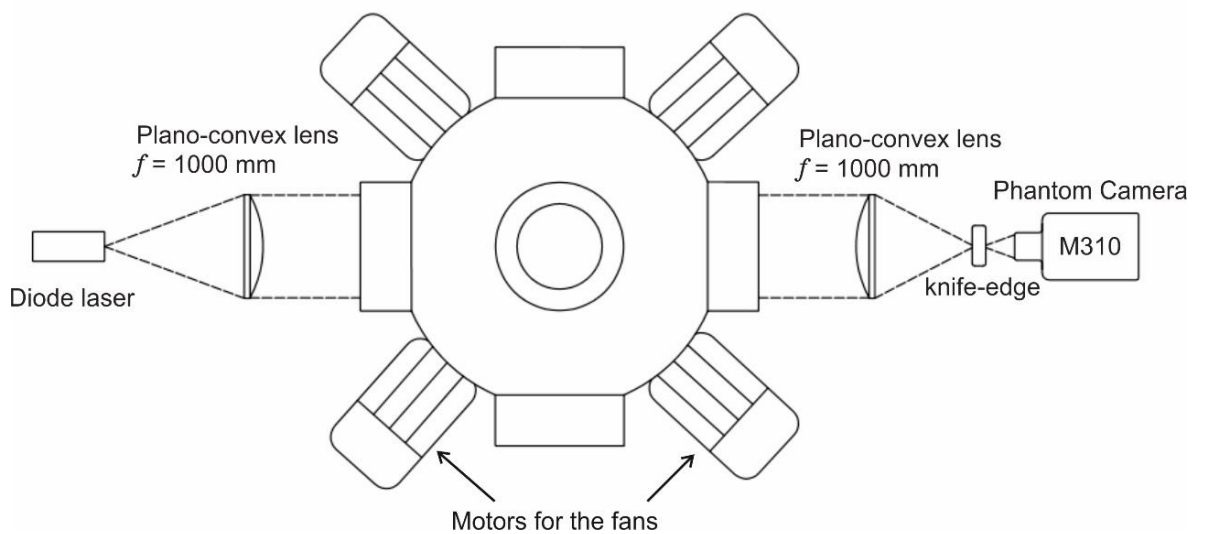


**Figure 2.4** Plan view of the schlieren image photography system on the spherical vessel

### 2.4.1.1  Calibration of the Schlieren System and the Repeatability of the Experiments

Collimation of the laser beam expanded from the plano-convex lens was checked daily in addition to the pixel size. This required a 10 mm x 10 mm grid imprinted onto a transparent sheet. This was mounted in the collimating beam area in front and behind the vessel's windows. The high-speed camera to captured images for that placed sheet. The beam collimation was assured, if the images in front and behind the vessel windows were showing the same grid size, see Fig. 2.5. The pixel size was checked via an image analysis tool

in MATLAB. This tool superimposed a best fit grid as a reference size and pixel resolution over the grid imprinted sheet.
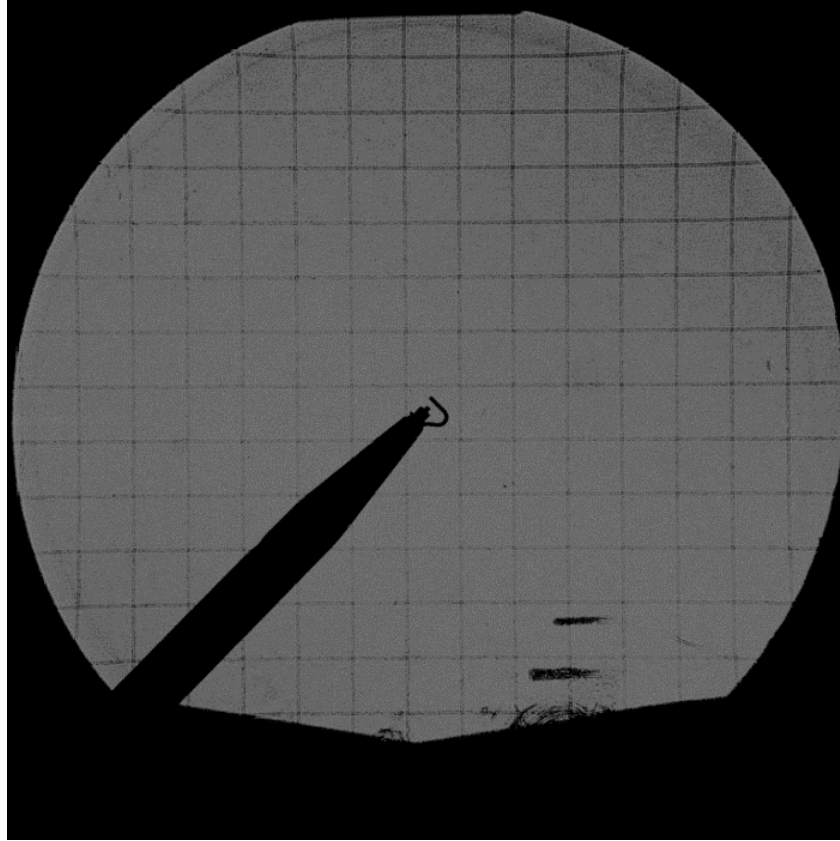


**Figure 2.5** Calibration of schlieren image photography system

Five experiments were performed for both laminar and turbulent explosions to check the repeatability error. The consistency of the experiments was confirmed from all pressure records measured.

### 2.4.1.2 Synchronisation and Triggering Systems

To capture the schlieren images simultaneously with pressure rise, the timing for the dynamic pressure recording through VI, the high-speed camera for recording the flame propagating images and the spark system for giving the spark energy had to be synchronised. A +5V TTL trigger signal gave rising and falling edges via an ignition switch. From the onset of triggering time, the high-speed camera starts writing data on the memory and the dynamic pressure transducer initiates recoding. A +12V CMOS pulse was then

introduced through the falling edge to initiate the spark. The actual time for any explosion was recorded, along with the time prior to the spark generation. There was nearly 3 ms for camera recording until the real captured flame propagating images. This ensured all the data from the ignition frame to the final propagating frame of the flame were recorded. All these frames were saved in the PC at specific extensions. These images evaluated the flame radii and the burning rates to be determined.

## 2.4.2   3D Laser Swinging Sheets System

A novel technique of capturing laser sheet images of Mie scattering in explosion flames was developed by Harker et al. (2012), in what has become known as the swinging sheet laser imaging system is shown in Fig. 2.6.

This technique depends on the generation of a number of separated laser sheet images from a high-repetition rate laser, synchronized with a rotating mirror to generate separate sheets, and a high-speed camera to capture the images. Details of this technique are described in (Harker et al., 2012) and the modified technique in (Thorne, 2017).
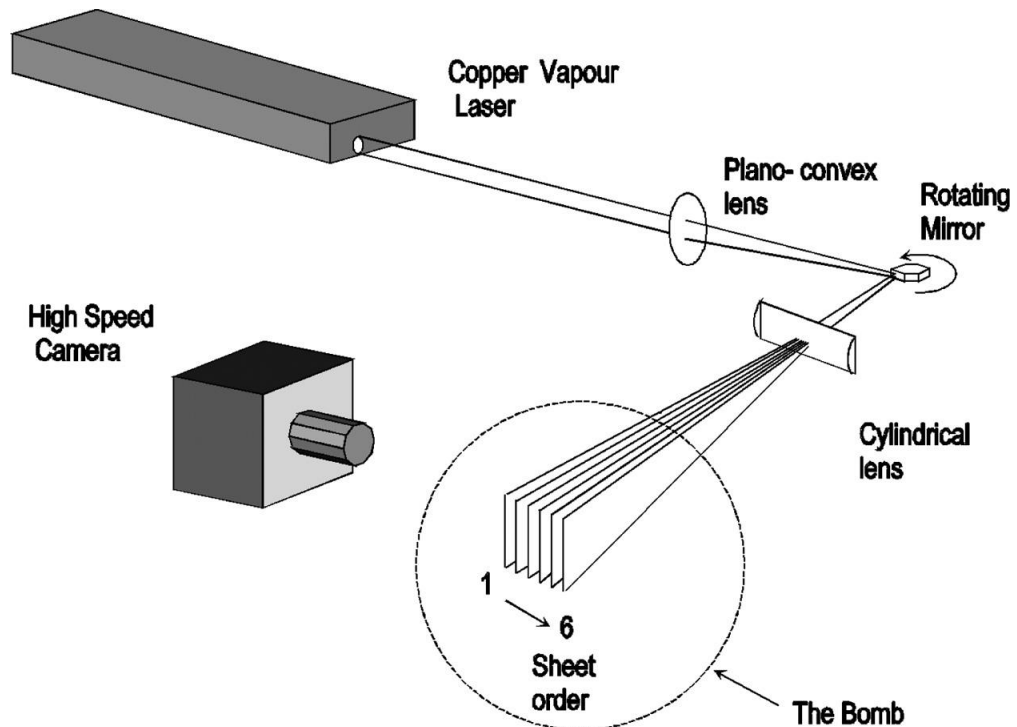


**Figure 2.6** Schematic diagram of swinging sheets imaging experiment (Harker et al., 2012).

A number of thin slices of 532 nm Nd:YAG laser sweep through the flame propagates as shown in Fig. 2.7 for the updated system. This system is employed in flame quenching studies.

The laser has an adjustable repetition rates ranging from 5 kHz to 30 kHz with a pulsing energy ranging from 13 mJ to 1.9 mJ, respectively. These repetition rates are generated from only one cavity of the laser source.

Typically, laser sheet images can be generated in one sweep through a propagating flame via a 5-12 Hz rotating mirror, RM, with multiple facets (16), powered by an 8-pole synchronous hysteresis 6A motor and 30V AC. These comprises 1 µm diameter olive oil with a density of 970 kg/m$^3$ (Melling, 1997) atomisation occurs inside the bomb using a particles generator. Images are captured using a high speed digital Phantom camera V2011 (PCC 2.7), at a frequency of 54 kHz, with an image resolution of 512 x 512 pixels.

2D Images were recorded at each position, within about 1mm apart. The laser sheet in each sweep and a 3D constructed flames were then built. The 60 kHz maximum output frequency from the laser passes through an array of the convex lenses of focal length, $f$, 38.1 and 25 mm to attain a very thin sheet in the centre of the bomb, with a height of 100 mm.

Ignition of the mixtures is by a New Wave solo Nd:YAG ignition laser at a frequency of 532 nm, with a variable frequency up to 15 Hz  with 120 mJ of pulse energy. Triggering and synchronising the system is described in detail in (Thorne, 2017). Since the present study focuses on the quenching of the flame, therefore, it was necessary to choose mixtures that have a low laminar burning velocity.

For the present work the imaging laser and the ignition laser were pulsed at 51 up to 54 kHz and 12 Hz, respectively. Typically, 73 to 78 sheets were recorded in each sweep of 1.44 ms.
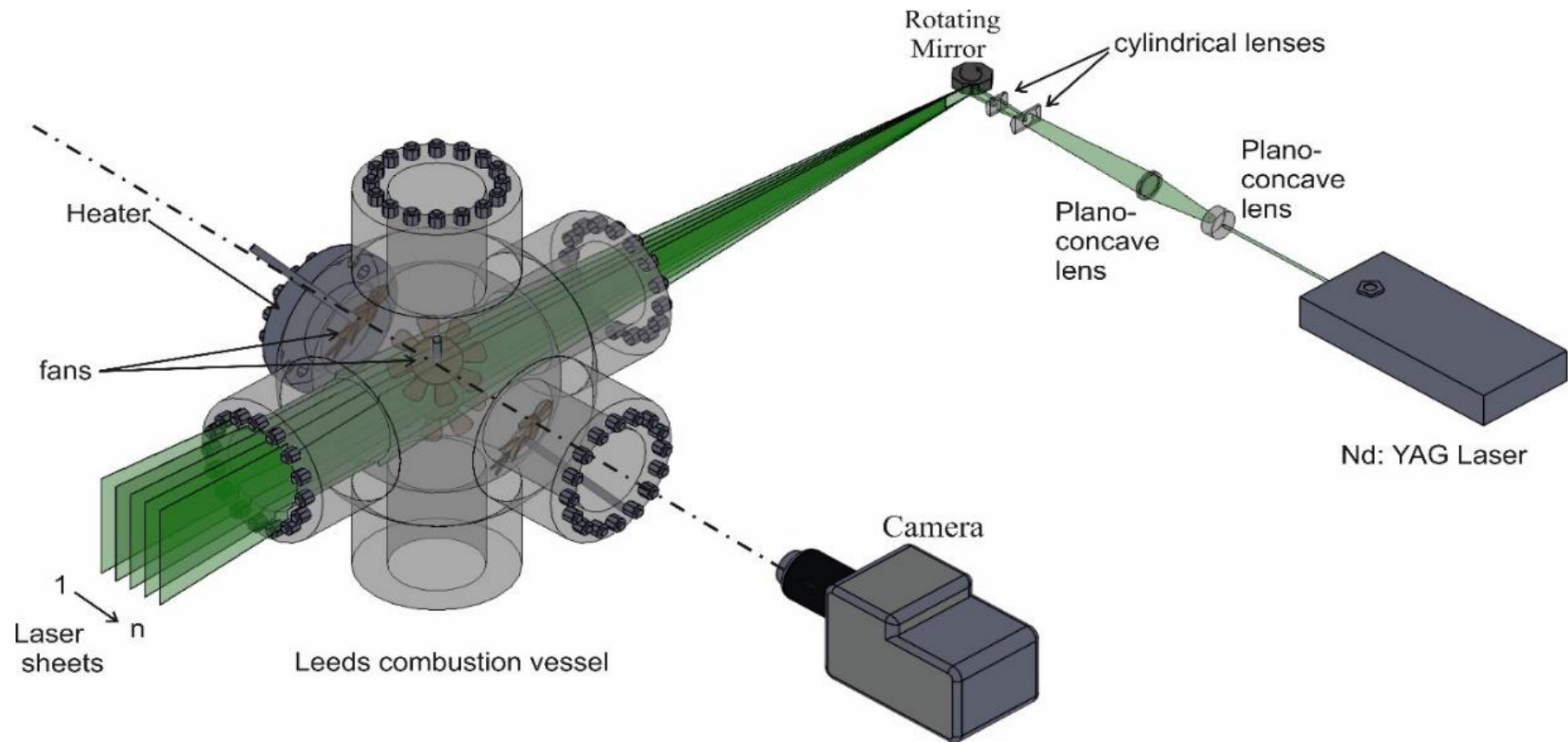
**Figure 2.7** Laser Swinging sheets system (Bradley et al., 2019)

## 2.5 Safety Procedures and Fuel Mixtures Preparation

Table 2.2 shows all the liquid and gaseous fuels used in the present flame quenching studies. Dealing with gaseous fuels such as: $H_2$, $O_2$, $N_2$, and $CH_4$ required secured and restricted regulations; in accordance with normal safety procedures. All cylinders housed outside of the school laboratory in a safety cage and are checked regularly via internal and external gauges. Control valves and micro switches are connected to the vessel through the inlet ports and are checked each day.

In the mixing of $H_2$ with $O_2$ and $N_2$, partial pressures for them were well-controlled through three valves. Changes in pressure were immediately monitored on the static pressure display described in Section 2.3.3.

**Table 2.2** Fuels used in the current work.

| Fuel | Supplier | Purity (ppm) | Density (g/ml @ 25°C) | Molecular Mass (g/mol) |
|:---:|:---:|:---:|:---:|:---:|
| $H_2$ | BOC | 99.99% | 0.069 | 2.02 |
| $O_2$ | BOC | 99.95% | No data available | 32 |
| $N_2$ | BOC | 99.998% | 0.97 | 28.01 |
| $CH_4$ | BOC | 99.5% | 0.6 | 16.04 |
| *l*-Octane | Fisher Scientific | 99.91% | 0.619 | 114.23 |
| *n*-Butanol | Fisher Scientific | 99.89% | 0.810 | 74.14 |

Liquid fuels were stored in 250 ml glass bottles at 5°C outside the combustion room in a refrigerator. Prior to use, they were taken to a fume cupboard and left until thermal equilibrium with room temperature. This took about 30 minutes, but, it guaranteed that the thermodynamic properties were at room temperature; as it was employed in the fuel volume calculations. A Hamilton glass gas tight syringes of different volumes of 5 and 10 ml with a 1 mm

needle's diameter were available to measure an accurate volume for injection and premixing procedure. All syringes and bottles using the same fuel were labelled by different distinguished colours.

## 2.6  Procedures of Experiments

Monitoring the static pressure in the vessel was necessary before doing any laminar or turbulent experiment, so as to avoid leakage. Therefore, for experiments that require high or low initial temperatures, the bomb was pressurised to the required initial pressure with dry air and check the sealing for five minutes.

The vessel was vacuumed twice to 0.0014 MPa from atmospheric pressure, before and after each experiment. This ensured that there were no residuals from gaseous mixtures. These checks were done regularly, as shown in Figs 2.8 & 2.9. The pressure and temperature were monitored for 5 minutes at fan speed of 250 rpm.
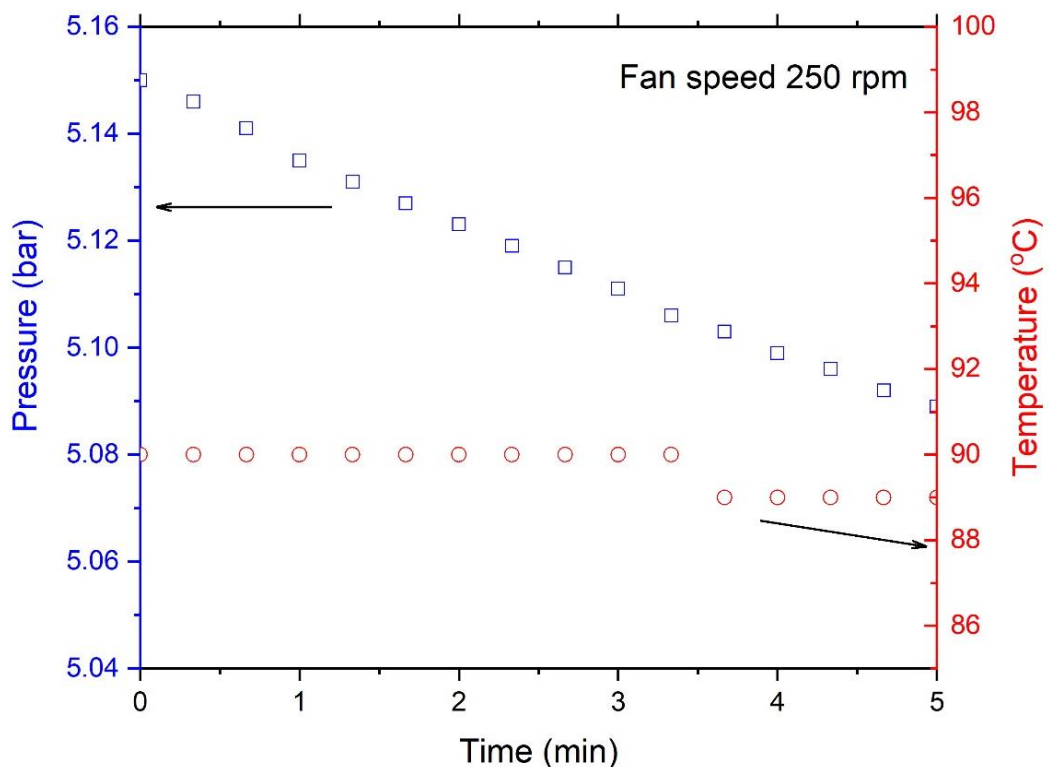


**Figure 2.8** Experimental check for the vessel at 5 bar and 363 K fan speed at 250 rpm.
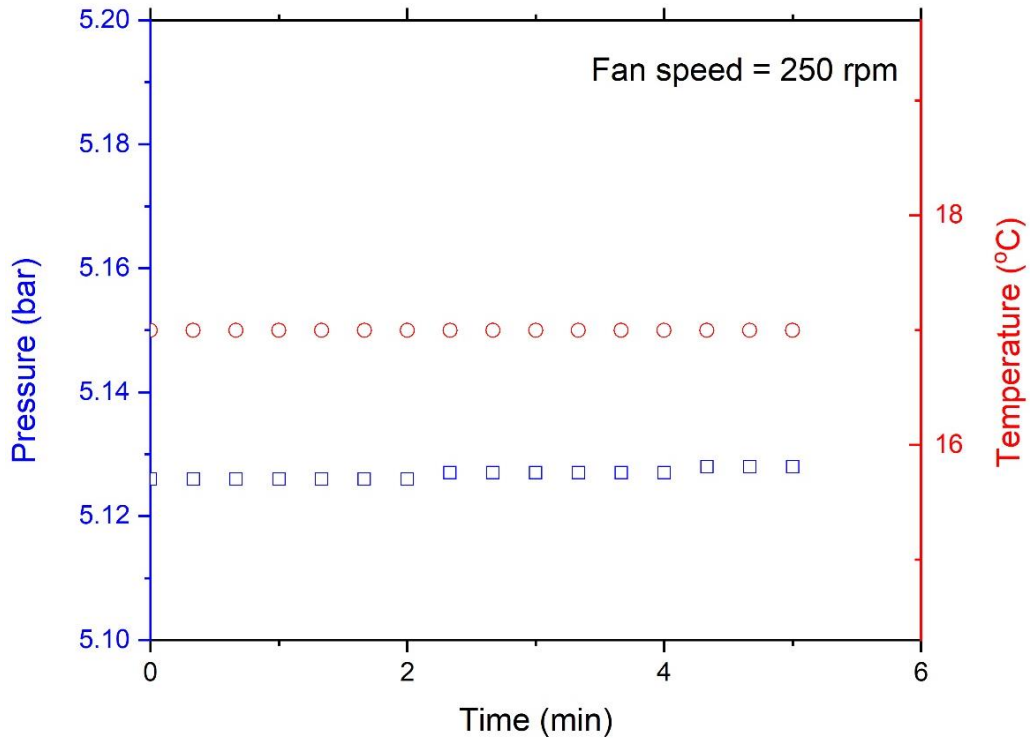
**Figure 2.9** Experimental check for the vessel at 5 bar and room temperature with fan speed at 250 rpm.

In preparing fuel mixtures for the experiment, volumes of fuels were calculated according to the ideal gas assumption. Volumes of gaseous fuels needed were calculated directly from partial pressures. Liquid fuels volumes with the ideal gas assumption were also calculated knowing the fuel composition, density of the fuel at room temperature and volume of the vessel. Getting the number of moles of fuel at the required initial pressure and temperature will result in getting the volume of liquid fuel needed to be measured in the scaled suitable syringes with 0.5 % manufacturer accuracy.

Delivering the gaseous fuels occurs through tubes directly attached to the vessel with control valves. Liquid fuels were injected from the syringes through the vessel's fuel inlet port attached to a needle valve. Prior to the delivery of the fuels, the vessel was vacuumed to 0.0015 MPa and the gaseous fuels were entering to the vessel from their specific ports and then the dry air was added to reach the required initial pressure. Liquid fuels were injected and drawn into the vessel which was under the same vacuum. During fuels

delivery to the vessel, the pressure was monitored until the explosion. Temperature prior to the fuel drawing with higher than required high initial temperature with +8 K and the fans were running at speeds of 426 rpm for high initial temperature experiments and at 250 rpm for room temperature experiments to enhance the fuel vaporisation and mixing.

After that, the temperature was observed until it reaches the required initial condition and at that moment for laminar experiments, the fans were switched off and left for about 15-20s to assure the equilibrating of the mixture. During these seconds, remotely closing ball valves (for the static pressure and air supply) were closed and a final check to the initial pressure and temperature values, dynamic pressure tracing LabVIEW (VI) software was active to save data and then ignite the mixture.

In turbulent experiments, the fans continued to run and the turbulence intensity was gradually increased to the required u' during the dry air supply before ignition. Low temperature with highly turbulence experiments required much attention in controlling the fan speed taking a tolerance of +5 K of temperature before ignition.

In cases of room temperature experiments, the vessel was left to cool down, or the heaters were reactivated again for the high temperature experiments; then, it was kept under vacuum again for the next experiments.

## 2.7  Data Processing

All the data recorded with the high-speed cameras were saved whilst processing them required some MATLAB codes for laminar, turbulent and quenching experiments. During the processing of this data, some thermodynamic properties for the fuel mixtures were required to run these codes. Laminar codes for getting the flames radii and evaluation the laminar burning velocity and strain rate Markstein number, $Ma_{sr}$, are discussed in Section 2.7.2. For turbulent and quenching turbulent experiments, the procedures for processing these data are discussed in Section 2.7.3.

## 2.7.1    Properties of All Fuel Mixtures

For central outwardly propagating flames, the thermodynamic properties of all reactants and products in the bomb were pre-calculated using Gaseq, a chemical equilibrium software, for windows created by Morley (2005).Two database libraries for thermodynamic data (Thermdat.tdd) and (BURCAT.tdd) were employed in the present work. The software has the ability to do the calculations at various conditions. In the present work, the calculations were done at constant pressure conditions and adiabatic temperature assumption by neglecting any rise in the pressure during the flame propagating close to the vessel's windows. Unburned and burned gas densities were calculated knowing the mole fractions of the fuel-air mixture, initial pressure, initial temperature and equivalence ratio.

## 2.7.2    Processing of Laminar Images from Schlieren System

Two codes used for laminar images resulted from the schlieren image photography system. In Section 2.7.2.1, the first MATLAB code was described to get the radii for the flame from the time of ignition to the time when the flame reaches the edges of the vessel's windows, flame speed, $s_n$, and the stretch rate, $\alpha$. Calculating the Markstein number for strain rate achieved with a second MATLAB code depending on some inputs produced from the first code; as discussed in Section 2.7.2.2.

### 2.7.2.1  Determination of Schlieren Flame Radii, Flame Speeds and Stretch Rates

Different cases for flame edge, clear or faint especially in hydrogen flames were processed depending on a MATLAB code created by Sharpe (2011). Directly before the ignition, a schlieren image was saved and the location of the tip of the spark plug and the window's edge were specified before any flame interaction. A masking-off process of the sparkplug was identified to mitigate the sparkplug disturbance produced. The dimensions of the image (and all fixed location) were saved, and the same ones were then employed as a reference to the next frames containing the propagation flame. Flame edge was specified from the last frame where the flame was close to the vessel's windows; after that, the referenced masking off process and the

window's edge were superimposed on the last frame and the other frames in this reversed sequence in what is called level set technique (Tripathi, 2012).

Consequently, the burned and unburned regions were specified, and the average flame radii were calculated via a best fit circle for all frames with time. Then, the code plotted the radii vs time and flame speed, $s_n$ vs radius and stretch rate, $\alpha$ from Section 1.2.1.3. An extrapolation to zero stretch rate was performed in the code to get the un-stretched flame speed, $S_s$.

### 2.7.2.2  Determination of Markstein Number for Strain Rate

A multiple regression method described in (Edwards, 1984) was employed in the study of Bradley et al. (1996) for calculating Markstein lengths. These lengths relied upon the experimental data of flame speeds and radii; which were already calculated in Section 2.7.2.1. Calculating the stretch rate; two components; strain rate, $\alpha_s$, and curvature, $\alpha_c$; were evaluated according to the available experimental data of laminar burning velocity and the density ratio defined in Section 1.2.1.3. The code was developed by Bradley et al. (2018). This code was employed to calculate Markstein numbers according to this multiple regression method.

### 2.7.3  Processing of Turbulent and Quenching Flame Images from Schlieren System

A MATLAB batch processing tools developed by Mansour (2010) consists of multiple scripts was employed in the present work for processing the turbulent flame images. The first script written was functioned to delete the pre-flame images recorded by phantom Mira M310 camera and create a zeros matrix equal to the size of the first image.

Following this, other scripts worked on subtracting the pre-flame image from the other images where the flame propagates without any interaction of the sparkplug. The grey images were converted into binary images distinguishing the flame from the surrounded unburned gases (as seen in Fig. 2.10) for turbulent rich iso-octane flames. A spherical flame assumption yielded the flame area from the pixels of the flame and the mean radius was calculated accordingly. This script is used in Section 3.4.

Another MATLAB code was developed to obtain the flame area from the binary images produced from the first code (on the same assumption of a spherical flame). Flame radius was evaluated for quenching flame cases in Section 3.5 as shown in Fig. 2.11 for lean *n*-butanol flames (Appendix A).



(a) Raw image          (b) Binary image (rotated by 225.5$^{o}$)
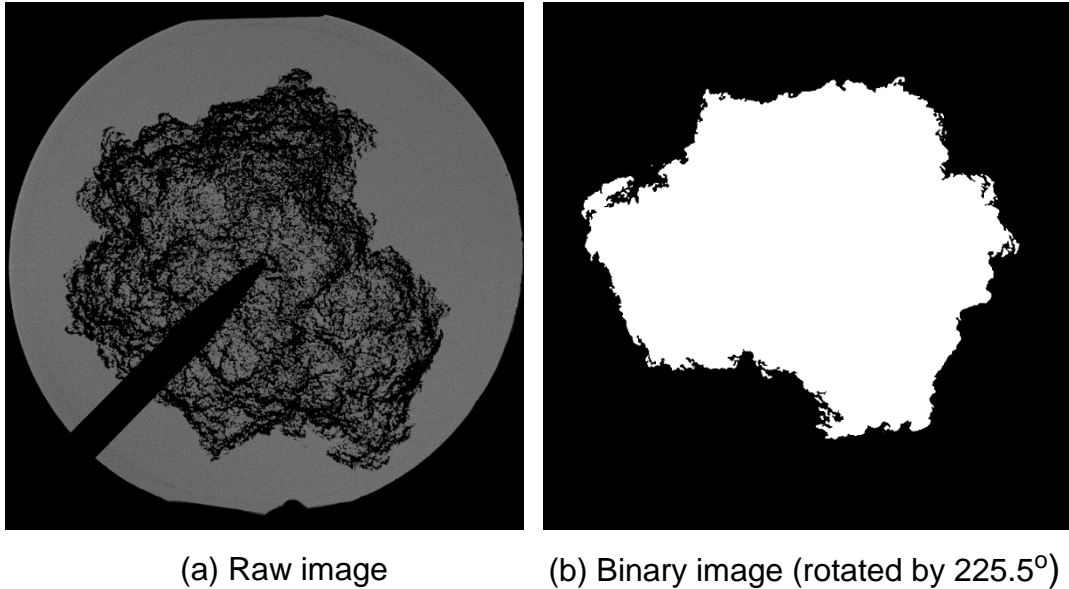
Figure 2.10 Turbulent *i*-octane air mixture at $\varphi$= 1.35, 0.5 MPa, 365 K and $u'$= 3 m/s with $r_{sch}$= 50.594 mm.



(a) Raw image                    (b) Binary image
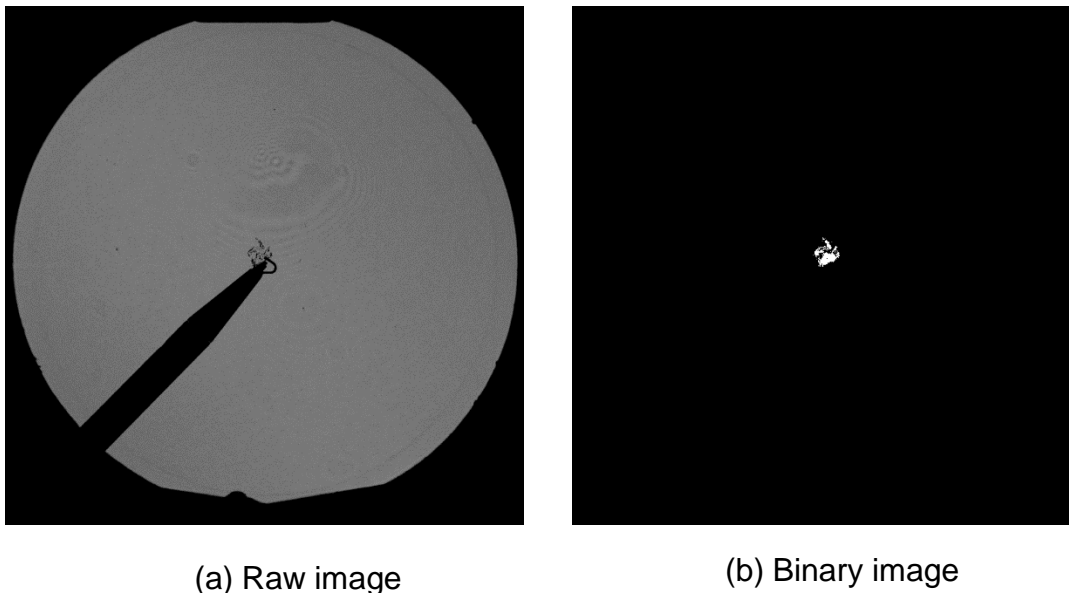
Figure 2.11 Quenched *n*-butanol air mixture at $\varphi = 0.8$, 0.5 MPa, 365 K and $u'$= 2 m/s with $D = 6.2$ mm.

# Chapter 3 - Turbulent Burning Velocity of H₂/O₂/N₂ mixtures and Flame Quenching of Different Fuel Mixtures

## 3.1 Introduction

The schlieren image photography technique described in Section 2.4 enabled studies of turbulent flame structure, quenching and the measurement of turbulent burning velocities.

The measurement of $u_l$ and $Ma_{sr}$ is first determined. This is followed by measurements of $u_{tr}$ and $K$ with regard to the studies of turbulent flame quenching, limiting values of $K$ were found and also the size of the flame kernel measured for flame quenching.

Section 3.2 and 3.3 present measurements of the laminar flame speed and burning velocity of H₂/O₂/N₂ and *n*-butanol mixtures employed throughout the present study, using the schlieren imaging technique described. Section 3.4 presents the schlieren images of H₂/O₂/N₂ flames at high turbulence and the possibilities of flame quenching. In Section 3.5 and 3.6, the quenching data analysis and correlations are presented.

The experimental work is divided into two stages. In the first stage, the schlieren technique is used to calculate the mass burned turbulent burning velocity and Karlovitz stretch factor, at different fan speeds until quenching. During this stage, different fuel mixtures are used, and the probability of flame propagation is identified. The second stage focuses on the quench analysis and employs the 3D Laser swinging sheet technique for near- quench flames alongside a comparison between this technique and schlieren system.

## 3.2 Experimental Results of Laminar H₂/O₂/N₂ Mixtures Using Schlieren Image Technique

H₂ mixtures have a strong resistance to quenching and were studied for this reason initially necessary to determine the fundamental parameters. As shown in the experimental matrix of Table 3.1, the experiments were carried out on a lean mixture ($\varphi = 0.5$) of hydrogen-oxygen-nitrogen mixture

(H2/N2/O2), with different three volume fractions of N2/O2. Laminar and turbulent velocities are measured at a flame radius, $r_{sch}$ of 30 mm, and at an initial temperature and pressure 300 K and 0.1 MPa.

**Table 3.1** Experimental work matrix for lean hydrogen/oxygen/nitrogen mixtures.

| Fuel mixture | Temperature (K) | Pressure (MPa) | Equivalence ratio |
|---|---|---|---|
| H2+0.118O2+0.882N2 | 300 | 0.1 | 0.5 |
| H2+0.115O2+0.885N2 | 300 | 0.1 | 0.5 |
| H2+0.11O2+0.89N2 | 300 | 0.1 | 0.5 |

### 3.2.1    Stretched Laminar Flame Speed with Stretch Rate for H2/O2/N2 Mixtures

Figure 3.1 to 3.3 show the variation of $S_n$ against $\alpha$ of the different volume fractions. These variables were calculated from schlieren images using the method described in Section 1.2.1.3. The laminar burning velocity, $u_l$, is calculated for five explosions, as a function of the un-stretched laminar flame speed, $S_s$.  Via extrapolating the resulting curve to a theoretically zero stretch rate, the unstretched flame speed, $S_s$ was evaluated.
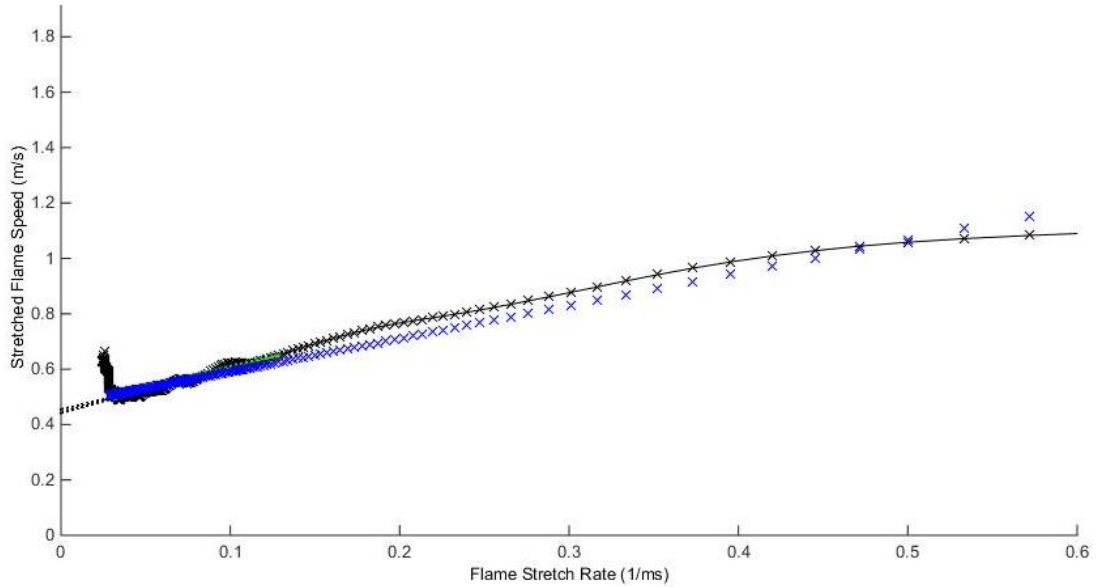
**Figure 3.1** A typical graph of the variation of stretched laminar flame speed, $s_n$, with stretch rate, for H₂/0.118 O₂/0.882 N₂ at 300 K, 0.1 MPa and $\varphi$ = 0.5. Solid blue and black lines denote linear and nonlinear relationships for $L_b$ through data points.
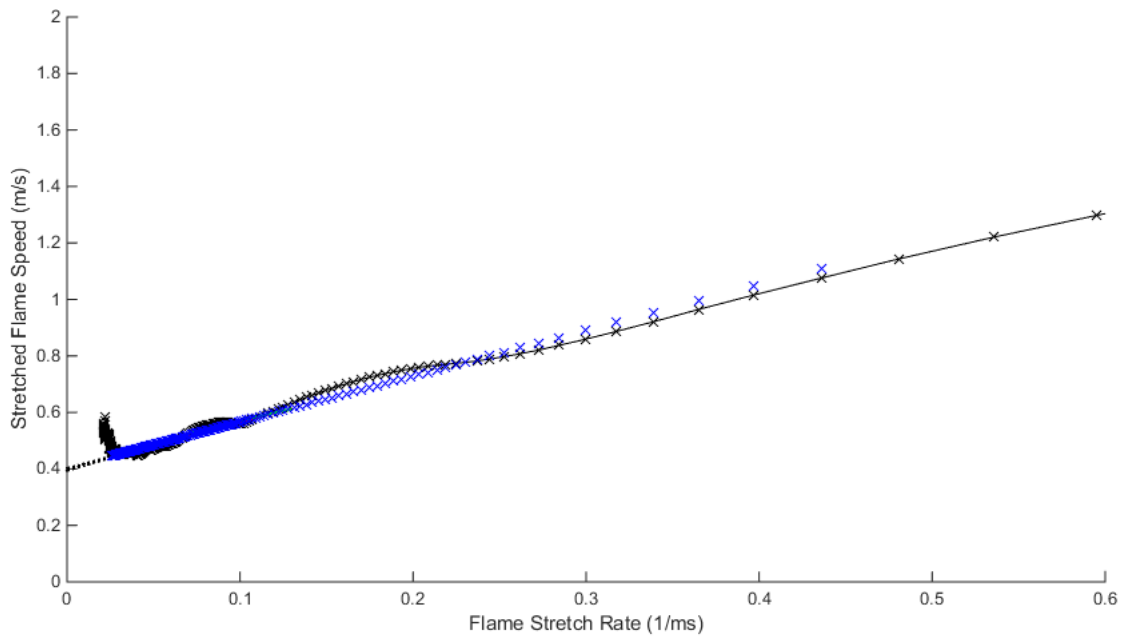


**Figure 3.2** A typical graph of the variation of stretched laminar flame speed, $s_n$, with stretch rate, for H₂/0.115 O₂/0.885 N₂ at 300 K, 0.1 MPa and $\varphi$ = 0.5. Solid blue and black lines denote linear and nonlinear relationships for $L_b$ through data points.
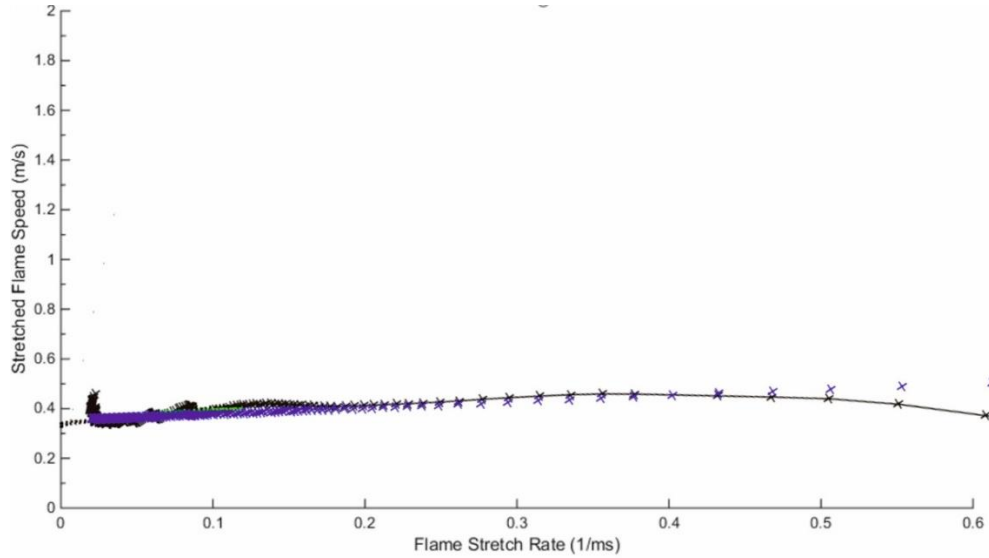
**Figure 3.3** A typical graph of the variation of stretched laminar flame speed, $s_n$, with stretch rate, for H₂/0.11 O₂/0.89 N₂ at 300 K, 0.1 MPa and $\varphi$ =0.5. Solid blue and black lines denote linear and nonlinear relationships for $L_b$ through data points.

### 3.2.1.1 Stretched Laminar Flame Speed with Flame Radius

The flame speed was high at small radii, this is because of the boosting of the flame due to the ignition energy used (Tripathi, 2012). It reduced to a stable value as the flame grows as shown in Figs 3.4 to 3.6.
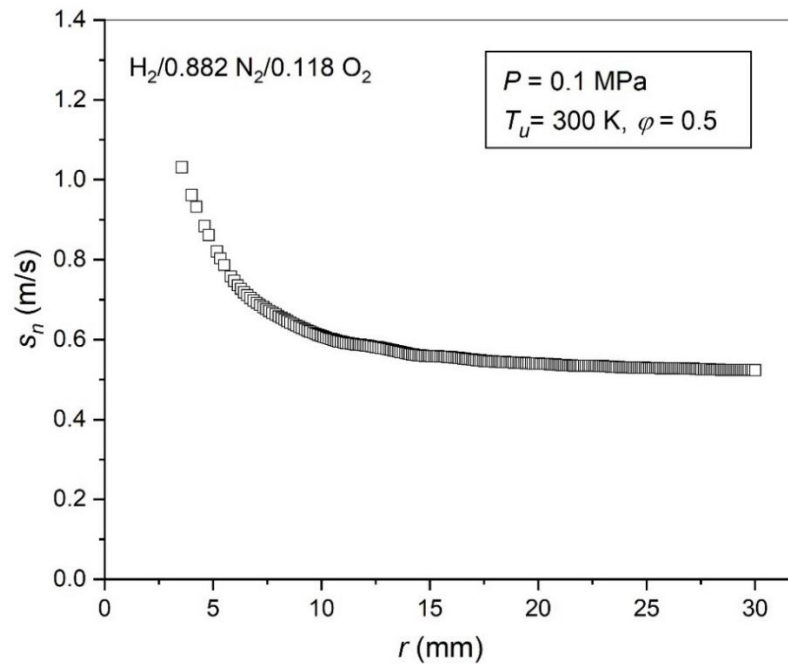


**Figure 3.4** A typical graph of the variation of stretched laminar flame speed with flame radius, for H₂/0.118 O₂/0.882 N₂ at 300 K, 0.1 MPa and $\varphi$ = 0.5, laminar.
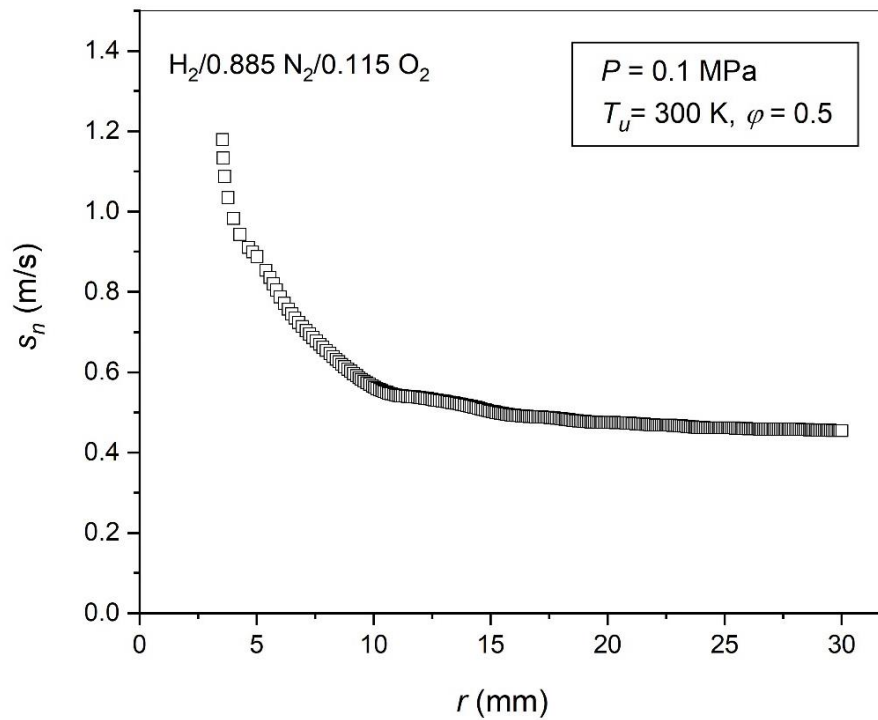
**Figure 3.5** A typical graph of the variation of stretched laminar flame speed with flame radius, for $H_2/0.115\ O_2/0.885\ N_2$ at 300 K, 0.1 MPa and $\varphi = 0.5$.
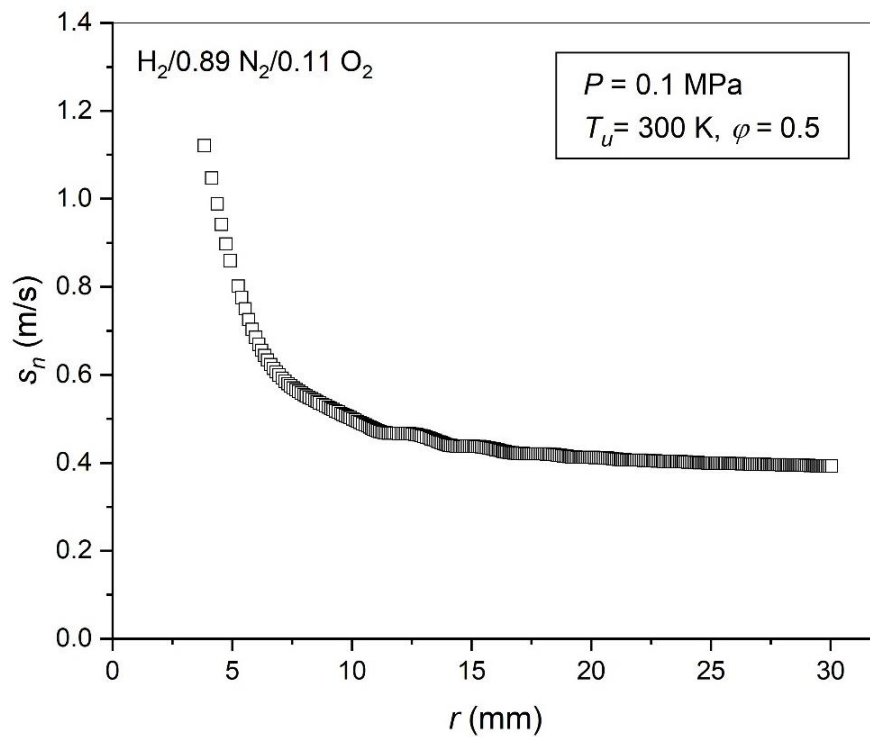


**Figure 3.6** A typical graph of the variation of stretched laminar flame speed with flame radius, for $H_2/0.11\ O_2/0.89\ N_2$ at 300 K, 0.1 MPa and $\varphi = 0.5$.

Over five experiments, the average value of $Ma_{sr}$ was calculated for the different fuel mixtures of $O_2$/$N_2$ fraction of 0.118/0.882, 0.115/0.885 and 0.11/0.89, respectively. Eqs. (1.10) and (1.11) were employed in the multiple regression method discussed in Section 2.7.2.2. All the parameters used in the present study are given in Table 3.2.

**Table 3.2** All parameters calculated for $H_2$/$O_2$/$N_2$ mixtures at 300K, 0.1 MPa and $\varphi$ =0.5.

| Fuel | $l$ (m) | $\nu$ (m²/s) | $\rho_u/\rho_b$ | $\delta_l$ (mm) | $u_l$ (m/s) | $Ma_{sr}$ |
|---|---|---|---|---|---|---|
| $H_2$+0.118$O_2$+0.882$N_2$ | 0.02 | 1.77E-05 | 3.61 | 0.143 | 0.124 | -0.4 |
| $H_2$+0.115$O_2$+0.885$N_2$ | 0.02 | 1.77E-05 | 3.56 | 0.16 | 0.111 | -0.1 |
| $H_2$+0.11$O_2$+0.89$N_2$ | 0.02 | 1.76E-05 | 3.47 | 0.18 | 0.0975 | 0.03 |

### 3.2.1.2  Comparison of Laminar Burning Velocity of $H_2$/$O_2$/$N_2$ Mixtures

The average laminar burning velocity of present mixture is calculated but at the same time it is important to compare these values with the literature. The current volume fractions and conditions are not studied in the literature; however, the pressure, temperature and equivalence ratio were the same. A higher and lower fraction of ($O_2$/$O_2$+$N_2$) were found in the study of Egolfopoulos and Law (1991) and Aung et al. (1998). The conditions studied in these references are shown in Fig. 3.7 and they showed a reasonable trend with the present conditions.
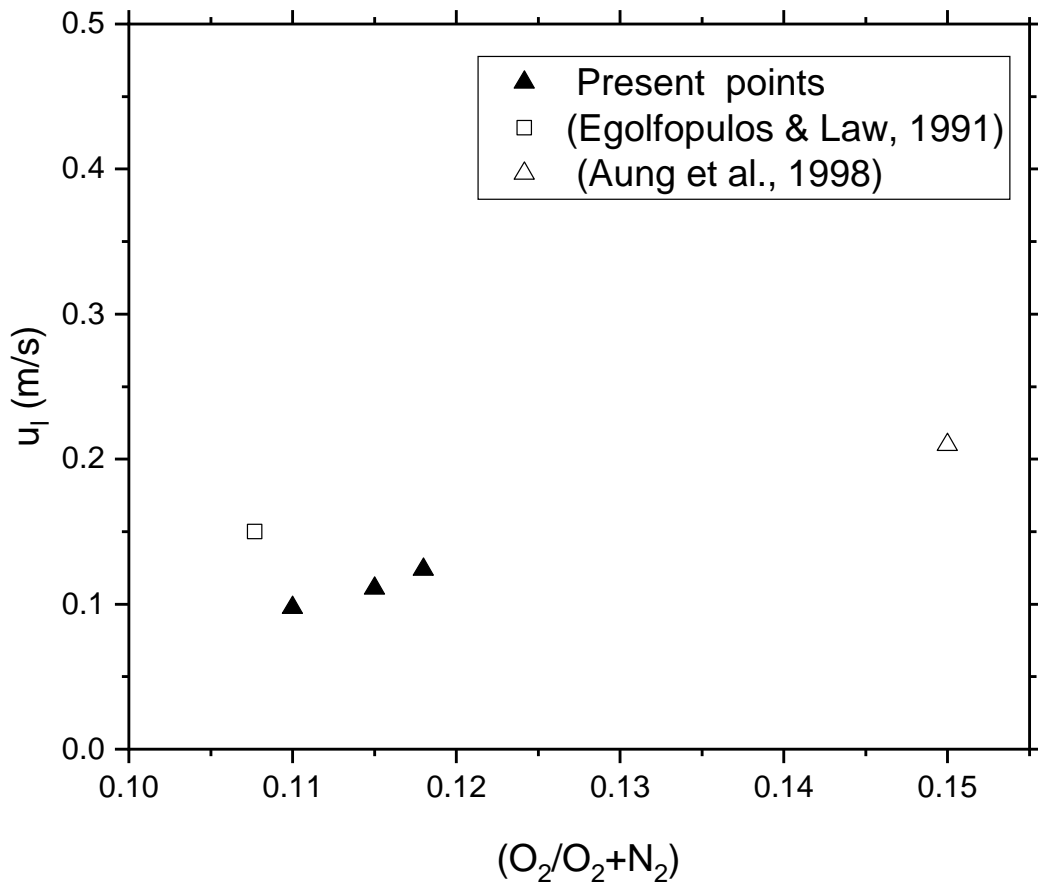
**Figure 3.7** Comparison of laminar burning velocity of $H_2/O_2/N_2$ mixture at different $O_2/(O_2+N_2)$ fraction.

## 3.3  Experimental Results of Laminar *n*-butanol/air Mixtures Using Schlieren Imaging Technique

*N*-butanol/air mixture was studied for certain cases where the laminar burning velocity is low. This occurred for lean butanol/air mixtures, ($\varphi = 0.7$) at 0.5 MPa and 1.0 MPa. The mixtures have been studied at 360 K as shown in Table 3.3.

**Table 3.3** Experimental work matrix for lean *n*-butanol/air mixtures.

| Fuel mixture | Temperature (K) | Pressure (MPa) | Equivalence ratio |
|---|---|---|---|
| *n* -butanol/air | 360 | 0.5 | 0.7 |
| *n* -butanol/air | 360 | 1 | 0.7 |

### 3.3.1 Stretched Laminar Flame Speed with Stretch Rate for *n*-butanol Mixtures

Using the same procedure which applied in Section 3.2.1.1, the unstretched laminar burning velocity is determined using $s_n, \alpha$ plot for the cases. Figures 3.8 and 3.9, show the effect of flame stretch rate on the flame speed. The linear extrapolation of the curve gives the unstretched laminar burning velocity, $S_s$.
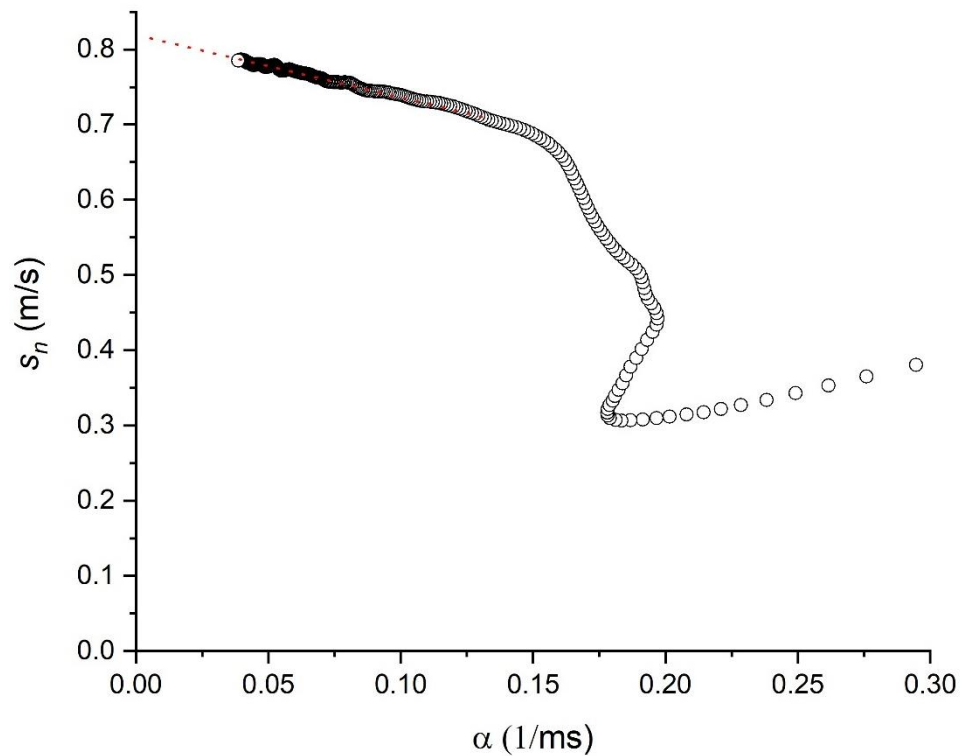


**Figure 3.8** A typical graph of the variation of stretched laminar flame speed with stretch rate, for *n*-butanol/air mixture at 360 K, 0.5 MPa and $\varphi$ =0.7. Solid red line denote linear relationship for $L_b$ through data points.
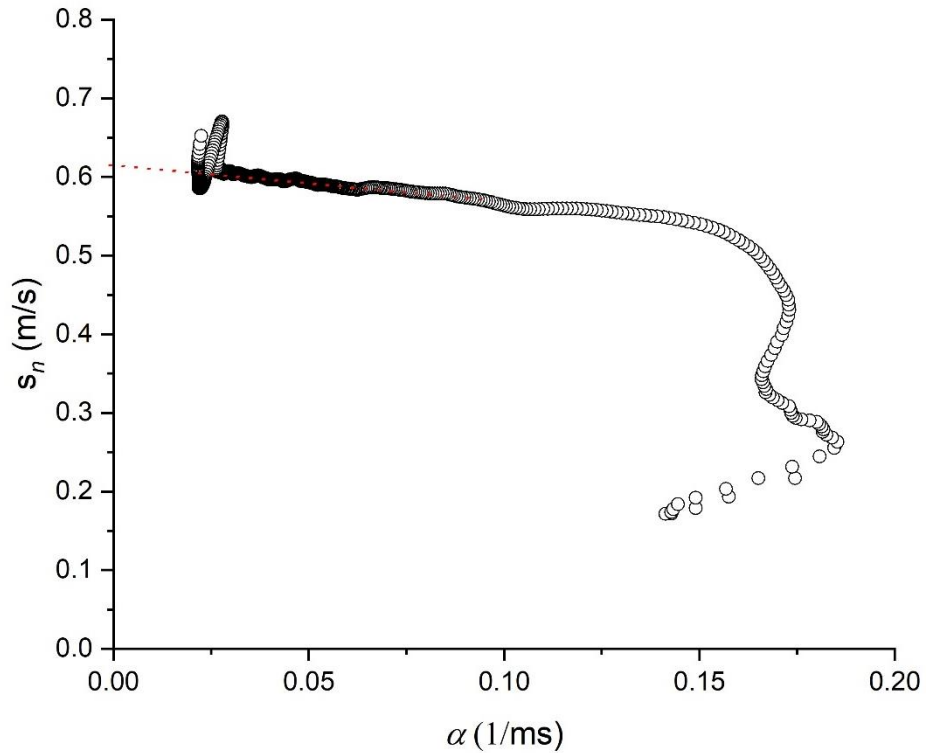
**Figure 3.9** A typical graph of the variation of stretched laminar flame speed with stretch rate, for *n*-butanol/air mixture at 360 K, 1 MPa and *φ* =0.7. Solid red line denote linear relationship for $L_b$ through data points.

The laminar burning velocity for the two cases were calculated using Eq. (1.3) knowing the density ratio, $\rho_b/\rho_u$ , using the Gaseq code (Morley, 2005). As mentioned in Section 1.2.1.3, the effect of stretch rate on laminar burning velocity is characterised by Markstein number for strain rate, $Ma_{sr}$.

From five explosions, the average $Ma_{sr}$ is calculated for *n*-butanol at 0.5 MPa and 1 MPa. It is evaluated to be 9 for *n*-butanol/air mixture at 0.5 MPa and 6 at 1 MPa. All the parameters are listed in Table 3.4.

**Table 3.4** All parameters for *n*-butanol/air mixtures at 360K, 0.5 and 1 MPa and *φ* =0.7.

| Fuel | P (MPa) | $l$ (m) | $\nu$ (m²/s) | $\rho_u/\rho_b$ | $\delta_l$ (mm) | $u_l$ (m/s) | $Ma_{sr}$ |
|---|---|---|---|---|---|---|---|
| *n*-butanol/air | 0.5 | 0.02 | 4.27E-6 | 5.61 | 0.029 | 0.147 | 9 |
| | 1 | 0.02 | 2.14E-6 | 5.61 | 0.0225 | 0.095 | 6 |

## 3.4  Experimental Results of Turbulent Expanding H₂/O₂/N₂ Flames

Experiments were performed for rms velocities, $u'$, ranging from 6 to 10 m/s to see the effect of excessive flame stretch on the structure of the flame and probability of quenching. As shown in Table 3.2, the laminar burning velocities, $u_l$, of the three mixtures are low and this is the reason why these mixtures are employed. Therefore, it will be able to check the probability of flame propagation at high turbulence.

Five experiments were conducted for the three mixtures at different $u'$. In essence, the increase in turbulence led to a higher value of Karlovitz numbers, $K$.

Particularly, in these turbulent experiments, it was difficult to maintain a constant room temperature at high fan speed and atmospheric pressure. Temperatures could only be maintained with a tolerance of $\pm$5K. Schlieren images are captured for all experiments at time intervals between frames of 0.1852 ms as the sampling rate is 5400 fps.

At $u'$ =10 m/s, H₂/0.118O₂/0.882N₂ mixture has a probability of propagation, of 40%, $p_{0.4}$, and this percentage is highest among the three mixtures. For H₂/0.115O₂/0.885N₂, the flame propagated only once from five experiments, $p_{0.2}$, whilst there was no propagation for H₂/0.11O₂/0.89N₂. This is the limiting rms velocity for the spherical vessel, which we cannot go beyond. At lower values of $u'$, the probability of the flame propagation varies for different mixtures and consequently, turbulent burning velocity are calculated. Schlieren frames are presented in Figs. 3.10 to 3.13 for the different mixtures at different $u'$ and time from ignition. It is clearly seen how increasing $u'$, enhances the wrinkling of the turbulent flames.

| $P\ (MPa)$ | $u'(\frac{m}{s})$ | | |
|---|---|---|---|
| | 7 | 9 | 10 |
| 0.1 |  1.85 ms |  0.5 ms |  1.85 ms |
| |  3.14 ms |  1.85 ms |  3.14 ms |
| |  5 ms |  3.14 ms |  5 ms |
| |  6.5 ms |  4 ms |  6.5 ms |
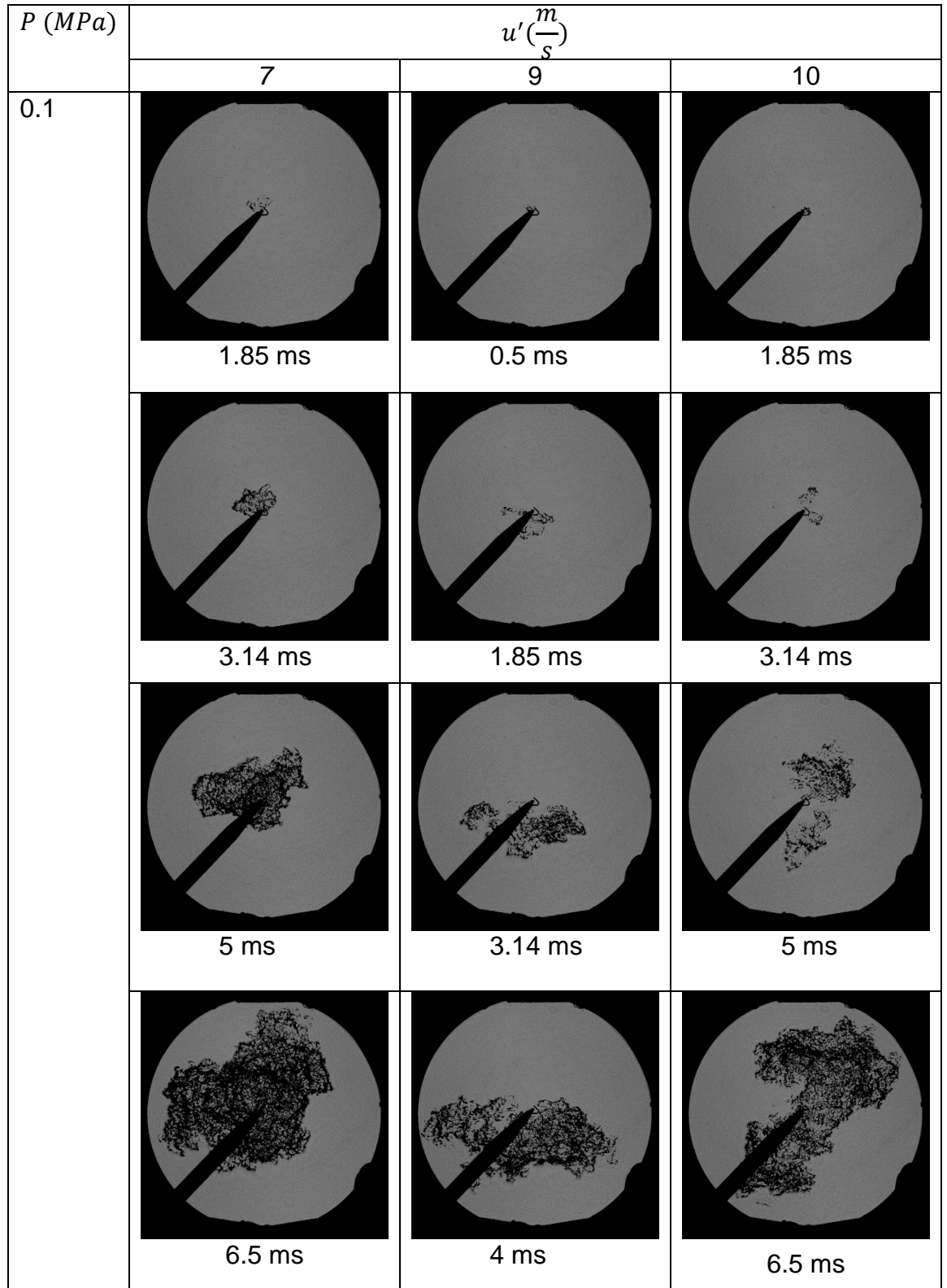
**Figure 3.10** Turbulent flame propagation in lean H₂/0.118O₂/0.882 N₂ mixture, $\varphi$ = 0.5, 300±5K, 0.1 MPa at $u'$ =7,9,10 m/s and different $t$.

| $P\ (MPa)$ | $u'(\frac{m}{s})$ | | |
|---|---|---|---|
| | *6* | *7* | *9* |
| 0.1 |  1.85 ms |  1.85 ms |  0.5 ms |
| |  3.14 ms |  3.14 ms |  1.85 ms |
| |  5 ms |  5 ms |  3.14 ms |
| |  8.9 ms |  6.1 ms |  5 ms |
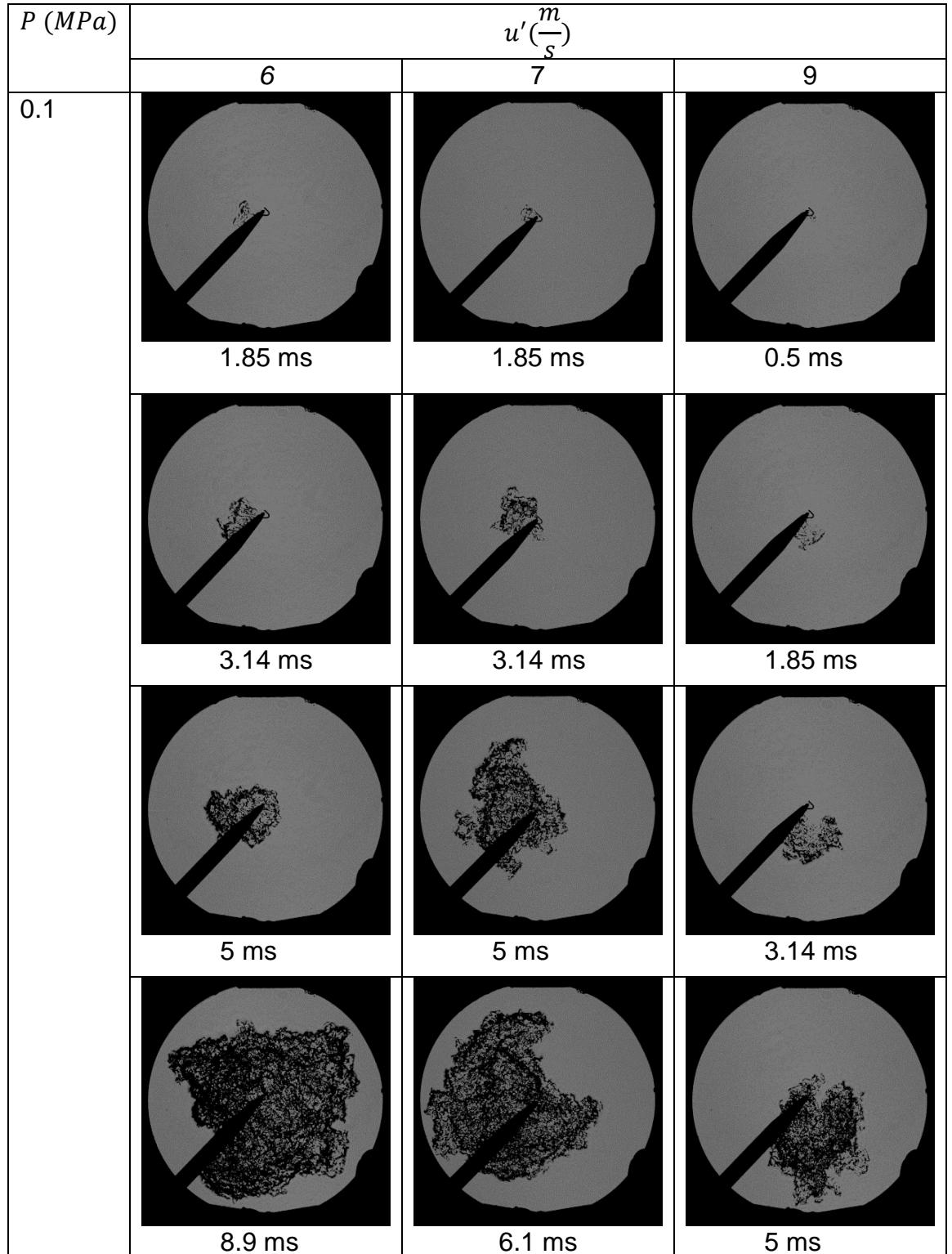
**Figure 3.11** Turbulent flame propagation in lean H₂/0.115O₂/0.885N₂ mixture, $\varphi$ = 0.5, 300±5K, 0.1 MPa at $\boldsymbol{u'}$ =6,7,9 m/s and different *t*.
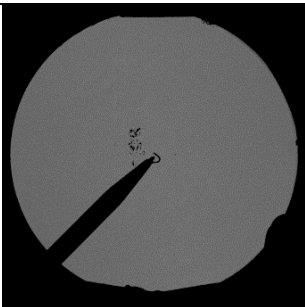
| $Po\ (MPa)$ | $u'(\frac{m}{s})$ |
|---|---|
| | 10 |
| 0.1 |  0.5 ms |
| |  1.48 ms |
| |  2.7 ms |
| |  3.9 ms |

**Figure 3.12** Turbulent flame propagation in lean H₂/0.115O₂/0.885N₂ mixture, $\varphi$ = 0.5, 300±5K, 0.1 MPa at $\boldsymbol{u'}$ = 10 m/s and different *t*.

| $P\ (MPa)$ | $u'(\frac{m}{s})$ | | |
|---|---|---|---|
| | *6* | *7* | *9* |
| 0.1 |  1.85 ms |  1.85 ms |  1.85 ms |
| |  3.14 ms |  3.14 ms |  3.14  ms |
| |  5 ms |  5 ms |  5 ms |
| |  7.7 ms |  7.7 ms |  7.7 ms |
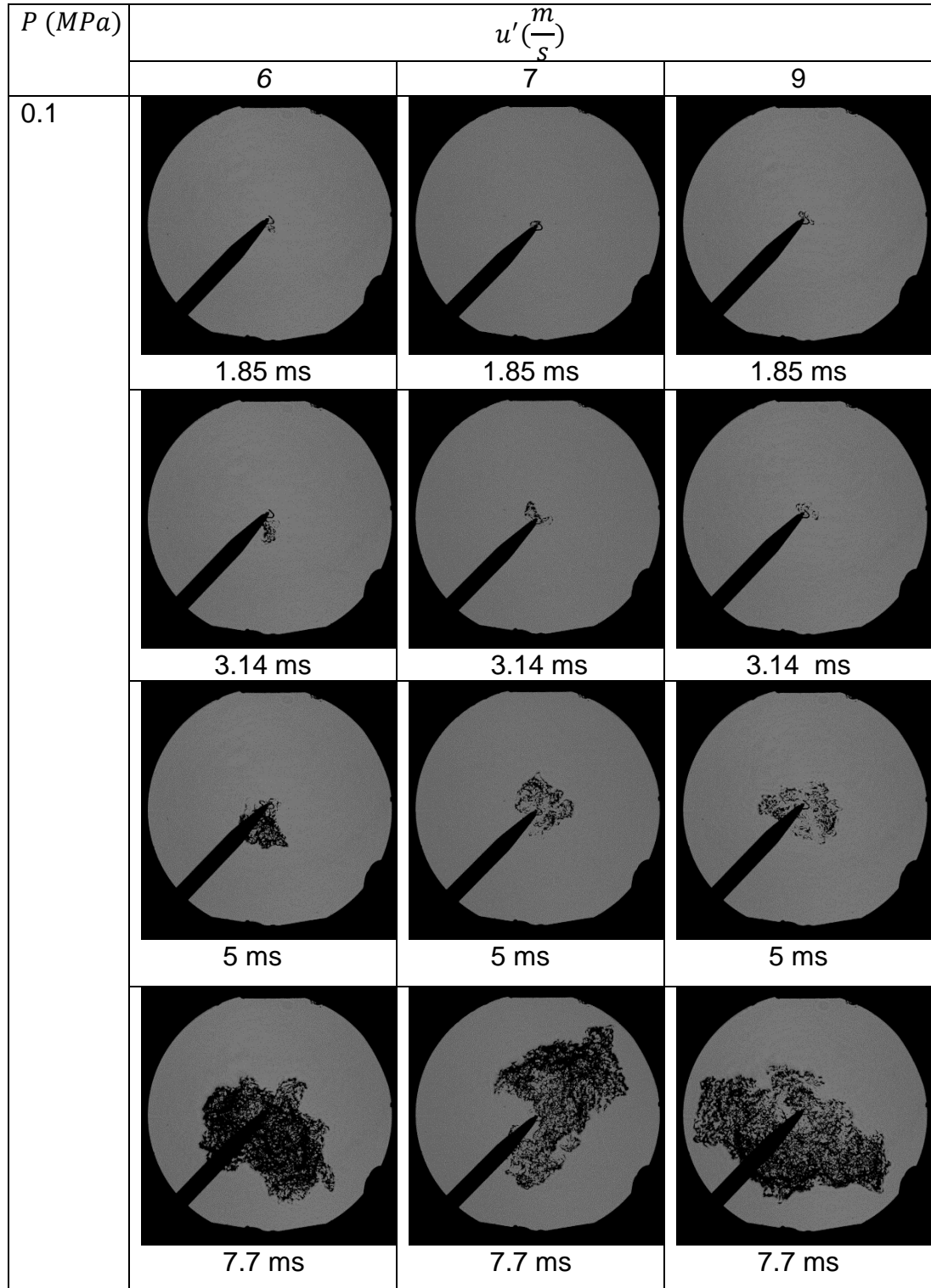
**Figure 3.13** Turbulent flame propagation in lean H₂/0.11O₂/0.89N₂ mixture, $\varphi = 0.5$, 300±5K, 0.1 MPa at $\boldsymbol{u'}$ = 6,7,9 m/s and different *t*.

Figures 3.14 to 3.16 show the change of $u'_k$ with $u_{tr}$ at different rms velocity, $u'$. It is shown that $u_{tr}$ is increasing with $u'_k$ at different $u'$. It is also presented that erratic behaviour starts to progress due to the high turbulence even the flame kernel was convected from the spark gap it is still difficult to propagate easily due to the flame stretch at higher rms velocity.
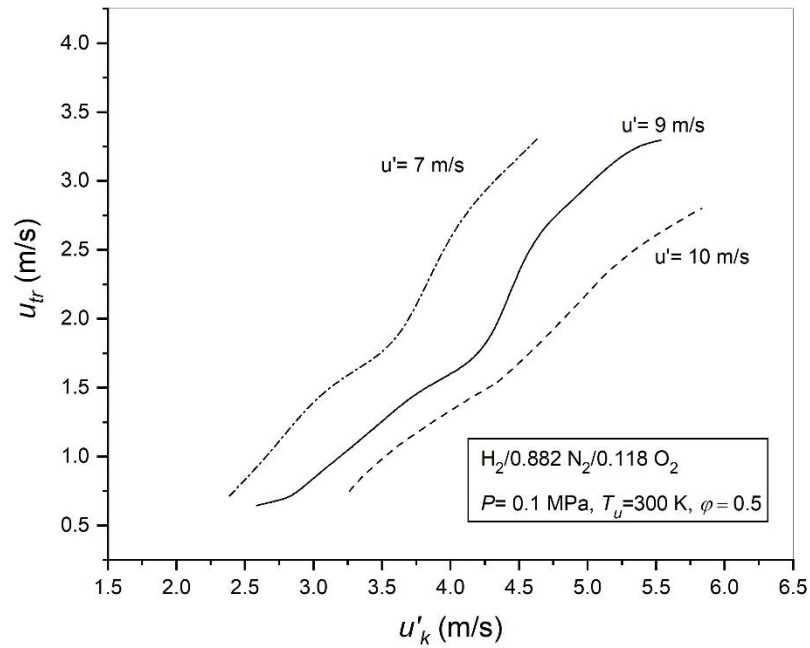


**Figure 3.14** Variation of $u'_k$ with $u_{tr}$ at different $u'$ for H₂/0.118O₂/0.882N₂.
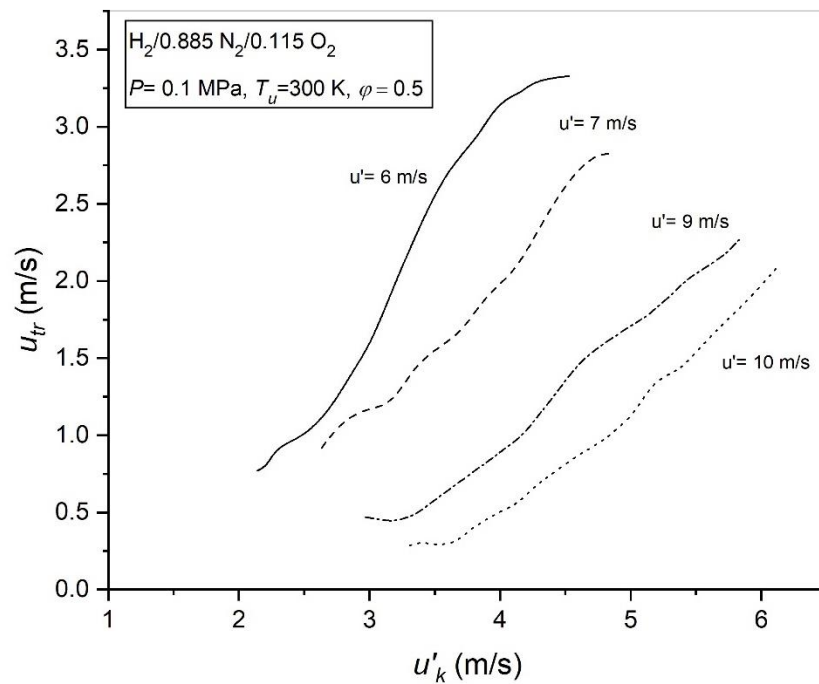


**Figure 3.15** Variation of $u'_k$ with $u_{tr}$ at different $u'$ for H₂/0.115O₂/0.885N₂.
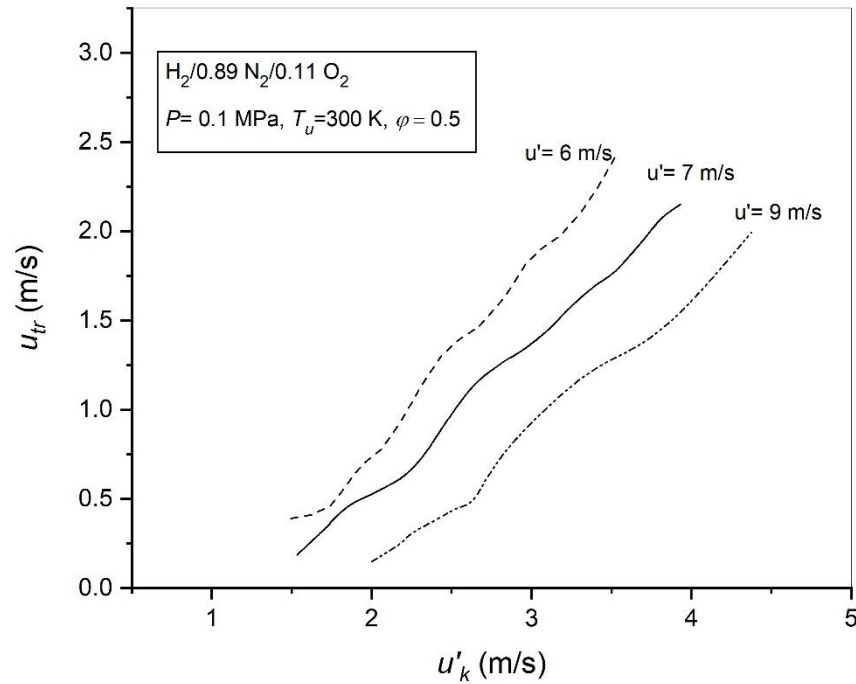
**Figure 3.16** Variation of $u'_k$ with $u_{tr}$ at different $u'$ for H₂/0.11O₂/0.89N₂.

### 3.4.1   Calculated and Measured Turbulent Burning Velocity

The calculated turbulent burning velocity is evaluated as a function of $U$ using $K$ and $Ma_{sr}$. Eqs. (1.32) to (1.34) have been used knowing the values of $K$ and calculated $Ma_{sr}$ from laminar experiments data. These calculated $U$ have been compared with the experimental ones. All the results are listed in Tables 3.5 to 3.7. The error evaluated between the calculated and measured values is about 15:20% due to the extreme turbulence.

The probability of burning is evaluated for all mixtures at different u'. The results showed that the probability of burning, $P_b$ at the highest $u'$ =10 m/s was 0.4 for H₂/0.118O₂/0.882N₂ and 0.2 for H₂/0.115O₂/0.885N₂. Also, the probability of burning at 9 m/s was 0.8, 0.6, and 0.2 for H₂/0.118O₂/0.882N₂, H₂/0.115O₂/0.885N₂ and H₂/0.11O₂/0.89N₂, respectively.

**Table   3.5** Experimental   result   for   turbulent   explosion   of   lean H₂/0.118O₂/0.882N₂ at 0.1 MPa and 300 K.

| $u'$ (m/s)     | 7     | 9     | 10    |
|----------------|-------|-------|-------|
| $K$            | 9.014 | 13.14 | 15.39 |
| $U$ calculated | 0.473 | 0.432 | 0.416 |

| $U$ experimental | 0.559 | 0.36 | 0.32 |
|---|---|---|---|
| $P_b$ | 1 | 0.8 | 0.4 |

**Table 3.6** Experimental result for turbulent explosion of lean H$_2$/0.115O$_2$/0.885N$_2$ at 0.1 MPa and 300 K.

| $u'$ (m/s) | **6** | **7** | **9** | **10** |
|---|---|---|---|---|
| $K$ | 8.87 | 11.284 | 16.451 | 19.267 |
| $U$ calculated | 0.474 | 0.448 | 0.410 | 0.395 |
| $U$ experimental | 0.561 | 0.426 | 0.34 | 0.27 |
| $P_b$ | 1 | 0.8 | 0.6 | 0.2 |

**Table 3.7** Experimental result for turbulent explosion of lean H$_2$/0.11O$_2$/0.89N$_2$ at 0.1 MPa and 300 K.

| $u'$ (m/s) | **6** | **7** | **9** |
|---|---|---|---|
| $K$ | 11.46 | 14.445 | 21.1 |
| $U$ calculated | 0.446 | 0.423 | 0.386 |
| $U$ experimental | 0.46 | 0.38 | 0.343 |
| $P_b$ | 0.8 | 0.6 | 0.2 |

## 3.5  Flame Quench Analysis

Using schlieren image photography, it was possible to capture continuous record of flames starting from the ignition until quenching. A mixture of *i*-octane/air,$\varphi$=0.8 at 0.5 MPa, and 360 K was recorded from the point of ignition till the point of quenching where the rms velocity, $u'$ was 6 m/s. Four frames at different times from ignition are shown in Fig. 3.17. As seen, the flame propagates and then starts disintegration after 4 ms.
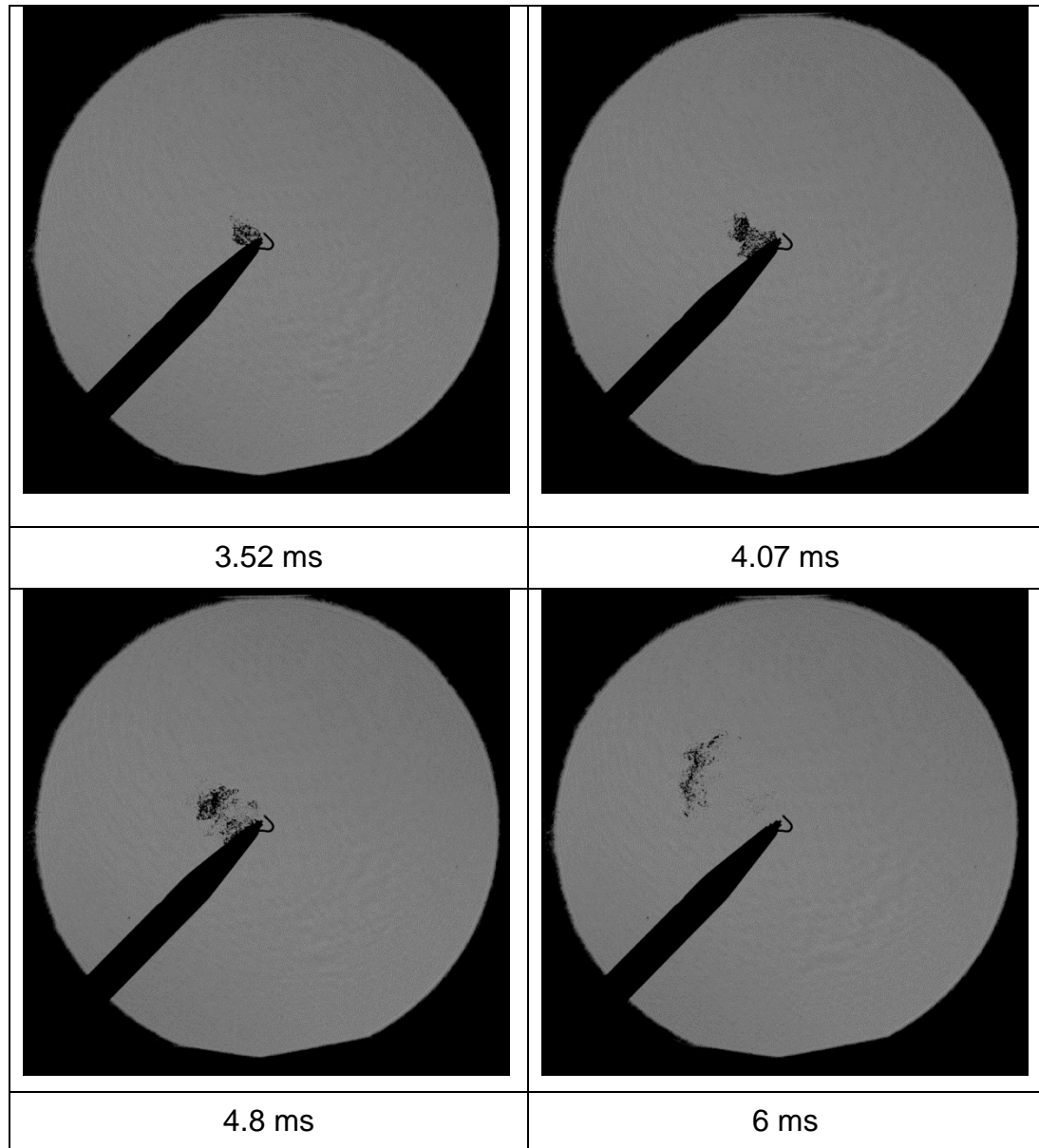
**Figure 3.17** Quenching of lean iso-octane/air mixture, $\varphi$ =0.8, at 0.5 MPa and 360 K with $u'$ = 6 m/s,$p_{0.6}$.

Here the mixture seems to quench due to the excessive stretching. The high turbulence counters the propagation of the flame and ultimately leads to extinction.

Conversely, another mixture of methane/ air as shown in Fig. 3.18 at $\varphi$=1.35 at 0.5 MPa, and 365 K with $u'$= 3 m/s had a different behaviour. Differently, the flame propagates and it was about to quench after 2 ms before it continued growing as a normal propagating turbulent flame. The flame after 4 ms had a curl like-shape and it kept continuously propagating. Ultimately, this flame did not quench.

|  |  |
|---|---|
| 2.2 ms | 3.33 ms |
| 4.81 ms | 5.55 ms |
| 6.7 ms | 7 ms |
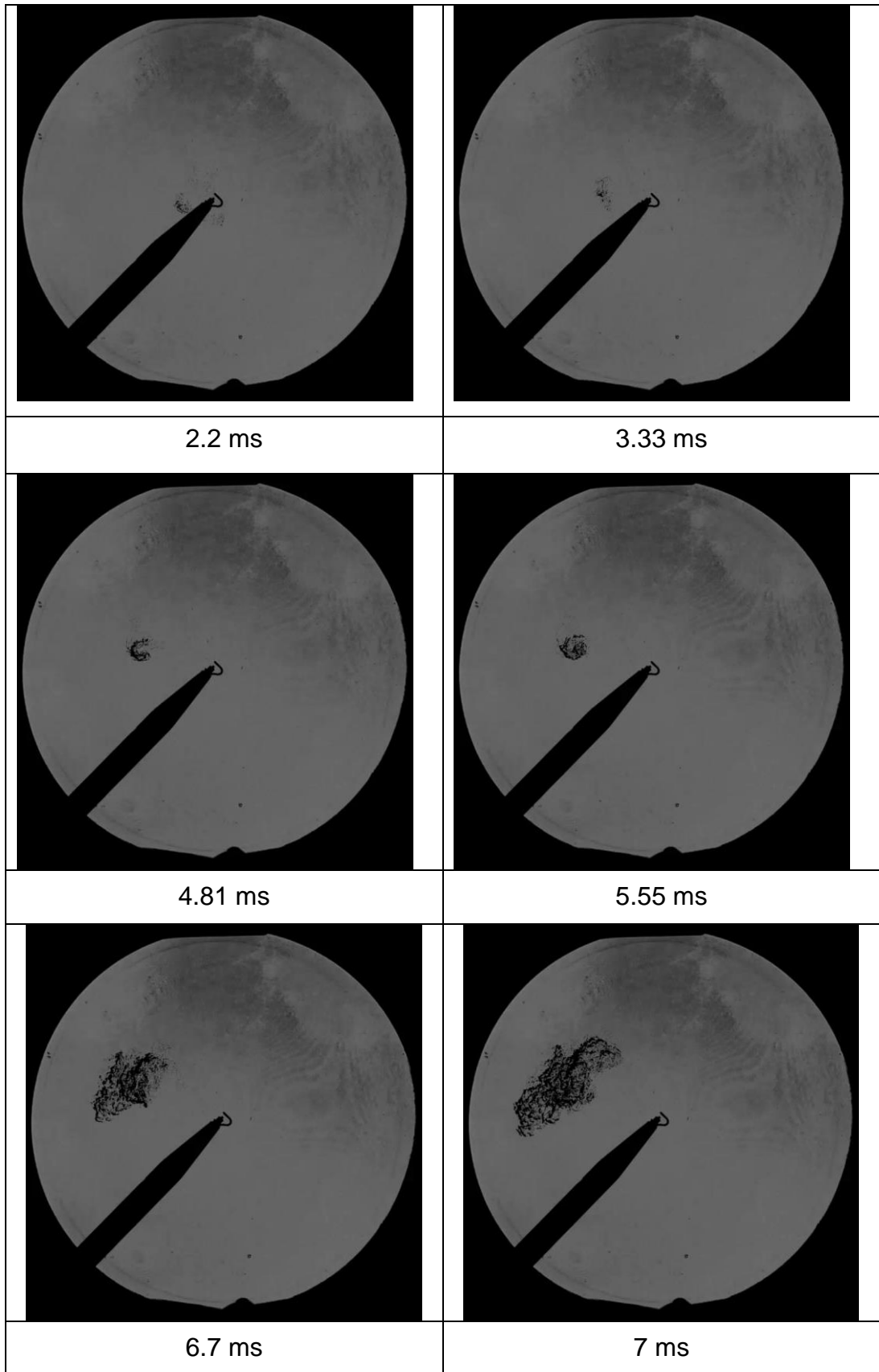
Figure 3.18 Propagation of rich methane/air mixture, $\varphi$=1.35, at 0.5 MPa and 360 K with $u'$= 6 m/s, $p_{0.8}$.

From those frames shown in Figs 3.17 &3.18, it is seen that the probability of burning, $p_b$ has a role on flame quenching but, at the same time, the stretch rate and the flame size also were found to be playing a biggest role.

To obtain the equivalent diameters of the schlieren image flame kernels, the 2-D projected areas were measured using MATLAB code, and the flame surface areas calculated from the black pixels in the binary images (Section 2.7.3).

A criterion has been applied to examine different fuel mixtures, whether they will quench or propagate. The measurements of turbulent quenching diameters and stretch rates have been carried out and correlated. A critical flame kernel diameter to thickness ratio is then defined for quench. These will be presented in the next subsections.

### 3.5.1   Preheat Zone Flame Thickness

At the start of the analysis, it was necessary to calculate the laminar flame thickness for the correlation as are presented in Göttgens et al. (1992). This chemically inert preheat zone thickness is:

$$\delta_k = \frac{(\frac{K}{C_p})_{To}}{\rho_u u_l},$$                    (3.1)

where $k$ and $c_p$ are the thermal conductivity and specific heat at constant pressure at the inner layer temperature, $T^o$. The unburned gas density is $\rho_u$. Values of all the required physicochemical data were obtained from the Gaseq code (Morley, 2005).

The inner layer temperatures, for CH$_4$ and H$_2$, $T^o$, were evaluated from (Göttgens et al., 1992) at the different pressures. For $i$-octane, $T^o$ was evaluated from (Müller et al., 1997). Due to the lack of data for $n$-butanol, $T^o$ was estimated from the data for methanol and ethanol (Müller et al., 1997; Röhl et al., 2009). With $u_l$  and $\rho_u$, it was possible to find $\delta_k$.

### 3.5.2   Flame Quenching

An example of the evolution of quenching kernels, revealed by 2D schlieren images, is shown by the continuous curve in Fig. 3.19. Values of $d$, normalised by $\delta_k$ are plotted against the time from ignition. Two images are shown, one

just after kernel generation, the other of the quenching kernel. A scaling bar for 15 mm of kernel size is shown. Soon after ignition the flame develops until it reaches a maximum value of $d$, the critical value, $d_k$, after which the flame starts to disintegrate and ultimately quench. The broken curve is of $u'_k$, obtained from the measured $u'$ and Eq. (1.25).

Derived equivalent diameters of flame kernels, $d$, are going to be normalised by the corresponding values of $\delta_k$.

These thicknesses are obtained from the expression of Göttgens et al. (1992). This identifies an inner layer, the thickness of which is defined by the location of a temperature $T^o$, below which there is no reaction.
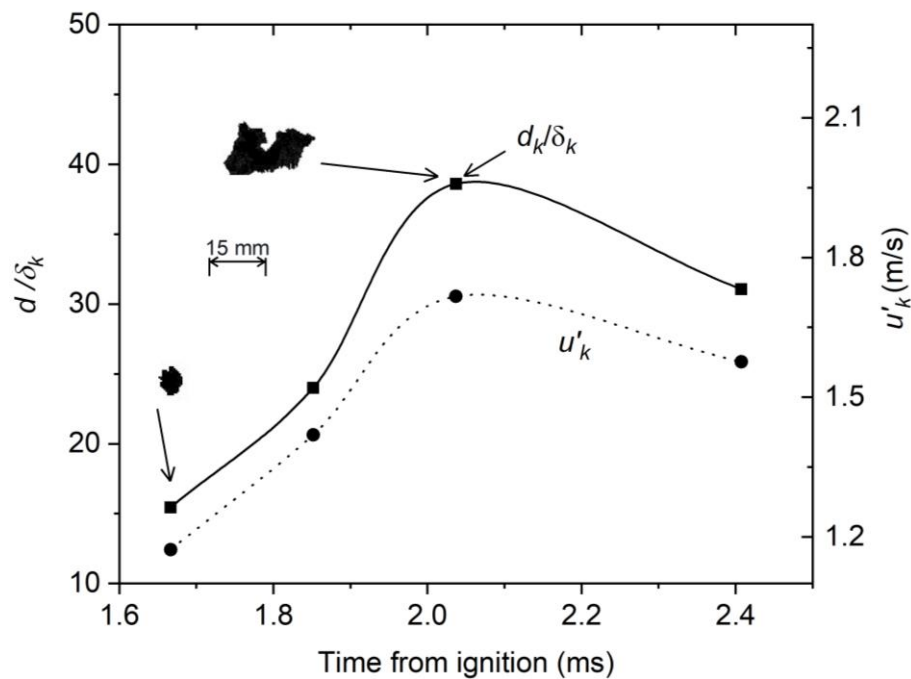


**Figure 3.19** Temporal variation of $d/\delta_k$ and $u'_k$ from ignition, for quenching of a CH₄/air kernel at 0.5 MPa and 365 K at $\varphi$ =0.6, $K$ = 11.6.

### 3.5.3   Collected Experimental Results

Numerous experiments were performed for different fuel mixtures at the conditions of quenching.  All the experimental data are listed in Table 3.8. Conditions were employed, at pressures of 0.1, 0.5, and 1.0 MPa. Temperatures were 300, 360 and 365 K. Laminar burning velocity of H₂/O₂/N₂ and *n*-butanol air mixtures data are used from Table 3.2 and 3.4 alongside with $Ma_{sr}$.The probability of burning for all data is presented. Owing to the

importance of the smaller length scales in quenching, it might be thought advantageous to plot these values against a Karlovitz number, $Ka$, based upon the smaller Kolmogorov eddy time scale. This anticipation holds no advantage, principally because it can be shown that $Ka/K \approx 15^{0.5}$. Values of $Ka$ are given in the Table 3.8.

**Table 3.8** Experimental Quench Data from schlieren imaging technique.

| Fuel/air mixture | Method | $T$ (K) | $P$ (MPa) | $\varphi$ | $u'$ (m/s) | $u'_k$ (m/s) | $\dfrac{d_k}{\delta_k}$ | $T^o$ (K) | $u_l$ (m/s) | $\nu$ (m²/s) | $K$ | $Ma_{sr}$ | $Ka$ | $p_b$ |
|---|---|---|---|---|---|---|---|---|---|---|---|---|---|---|
| H$_2$/0.11 O$_2$/0.89 N$_2$ | schlieren system | 300 | 0.1 | 0.5 | 6 | 2.14 | 16 | 1003 | 0.0975 | 1.76E-05 | 11.46 | 0.03 | 48 | 0.8 |
| H$_2$/0.115O$_2$/0.885 N$_2$ | | 300 | 0.1 | 0.5 | 7 | 3.062 | 17 | 1003 | 0.111 | 1.77E-05 | 11.28 | -0.1 | 46 | 0.8 |
| H$_2$/0.11 O$_2$/0.89 N$_2$ | | 300 | 0.1 | 0.5 | 7 | 2.8 | 21 | 1003 | 0.0975 | 1.76E-05 | 14.45 | 0.03 | 58.6 | 0.6 |
| H$_2$/0.118 O$_2$/0.882N$_2$ | | 300 | 0.1 | 0.5 | 9 | 3.38 | 23 | 1003 | 0.124 | 1.77E-05 | 13.14 | -0.4 | 53.3 | 0.8 |
| H$_2$/air | | 365 | 0.5 | 0.15 | 2.25 | 0.82 | 24 | 1172 | 0.036 | (Bradley et al., 2007b) | 4.79E-06 | 10.08 | -2 | (Bradley et al., 2007b) | 39.7 | 0.8 |

**Table 3.8** : Cont'd

| Fuel/air mixture | Method | $T$ (K) | $P$ (MPa) | $\varphi$ | $u'$ (m/s) | $u'_k$ (m/s) | $\dfrac{d_k}{\delta_k}$ | $T^o$ (K) | $u_l$ (m/s) | | $\nu$ (m²/s) | $K$ | $Ma_{sr}$ | | $Ka$ | $p_b$ |
|---|---|---|---|---|---|---|---|---|---|---|---|---|---|---|---|---|
| $n$-$C_4H_{10}O$/air | | 360 | 1 | 0.7 | 0.6 | 0.121 | 62 | 1500 | 0.095 | | 2.14E-6 | 0.121 | 6 | | 0.39 | 0.8 |
| $n$-$C_4H_{10}O$/air | | 360 | 0.5 | 0.7 | 2 | 0.66 | 76 | 1400 | 0.147 | | 4.27E-06 | 0.478 | 9 | | 1.89 | 0.4 |
| $n$-$C_4H_{10}O$/air | schlieren system | 360 | 0.5 | 0.7 | 2 | 0.61 | 80 | 1400 | 0.147 | (Bradley et al., 2007b) | 4.27E-06 | 0.478 | 9 | (Bradley et al., 2007b) | 1.89 | 0.4 |
| $i$-$C_8H_{18}$/air | | 365 | 0.5 | 0.8 | 6 | 2.3 | 125 | 1320 | 0.2 | | 4.37E-06 | 1.344 | 5 | | 5.47 | 0.6 |
| $i$-$C_8H_{18}$/air | | 365 | 0.5 | 0.8 | 6 | 2.34 | 127 | 1320 | 0.2 | | 4.37E-06 | 1.344 | 5 | | 5.47 | 0.6 |
| $i$-$C_8H_{18}$/air | | 365 | 0.5 | 0.8 | 6.5 | 2.57 | 131 | 1320 | 0.2 | | 4.37E-06 | 1.516 | 5 | | 6.51 | 0.4 |
| $CH_4$/air | | 365 | 0.5 | 1.35 | 3 | 0.83 | 37 | 1328 | 0.095 | | 4.60E-06 | 2.183 | 6 | | 8.54 | 0.8 |

### 3.5.4    Variations of *d/δ$_k$* for Different Quenching Flames During Time

In Fig. 3.20, the *n*-butanol/air, $\varphi$ = 0.7, schlieren images at 360 K and 0.5 MPa are of interest, in that the kernel is about to extinguish at $d/\delta_k$ = 55. Then propagation revives, with extinction finally occurring at $d_k/\delta_k$ = 77.
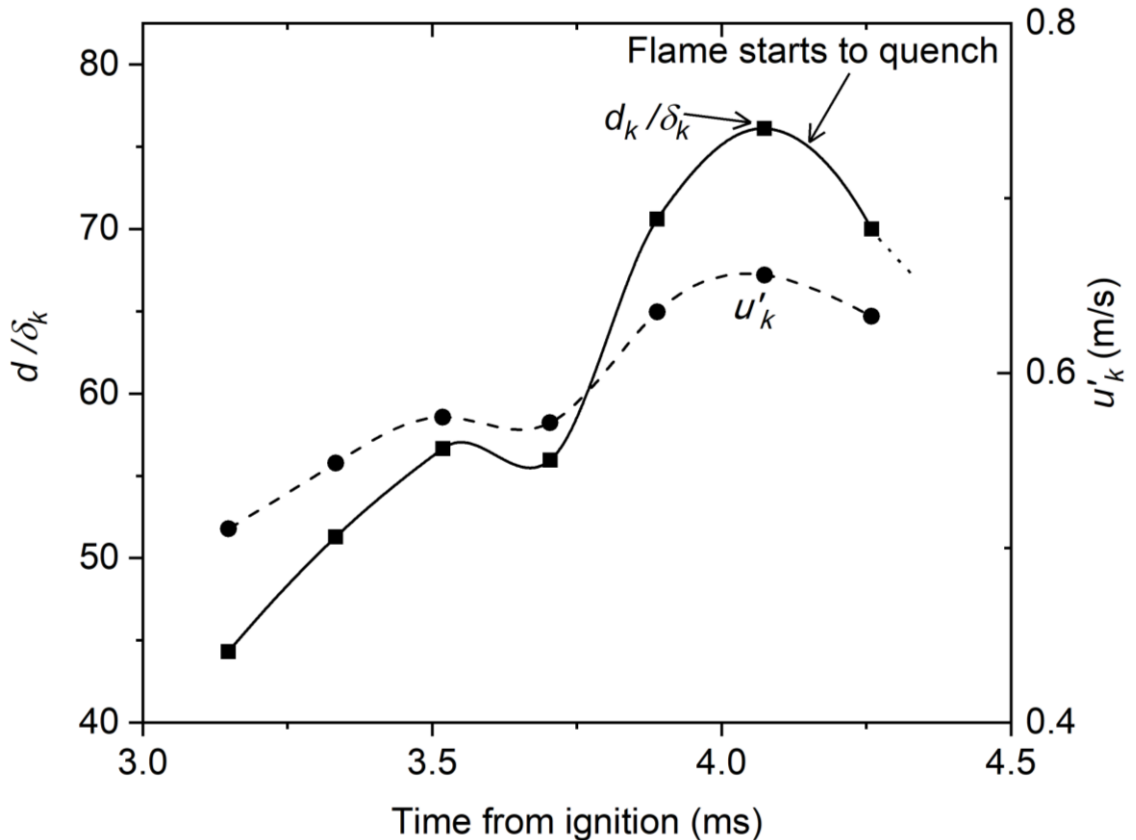


**Figure 3.20** Temporal variation of *d/δ$_k$* and *u'$_k$* from ignition for *n*-butanol/air at 360 K, 0.5 MPa, $\varphi$ =0.7 and *u'* = 2 m/s, *K*= 0.478, $p_{0.4}$.

Figure 3.21 is of interest in showing how, for the same conditions, temporal profiles of $d/\delta_k$ can differ yet yield similar values of $d_k/\delta_{k.}$. While Fig. 3.22 shows combustion of H₂ to be the most rapid, with the smallest values of $d_k$. The hydrogen flame fragments were smaller and took a longer time to disappear than those of CH₄.
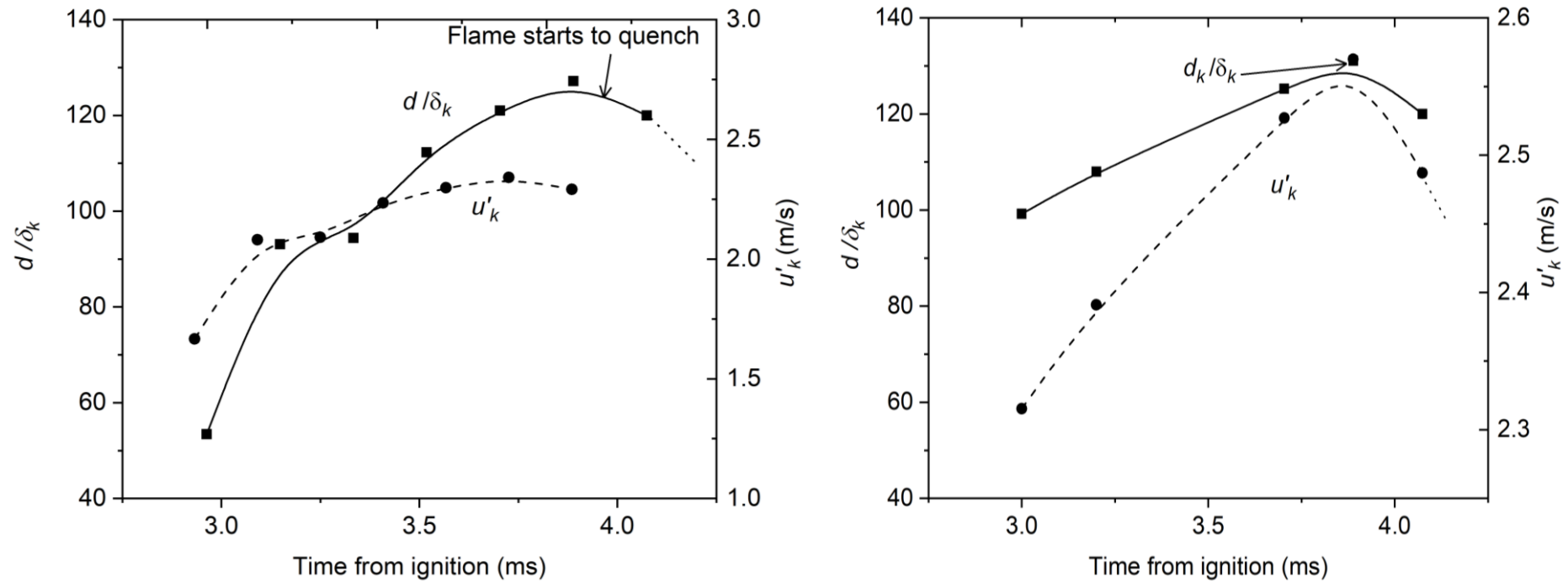
**Figure 3.21** Contrasting temporal variations of $d/\delta_k$ and $u'_k$ with time from ignition from two experiments of the same mixture of $i$-$C_8H_{18}$/air mixtures at the same conditions of 365 K, 0.5 MPa, $\varphi = 0.8$ and u'= 6 m/s, $K$=1.34, $p_{0.6}$.
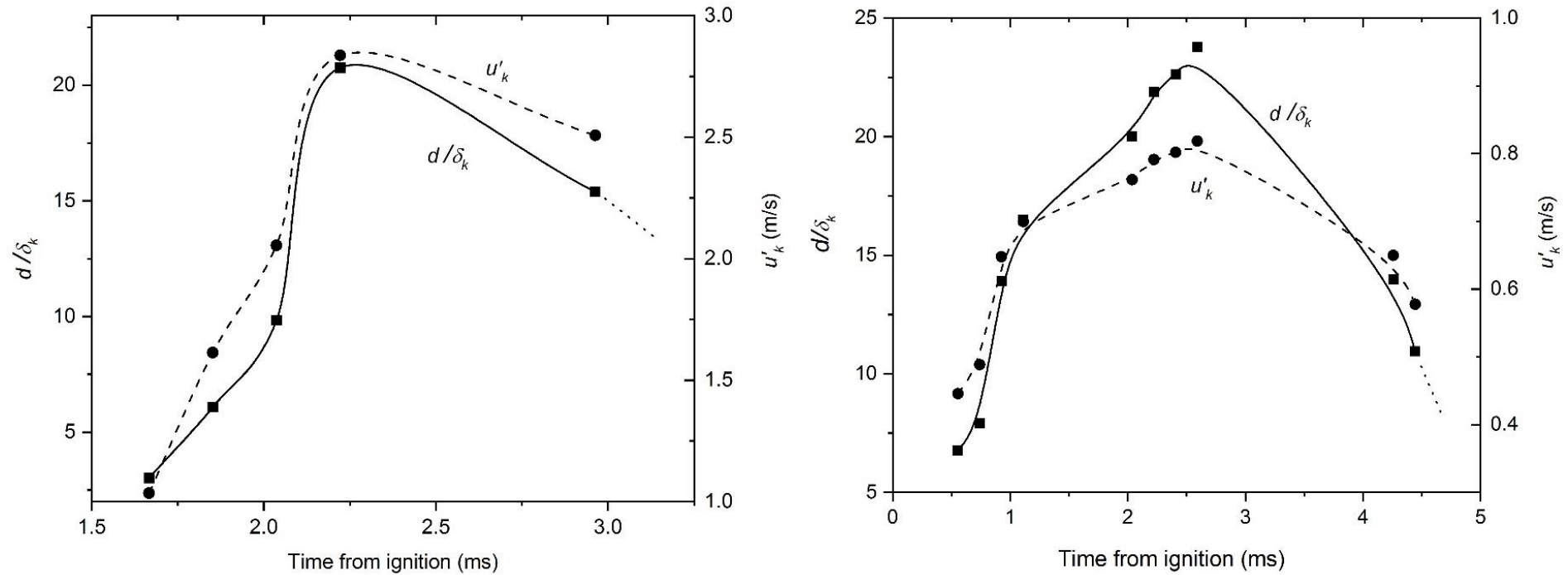
(a) H₂/0.11O₂/0.89N₂ mixtures at 300 K, 0.1 MPa, $\varphi = 0.5$ and $u' = 7$ m/s, $K = 14.4$, $p_{0.6}$.

(b) H₂/air mixtures at 300 K, 0.5 MPa, $\varphi = 0.15$ and $u' = 2.25$ m/s, $K = 10.08$, $p_{0.8}$.

**Figure 3.22** Variation of $d/\delta_k$ with time from ignition for Hydrogen mixtures.

### 3.5.5   Comparison between 2D Schlieren, and 3D Swinging Sheet Flames

Well time-resolved, detailed, sequences of flame quenching could only be captured using schlieren photography. But with a maximum 60 kHz laser imaging repetition frequency too low for the swinging sheet technique to record fully a detailed quenching sequence. Therefore, only near-quench flames were employed using swinging sheet technique.

Comparison between the two techniques were carried-out for near-quench flames. Figure 3.23 compares the changing values of $d/\delta_k$ from both 2D schlieren, and 3D swinging sheet, images for CH4/air, $\varphi$ = 1.35 at 365 K and 0.5 MPa, for $u'$ = 3 m/s in (a), and 2 m/s in (b). In Fig 3.23(a) the earlier images reflect their origin around an electric spark. The five images show the initial establishment of a predominantly laminar flame that makes a transition to a turbulent flame.
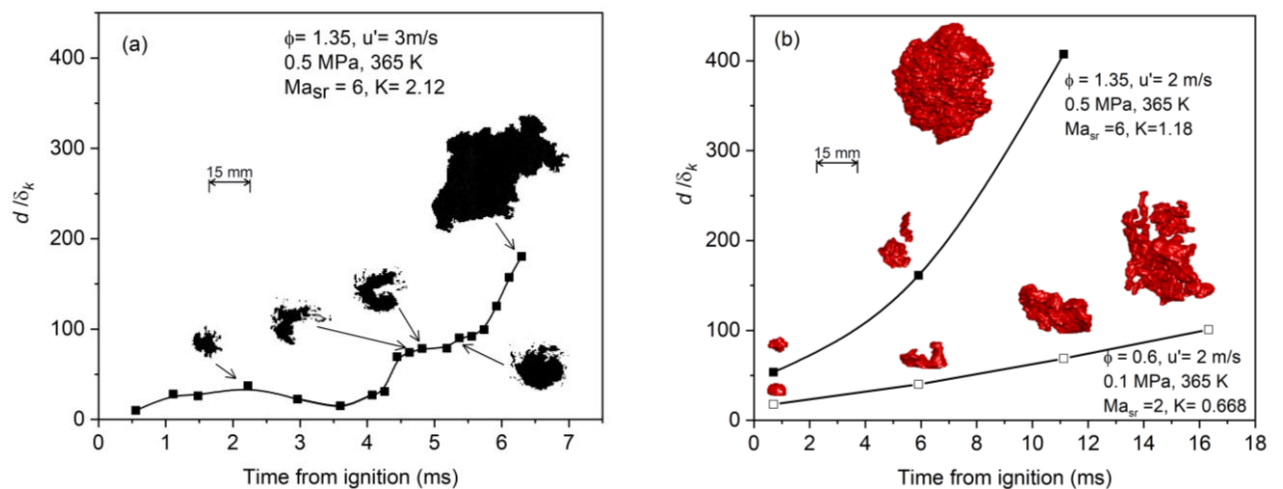


(a) Schlieren 2D images, $u'$ = 3 m/s.        (b) Laser swinging sheet 3D images, $u'$ = 2 m/s.

**Figure 3.23** Temporal variations of $d/\delta_k$ from ignition for CH4-air at 365 K from (a) schlieren, and (b) laser swinging sheets.  Complete mixture details on the figures. (Bradley et al., 2019)

A near-spherical core of burned and burning gas supports the propagating flame. The flame is close to quench, but survives. However, it resides in a

regime located at the edge of a new quench regime that was previously addressed on *U/K* diagram in Fig. 1.10. Figure 3.23(b) are two sets of 3D swinging sheet images. These give more spatial information on flame structure, although the schlieren images give a more continuous record, on account of the shorter time interval between the adjacent sheets.

The 3D images clearly show, for both flames, a struggle for survival against increasing turbulence. The lower flame kernels with a broken cusp/like shape at 6 ms, reflect this more acutely, but both of the marginal flames in Fig. 3.23(a) and (b) survived unquenched.

An interesting observation in the comparison of Fig. 3.23(a) and the upper curve in Fig. 3.23(b) was that both the techniques yielded similar $d_k$ values in the early stage of flame development up to critical times for quench.

### 3.5.5.1  Experimental Data for Laser Swinging Sheet

Experimental data extracted from laser swinging images on $d_k/\delta_k$ are for near-quench flames as mentioned. Table 3.9 presents this data in a similar form of Table 3.8. With the available data points of Karlovitz stretch factor, $K$, and $d_k/\delta_k$ from both schlieren and swinging sheet techniques, Fig. 3.24 shows the interrelationships of this data and other key parameters.

Figure 3.24 shows the $d_k/\delta_k$ data points and the continuous curves are plots of these against $K$, for H₂, CH₄, and the grouping of the higher hydrocarbons, listed in Tables 3.8 and 3.9. Unique symbols are used for each fuel category. The hydrocarbons display similar values of $d_k/\delta_k$, although they are more conveniently correlated in terms of $p_{0.4}$. The regime of flame quenching lies beneath these plotted curves for all the different fuels.

The hydrocarbons are the most easily quenched, at the lowest values of $K$, and are associated with the highest values of $Ma_{sr}$. Hydrogen mixtures are the most difficult to quench, at the highest values of $K$, and these are associated with the lowest and negative values of $Ma_{sr}$ Methane mixtures have intermediate $Ma_{sr}$ values.

**Table 3.9** Near-quench experimental data from Laser swinging sheet technique (Bradley et al., 2019).

| Fuel/air mixture | Method | $T$ (K) | $P$ (MPa) | $\varphi$ | $u'$ (m/s) | $u'_k$ (m/s) | $\dfrac{d_k}{\delta_k}$ | $T^o$ (K) | $u_l$ (m/s) | | $\nu$ (m²/s) | $K$ | $Ma_{sr}$ | | $Ka$ | $p_b$ |
|---|---|---|---|---|---|---|---|---|---|---|---|---|---|---|---|---|
| CH₄/air | Swinging sheets system | 365 | 0.1 | 0.6 | 2 | 0.588 | 22 | 1220 | 0.189 | (Bradley et al., 2007b) | 2.28E-5 | 0.668 | 2 | (Bradley et al., 2007b) | 2.65 | 0.9 |
| CH₄/air | | 365 | 0.1 | 0.6 | 2 | 0.6 | 24 | 1220 | 0.189 | | 2.28E-5 | 0.668 | 2 | | 2.65 | 0.9 |
| CH₄/air | | 300 | 0.1 | 1.3 | 2 | 0.64 | 25 | 1220 | 0.16 | (Bradley et al., 1996) | 1.63E-05 | 0.788 | 4 | (Bradley et al., 1996) | 3.06 | 0.8 |
| CH₄/air | | 300 | 0.1 | 1.3 | 2 | 0.69 | 32 | 1220 | 0.16 | | 1.63E-05 | 0.788 | 4 | | 3.06 | 0.8 |
| CH₄/air | | 365 | 0.5 | 1.35 | 2 | 0.728 | 68 | 1328 | 0.095 | (Bradley et al., 2007b) | 4.60E-06 | 1.188 | 6 | (Bradley et al., 2007b) | 5.06 | 0.8 |
| CH₄/air | | 365 | 0.5 | 1.35 | 2 | 0.74 | 77 | 1328 | 0.095 | | 4.60E-06 | 1.188 | 6 | | 5.06 | 0.8 |

### 3.5.6   Quenching of Lifted Jet Flames

Turbulent fuel jets of lifted jet flames entrain air, and the leading reaction zone is the most reactive region, where the local mixture attains the maximum laminar burning velocity, $u_{lm}$, (Bradley et al., 1998a). Thereafter, with increasing fuel jet velocity more air is entrained and its reaction with the fuel is aided by the mixing with the hot gases created in the initial most reactive zone. Eventually the jet entrains more than sufficient air for reaction, the flame quenches, and blows off the burner.

For a given fuel jet velocity, pipe diameters, $D$, that are less than a critical size, cannot maintain a flame. This size represents the critical jet flame diameters before blow-off for the given conditions. It is normalised by the jet flame laminar flamelet thickness of the most reactive mixture, to give $(D_b/\delta_k)$. The fuel jet flow rate is characterised by a dimensionless flow number, $U^* = (u/u_{lm})(\delta_k/D)^{0.4}(P_i/P_a)$. Values of $U^*$ at blow-off are $U_b^*$. Values of $D_b/\delta_k$, are plotted against $U_b^*$ in Fig. 3.24, with values taken from (Palacios & Bradley, 2017).

From its derivation, it is apparent that the flow number has a similarity with the Karlovitz stretch factor, $K$ (Palacios & Bradley, 2017; Williams, 1985). $U_b^*$ therefore, appears as the secondary x-axis, against which the present experimental values of $D_b/\delta_k$, on the secondary y-axis, are plotted by the dotted curves, for different values of $p_b$. For both CH₄ and hydrocarbons, choked jet flow, develops above about $U_b^*$= 200.

Although the limiting values of $d_k/\delta_k$ and $D_b/\delta_k$ in the two sets of diverse results are rather different, they reflect the underlying similarity between premixed and jet flamelet structures and are similarly influenced by $Ma_{sr}$. A striking aspect of both sets of curves is the sharp increases in $d_k/\delta_k$ and $D_b/\delta_k$ with $K$ and $U_b^*$, respectively. This implies that large increases in $u'$ and $u$ can create high burning rates, only if they are accompanied by large commensurate increases in, respectively, explosion vessel sizes and burner diameters.
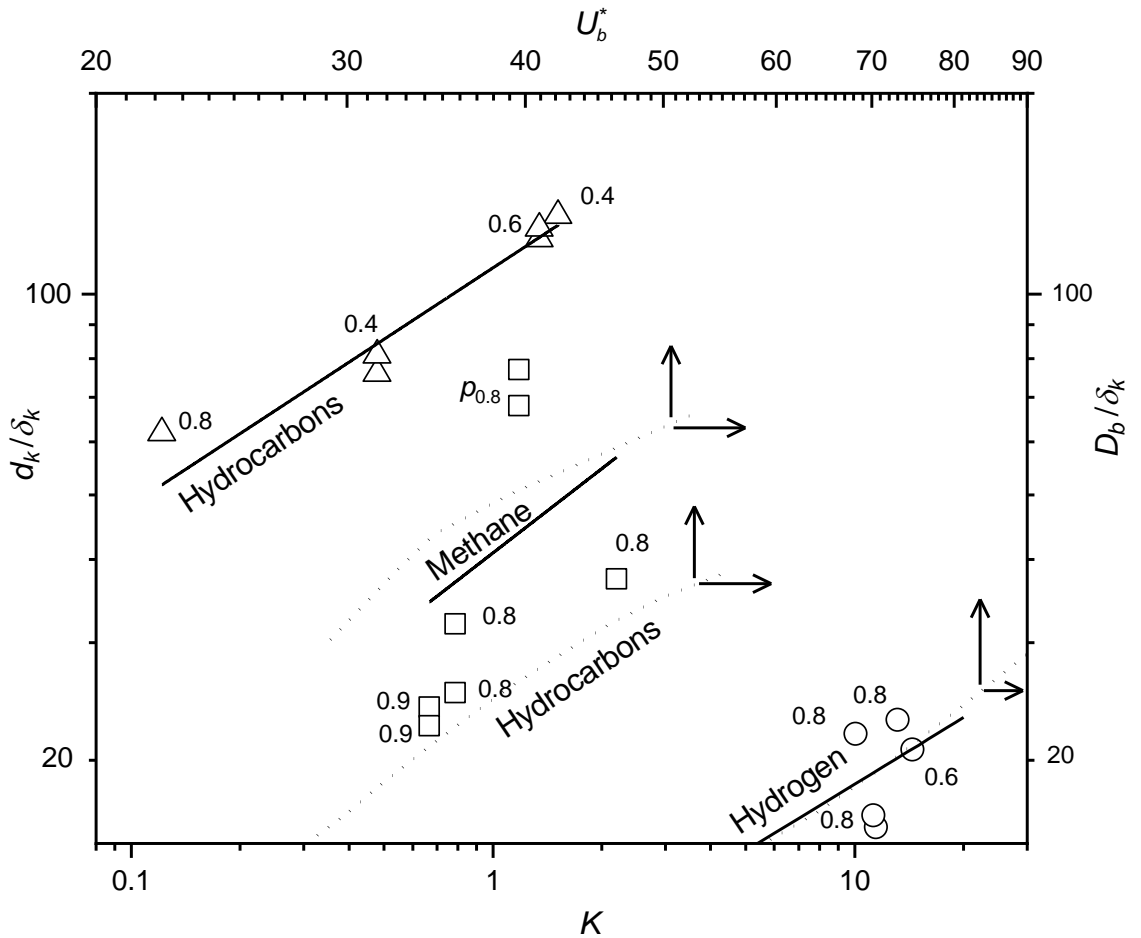
**Figure 3.24** Symbols show probabilities of flame propagation for $d_k/\delta_k$ and $K$. Dotted curves show jet flame $D_b/\delta_k$ values at $U^*_b$ from (Palacios & Bradley, 2017). Numbers adjacent to symbols are $p_b$ values. Flame quenching occurs beneath the curves. Symbols: ($\triangle$), for hydrocarbons, ($\square$), for CH₄, and, ($\bigcirc$), for H₂ (Bradley et al., 2019).

## 3.6  Flame Quenching on the *U/K* Diagram

The flame quenching regime, indicated by (C) in Fig. 1.10, was re-examined in the light of the data in Bradley et al. (2007b) and Tables 3.8 and 3.9. The procedure adopted was, initially, to plot all the $p_{0.8}$ data from these sources in Fig. 3.25 and then derive, the best fit curve of $Ma_{sr}$ against $K$. Figure 3.25 shows values of $Ma_{sr}$, for $p_{0.8}$, plotted against $K$, for the different mixtures. The open symbols show the data taken from Bradley et al. (2007b), whilst filled

symbols are from the present study. The dotted curve shows the best fit curve through the data from Bradley et al. (2007b), given by the Eq. (1.43), and the solid curve is the best fit through all the data points, including the present ones. This gives,

$$Ma_{sr} = \text{-2.24 ln } (K) + 3.8 \tag{3.2}$$

Unsurprisingly, the quenching tendency is increased with an increase in $K$, whilst at the larger values of $K$, negative values of $Ma_{sr}$ become necessary for flame survival. No flame quenching was observed for H₂/air at $Ma_{sr}$ = -2.8 (Bradley et al., 2007b), even when $u'$ was increased to 10 m/s, the maximum attainable value with the present fan-stirred vessel.
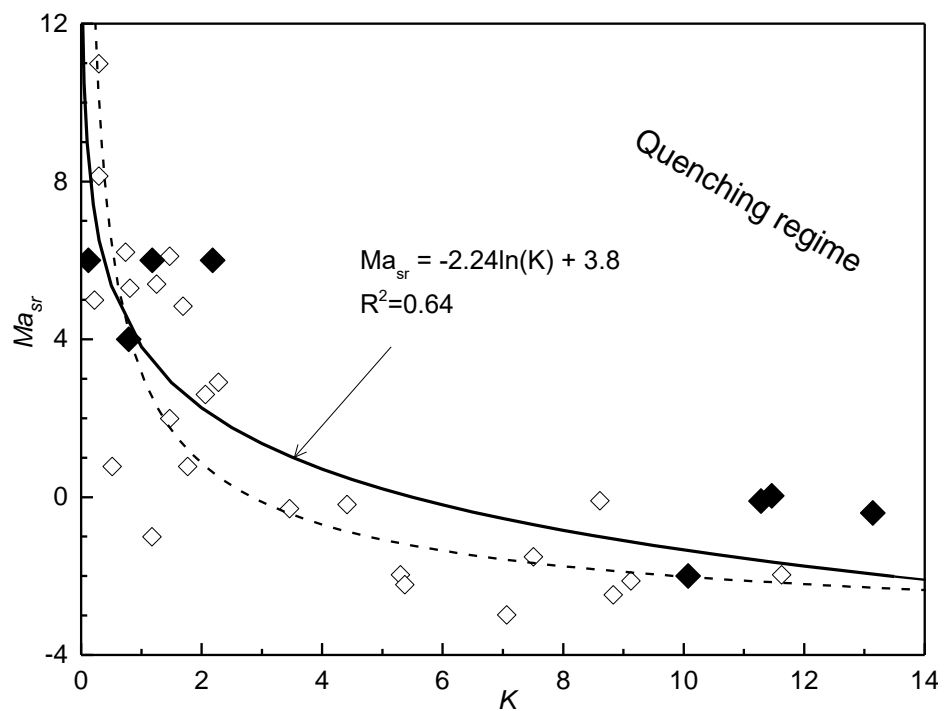


**Figure 3.25** Measured *K* values at *p₀.₈* as a function of *Maₛᵣ*. Open symbols from (Bradley et al., 2007b), and solid symbols from the present study (Bradley et al., 2019).

These correlations contribute to the revised form of Fig. 1.10, with the plot of $U$ against $K$ for different $Ma_{sr}$ in Fig. 3.26. Mindful that values of $Ma_{sr}$ are not known with high accuracy, the plots of $U$ against $K$ for different $Ma_{sr}$ were optimised further, making allowance for this. The quenching limits of Fig. 1.10 extend beyond the previous limit, shown by the dashed curve, and $p_{0.8}$ is

expressed by the bold curve in Fig. 3.26 as a new quenching regime boundary. The onset of flame quenching is defined by $p_{0.8}$. In addition to the influences of the correlations in Fig. 3.25, due regard was paid to the observed sustainability of near-marginal flames, such as those in Fig. 3.23, in constructing the curve for the onset of quenching. This curve is obtained by using a best fit curve through the experimental quench points shown by solid symbols and an empirical correlation is evaluated. Since $U$ is a function of $Ma_{sr}$ and $K$, the best fit curve presented in Fig. 3.25 should also hold good for the quench limit, shown by the solid line in Fig. 3.26. The quench regime now covers higher values of $K$ and $Ma_{sr}$. Using the $Ma_{sr}/K$ correlation of Fig. 3.25, the $Ma_{sr}$ values for different $K$ from Eq. (3.2), were used to calculate $U$ values for different $K$, using Eqs. (1.32) to (1.34).
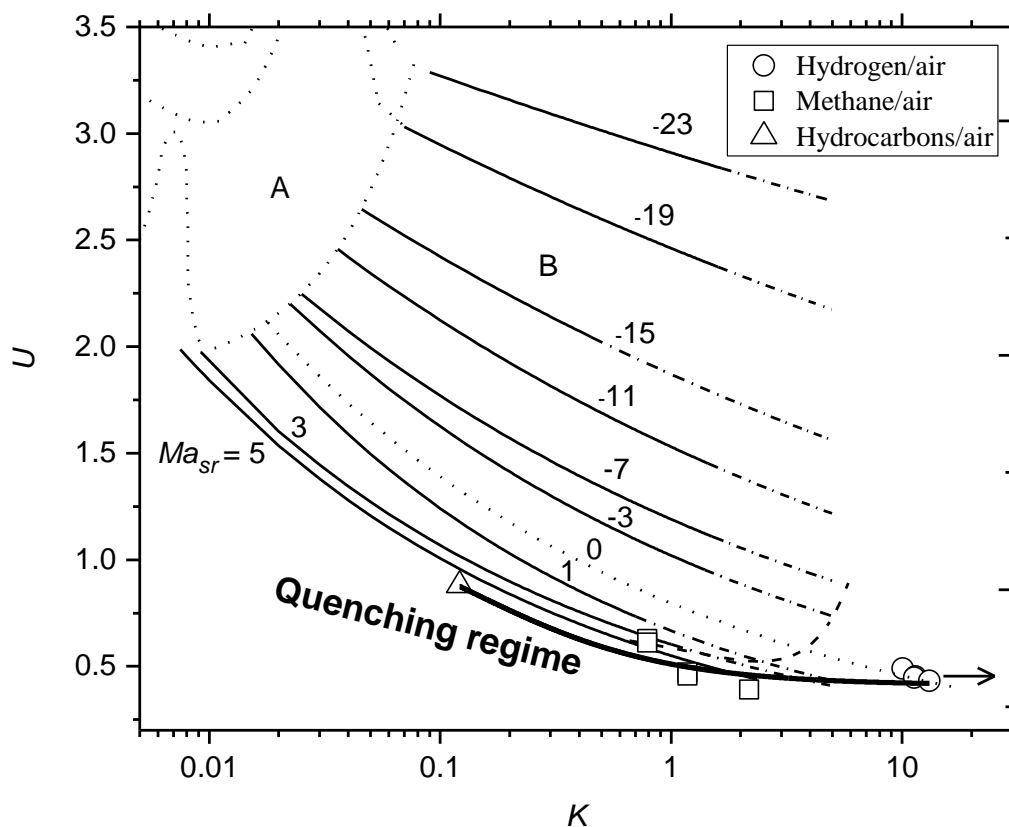


**Figure 3.26** Diagram of turbulent combustion, including the new limits of quenching for $p_{0.8}$. Dashed curve is the limit reported in (Bradley et al., 2013). Symbols show the present experimental points (Bradley et al., 2019).

## 3.7  Frames of Partial Quenching Flames Resulted from Laser Swinging Sheet

Figure 3.27 gives an example of a consequence of centre sheet image of partially quenched lean H₂/air mixture, $\varphi$ =0.15 at 0.5 MPa, 365K and $u'$= 3 m/s where this data point is located on the new quenching border on *U/K* diagram at $K$=15.5 and $Ma_{sr}$ = -2. It was not possible to reconstruct this flame, despite this case being approached after long trials of capturing a fully quenching flame, due to the high distortion. Flame edges cannot be addressed here. These trials could be enhanced using an imaging laser with a higher reputation rate than the currently available one.



(a)                              (b)                              (c)
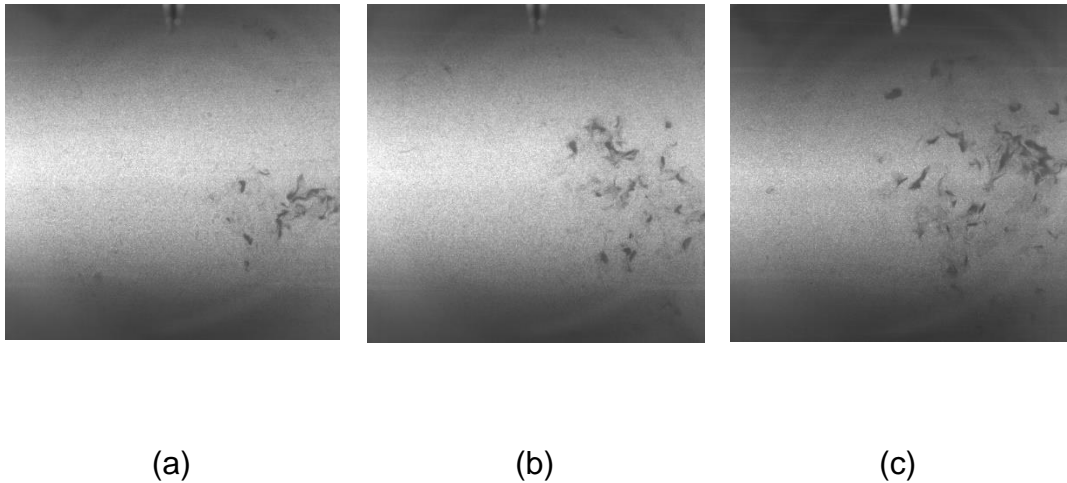
**Figure 3.27** Centre sheets of three consecutive sweeps for a partially quenched H₂/air mixture, $\varphi$ = 0.15 at 0.5 MPa, 365 K and u'= 3 m/s, *K* =15.5.

# Chapter 4 - Results of Deflagration to Detonation Transition (DDT) in Stoichiometric H₂/O₂ Mixture

## 4.1 Introduction

The analysis is based on a one dimensional DDT, as in (Bradley et al., 2008), and indicated by Fig. 4.1, with an accelerating flame that creates an ever-stronger shock wave. Major factors for the attainment of laminar flow DDT are low values of $\tau_i$, combined with high values of $u_\ell$ and kinematic viscosity, $v$. This schematic diagram depicts the propagation of the flame from the closed end of a duct, generating a shock wave ahead of it.



**Figure 4.1** Flame and shockwave propagation in an open-ended tube. Ignition initiated from the closed end (Bradley et al., 2008).

The analytical approach requires a detailed knowledge of $u_\ell$ of the mixture, as well as of $\tau_i$, both at high temperatures and pressures. Limitations of the approach are the one dimensionality, incomplete and insufficiently accurate data on $u_\ell$ and $\tau_i$, and no allowance for transverse weak shock waves.

In (Bradley et al., 2008), it is shown that the flame speed in the duct is given by:

$$S_f = (A/a)\sigma u_\ell, \tag{4.1}$$

in which $A$ is the flame surface area, $a$ the cross sectional area of the duct, and $\sigma$ the ratio of unburned to burned gas density. The gas velocity ahead of the flame, towards the shock, $S_g$, is given by:

$$S_g = (A/a)(\sigma - 1)u_\ell. \tag{4.2}$$

Close to the shock wave, if $S_h$ is the shock wave speed along the duct, and $u_2$, the gas velocity relative to the shock wave, away from it and towards the flame, then,

$$S_g = S_h - u_2. \tag{4.3}$$

The increased temperature and pressure due to the confinement and shock increase $u_\ell$, which also elongates the flame area, both of which further increase $S_g$ and strengthen the shock.

It is assumed that there is no gas velocity just ahead of the shock wave, where conditions of the unburned gas are designated by the suffix 1. The unburned gas velocity, $u_1$, into the shock wave, and relative to it, must be equal to $S_h$.

The shock wave equations (Bradley et al., 2008) give the ratio of velocities into and out of the planar shock wave as:

$$\frac{u_2}{u_1} = \frac{2+(\gamma-1)M_1^2}{(\gamma+1)M_1^2} \ . \tag{4.4}$$

Here $M_1$ is the Mach number associated with the speed of the shock wave along the duct, given by $u_1/a_1$, with $a_1$, the acoustic velocity ahead of the shock.

Equation (4.3), with $S_h = u_1$, yields:

$$S_g/u_1 = 1 - u_2/u_1 \ , \tag{4.5}$$

which, with Eq. (4.4), gives

$$S_g = \frac{2(M_1^2-1)a_1}{(\gamma+1)M_1} \ . \tag{4.6}$$

Equations (4.2) and (4.6) give a quadratic equation in $M_1$ with a real solution:

$$M_1 = (c/2) + (1 + c^2/4)^{1/2}, \text{ where} \tag{4.7}$$

$$c = (S_g/a_1)(\gamma + 1)/2 = (A/a)\, u_l(\sigma - 1)(\frac{\gamma+1}{2a_1}). \tag{4.8}$$

The pressure and temperature ratios at the planar shock wave are given by:

$$\frac{p_2}{p_1} = \frac{2\gamma M_1^2}{\gamma+1} - \frac{\gamma-1}{\gamma+1} \ , \text{ and} \tag{4.9}$$

$$\frac{T_2}{T_1} = \left(\frac{2\gamma M_1^2-(\gamma-1)}{(\gamma+1)}\right)\left(\frac{2+(\gamma-1)M_1^2}{(\gamma+1)M_1^2}\right) \ . \tag{4.10}$$

The $c$ parameter provides a link to the flame equations. A high value of $c$ implies high values of $M_1$ and of the pressure and temperature ratios at the shock, with a consequent increased propensity for autoignition.

## 4.2 Evaluating the Laminar Burning Velocity of Hydrogen/oxygen Mixture

To understand the acceleration of this mixture, it is essential to know the relevant properties. As the flame propagates, a shock wave forms in front of it as the gas velocity ahead of the flame increases. After the shock, values of pressures and temperatures can be high, so that there is a dearth of values of $u_\ell$, not least because of the increased hazard in making measurements. Bartholomé (1949) measured $u_\ell$ for stoichiometric H$_2$/O$_2$ at 298 K and 0.1 MPa, using a burner. Koroll and Mulpuru (1988)  later made measurements under atmospheric conditions for the stoichiometric mixture with diluents using a nozzle-burner.

Gelfand et al. (2012) reviewed the variations of $u_\ell$ with temperature for stoichiometric H$_2$/O$_2$ at atmospheric pressure, using burner results from (Edse & Lawrence, 1969) and the computations of (Kusharin et al., 1995). The experimental measurements were confined to maximum values of about 500 K. Computed values covered a wider range. Kuznetsov et al. (2005a) calculated $u_\ell$ for the mixture using the FP code (Gavrikov et al., 2001)  in the pressure range 0.02 to 0.8 MPa, at 300 K.

Numerical and experimental evaluations of $u_\ell$ for stoichiometric H$_2$/O$_2$ mixture in (Kuznetsov et al., 2011) have different proportions of steam between 0.1 and 7.2  MPa and temperatures from 383 to 573 K. Steam concentrations were between 0 and 80% H$_2$O. The highest $u_\ell$ values without steam were 29.8 and 24.9 m/s at 1 and 7.2 MPa, respectively, and 573 K. The burning velocity was calculated using four different H$_2$/O$_2$ kinetic mechanisms. Computed $u_l$ data, using the reduced mechanism of Boivin et al. (2011), extending to 10 MPa and 750 K, have been presented by Mari et al. (2016). These data included in Fig. 4.2, show the effect of temperature, up to about 800 K, at atmospheric pressure, for stoichiometric H$_2$/O$_2$, along with data from six different studies.
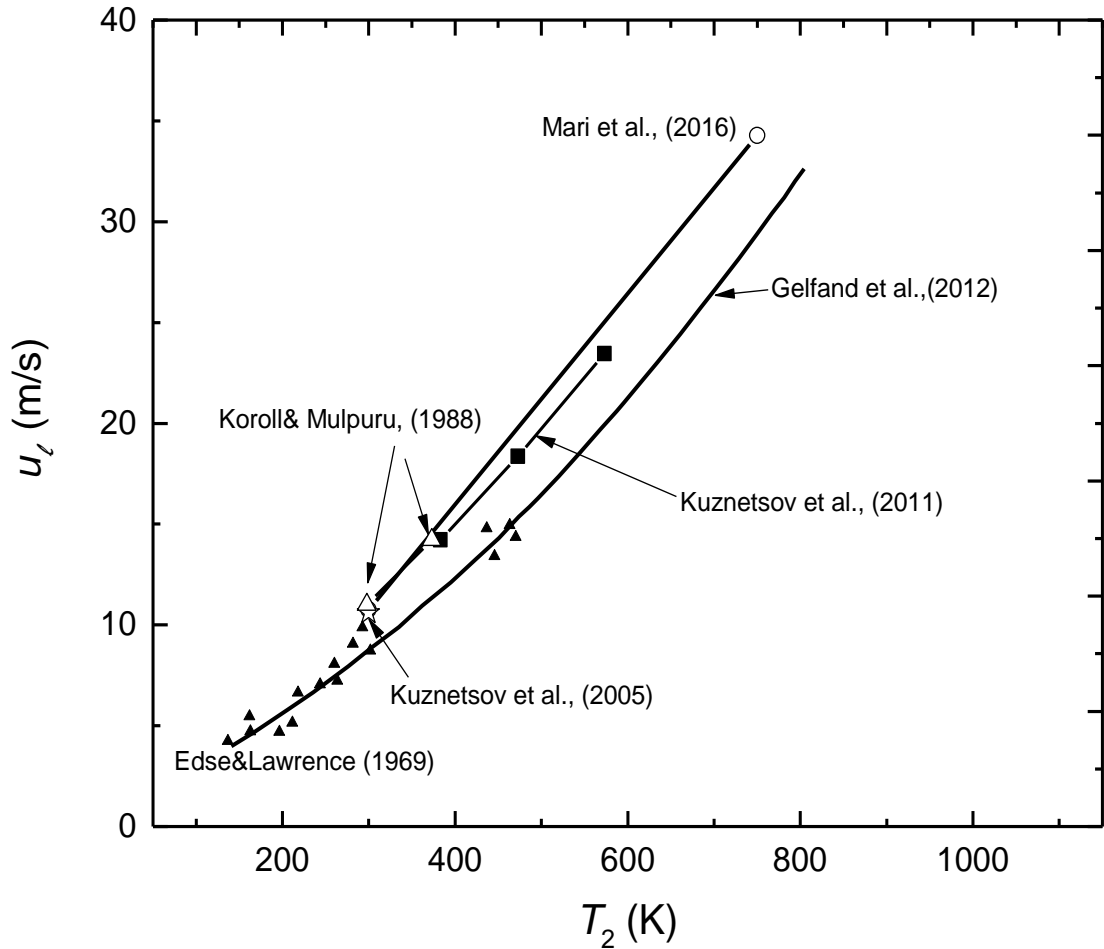
**Figure 4.2** Measured and computed values of $u_l$ for stoichiometric $H_2/O_2$ at atmospheric pressure.

Although these available data on laminar burning velocity are valuable, they are not enough as they are limited to less than 800 K and extrapolation of these values is necessary.

Values of $u_\ell$ at $T$ and $P$ are empirically correlated over a given range of $T$ and $P$ by:

$$u_\ell = u_{\ell 0}(\frac{T}{T_0})^{\alpha}(\frac{P}{P_0})^{\beta},\qquad\qquad\qquad (4.11)$$

with $\alpha$ and $\beta$ numerical constants, and $T_0$ and $P_0$ a reference temperature and pressure. The value $u_{\ell 0}$ is the laminar burning velocity at the reference conditions. In the present case these are 300 K and 0.1 MPa. Values of $\alpha$ and

$\beta$ were plotted against against maxima of $P$ or $T$ over the respective ranges and these values were extrapolated to values at higher $P$ and $T$. The associated extrapolated values of $u_\ell$ are shown by the broken curve, up to 1100 K, in Fig. 4.3.
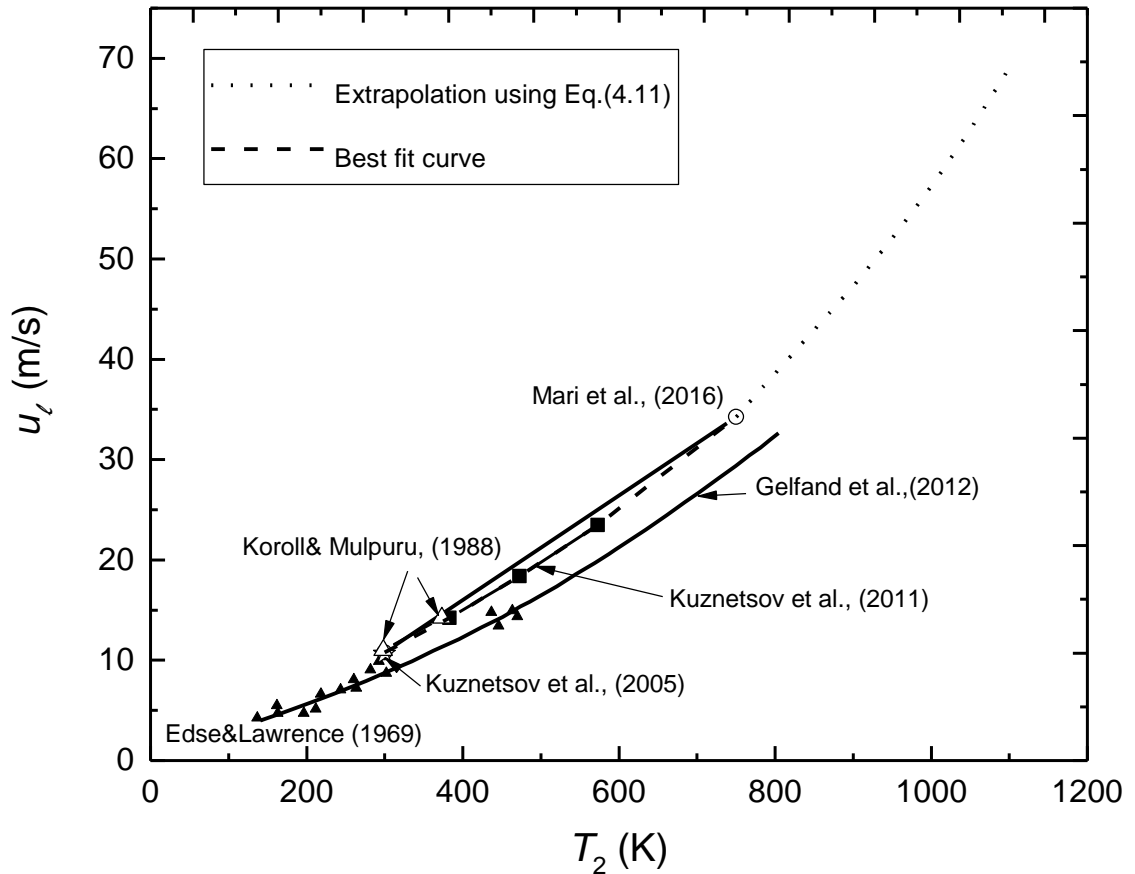


**Figure 4.3** Best fit curve and extrapolated values of $u_l$ for stoichiometric H$_2$/O$_2$ at atmospheric pressure.

The effect of pressure is shown for different temperatures in Fig. 4.4. The computed data in (Kuznetsov et al., 2011) extended to 7.2 MPa and employed a variety of different reaction mechanisms. The mechanism of (Lutz, 1988) was recommended in (Kuznetsov et al., 2011), due to its good agreement with that of (Maas & Warnatz, 1988). Gelfand et al. (2012) employed kinetic simulations for pressures up to 10 MPa at 298 K. The reduced mechanism of Boivin et al. (2011) was used to calculate $u_\ell$ at 300 K between 0.1 and 10 MPa, and 750 K at 0.1 MPa (Mari et al., 2016). These values are plotted in

Fig. 4.4 in the form of different isothermal values of $u_\ell$ as a function of the pressure, $P_2$.
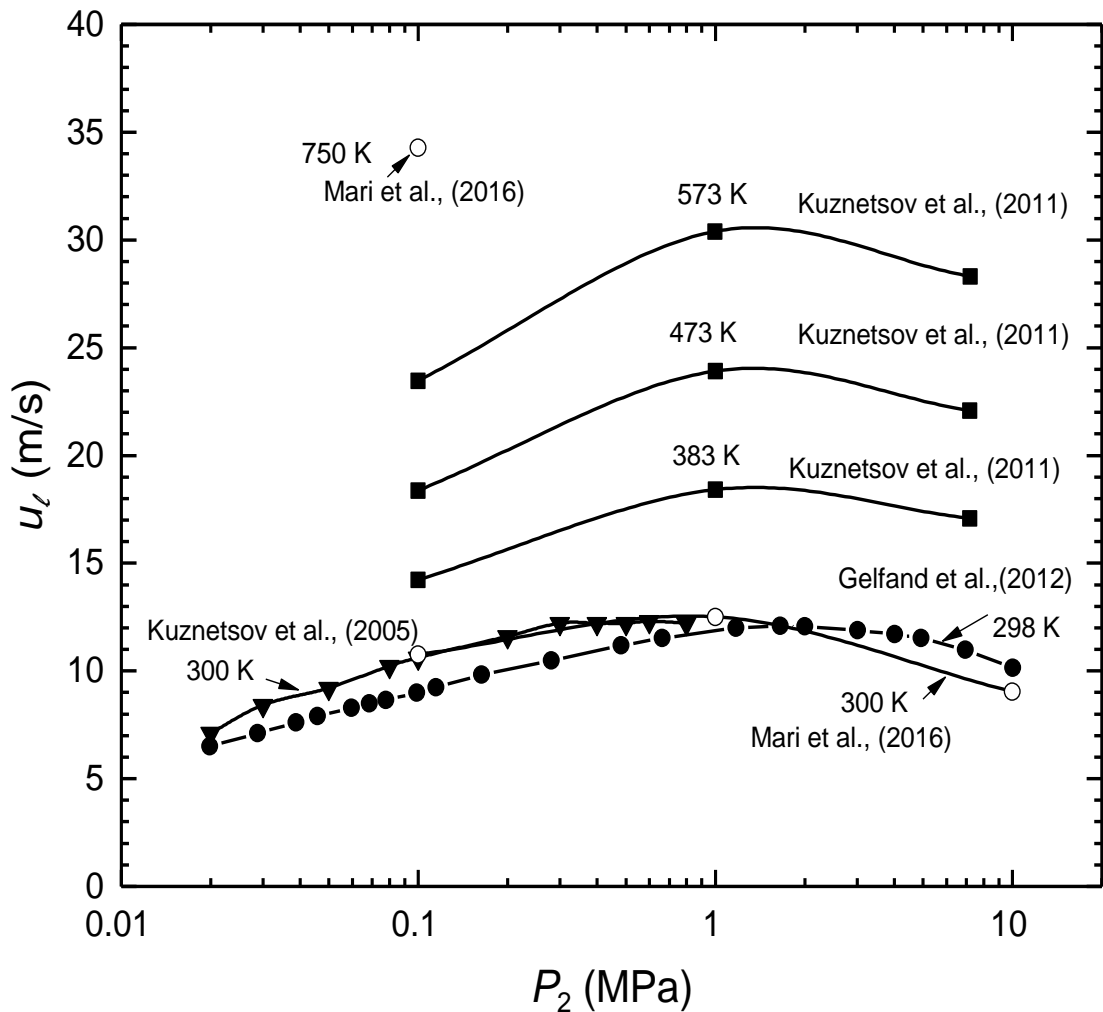


**Figure 4.4** Measured and computed values of $u_l$ for stoichiometric H₂/O₂ for different temperatures up to 750 K from different sources.

Figure 4.5 presents an extensive range of experimental, theoretical, and extrapolated values of $u_\ell$ plotted against pressure for different isotherms relevant to the present work. Temperatures extend to 1100 K and pressures to 7.2 MPa. Extrapolated values are indicated by dotted curves. There is clearly a dearth of data at the higher temperatures, with excessive reliance on extrapolated values. An essential role of the $u_\ell$ data is, for a given value of $c$, the derivation of the minimal value of $A/a$ for autoignition from Eq. (4.8). This value, along with that of $\sigma$, also enable $S_f$ to be found from Eq. (4.1).
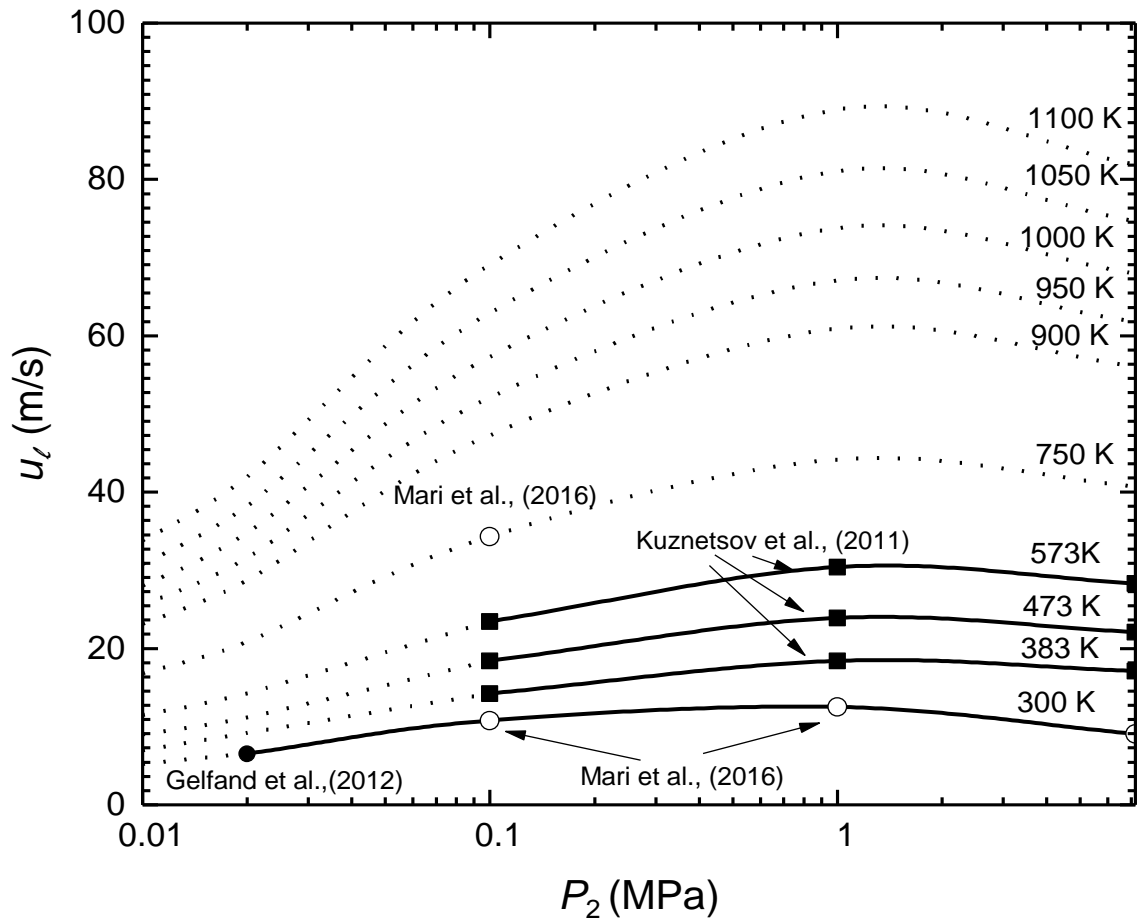
**Figure 4.5** Variations of $u_l$ for stoichiometric H₂/O₂ with pressure and temperature. Extrapolated values indicated by dotted curves (Bradley & Shehata, 2018).

## 4.3  Calculating the Values of Autoignition Delay Times of Stoichiometric Hydrogen/oxygen Mixtures

To evaluate the probability of detonation, auto-ignition delay time data should be available. Detonation and autoignition delay time are inversely related. If the autoignition delay time is short enough as mentioned in Section 1.4, detonation will be facilitated. Bradley et al. (2008), estimated that the attainment of a DDT in a duct of 7 m length would require a value of $\tau_i$ of less than 3.8 ms. The procedure adopted was to identify the values of $c$ and the shock conditions necessary to generate values of $\tau_i$ of 0.05, 0.1, 1 and 5 ms.

Bearing in mind the practical length of a detonation tube, autoignition delay times, $\tau_i$, of the order of 1 ms might be necessary for the onset of autoignition and a DDT, without excessive tube lengths.

Many chemical kinetic modelling studies (Ivanov et al., 2011a; Ivanov et al., 2011b; Kiverin et al., 2013; Liberman et al., 2012; Meyer & Oppenheim, 1971; Smirnov et al., 2013; Voevodsky & Soloukhin, 1965) have yielded $\tau_i$ values for stoichiometric H$_2$/O$_2$ at different pressures and temperatures. In an early study, Voevodsky and Soloukhin (1965) measured $\tau_i$ in a shock tube at 0.1, 0.2 and 0.3 MPa, and compared these values with those from a chemical kinetic model. The comparison showed discrepancies at low temperatures. In a later experimental study on explosion limits with strong and weak autoignition, Meyer and Oppenheim (1971) employed the kinetic schemes of Skinner and Ringrose (1965) and (Gardiner & Wakefield, 1969) to obtain $\tau_i$ at different temperatures, in the pressure range 0.02 to 0.2 MPa.

Ivanov et al. (2011b) studied the effect of the width of the no-slip wall duct at different diameters on the onset of detonation for stoichiometric H$_2$/O$_2$. The study was performed under atmospheric conditions with different chemical kinetics in six reaction schemes (Bokhon et al., 1998; Gal'burt et al., 2007; Popov, 2007; Shatalov et al., 2009; Smith et al., 1999; Starik & Titova, 2003) and a one-step Arrhenius kinetic scheme.

Liberman et al. (2012) studied the effect of initial temperature non-uniformity on the initiation of chemical reaction and propagation of combustion waves, and employed a detailed chemical kinetic model to compute $\tau_i$ for stoichiometric H$_2$/O$_2$ and H$_2$/air mixtures between 0.001 to 5 MPa. Values of $\tau_i$ for stoichiometric H$_2$/O$_2$ at sub-atmospheric pressures were included in the mathematical model of Smirnov et al. (2013) in the range 0.01 to 10 MPa.

These values of $\tau_i$ for stoichiometric H$_2$/O$_2$ from (Liberman et al., 2012) and (Smirnov et al., 2013) at different temperatures, for pressures above atmospheric, are shown in Fig. 4.6. Also shown, are the earlier computed and

lower experimental (triangle symbol) data of Voevodsky and Soloukhin (1965).

Of particular interest is the sharp decrease in $\tau_i$ at the highest temperatures when the pressure falls to 0.3 MPa. Figure 4.7 shows values of $\tau_i$ at sub - atmospheric pressures, and the same trend continues down to about 0.04 MPa, when it is reversed, and $\tau_i$ increases with pressure decrease.
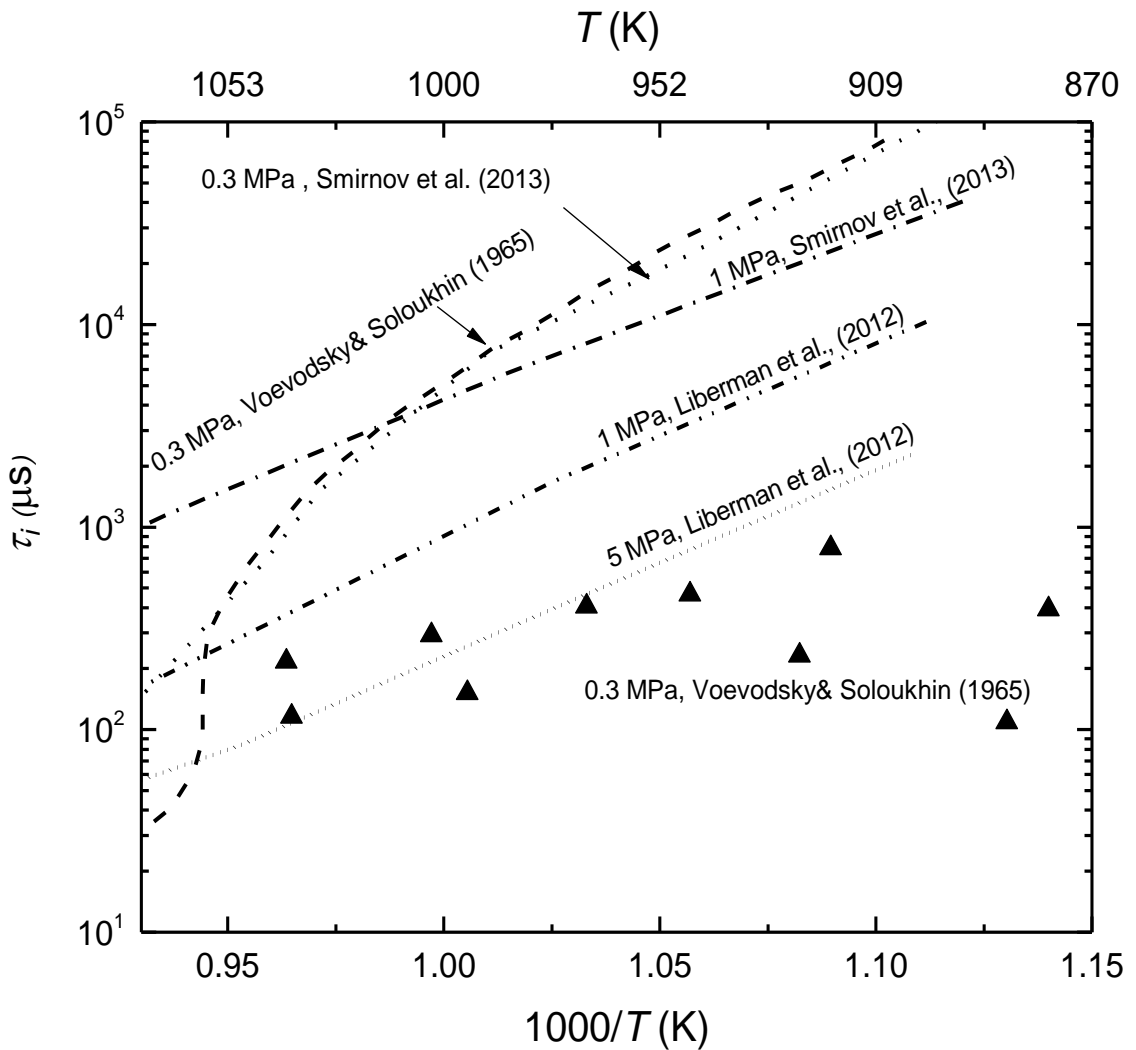


**Figure 4.6** Autoignition delay time of stoichiometric $H_2/O_2$ mixture at different temperatures and pressures > 0.1 MPa.
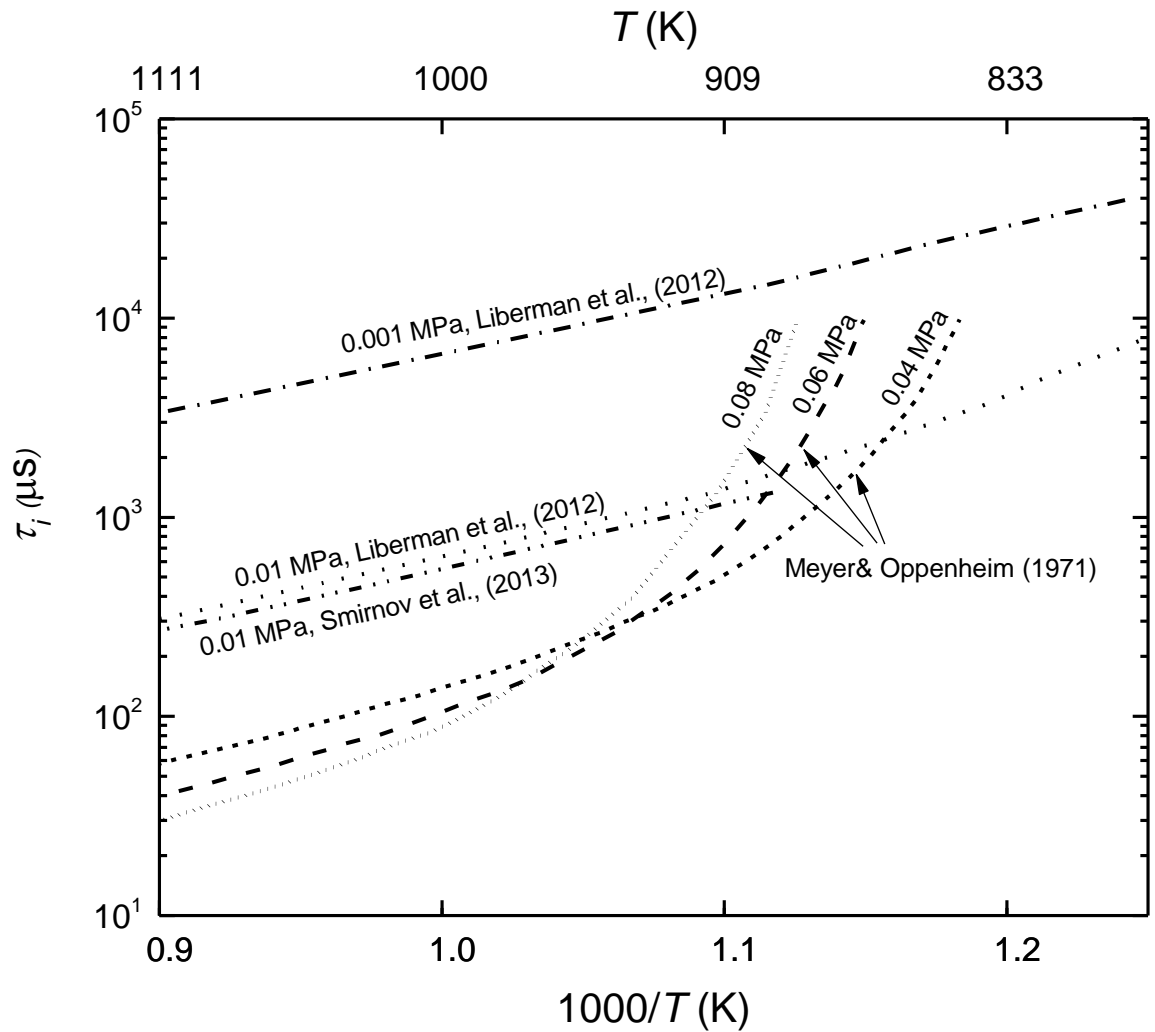
**Figure 4.7** Autoignition delay time of stoichiometric H$_2$/O$_2$ mixture at different temperatures and sub-atmospheric pressures.

Much of the available data on $\tau_i$ at 0.1 MPa are shown for different temperatures in Fig. 4.8. All of these values are computed, except the experimental results of Voevodsky and Soloukhin (1965), which again are significantly less than the modelled values. The modelled results of Liberman et al. (2012), and Smirnov et al. (2013) are also shown.

The present focus is on the range, 833 ≤ $T$ ≤ 1111 K. There continues to be uncertainties in the chemical kinetic detail of what might appear to be a relatively simple, yet very important, oxidation. There is a maximum spread of about two orders of magnitude in values of $\tau_i$.
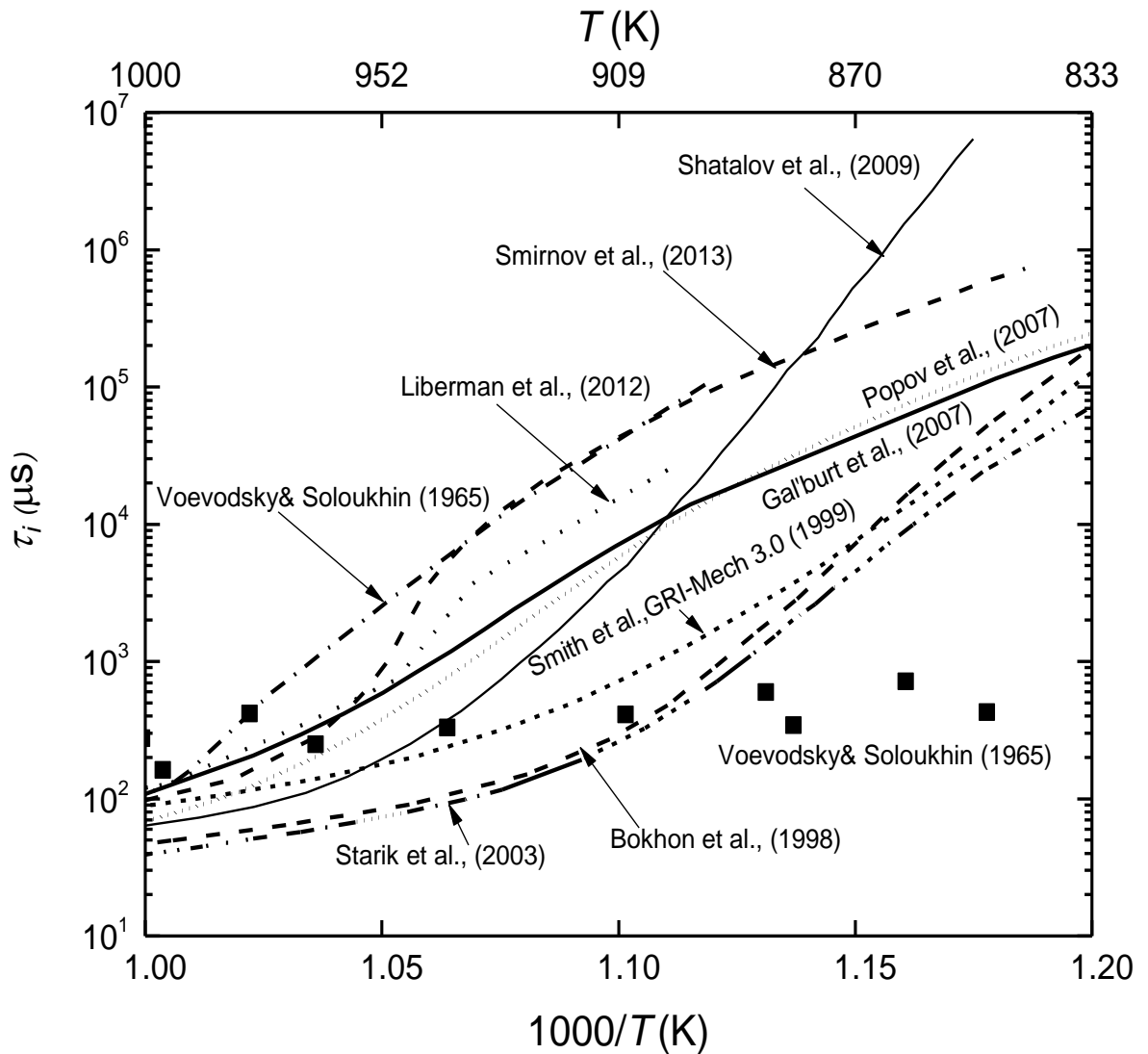
**Figure 4.8** Autoignition delay time of stoichiometric $H_2/O_2$ at different temperatures at 0.1 MPa.

The low pressure data in Fig. 4.9 compare earlier values of Meyer and Oppenheim (1971) with the current computations using the data of Varga et al. (2015) at pressures of 0.04, 0.06 and 0.08 MPa (Appendix A). Low pressures, combining low values of $\tau_i$ and high values of $\nu$ are conducive to laminar DDT.
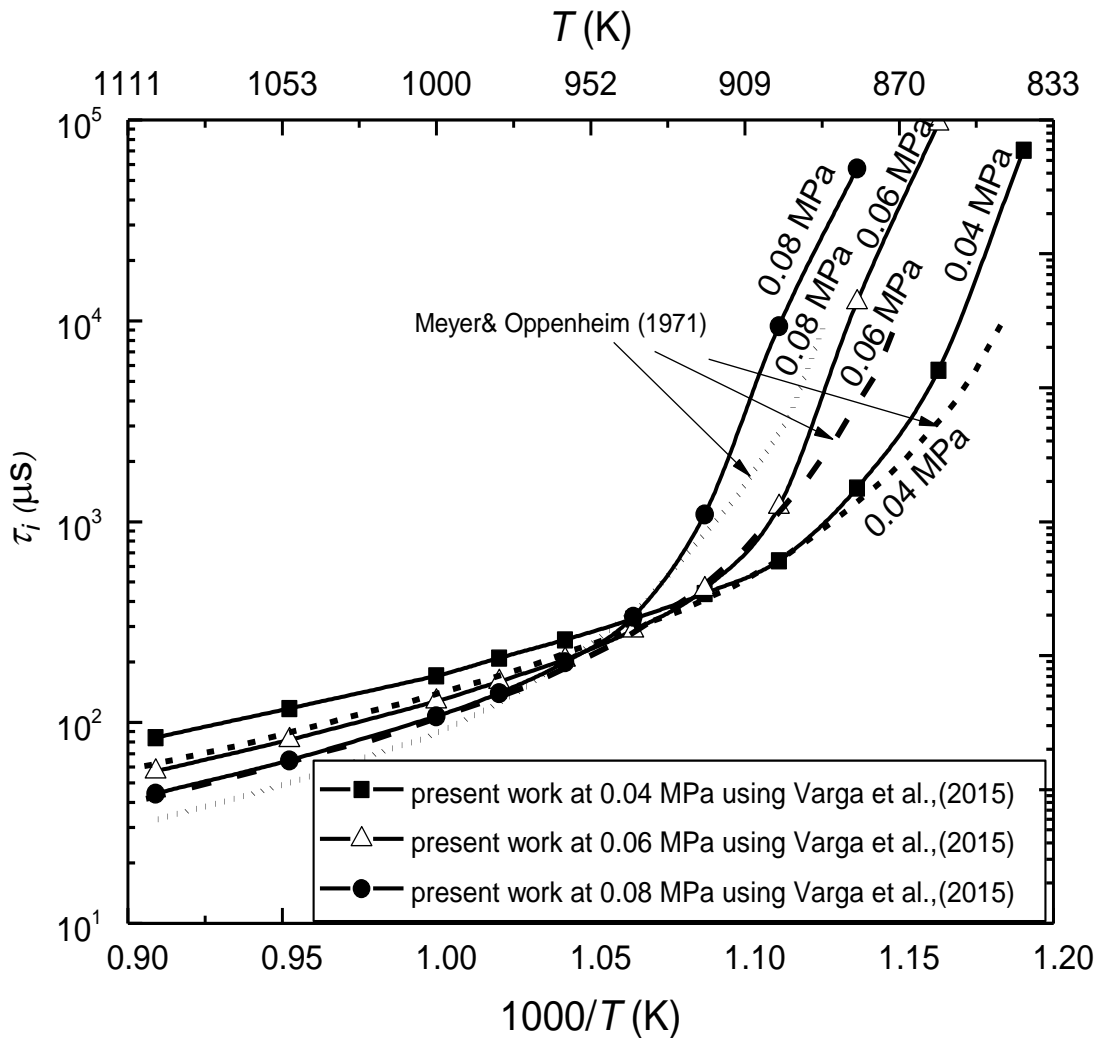
**Figure 4.9** Comparison of ignition delay time between Meyer and Oppenheim (1971) and the present simulation using Varga et al. (2015) mechanism.

The review in Olm et al. (2014) favours that of Kéromnès et al. (2013), optimised by Varga et al. (2015), and based on the CHEMKIN code ("Design Reaction, CHEMKIN ", 2013). This was employed in the present work, after review of the results shown in Figs. 4.9 to 4.12. These current computations give values close to the average of all the data in Fig. 4.11.
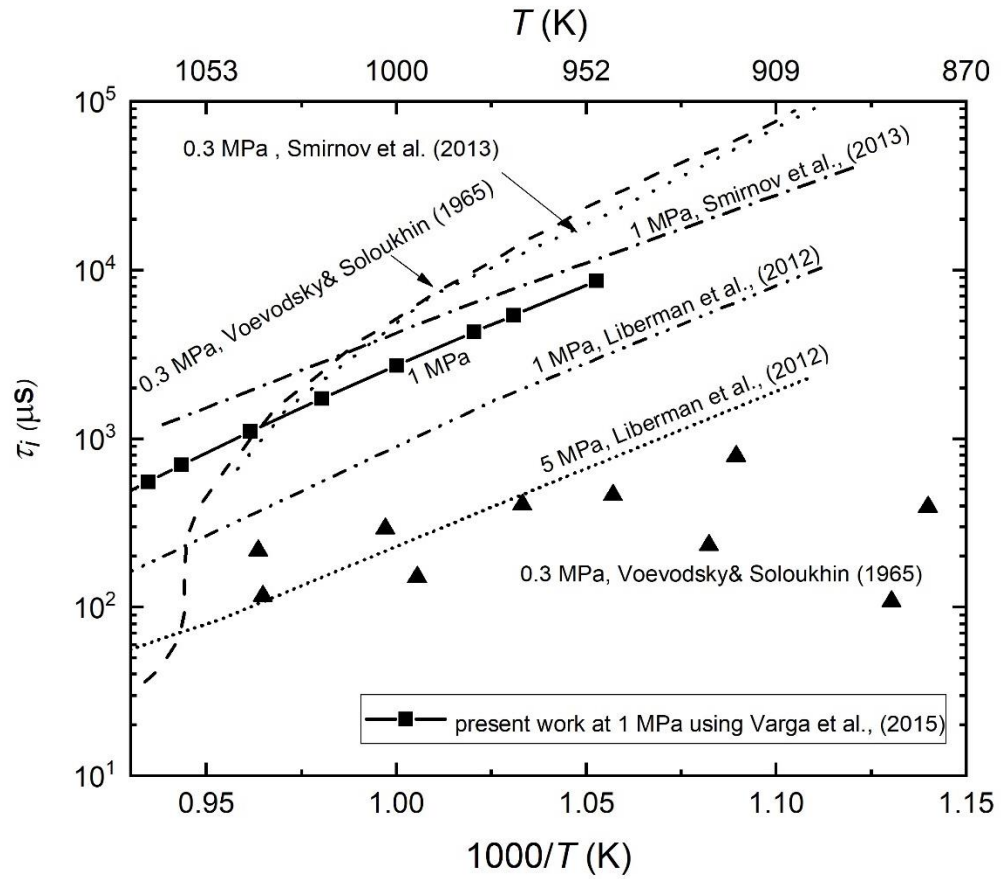
**Figure 4.10** Autoignition delay time of stoichiometric $H_2/O_2$ mixture at high pressures compared with present simulation at 1 MPa.
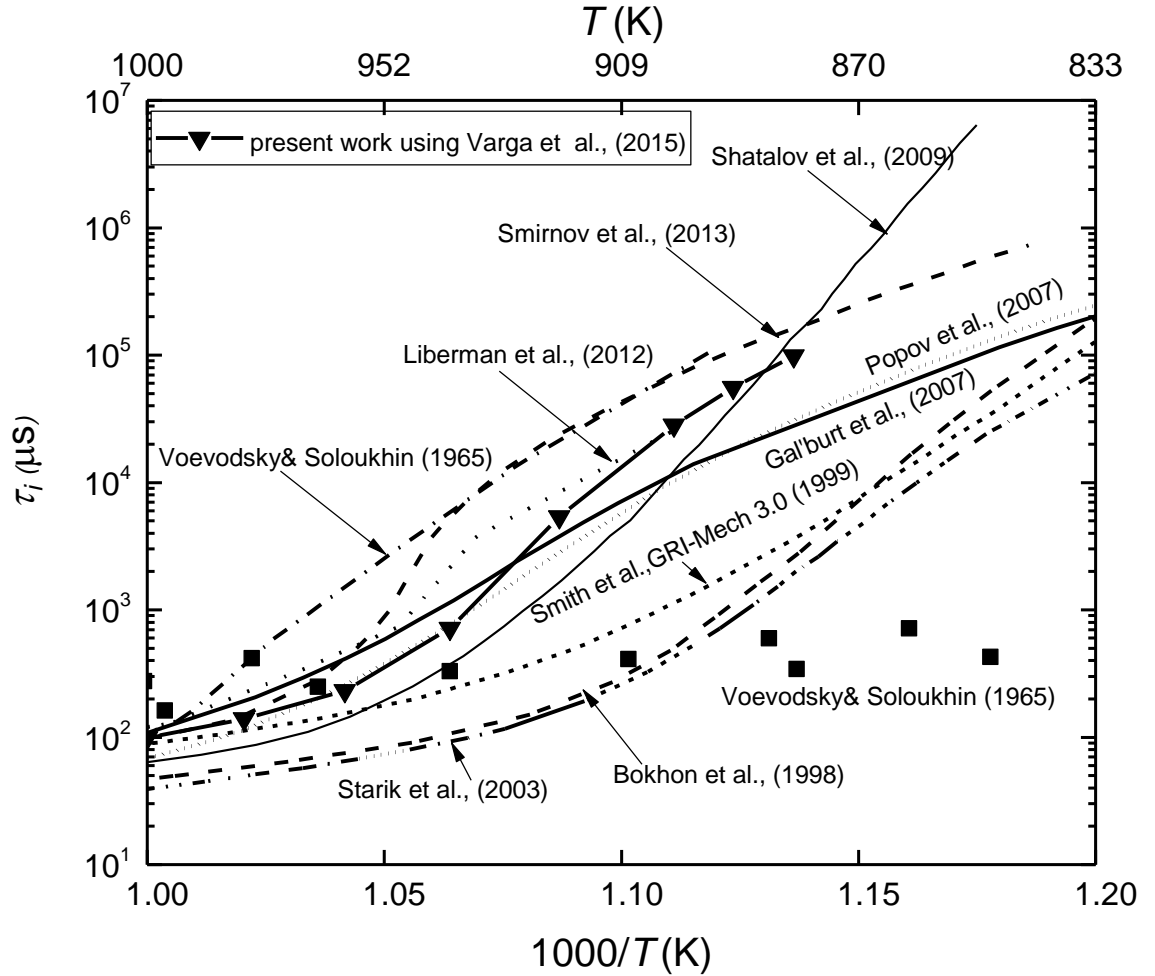
**Figure 4.11** Autoignition delay time of stoichiometric H₂/O₂ mixture at 0.1 MPa compared with present simulation.

Figure 4.12 shows values of $\tau_i$, and utilised in the present work. The lowest values of $\tau_i$ occur at the highest temperatures between 0.01 and 0.04 MPa. Below 1000 K, values of $\tau_i$ peak between 0.1 and 0.3 MPa and then decrease with decreasing $P$ down to about 0.06 MPa. They then increase with further decrease in the pressure. From Fig. 4.12, a regime of minimal $\tau_i$ exists below 0.08 MPa and above 900 K, characterised by low $\tau_i$ and activation energies, given by:

$$E/R = \partial \, ln\tau_i/\partial(1/T). \tag{4.12}$$

where the auto-ignition delay time is expressed by :

$$\frac{\partial \tau_i}{\partial T} = \tau_i\left(\frac{E}{RT^2}\right) \tag{4.13}$$
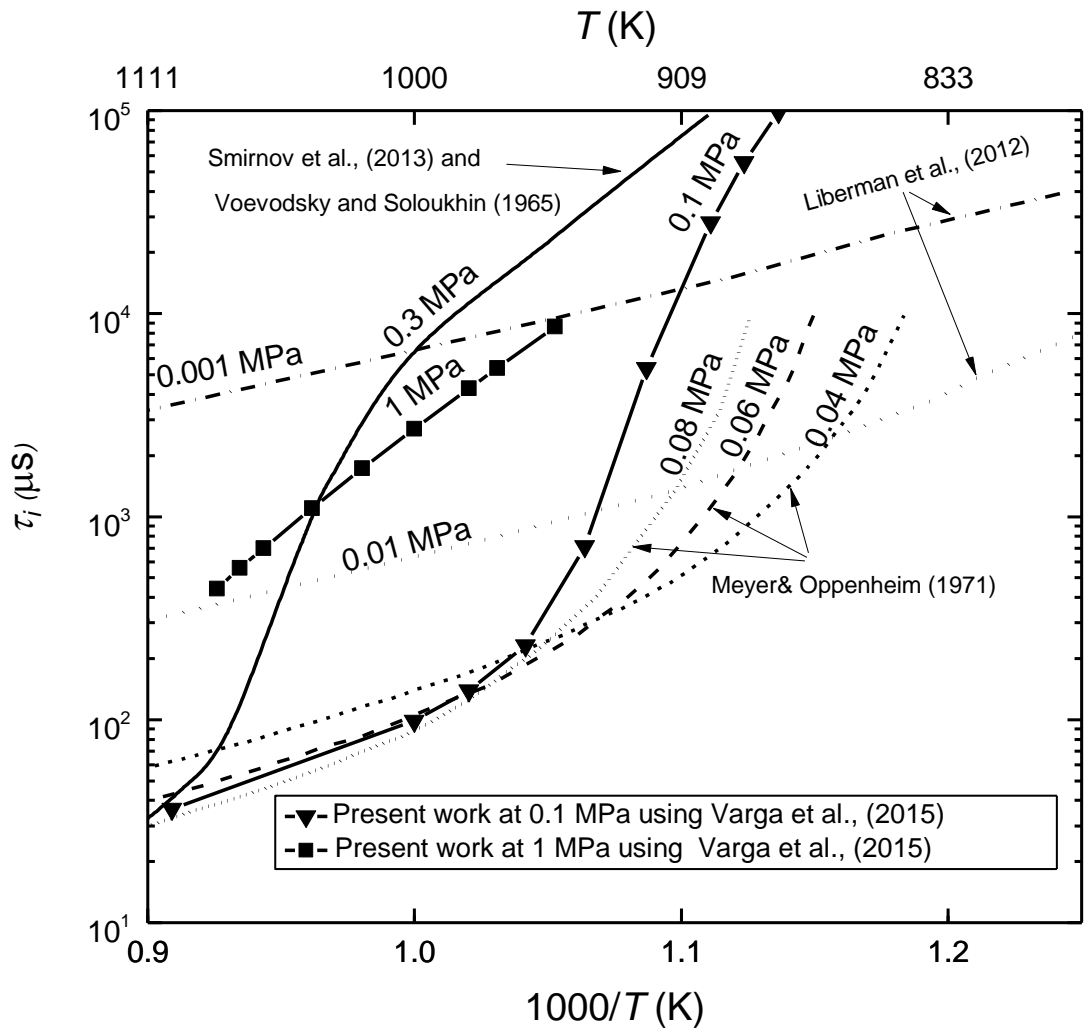
**Figure 4.12** Autoignition delay times of stoichiometric H₂/O₂ employed in the present work (Bradley & Shehata, 2018).

The present analysis is for a variety of conditions, with the initial pre-shock temperature, $T_1$, equal to either 300 or 375 K. It is necessary to derive values of $c$ for the different values of $\tau_i$. For a given $\tau_i$, associated values of $T_2$ and $P_2$ are identified in Fig. 4.12. For the given value of $T_2$, because $T_1$ is known, $M_1$ can be found from Eq. (4.10). This enables $c$ to be found from Eq. (4.7). Values of $c$ are consequently a function of $T_2$ only.

In the same way, with the same value of $M_1$, because $P_2$ is known, the pre-shock pressure, $P_1$, can be found from Eq. (4.9). This approach enables isobars to be constructed based on different values of $P_2$ and $P_1$, as shown in

Fig. 4.13 for $T_1$ = 300 K. The isobars are labelled with the value of $P_1$. Values of $c$ are shown for different values of $T_2$ to the right of the $P_1$ = 0.1 MPa isobar.
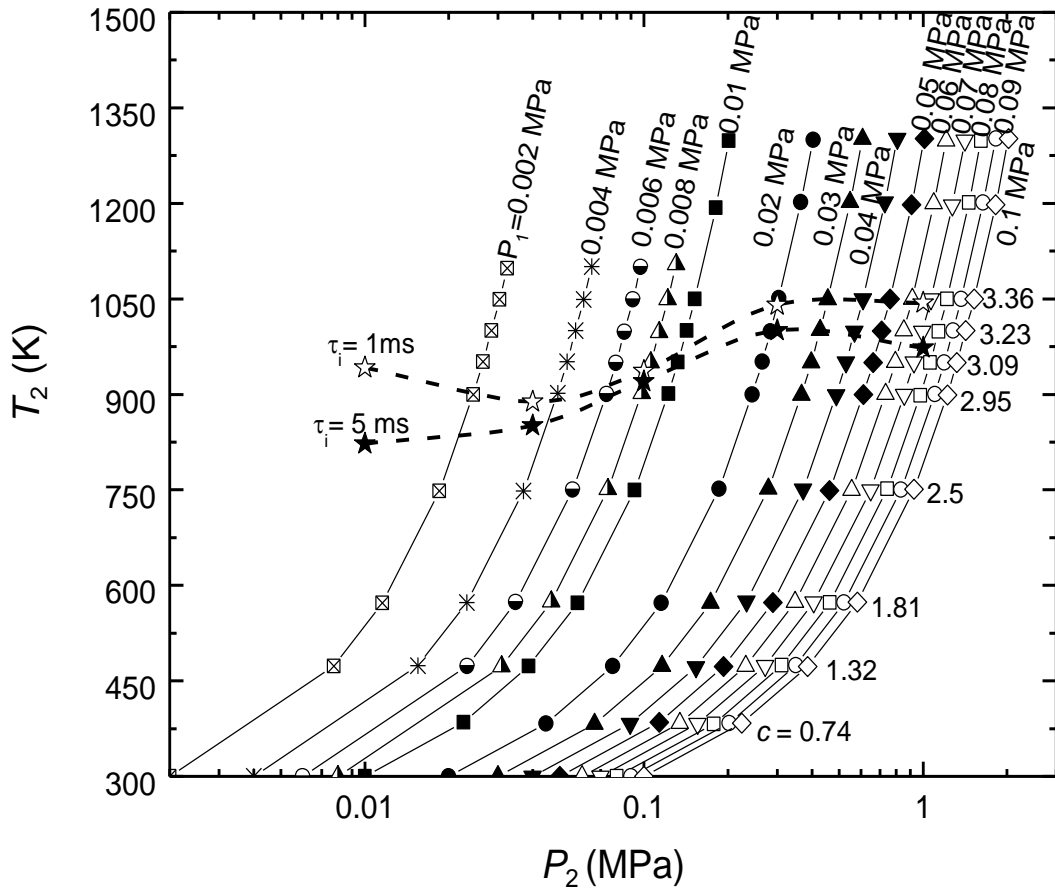


**Figure 4.13** Different isobars, showing the $T_2/P_2/c$ relationship for $T_1$= 300 K, and $\tau_i$ values of 1 and 5 ms. Values of $c$ on the right of $P_1$= 0.1 MPa isobar.

## 4.4  Laminar Flame Propagation in a Tube of Circular Cross Section

A high area ratio, $A/a$, is necessary for the attainment of a sufficiently high value of $S_g$, and consequently of $c$, for autoignition. For turbulent flows, within the mean flame area $A$, the turbulent burning velocity, $u_t$ expresses the effects of the micro-wrinkling of that front in increasing $u_t$. The ratio, $A/a$, expresses a further increase in the overall burning surface of area $A$, beyond that of the tube cross section of area, $a$, associated with $S_g$. For laminar flames the

increase in flame area is entirely due to the increasing elongation of the flame front accompanying increases in $u_\ell$, both of which increase $S_g$. Values of $A/a$ are significantly larger than for turbulent flames.

The explosive growth in $A/a$ results in a very rapid acceleration in $S_g$ as autoignition is approached. The numerical simulations of Gamezo and Oran (2006) of flame propagation of stoichiometric acetylene/oxygen in hypodermic tubes revealed rapidly accelerating flames that attained values of $A/a$ of up to 30 in 0.5 ms in channel lengths of up to 8 cm. As the boundary layer developed, so did the velocity profile across the channel and the shape of the flame was similar to the velocity profile. With such a similarity the flame length is proportional to $S_g$.

In a study of the more sedate transition of a laminar flame from a spherical kernel to a finger-shaped front at the entry to a tube, Bychkov et al. (2007) derived an approximate expression for $A/a$:

$$A/a = \frac{2\sigma^2}{\sigma+1} \tag{4.14}$$

As the flame thickness tended to zero, $A/a$ tended to 14.

With a larger diameter, of 21 mm, Kerampran et al. (2001) observed a rapid acceleration of a stoichiometric propane/air flame as it rapidly elongated, attaining an an $A/a$ value of 9.3 after 12 ms in a duct length of 1.6 m.

With a parabolic distribution of the flow velocity, $u$, at radius, $r$, in a tube of diameter, $D$, is given by Massey (1989):

$$u = 2S_g(1 - 4\,r^2/D^2) \tag{4.15}$$

The maximum velocity is $2S_g$ at the centre of the tube, and the flow strain rate is a maximum at the tube walls, given by:

$$(du/dr)_m = 8\,S_g/D \tag{4.16}$$

## 4.5 Flame Extinguishing of H₂/O₂ Mixtures and the Possibility of Laminar Autoignition

Although the explosive increases in both $u_l$ and $A/a$ very effectively increase $S_g$, the increasingly high strain rate at the tube walls due to $S_g$ can lead to localised flame extinctions there and flame flashback.

To assess this possibility for laminar flames a generalised laminar extinction Karlovitz stretch factor, $K_{ql+}$ has been employed in an attempt to generalise the accumulated data on such extinctions. This is the hydrodynamic strain rate normalised by a chemical time, given by the laminar flame thickness, expressed by $\nu/u_\ell$, divided by $u_\ell$ (Bradley et al., 2007b), Hence,

$$K_{ql+} = (8\,S_g/D)\,\nu/u_\ell{}^2 \ . \tag{4.17}$$

For strain rate Markstein numbers between -2 and +2, $K_{ql+}$ is approximately unity. Because of the difficulty of generating and measuring extinguishing stoichiometric H₂/O₂ flames, no data are known to the author for stoichiometric H₂/O₂ extinction, but some data are available for lean H₂/air flames (Dong et al., 2005). An extensive extrapolation of these data to the stoichiometric H₂/O₂ conditions suggested a value of $K_{ql+}$ of about 2. While a degree of quenching might be tolerated, an increase in $D$ would be necessary to reduce it. Close to this limit, it was calculated that the viscous dissipation term in the energy equation showed the mixture could be sufficiently heated to autoignite, although heat loss to the wall would reduce this. For some time there has been strong evidence for such boundary layer-induced autoignitions (Sivashinsky, 2002).

Numerical simulations for H₂/O₂ mixtures (Dziemińska & Hayashi, 2013) show the shock wave heating the boundary layer. This is followed by secondary shock waves, between the main shock and the flame, further heating the boundary layer, to the point of autoignition, with transition to detonation.

In contrast, with micro tubes the heat loss will be significant, although insufficient to inhibit strong flame acceleration and possible transition to detonation. In the earlier stages, the effect would be to require a longer transitional distance. In the final stage of a transition to auto-ignition, there is a similar effect.

## 4.6  Results of the Laminar Deflagration to Detonation Transition

The crucial limiting conditions for autoignition in laminar flow rest upon the attainment of the limiting Reynolds number, $Re_c$ = 2300 for such flow. The corresponding critical values of $D$ are $D_c$. These are are listed in Tables 4.1 and 4.2 for $T_1$ = 300 K, with $\tau_i$ =1 and 5 ms, and in Table 4.3 and 4.4 for the more reactive conditions of $T_1$ = 375 K with $\tau_i$ = 0.1 and 0.05 ms. All Tables cover the same three different values of $P_2$, whilst Tables 4.1 and 4.2 additionally cover two further values. Tables 4.1& 4.2 tend to be characterised by higher values of $c$ and lower values of $T_2$, and Tables 4.3 & 4.4 by lower values of $c$ and higher values of $T_2$.

The parameters are presented, reading from left to right, in the order they are presented at the ends of Sections 4.2 and 4.3. Values of $D_c$ are found from the values of $S_g$ and $v$. In addition to $Re_c$, $K_{ql+}$ can be a limiting factor, and these values comprise the final listing in the Tables. Values of $\sigma, \gamma$ and $v$ were found from the GasEq code (Morley, 2005) and those of $S_g$ were found from the different values of $c$ and Eq. (4.8).

Bearing in mind the restrictive influences of high values of $K_{ql+}$ and the practical problems of values of $D_c$ less than 0.4 mm, only four conditions seem practical for autoignition in laminar flow. These conditions are identified by A, B, C, D, adjacent to the final $K_{ql+}$ column. This is rather restrictive, because, in practice, the generation of some turbulence is favourable and will be discussed in Section 4.7.

### 4.6.1  Analysis of the Possibilities of Laminar Deflagration to Detonation Transition

A key factor is that $S_g$ must be large enough to create autoignition and, yet not so large as to exceed Re$_c$. As a consequence, for laminar autoignition, $\nu$ should be large in order to make $D$ as large as possible. This also beneficially reduces $K_{ql+}$.

From Table 4.1, for $T_1$ = 300 K and $\tau_i$ =1 ms, if the value of $K_{ql+}$ = 4.5, which exceeds the extrapolated limit of 2, were to be accepted then $D$ could be 1 mm. The corresponding value of $A/a$ of 18 is rather high but might be attainable. More cautiously, a lower value of $D$ = 0.43 mm would probably be more practical, with $K_{ql+}$= 2.6 and $A/a$ = 14.7. In practice, if Re$_c$ were to be exceeded, micro-turbulence would develop on the large flame area, $A$, increasing the burning velocity and further strengthening the shock. Flame imaging of such flames suggests their appearance would initially be indistinguishable from that of a laminar flame.

It is difficult to know the upper limit to $K_{ql+}$, because of the uncertainty in the extrapolated value and the degree of quenching that might be tolerated, yet partially countered by dissipation-induced autoignition, with an upper limit of 2.6, only the bottom three entries in Tables 4.1 and 4.2 would support a purely laminar autoignition. Tables 4.3 and 4.4 cover more reactive mixtures, resulting from preheating to 375 K. For $\tau_i = 0.05$ ms, a maximum value of $D_c$ of about 1.3 mm is possible, albeit at a low value of $P_1$ and high value of $A/a$. At the higher values of $P_2$ of 0.3 MPa, higher values of $S_g$ are required, and $D$ becomes impractically smaller.

The laminar flames become more elongated with increasing $u_\ell$, leading also to an associated increase in $A/a$. Consequently, autoignition is enhanced, not only by a high value of $u_\ell$, but also by the associated increase in flame surface area.

Of the different values of $D_c$ listed in the Tables, only those four between 0.42 and 0.52 mm would seem to be in any way practical for laminar autoignition.

With $\tau_i$ = 1 ms, autoignition is probable and practical. At the higher values of $S_g$, $D_c$ becomes impractically small, with values of less than 0.1 mm.

It is estimated for Condition B, in Table 4.4, with $D_c$= 0.494 mm, that in the critical region between the shock wave and the flame, heat transfer would reduce the mixture temperature by about 36 K from 997 K. In practice, this would require further flame acceleration and compression before autoignition. If the large value of $K_{ql+}$ proved to be not so inhibiting, the condition labelled E in Table 4.3, would have a reduced heat transfer rate due to the larger $D_c$ of 1.35 mm. In this case, the mixture temperature 1131 K would only fall by 8 K (Appendix A).

**Table 4.1** Autoignitions of stoichiometric $H_2/O_2$ with $\tau_i=$ 1 ms at $T_1=$ 300 K.

| $T_1$ (K) | $P_2$ (MPa) | $T_2$ (K) | $c$ | $M_1$ | $P_1$ (MPa) | $S_g$ (m/s) | $u_\ell$ (m/s) | $A/a$ | $\sigma$ | $\nu$ (m²/s) | $S_f$ (m/s) | $D_c$ (mm) | $K_{ql+}$ | |
|---|---|---|---|---|---|---|---|---|---|---|---|---|---|---|
| 300 | 0.01 | 941.9 | 3.07 | 3.37 | 0.00076 | 1381 | 22.3 | 38 | 2.62 | 2.6E-3 | 2231 | 4.3 | 13.3 | |
| 300 | 0.04 | 888 | 2.9 | 3.23 | 0.0033 | 1313 | 36.5 | 19 | 2.9 | 5.8E-4 | 2007 | 1 | 4.4 | |
| 300 | 0.1 | 936 | 3.06 | 3.36 | 0.0077 | 1374 | 50.7 | 14.7 | 2.83 | 2.6E-4 | 2123 | 0.43 | 2.6 | **C** |
| 300 | 0.3 | 1040 | 3.33 | 3.61 | 0.02 | 1498 | 73 | 12.3 | 2.67 | 1.0E-4 | 2394 | 0.16 | 1.5 | |
| 300 | 1 | 1043.8 | 3.34 | 3.62 | 0.066 | 1502 | 80 | 10.7 | 2.76 | 3.0E-5 | 2355 | 0.05 | 1.2 | |

**Table 4.2** Autoignitions of stoichiometric $H_2/O_2$ with $\tau_i=$ 5 ms at $T_1=$ 300 K.

| $T_1$ (K) | $P_2$ (MPa) | $T_2$ (K) | $c$ | $M_1$ | $P_1$ (MPa) | $S_g$ (m/s) | $u_\ell$ (m/s) | $A/a$ | $\sigma$ | $\nu$ (m²/s) | $S_f$ (m/s) | $D_c$ (mm) | $K_{ql+}$ | |
|---|---|---|---|---|---|---|---|---|---|---|---|---|---|---|
| 300 | 0.01 | 822 | 2.72 | 3.05 | 0.00094 | 1224 | 17.6 | 35.3 | 2.96 | 2.1E-3 | 1848 | 3.87 | 16.7 | |
| 300 | 0.04 | 851 | 2.81 | 3.13 | 0.0036 | 1264 | 35 | 18 | 3 | 5.5E-4 | 1895 | 0.997 | 4.5 | |
| 300 | 0.1 | 920 | 3.01 | 3.31 | 0.008 | 1354 | 49 | 14.6 | 2.9 | 2.5E-4 | 2074 | 0.42 | 2.6 | **D** |
| 300 | 0.3 | 1000 | 3.23 | 3.5 | 0.021 | 1451 | 67 | 12.3 | 2.77 | 9.5E-5 | 2273 | 0.15 | 1.6 | |
| 300 | 1 | 973 | 3.16 | 3.45 | 0.073 | 1419 | 70 | 10.4 | 2.94 | 2.7E-5 | 2150 | 0.044 | 1.4 | |

**Table 4.3** Autoignitions of stoichiometric H$_2$/O$_2$ with $\tau_i$= 0.05 ms at $T_1$ = 375 K.

| $T_1$ (K) | $P_2$ (MPa) | $T_2$ (K) | $c$ | $M_1$ | $P_1$ (MPa) | $S_g$ (m/s) | $u_\ell$ (m/s) | $A/a$ | $\sigma$ | $\nu$ (m$^2$/s) | $S_f$ (m/s) | $D_c$ (mm) | $K_{ql+}$ | |
|---|---|---|---|---|---|---|---|---|---|---|---|---|---|---|
| 375 | 0.04 | 1131 | 2.97 | 3.27 | 0.0032 | 1488 | 57.7 | 19.5 | 2.323 | 8.8E-4 | 2614 | 1.35 | 2.3 | **E** |
| 375 | 0.1 | 1061 | 2.81 | 3.13 | 0.0089 | 1407 | 64.23 | 14.3 | 2.532 | 3.2E-4 | 2325 | 0.517 | 1.7 | **A** |
| 375 | 0.3 | 1092 | 2.88 | 3.19 | 0.026 | 1443 | 78.6 | 11.8 | 2.556 | 1.1E-4 | 2371 | 0.175 | 1.2 | |

**Table 4.4** Autoignitions of stoichiometric H$_2$/O$_2$ with $\tau_i$ = 0.1 ms at $T_1$ = 375 K.

| $T_1$ (K) | $P_2$ (MPa) | $T_2$ (K) | $c$ | $M_1$ | $P_1$ (MPa) | $S_g$ (m/s) | $u_\ell$ (m/s) | $A/a$ | $\sigma$ | $\nu$ (m$^2$/s) | $S_f$ (m/s) | $D_c$ (mm) | $K_{ql+}$ | |
|---|---|---|---|---|---|---|---|---|---|---|---|---|---|---|
| 375 | 0.04 | 1031.7 | 2.73 | 3.06 | 0.00372 | 1371 | 48 | 18.8 | 2.52 | 7.5E-4 | 2272 | 1.26 | 2.8 | |
| 375 | 0.1 | 997 | 2.65 | 2.98 | 0.0098 | 1327 | 56.9 | 13.9 | 2.678 | 2.8E-4 | 2118 | 0.494 | 1.9 | **B** |
| 375 | 0.3 | 1072.6 | 2.83 | 3.15 | 0.0263 | 1420 | 75.8 | 11.73 | 2.597 | 1.1E-4 | 2309 | 0.173 | 1.2 | |

## 4.7 Laminar with Mild Turbulence Autoignition of Stoichiometric H₂/O₂ Mixture

Introducing turbulence makes the mixture easier to autoignite than laminar flames. Computations for turbulent autoignition were carried out for the less reactive conditions in Tables 4.1 and 4.2 at $T_1 = 300$ K. Here the transition regime of laminar flamelet/turbulent instabilities shown in Fig. 4.14 as regime (A). As described, the diagram is expressed as a function of a particularly important parameter, $Ma_{sr}$

Markstein number for H₂/O₂ was not well covered in the literature except for diluted H₂/O₂ mixtures reported by (Kwon & Faeth, 2001) and diluted H₂/30%O₂/70%N₂ by Qiao et al. (2005) and steam diluted H₂/O₂ by Kuznetsov et al. (2011).

Kuznetsov et al. (2011) reported $Ma$ for undiluted stoichiometric H₂/O₂ at 573 K and 1 bar as 0.144. Comparing this case to the studied case at 300 K and sub-atmospheric pressure, $Ma$ was predicted to be about 1 at a location denoted by (F) in Fig.4.14.
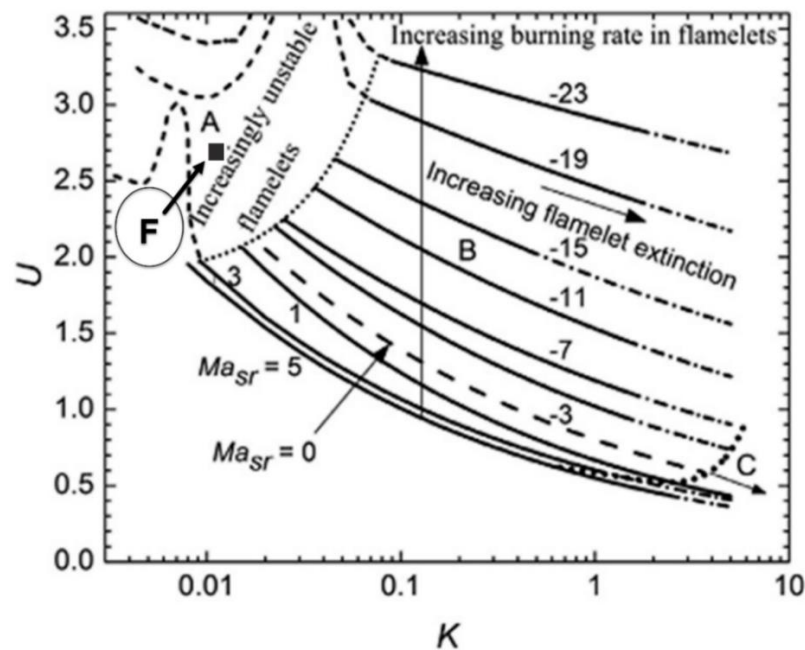


**Figure 4.14** Turbulent combustion regime (*U/K*) diagram (Bagdanavicius et al., 2015) with laminar/turbulent condition (F).

Equations (4.2) and (4.8) in addition to the turbulent to laminar burning velocity ratio (Bradley et al., 2008) is readily shown that:

$$u_t/u_\ell = U\left(\frac{u'_k}{u'}\right)(4K)^{\frac{2}{3}}\left(\frac{u_l l}{\nu}\right)^{1/3},$$

(4.18)

where $l$ is the integral length scale of turbulence in the tube. This value was evaluated as a function of tube diameter as follows (Laufer, 1951):

$$l = 0.1\, D$$

(4.19)

Using Eqs. (1.24) & (4.8):

$$K = 0.25(u'/u_\ell)^{3/2}\,(\nu/u_\ell l)^{1/2},$$

(4.20)

and

$$c = \left(\frac{A}{a}\right) U \left[\frac{K}{0.25}\left(\frac{u_\ell l}{\nu}\right)^{0.5}\right]^{\frac{2}{3}} u_\ell(\sigma - 1)\left(\frac{\gamma+1}{2a_1}\right).$$

(4.21)

The study based on comparing the laminar cases with the mild turbulent case at initial temperature 300 K in a similar tube size.

The calculations are characterised by:

   i.   Selecting a value of $c$ for initial conditions that can give a required value of $\tau_i$ at a particular $P_2$ and $T_2$.

   ii.  By replacing $u_\ell$ with $u_t$ in Eq. (4.8) and using Gaseq code (Morley, 2005) for equilibrium properties for the mixture to find $u_t$.

   iii. Deciding the value of $l$ and duct diameter, $D$, recognising the coupling between them.

   iv.  Finding $s_g$ from Eq. (4.8) and deriving $K_{ql+}$.

All properties and the results for laminar/turbulent mixture are listed in Table 4.5.

**Table 4.5** Laminar-turbulent autoignitions of stoichiometric H₂/O₂ with $\tau_i$=0.4 ms at $T_1$ = 300 K.

| Case F | |
|---|---|
| $T_1$ (K) | 300 |
| $P_2$ (MPa) | 0.11 |
| $T_2$ (K) | 950 |
| $c$ | 3.27 |
| $M_1$ | 3.56 |
| $P_1$ (MPa) | 0.0077 |
| $S_g$ (m/s) | 1500 |
| $u_\ell$ (m/s) | 53.6 |
| $A/a$ | 8.5 |
| $\sigma$ | 2.8 |
| $v$ (m²/s) | 2.37E-4 |
| $l$ (mm) | 0.2 |
| $D$ (mm) | 2 |
| $K_{ql+}$ | 0.018 |

Results show that turbulence facilitated autoignition for H₂/O₂ to auto-ignite at the same temperature and similar tube size of the laminar cases C and D in Tables 4.1 and 4.2 with an ignition delay time of 0.4 ms. $A/a$ ratio was 8.5 comparing to cases C and D. $K_{ql+}$ was low enough to resist the quenching of the flames.

# Chapter 5 – Discussion of DDT and Flame Quenching

## 5.1 Discussions of Laminar and with Mild Turbulent Auto-ignition

In case of laminar autoignition, the four most probable conditions, A-D, had been established in Tables 4.1 to 4.4 in Section 4.6.1, the likelihood of a detonation remains to be assessed alongside the laminar/mild turbulent autoignition, condition, F (Section 4.7). Unlike condition C and D, condition F is more reactive as they all have the same initial temperature, and pressure despite in the mild turbulence condition, the tube size is a bit bigger but, it is still comparable.

In addition to a developing detonation, the other possibilities, following upon autoignition, include continuing normal flame propagation, and thermal explosion. These regimes were located relative to the detonation peninsula shown in Fig. 5.1. This plots the ratio of acoustic to autoignitive velocity, $\xi$, against $\varepsilon$ as described in Section 1.4.3.

Values of $\tau_i$ and $E/R$ at $P_2$ and $T_2$, for the five conditions A to F, were obtained from Fig. 4.12 of autoignition delay times of $H_2/O_2$ at different pressures and temperatures. Those of $\tau_e$ were found by computing the temporal heat release rates, as outlined in (Bates et al., 2017b), using the Cantera code (Goodwin, 2005). The pressure, $P_2$, for the five selected diameters was the same and equal to 0.1 MPa, but the temperatures, $T_2$, were variable. The values of these parameters, from which they are derived, are given in Table 5.1. A value of $(dT/dr)_c$ = 1 K/mm, occurred at $T_2$ = 1040 K.

To evaluate $\xi$, it was necessary to attribute a general value to $(dT/dr)$ in Eq. (1.44). This value is determined less by the physico-chemical parameters and more by micro-flow patterns and energy transfers that are variable, and stochastic. A value of -2 K/mm was chosen, on the basis of engine and other measurements (Bates et al., 2017b). Values of $\bar{E}$ are given in Table 5.1 for an assumed hot spot radii of 5 mm.

**Table 5.1** Autoignition parameters for atmospheric stoichiometric $H_2/O_2$ mixture at $dT/dr$ = -2 mm

| | $T_1$ (K) | $T_2$ (K) | $\tau_i$ (ms) | $\tau_e$ (μs) | $\dfrac{\tau_i}{\tau_e}$ | $\dfrac{E}{R}$ (K) | $\dfrac{E}{RT}$ | $\bar{E}$ | $a$ (m/s) | $\dfrac{E}{RT^2}$ (K⁻¹) | $\left(\dfrac{d\tau_i}{dT}\right)^{-1}$ | $\left(\dfrac{dT}{dr}\right)_c$ (K/mm) | $u_a$ (m/s) | $\xi$ | $\varepsilon$ | $\dfrac{dlnT}{d\bar{r}}$ | $\dfrac{\bar{E}\,dlnT}{d\bar{r}}$ |
|---|---|---|---|---|---|---|---|---|---|---|---|---|---|---|---|---|---|
| **A** | 375 | 1061 | 0.05 | 2 | 25 | 9,519 | 8.97 | 225.2 | 995.8 | 0.0085 | 2,355,785 | 2.37 | 1178 | 0.85 | 2.5 | 0.0094 | 2.11 |
| **B** | 375 | 997 | 0.1 | 1.98 | 52 | 17,149 | 17.2 | 895 | 966.8 | 0.0173 | 562,733 | 0.58 | 281.3 | 3.44 | 2.6 | 0.0099 | 8.93 |
| **C** | 300 | 936 | 1 | 1.93 | 504 | 44,141 | 47.16 | 23,760 | 938.1 | 0.0504 | 20,413 | 0.012 | 10.21 | 91.9 | 2.7 | 0.0106 | 253 |
| **D** | 300 | 920 | 5 | 1.8 | 2778 | 59,161 | 64.28 | 178,568 | 930.5 | 0.0698 | 2863 | 0.003 | 1.432 | 650 | 2.9 | 0.0108 | 1930 |
| **F** | 300 | 950 | 0.4 | 1.94 | 206 | 41,137 | 43.3 | 8928.87 | 944.8 | 0.0456 | 54,847.3 | 0.058 | 27.42 | 34.4 | 2.7 | 0.0105 | 94 |

### 5.1.1 ε/ξ Detonation Peninsula

In Fig. 5.1, low values of $\xi\varepsilon$ are indicative of stable developing detonations. At the high values, autoignitive propagation begins to fail and be replaced by normal flame deflagrations.

The five chosen conditions for both laminar and laminar/mild turbulent autoignition studied are labelled A, B, C, D, F in Tables 4.1 to 4.5 in Sections 4.6 and 4.7, as depicted in Table 5.1. Their coordinates in the $\xi/\varepsilon$ diagram are shown in Fig. 5.1.

For laminar conditions, each point lies in a different one of the four, contrasting regimes. For mild turbulent condition, point F, it lies in the regime where combustion would be by autoignitive propagation, like point C, as $T_1 = 300$ K. Point F has a lower $\xi$ than point C due to its higher reactivity. Whilst in D, $T_1 = 300$ K, there would probably be normal flame deflagration.

Of these, A and B, with $T_1 = 375$ K lie in the most reactive regimes, culminating in a thermal explosion and a developing detonation.
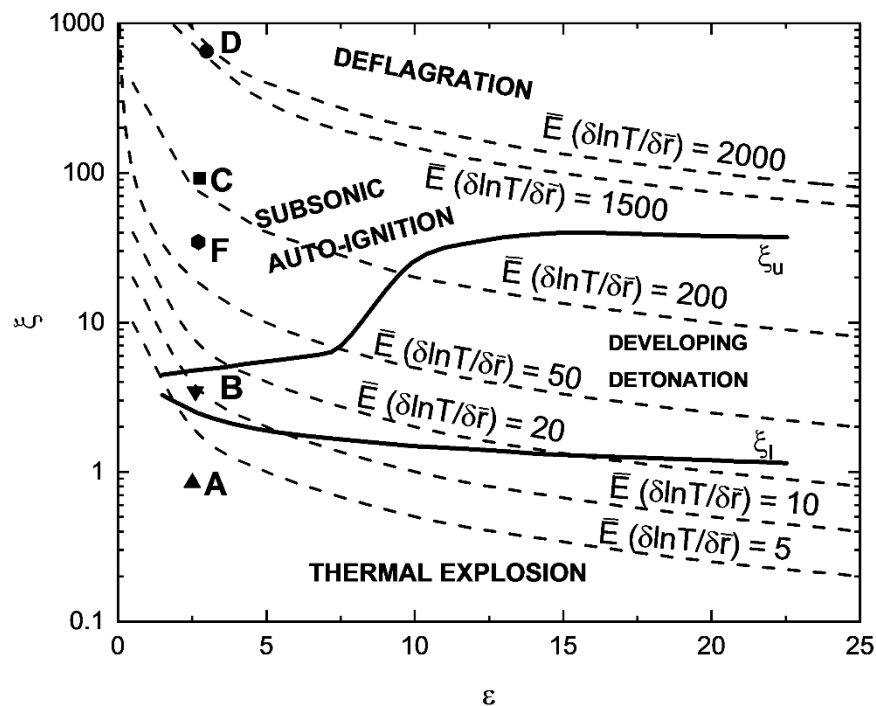


**Figure 5.1** Detonation peninsula diagram showing ξ/ε variations, and regime points A, B, C,D and F.

As a further check on the propensity to undergo a laminar DDT, the marginal conditions for $D_c$= 1.35 mm in Table 4.3, with rather high values of $A/a$ and $K_{ql+}$, were examined. If autoignition were to occur in this otherwise reactive mixture, either a thermal explosion or a detonation would develop. This would suggest the possibility of a laminar DDT, in hypodermic tubes of between 0.5 and 1.3 mm diameter, with $T_1$ = 375 K.

Laminar/mild Turbulent autoignition would occur with lower $A/a$ ratio and $K_{ql+}$. For the condition studied, the flame would auto-ignite at $D_c$= 2 mm, with $T_1$ = 300 K.

## 5.2  Findings on $H_2$/$O_2$ Autoignition and Detonation

The limitations to the induction of detonation in laminar flames are well established in Section 4.6. After the study of whether a laminar flow might induce detonation, it is an interesting question whether such a detonation is of practical value. One application could be in a pulse detonation engine for space flight. The question remains whether the principle might be applied in a stationary power unit, Fig. 5.2 is a diagram of the cycle for such a unit. The exhaust heat from the turbine could be used to preheat the $H_2$ and $O_2$.

It is proposed that the turbine should operate between 0.1 and 0.005 MPa. The pressure on moon is about $3 \times 10^{-16}$ MPa and on Mars 0.0006 MPa.

Despite the apparent simplicity of such engines, this technology is yet to be established due to the difficulties in stabilising a sustainable continuous detonation front in the detonation chamber.

The high reactivity of hydrogen-oxygen mixtures and the occurrence of DDT in hypodermic tubes in laminar or near laminar flows is the basis of a detonation engine using the laminar DDT results in Section 4.6.  Conditions A and B in Tables 4.3 and 4.4 are employed in this brief study. The power unit as seen in Fig. 5.2 is comprised of:

- Gas cylinders of $H_2$ and $O_2$.

- An array of hypodermic tubes for the mixture, diameter 0.5 mm.

- An initial mixing chamber (Mix 1) for $H_2$ and $O_2$.

- A second mixing chamber (Mix 2) at the exit of the detonation tubes.

- A pressure compounded multi-stage impulse turbine.

- Exhaust of cooled burned gases to atmosphere.
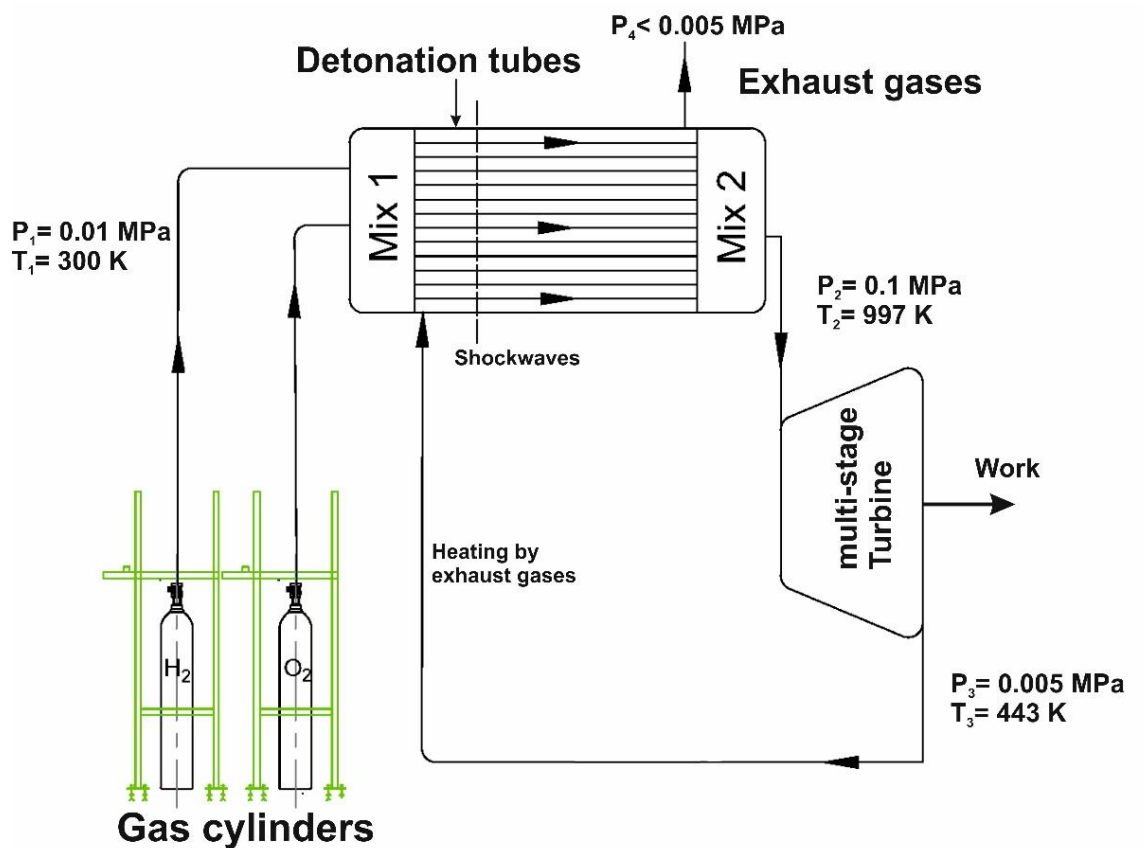


**Figure 5.2** ($H_2$-$O_2$) proposed detonation cycle

$H_2$ and $O_2$ gases are mixed stoichiometrically in the mixing chamber (1) at 0.01 MPa. The mixture ignites in an array of many 0.5 mm diameter

hypodermic tubes subjected in an in-line arrangement to generate shockwaves and ultimately trigger the transition to detonation.

The exhaust gases are then mixed in the mixing chamber (mix 2) prior to isentropic expansion in multi-stages impulse turbines from 0.1 to 0.005 MPa, in which the gas velocity changes and the power output is obtained. The exhaust gases preheat the $H_2$ and $O_2$ via heat exchange in the detonation tubes.

### 5.2.1   Proposed Detonation Cycle.

For the case B in Table 4.4 of the laminar DDT study in Section 4.6, the velocity of the detonated gases at 997 K and 0.1 MPa is $S_g$= 1327 m/s. This mixture enters the first nozzle of the multi-stage turbine with this velocity where it increases through the nozzle before it starts dropping through the moving blades in the first stage. The velocity then increases in the nozzle of the following stage before dropping again. The pressure drop occurs through number of stages as shown in Fig. 5.3.
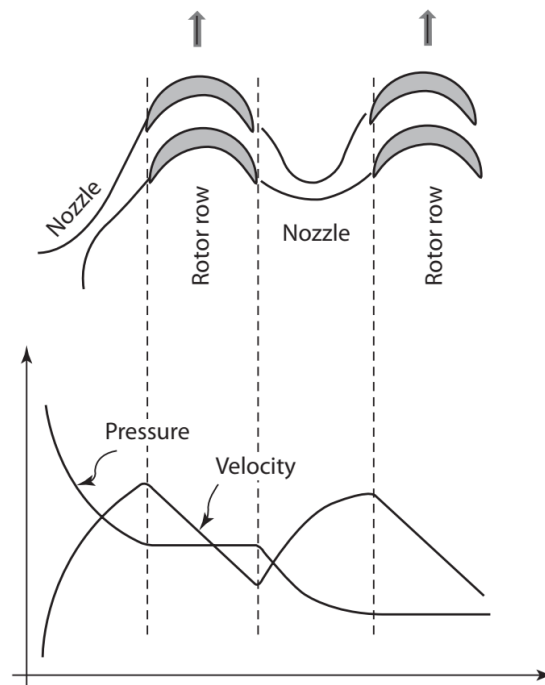


**Figure 5.3** Multi-stage pressure compounding impulse turbine with pressure and velocity profiles (Dakshina Murty, 2018).

Applying the steady adiabatic flow energy equation between point (2) and point (3):

$$h_2 + \frac{V_2^2}{2} = h_3 + \frac{V_3^2}{2} + W_t \tag{5.1}$$

where $V_2 = S_g$.

Assuming the isentropic efficiency of the moving blades are 88%.

The efficiency of the nozzle, $\eta_{isen}$, is defined as:

$$\eta_{isen} = \frac{Actual\ enthalpy\ change}{Isentropic\ enthalpy\ change} = \frac{\Delta h_{act}}{\Delta h_{ideal}} \tag{5.2}$$

where $\Delta h_{ideal} = h_2 - h_{3s}$ (kJ/kg), $h_{3s}$ is the exit enthalpy of isentropic expansion. $\Delta h_{ideal}$ is calculated using Gaeq code (Morley, 2005).

At this point, $\Delta h_{act}$ would be 1246 kJ/kg. The tube diameter is 0.5 mm for this condition. All the data of the cycle is given in Table 5.2.

The work output from the turbine is then calculated as a function of stage loading coefficient, $\psi$, (Ingram, 2009):

$$\psi = \frac{W}{U_m^2} \tag{5.3}$$

where, $U_m$ is the rotational speed of the moving blades and is equal to (Ingram, 2009):

$$U_m = \omega . r \tag{5.4}$$

where $\omega$ and $r$ are the blade angular velocity and radius, respectively. As an impulse turbine with repeating stages, axial velocity, then $\psi = 2$.

Assuming the blade radius $r = 1$ m and rotating at 3000 rpm, then,

$W = 197$ kJ/kg/ stage.

To evaluate the number of stages, $N_{stages}$, (Ingram, 2009):

$$N_{stages} = \frac{\Delta h_{act}}{W} \tag{5.5}$$

Using Eq. (5.1) then, $V_3 = 1374$ m/s

Knowing that the mass flow rate of the exhaust gas per tube, $m^.$, is defined:

$$m^{\cdot} = \rho_2 S_g a \qquad\qquad\qquad\qquad (5.6)$$

where $a$ is the cross-sectional area of the tube, $\rho_2$ is the density of the exhaust gas $= 0.1449$ kg/m$^3$.

The power output from the cycle/ tube is then calculated with:

$$P = m^{\cdot} W_t \qquad\qquad\qquad\qquad (5.7)$$

where $W_t$ is the total work output.

**Table 5.2** Initial conditions of the proposed detonation engine.

| $P_2$ (MPa) | $T_2$ (K) | $P_3$ (MPa) | $T_3$ (K) | $h_2$ (kJ/kg) | $h_{3s}$ (kJ/kg) | $d$ (mm) | $\eta_{isen}$ | $\psi$ | $r$ (m) | $N$ (rpm) |
|---|---|---|---|---|---|---|---|---|---|---|
| 0.1 | 997 | 0.005 | 443 | 1770.53 | 354.7 | 0.5 | 0.88 | 2 | 1 | 3000 |

The main concern in the cycle is that the exhaust gas (4) which it leaves at a pressure lower than 0.005 MPa. This couldn't be implemented on the atmospheric pressure on earth. Therefore, per each cycle, a 45 W/tube is produced from the multi-stage turbine as shown in Table 5.3 while the exhaust gas (4) is rejected to the atmosphere in Mars or moon.

**Table 5.3** Performance of the proposed detonation engine.

| $m^{\cdot}$ (g/s) | $V_3$ (m/s) | $N_{stages}$ | $W$ (kJ/kg/stage) | $W_t$ (kJ/kg/tube) | $Power$ (Watt/tube) |
|---|---|---|---|---|---|
| 0.0377 | 1374 | 6 | 197 | 1182 | 45 |

## 5.3 Effect of Varying the Initial Pressure on the Autoignition of Turbulent Stoichiometric H$_2$/O$_2$ Mixture

In Section 4.7, the main purpose was to compare the autoignition of laminar/mild turbulent flames with laminar flames in similar hypodermic tube. In this study, the effect of changing the initial pressure has been studied on the autoignition of turbulent flames. Three turbulent cases have been studied

at different initial pressure, $P_1$, and same temperature, 300 K. The size of the tube was kept the same in the three cases, 12 mm. Three cases are located on regime (*B*) in *U/K* diagram as shown on Fig. 5.4 where the normal turbulent flame propagation is. At certain $K$ value, the three cases have been defined according to the initial pressure; 0.02, 0.07 and 1.0 MPa. Markstein number in this case is changing due to the change in $P_1$.
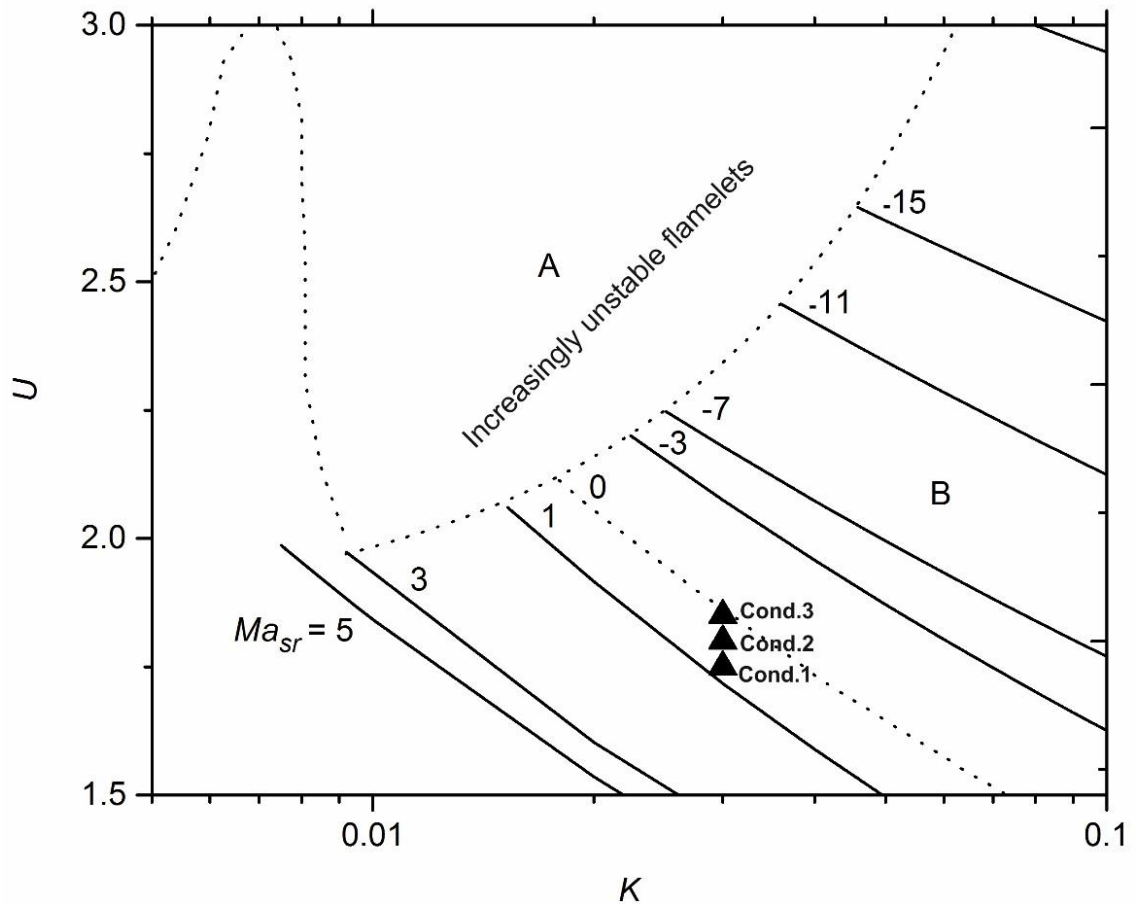


**Figure 5.4** *U/K* diagram (Bradley et al., 2013) showing the turbulent conditions studied.

As mentioned in Section 4.7, due to the lack of information on Markstein number at different pressures, their values were estimated according to the effect of increasing pressure on the decreasing Markstein number reported in (Bradley et al., 2007a; Bradley et al., 2007b). Table 5.4 show the three cases studied, the first case where the initial pressure is the lowest among the

others, 0.02 MPa while the third case has the highest pressure, 0.1 MPa. Same calculation procedures used in Section 4.7, were employed in this study.

It is found that increasing the initial pressure will result in dropping $A/a$ ratio and the delay time for auto-ignition. Therefore, the more reactive the mixture is, the less $A/a$ ratio occurs.

**Table 5.4** Effect of changing the initial pressure on the turbulent flame acceleration and auto-ignition.

| Condition | (1) | (2) | (3) |
|---|---|---|---|
| $T_1$ (K) | 300 | 300 | 300 |
| $P_1$ (MPa) | 0.02 | 0.07 | 0.1 |
| $P_2$ (MPa) | 0.3 | 1 | 1.54 |
| $T_2$ (K) | 995 | 995 | 995 |
| $c$ | 3.4 | 3.4 | 3.4 |
| $M_1$ | 3.67 | 3.67 | 3.67 |
| $S_g$ (m/s) | 1580 | 1562 | 1555 |
| $u_\ell$ (m/s) | 66 | 72 | 73 |
| $A/a$ | 3 | 1.7 | 1.4 |
| $\sigma$ | 2.78 | 2.89 | 2.92 |
| $\nu$ (m$^2$/s) | 9.09E-05 | 2.63E-05 | 1.84E-05 |
| $D_c$ (mm) | 12 | 12 | 12 |
| $K_{ql+}$ | 0.022 | 0.0053 | 0.0036 |
| $Ma_{sr}$ | 0.8 | 0.5 | 0.2 |
| $\tau_i$ (ms) | 10 | 3.46 | 3.01 |

The ignition delay times for condition 1 and 2 are evaluated from Fig.4.12, while the ignition delay time at 1.54 MPa is calculated using current computations using the (Varga et al., 2015) model.

## 5.4  Flame Quenching and Annular Pilot Flames

In the discussion of quenching in Section 3.5.6, the crucial rate of entrainment of air by fuel jets is briefly described. A similar entrainment of hot gases from a pilot flame of a turbulent burned flame can prevent it quenching at high levels of turbulence.

Wabel et al. (2017) have employed a burner configuration as shown in Fig. 5.5 with some similarities to a jet flame; in that it employs a lean mixture flame that entrains hot products from a surrounding pilot flame. By these means, the pilot flame is able to sustain a central highly turbulent flame and avoid quenching. This is achieved through an increase in the burning velocity of the burner reactants through their entrainment of pilot flame gases.



**Figure 5.5** Hi-pilot Michigan burner by (Driscoll et al., 2017).

The essential principle governing the use of pilot flames to support burner flames that are closer to extinction is that the mixing of the pilot flame gases will make the burner flame more resistant to extinction by being less prone to dilution by surrounding air and more reactive due to admixture with hot pilot

flame gases. The essential mechanism can be simplified in a simple mixing theory of pilot flame burned gas with the burner reactants.

Adiabatic mixing is expressed by:

$$m_{\dot{u}}c_{pb}(T_m - T_b) = m_{\dot{p}}c_{pp}(T_p - T_m) \tag{5.8}$$

where $m_{\dot{u}}$ is the flow rate of reactants to the burner, $T_b$ ,the temperature of the burner reactants, $c_{pb}$, the specific heat at constant pressure of the burner reactants, $T_m$, the temperature of the mixture, $m_{\dot{p}}$, the flow rate of pilot flame gases, $c_{pp}$, the specific heat at constant pressure of pilot flame gases, and $T_p$ the adiabatic temperature of the pilot flame gases.

If $m_{\dot{u}}$ is the mass fractional flow rate of unburned burner reactants, and $m_{\dot{p}}$, the mass fractional flow rate of burned pilot flame gas.

Clearly, $m_{\dot{u}}$+$m_{\dot{p}}$= 1.0. The proportion of pilot flame hot gases, the dilution *f*, in the mixture is $m_{\dot{p}}/(m_{\dot{p}}+ m_{\dot{u}})$ and this ranges from *f* = 0 for undiluted cold reactants, with no admixture of pilot flame gas,  to *f* = 1.0 for the hot products at the adiabatic flame temperature.

In the present study to identify the underlying mechanism, a simplified model is employed, in which the same mixture is supplied to both burners. It has two aspects. The first involves the existing data of Sidey et al. (2014) on the burning velocities of the mixtures that arise when the burned gases from a $CH_4$ flame, are adiabatically mixed with the original  unburned reactants. In the present case, it is assumed that burned pilot flame gases are adiabatically mixed with the burner reactants. Figure 5.6 and 5.7 show Sidey et al. (2014) calculated mixing temperatures and laminar burning velocities of $CH_4$ flame at $\varphi$= 0.6,1 and 1.3 for different dilution levels.
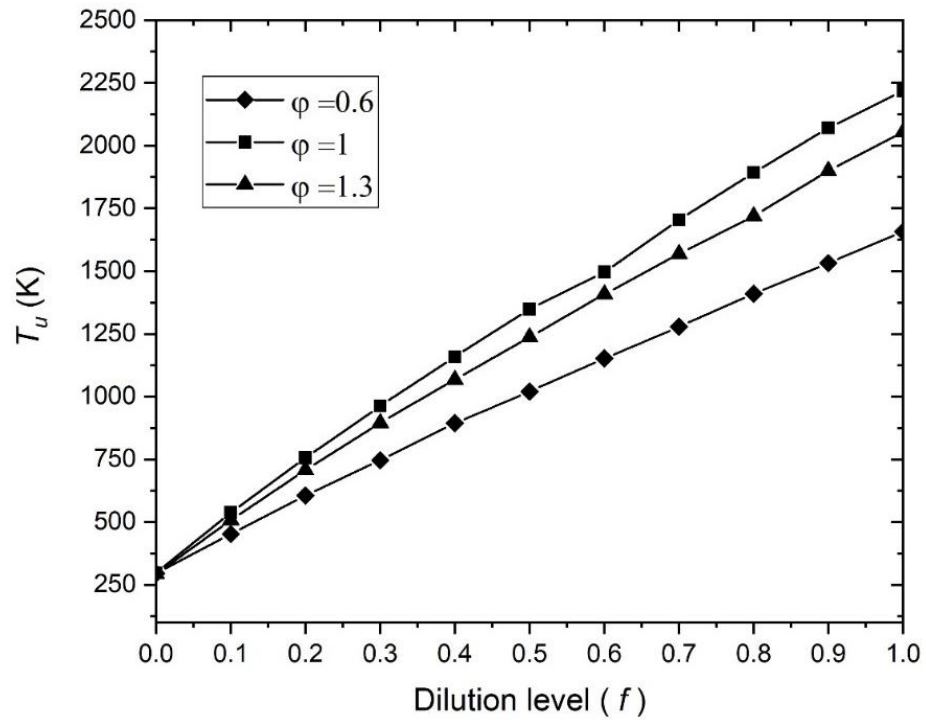
**Figure 5.6** The change in mixing temperature with dilution level at $\varphi$ =0.6,1,1.3 for methane/air mixture extracted from (Sidey et al., 2014).
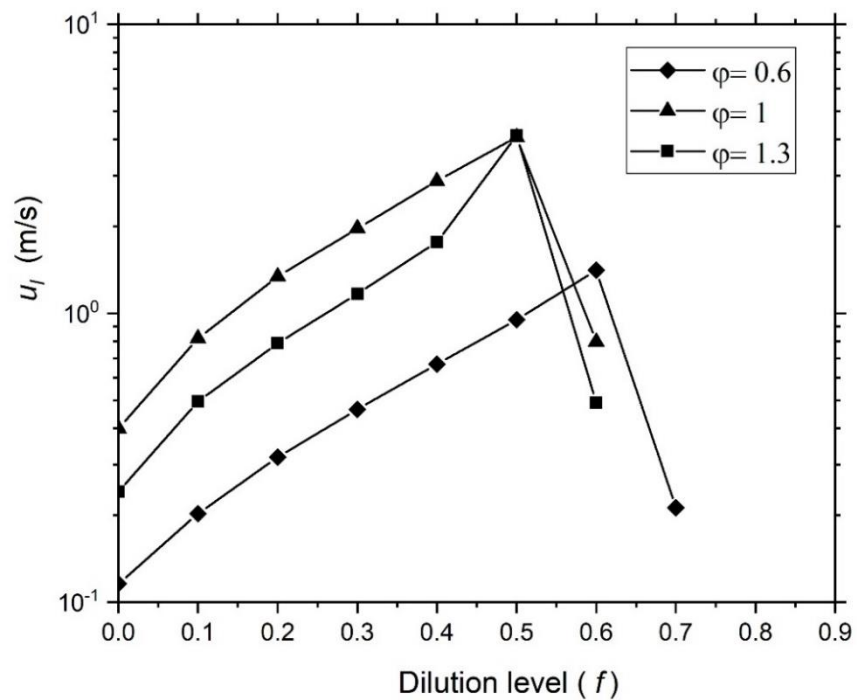


**Figure 5.7** The change in laminar burning velocity, $u_l$, with dilution level at $\varphi$ =0.6,1,1.3 for methane/air mixture extracted from (Sidey et al., 2014).

The second aspect of the study is to employ relevant piloted burner hydrodynamic data from the Michigan Hi-pilot burner (Wabel et al., 2017) for three different operational modes, A, B, and, C. In each of these the same $CH_4$/air mixture is supplied to the main and pilot burners. The three different mass fractions, $f = 0.1$, 0.2, and 0.3, of pilot flame gases, adiabatically burned, are mixed with the burner reactants. The three burner Modes operational details from (Wabel et al., 2017) are given on the left of Table 5.5, and the modelling details on the right.

The burner and pilot entry mixture was $CH_4$/air at $\varphi = 0.75$, atmospheric pressure, and 298 K, for all three operational modes, and $u_l$ was 0.23 m/s (Wabel et al., 2017). Unfortunately, no data for $u_l$ and its own product gases were available in (Sidey et al., 2014) for $\varphi = 0.75$.

**Table 5.5** Effect of different fractions of pilot flame entrainments on $K$ values, for Hi-pilot burner in (Wabel et al., 2017).

| Michigan Hi-pilot burner ($\varphi = 0.75$) (Wabel et al., 2017) | | | | | | $K$ values from Model (Sidey et al., 2014) ($\varphi = 0.8$) | | |
|---|---|---|---|---|---|---|---|---|
| Mode | $u'$ (m/s) | $L$ (mm) | $R_L$ | $u$ (m/s) | Burner $K$ | $f = 0.1$ | $f = 0.2$ | $f = 0.3$ |
| A | 37 | 41 | 99,000 | 78 | 20.9 | 6.6 | 3.3 | 1.8 |
| B | 29 | 12 | 22,300 | 72 | 27.1 | 8.5 | 4.2 | 2.4 |
| C | 38 | 17 | 40,900 | 89 | 33.3 | 10.7 | 5.3 | 3.0 |

The temperatures and laminar burning velocities used in the present study are computed from Sidey et al. (2014) at $\varphi = 0.8$ as shown in Figs 5.8 and 5.9.
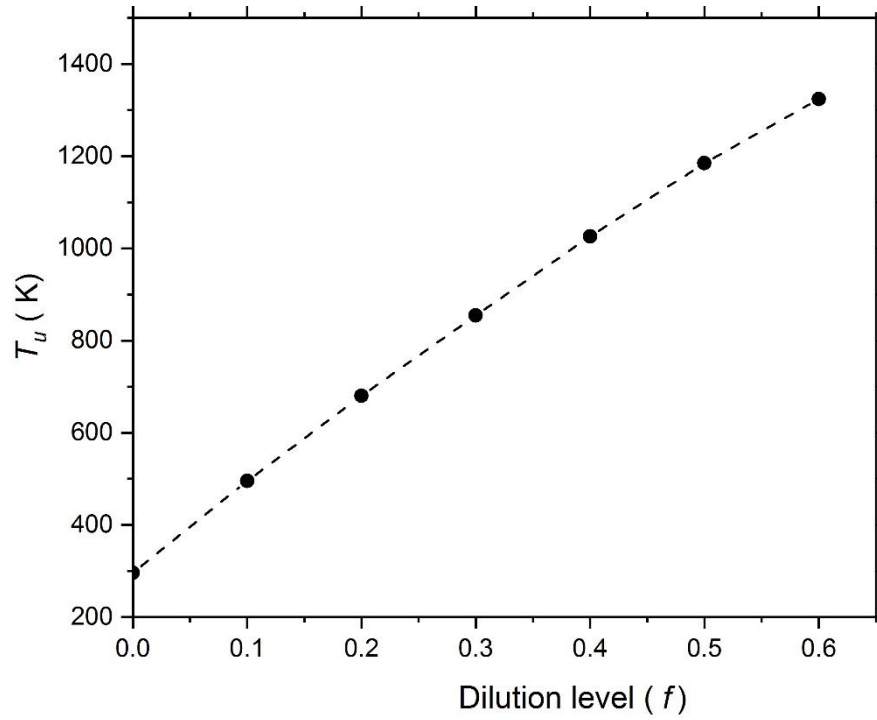
**Figure 5.8** Mixing temperature of lean methane/air mixture ($\varphi$ =0.8) averaged from (Sidey et al., 2014).
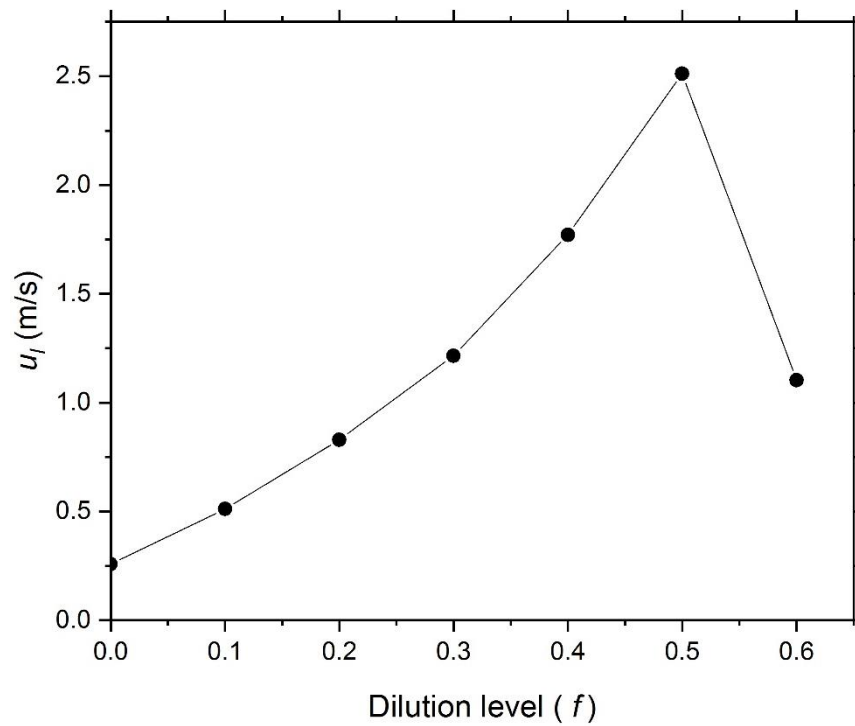


**Figure 5.9** Mixing laminar burning velocity of lean methane/air mixture ($\varphi$ =0.8) averaged from (Sidey et al., 2014).

The resulting temperatures of the mixtures and their burning velocities, from (Sidey et al., 2014), are given in Table 5.6 at $f$ = 0.1, 0.2, and 0.3.

**Table 5.6** Values of $u_l$ from (Sidey et al., 2014) for three mass fractions ,$f$, of burned mixture.

| $f$ | $T_u$ (K) | $u_l$ (m/s) |
|-----|-----------|-------------|
| 0.1 | 496 | 0.51 |
| 0.2 | 681 | 0.83 |
| 0.3 | 854 | 1.22 |

The temperature increases of the original mixtures also increase the mixture laminar burning velocities, to a greater extent than the dilution with burned gas decrease them as seen in Figure 5.8 and 5.9.

From the appropriate values of $u_l$ for the different mixtures, it was possible to derive burner entry values of $K$ from Eq. (1.24), and these are given in Table 5.5. With the possible exception of Case A, a burner with $K$ =20.9, the burner entry $K$ values are high enough to suggest from Fig. 3.26 that the flames would be quenched. However, when allowance is made for pilot flame entrainment, the highest Model entrainment $K$ value is 10.7 for Mode C, at which, with an estimated value of $Ma_{sr}$ of 2 from Fig. 3.26, would be just in the quench regime. The other listed model values suggest the pilot flame would ensure the occurrence of normal flame propagation.

## 5.5  Turbulent Flame Quenching and the Borghi Diagram

The bold curve in Fig. 3.25 shows the new experimental data to have extended the limits of flammability to higher values of both $K$ and $Ma_{sr}$. This is particularly marked above $K$ =1 where, compared with Fig. 1.10, there is a marked reduction in the quench regime, (C). However, the new data extend only to $Ma_{sr}$ = -3, due to the difficulty of quenching those mixtures with more negative values of $Ma_{sr}$, usually associated with the higher pressures and temperatures.

This study is coupled with the generalisation of critical kernel sizes and Fig. 3.24 innovatively couples this premixed flame study with the extinction of jet flames.  It is fruitful to employ the extended Borghi diagram from (Bradley et al., 1998b), to add to Figs. 3.24 and 3.26 as descriptors of flame regimes. Such a diagram is shown in Fig. 5.10, the upper bold DNS curve is from (Poinsot et al., 1991), with the lower limit given by the Klimov-Williams line. As with Fig. 3.24, values of $Ma_{sr}$ do not appear on this figure. In descending order of $u'/u_l$, are the values for $H_2$, $CH_4$, and mixed hydrocarbons. As on Fig. 3.24, these are in ascending order of $Ma_{sr}$. The largest differences between premixed and jet flame data in Fig. 3.24, might be associated with the larger values of $Ma_{sr}$. Interestingly, Fig. 5.10, like Fig. 3.24, also shows that a larger length scale, through the increase in $R_l$, combats flame quenching.

The quenching regime performance of the Hi-pilot burner, when based solely on the Mode C burner flame, unaffected by the pilot flame, $K$ = 33.3, in Table 5.5 is indicated by a solid star C(33.3) in Fig. 5.10. With an $Ma_{sr}$ value of about 2.7 (Gu et al., 2000), this suggests flame quenching. However, based on the modelled composition of the incoming $CH_4$/air burner mixture, as affected by the pilot flame, for $f$ = 0.1, again for Mode C, the value of $K$ would be 10.7. This condition is indicated by an open star C(10.7). If the pilot flame gas entrainment were to be increased to $f$ = 0.3, $K$ in Mode C would be reduced to 3.0 indicated by open star C(3.0) in the figure. Clearly, the entrainment of pilot flame gases reduces the quenching tendencies.
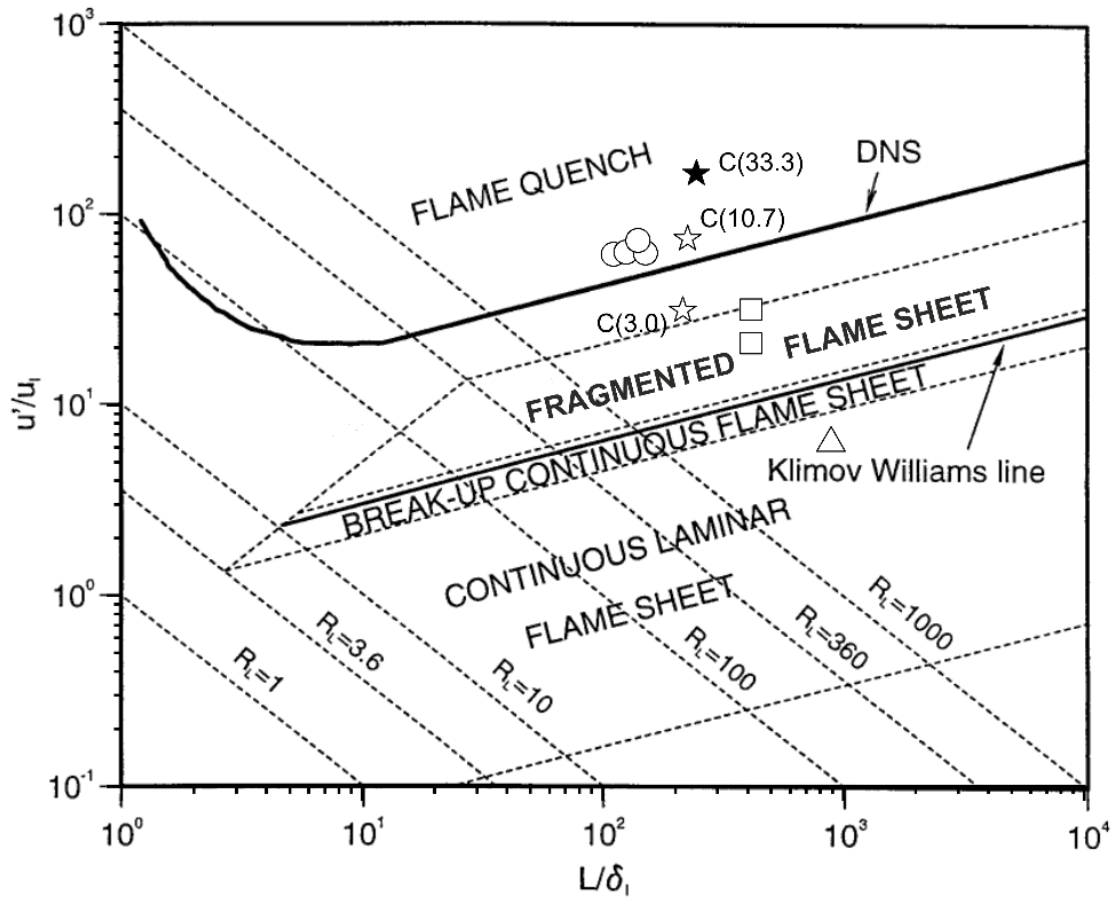
**Figure 5.10** Extended Borghi diagram (Bradley et al., 1998b) showing the
boundary for $p_{0.8}$ flame quenching and the influence of a pilot flame.
($\bigcirc$) for $H_2$, ($\square$) for $CH_4$, ($\triangle$) for hydrocarbons. Pilot flame burner. ($\bigstar$),
indicates Mode C Burner $K = 33.3$ in Table 5.5. ($\star$), indicates Mode C
Model $K = 10.7$ and 3.0.

# Chapter 6 - Conclusions and Recommendations for Future Work

## 6.1 Quenching of Premixed and Jet Flames

High speed schlieren photography, in combination with swinging sheet 3D flame kernel imaging, has revealed the detailed nature of turbulent flame quenching. This has enabled normalised quenched premixed flame kernel mean diameters to be correlated with the Karlovitz stretch factor, $K$, and strain rate Markstein number, $Ma_{sr}$. The scope of the study was extended further to cover, for the first time, the quenching of lifted jet flames. In this case, the quenching was correlated with a parameter $U^*$, related to $K$, demonstrating the commonality of premixed and jet flame quenching. There are, however, differences in detail in that, with premixed combustion, $d_k$ is the mean diameter of a flame fragment, whereas in jet flames, $D_b$ is the minimal jet pipe diameter for sustaining a flame. Generalised quench data, acquired in this way, covered new fuels such as n-butanol, hydrogen, and more conventional fuels. The H$_2$ mixtures are of interest in not being easy to quench, even with high turbulence.

## 6.2 Extension of Quenching Limits

The existing limit on the *U/K* diagram for the onset of premixed turbulent flame quenching has been found to extend by the study to higher values of $K$ and $Ma_{sr}$. The results also show that ever-larger explosions and burners are required to sustain flames at increasing Karlovitz stretch factor and flow number. Conversely, to extend quenching in explosion flames require smaller flame kernels, and, to extend flame trap quenching, require ever-smaller tubes. The low values of $d_k/\delta_k$ for premixed flames, show the flame distance scales to be close to Kolmogorov scales. However, the associated values of the Kolmogorov Karlovitz number, remain closely related to $K$.

## 6.3    Pilot Flame Entrainments

The mechanisms by which premixed flames on a burner are able to survive quenching, when burner mixture values of $K$ suggest quenching would occur, in the presence of a peripheral pilot flame, have been analysed. This demonstrated that the entrainment of pilot flame gas, into the burner mixture, made it more reactive and more resistant to turbulent flame quenching. When allowance was made for the entrainment process, values of $K$ became lower, and in several cases were low enough to explain why extinction did not occur. This has been quantified on both $U/K$ and Borghi diagrams.

## 6.4    Modelling Effective Detonation with Laminar Flames

Difficulties were posed in this computational study because of the large uncertainties, and even non-availability, in the values of $\tau_i$ and $\tau_e$. Values of the last were computed chemical kinetically. There were greater uncertainties concerning values of laminar burning velocities, $u_\ell$, of stoichiometric $H_2/O_2$ mixtures, particularly at high pressures and temperatures. Clearly further experimental and computational studies are necessary to resolve this problem.

A motivation of the study was whether a DDT could be achieved with laminar combustion. Small bore hypodermic tubes proved to be necessary for this.

The flame area increase associated with the laminar propagation in such tubes is greater than that with turbulent flames. Even without detonation, very high gas velocities can be generated. There is significant heat loss from such tubes, which is countered by an increase the tube length before the laminar conditions for DDT occur.

The important conclusion is that, with the present stoichiometric data, only when the initial temperature is raised to 375 K, do purely laminar

developing detonations become possible in hypodermic tube diameters between 0.5 and 1.35 mm.

Turbulence will be generated with larger diameters. Laminar/mild turbulent autoignition might occur in a 2 mm diameter tube with an initial temperature of 300 K. Allowance was made in the computation for the transition to mildly turbulent flow, and a brief indication has been given of the possible practicality of the extended regime. Increasing the initial pressure in turbulent flame propagation, reduces the autoignition delay times and will result in reduction in $A/a$ ratio. When the gas flow ahead of the $H_2/O_2$ accelerating flame causes $Re$ to exceed $Re_c$, the flame image continues to be elongated and appears to be laminar for some time. This may explain why transitions with lower turbulence have been described as laminar.

## 6.5  Proposed Detonation Engine

Although the low pressure DDT gives the closest approach to a laminar burning DDT, it has the practical disadvantage of requiring exhaust to be at sub-atmospheric pressure. A power generation cycle based on this is briefly analysed. It is doubtful whether such a cycle has any advantages over more conventional ones. Detonation, and near-detonation, power units are most likely to be applied in space propulsion.

# Appendix A

This Appendix presents some of the codes and calculations used in the work. Section A.1 and A.2 present the MATLAB codes for evaluating the radii for a globally quenched flame from the time of ignition to the final extinction and the multiple regression method for calculating the strain rate Markstein number for the present work.

Section A.3, A.4, and A.5 present some of the calculations used in the laminar $H_2/O_2$ study, in addition to the simulation results of auto-ignition delay times at different pressures and temperatures employed in the present work.

## A.1　　　Radii for Quenching Images

```matlab
% A code to read in a sequence of images in a folder
and get the radii%.
%this code should be used with black and white
images

% DOI:
clear all
close all
clc

% Import a sequence of images and process:

tifFiles = dir('*.bmp');
numfiles = length(tifFiles);
mydata = cell(1, numfiles);
i=1;
for k = 1:numfiles
  tic
    I = imread(tifFiles(k).name);
    %I = im2single(I);
  % I = I(:,:,1:3);
 % I = rgb2gray(I);
    % BW = im2bw(I);
    BW = I(:,:,1);
    BW = imcomplement(BW);
  %A(i,:) = I(i,:);
  %AB = edge(A, 'log');
  %AC = imfill(AB, 'holes');
total = bwarea(BW);
area(i,:)=total
act_area(i,:)=area(i,:)*0.1961*0.1961;
radii(i,:)= sqrt(act_area(i,:)/3.14159);
i = i+1;
plot(radii,'--b'),xlabel('images'),
ylabel('radius(mm)');
 toc

end
```

## A.2      Calculations of Markstein Number for Strain Rate Using the Multiple Regression Method

```matlab
% A code, authored by P. Shaik. This code calculates
Markstein lengths and Markstein numbers using
multiple regression method% (Bradley et al., 2018)

close all;
clear all;
clc;

fileID = fopen('C:\Users\Moustafa\Desktop\markstein
number\masr-890-4.txt','r');
formatSpec = '%f %f';
sizeSnr = [2 Inf];
Snr = fscanf(fileID,formatSpec,sizeSnr);
Snr = Snr';
Sn = Snr(:,1);
%Sn = Sn.*1000;
ru = Snr(:,2);
alpha = (2.*Sn)./ru;
alpha_m = mean(alpha);
Sn_m = mean(Sn);
a = alpha-alpha_m;
b = Sn-Sn_m;
ab=a.*b;
sumab = sum(ab);
sumaa = sum(a.*a);
Lb = -1.*(sumab./sumaa);
%fprintf('\nThe value of Lb is %f\n\n', Lb);
Dl = input('\nEnter the value of laminar flame
thickness, Dl = ');
Mab = Lb./Dl;
fprintf('\nThe value of burned gas Markstein number,
Mab is %f\n\n', Mab);
D_r = input('\nEnter the value of density ratio
rho_u/rho_b, D_r = ');
S = 1+1.2.*((Dl./ru)*(D_r.^2.2))-
0.15.*(((Dl./ru)*(D_r.^2.2)).^2);
Un = (Sn.*S)./D_r;
Un_m = mean(Un);
alpha_c = (2.*Un)./ru;
alpha_c_m = mean(alpha_c);
alpha_s = alpha-alpha_c;
```

```matlab
alpha_s_m = mean(alpha_s);

A11 = sum((alpha_s-alpha_s_m).^2);
A22 = sum((alpha_c-alpha_c_m).^2);
A12 = sum((alpha_s-alpha_s_m).*(alpha_c-alpha_c_m));
A10 = sum((alpha_s-alpha_s_m).*(Un-Un_m));
A20 = sum((alpha_c-alpha_c_m).*(Un-Un_m));

fprintf('\nThe value of Lb is %f\n\n', Lb);
%fprintf('\nThe value of burned gas Markstein
number, Mab is %f\n\n', Mab);

Ls = -1.*(((A10.*A22)-(A20.*A12))/((A11.*A22)-
(A12.*A12)));
Lc = -1.*(((A20.*A11)-(A10.*A12))/((A11.*A22)-
(A12.*A12)));

fprintf('\nThe value of Ls is %f\n\n', Ls);
fprintf('\nThe value of Lc is %f\n\n', Lc);
Lsr = (1/(D_r-1)).*(Lb-Ls);
fprintf('\nThe value of Lsr is %f\n\n', Lsr);
Masr = Lsr./Dl;
fprintf('\nThe value of strain rate Markstein
number, Masr is %f\n\n', Masr);
```

### A.3 Calculations of Heat Loss in Micro Tubes of $H_2/O_2$ Mixture.

$m = u\_1*rho\_1*dt*(PI/4)*D^2$     [kg]     "The mass at dt [s]"

"Heat balance at the shock wave"

$L*rho\_2* (PI/4)*D^2 = u\_1*rho\_1*dt*(PI/4)*D^2$

$u\_1 = M\_1*a\_1$                 "mixture velocity at condition (1)"

$G = h*(T\_2-375)*PI*D*L$         "heat loss to the walls"

$N\_u = h*D/K$                   "Nusselt number"

$G1 = (m/dt)*h\_2$           "heat transfer due to the shock"

$DeltaG = G1 - G$

"Temperature drop"

$DeltaT = DeltaG*dt/(c\_p*m)$

End

"============================================="

"Main Program "
"+++++++++++"

P_1 = 0.01 [MPa]
T_1 = 375 [K]
P_2 = 0.1 [MPa]
T_2 = 997 [K]
rho_1 = 0.039 [kg/m3]
rho_2 = 0.1449 [kg/m3]
a_1 = 601.6 [m/s]          "acoustic velocity at condition (1)"
M_1 = 2.98               "Mach number at condition (1)"
h_2 = 1769.81*10^3 [J/kg]

```
L_cm= L*100

$ifnot a parametric table
dt= 0.0001 [s]
$endif
c_p= 2545 [J/kg.K]                 "Heat capacity at average
temperature 0.5(T1+T2)"

K=0.163 [W/m.K]                    "Thermal conductivity at average
temperature"
"============================================"
D= 0.0005 [m]                      "diameter of the tube"


"============================================"
```

## A.4       One Dimensional Shockwave Theory

"Shockwave equations"

"gas velocity along the duct"

$Sg\_g= (2*(M1^2-1)*a1)/((Gamma+1)*M1)$

"Mach number of the shockwave"

$M1= (c/2)+(1+c^2/4)^0.5$

$c= (sg/a1)*(gamma+1)/2$
$c= A\_a*ul*(sigma-1)*((gamma+1)/ (2*a1))$

"Pressure and temperature ratios"

$P2/P1= ((2*gamma*M1^2)/(gamma+1))-((gamma-1)/(gamma+1))$
"Pressure ratio across the shockwave"

$T2/T1= (((2*gamma*M1^2)-(gamma-1))/(gamma+1))*((2+(gamma-1)*M1^2)/((gamma+1)*M1^2))$          "Temperature ratio across the shockwave"

$ifnot a parametric table
$sf= A\_a*ul*sigma
$endif

$sg\_1=A\_a*ul*(sigma-1)$

End

## A.5 Ignition delay times using Varga mechanism (Varga et al., 2015) at different pressures and temperatures.

P= 0.04 MPa

| End time | max step time | T (K) | time (s) | $\tau_i(ms)$ |
|---|---|---|---|---|
| 0.1 sec | 0.005 msec | 840 | 0.070515 | 70.515 |
| 0.05 sec | 0.005 msec | 860 | 0.00567 | 5.67 |
| 0.05 sec | 0.005 msec | 880 | 0.00147 | 1.47 |
| 0.05 sec | 0.005 msec | 900 | 6.38E-04 | 0.638 |
| 0.05 sec | 0.005 msec | 920 | 4.37E-04 | 0.437 |
| 0.05 sec | 0.005 msec | 940 | 3.27E-04 | 0.327 |
| 0.05 sec | 0.005 msec | 960 | 2.57E-04 | 0.257 |
| 0.05 sec | 0.005 msec | 980 | 2.09E-04 | 0.209 |
| 0.05 sec | 0.005 msec | 1000 | 1.70E-04 | 0.17 |
| 0.05 sec | 0.005 msec | 1050 | 1.17E-04 | 0.117 |
| 0.05 sec | 0.005 msec | 1100 | 8.40E-05 | 0.084 |

P= 0.06 MPa

| End time | max step time | T (K) | time (s) | $\tau_i(ms)$ |
|---|---|---|---|---|
| 0.1 sec | 0.005 msec | 860 | 0.096121 | 96.121 |
| 0.1 sec | 0.005 msec | 880 | 0.012352 | 12.352 |
| 0.05 sec | 0.005 msec | 900 | 0.001185 | 1.185 |
| 0.05 sec | 0.005 msec | 920 | 4.61E-04 | 0.461 |
| 0.05 sec | 0.005 msec | 940 | 2.87E-04 | 0.287 |
| 0.05 sec | 0.005 msec | 960 | 2.06E-04 | 0.206 |
| 0.05 sec | 0.005 msec | 980 | 1.59E-04 | 0.159 |
| 0.05 sec | 0.005 msec | 1000 | 1.27E-04 | 0.127 |
| 0.05 sec | 0.005 msec | 1050 | 8.15E-05 | 0.0815 |
| 0.05 sec | 0.005 msec | 1100 | 5.71E-05 | 0.0571 |

P= 0.08 MPa

| End time | max step time | T (K) | time (s) | $\tau_i(ms)$ |
|---|---|---|---|---|
| 0.1 sec | 0.005 msec | 880 | 0.057157 | 57.157 |
| 0.05 sec | 0.005 msec | 900 | 0.009387 | 9.387 |
| 0.05 sec | 0.005 msec | 920 | 0.001086 | 1.086 |
| 0.05 sec | 0.005 msec | 940 | 3.35E-04 | 0.335 |
| 0.05 sec | 0.005 msec | 960 | 1.99E-04 | 0.199 |
| 0.05 sec | 0.005 msec | 980 | 1.40E-04 | 0.14 |
| 0.05 sec | 0.005 msec | 1000 | 1.07E-04 | 0.107 |
| 0.05 sec | 0.005 msec | 1050 | 6.47E-05 | 0.0647 |
| 0.05 sec | 0.005 msec | 1100 | 4.41E-05 | 0.0441 |

P= 1 MPa

| End time | max step time | T (K) | time (s) | $\tau_i(ms)$ |
|---|---|---|---|---|
| 0.05 sec | 0.005 msec | 950 | 0.008649 | 8.648823 |
| 0.05 sec | 0.005 msec | 970 | 0.005394 | 5.393899 |
| 0.005 sec | 0.005 msec | 980 | 0.004278 | 4.277823 |
| 0.005 sec | 0.005 msec | 1000 | 0.002708 | 2.708498 |
| 0.005 sec | 0.005 msec | 1020 | 0.001725 | 1.725077 |
| 0.005 sec | 0.005 msec | 1040 | 0.001101 | 1.100789 |
| 0.005 sec | 0.005 msec | 1060 | 7.00E-04 | 0.700385 |
| 0.005 sec | 0.005 msec | 1070 | 5.57E-04 | 0.557003 |
| 0.005 sec | 0.005 msec | 1080 | 4.42E-04 | 0.441527 |

# References

Abdel-Gayed, R., Al-Khishali, K., & Bradley, D. (1984). Turbulent burning velocities and flame straining in explosions. *Proc. R. Soc. Lond. A, 391*(1801), 393-414.

Abdel-Gayed, R., & Bradley, D. (1985). Criteria for turbulent propagation limits of premixed flames. *Combust. Flame, 62*(1), 61-68.

Abdel-Gayed, R., Bradley, D., Hamid, M. N., & Lawes, M. (1985). Lewis number effects on turbulent burning velocity. *Symp. (Int.) Combust., 20*(1), 505-512. doi:http://dx.doi.org/10.1016/S0082-0784(85)80539-7

Abdel-Gayed, R., Bradley, D., & Lawes, M. (1987). Turbulent burning velocities: a general correlation in terms of straining rates. *Proc. R. Soc. Lond. A, 414*(1847), 389-413.

Abdel-Gayed, R., Bradley, D., & Lung, F.-K. (1989). Combustion regimes and the straining of turbulent premixed flames. *Combust. Flame, 76*(2), 213-218.

Abdel-Gayed, R. G., & Bradley, D. (1981). A two-eddy theory of premixed turbulent flame propagation. *Phil. Trans. R. Soc. Lond. A, 301*(1457), 1-25.

Abdel-Gayed, R. G., Bradley, D., Lawes, M., & Lung, F. K. K. (1988). Premixed turbulent burning during explosions. *Symp. (Int.) Combust., 21*(1), 497-504. doi:https://doi.org/10.1016/S0082-0784(88)80278-9

Al-Khishali, K., Bradley, D., & Hall, S. (1983). Turbulent combustion of near-limit hydrogen-air mixtures. *Combust. Flame, 54*(1-3), 61-70.

Alabbadi, S. A. (2012). Hydrogen oxygen steam generator integrating with renewable energy resource for electricity generation. *J Energy Procedia, 29*, 12-20.

Aung, K., Hassan, M., & Faeth, G. (1998). Effects of pressure and nitrogen dilution on flame/stretch interactions of laminar premixed $H_2/O_2/N_2$ flames. *Combust. Flame, 112*(1-2), 1-15.

Bagdanavicius, A., Bowen, P. J., Bradley, D., Lawes, M., & Mansour, M. S. (2015). Stretch rate effects and flame surface densities in premixed turbulent combustion up to 1.25 MPa. *Combust. Flame, 162*(11), 4158-4166.

Barrere, M. (1974). Some aspects of the combustion of solid propellants in permanent and transitory regimes. *Combustion of solid propellants.(A 75-15351 04-28) Paris, Institut Francais des Combustibles et de l'Energie, 1974*, 81-92.

Bartholomé, E. (1949). Zur Methodik der Messung von Flammengeschwindigkeiten. *Berichte der Bunsengesellschaft für physikalische Chemie, 53*(4), 191-196.

Bates, L., Bradley, D., & Flame. (2017a). Deflagrative, auto-ignitive, and detonative propagation regimes in engines. *Combust. Flame, 175*, 118-122.

Bates, L., Bradley, D., Gorbatenko, I., & Tomlin, A. S. (2017b). Computation of methane/air ignition delay and excitation times, using comprehensive and reduced chemical mechanisms and their relevance in engine autoignition. *Combust. Flame, 185*, 105-116.

Bates, L., Bradley, D., Paczko, G., & Peters, N. (2016). Engine hot spots: Modes of auto-ignition and reaction propagation. *Combust. Flame, 166*, 80-85.

Bédat, B., & Cheng, R. K. (1995). Experimental study of premixed flames in intense isotropic turbulence. *Combust. Flame, 100*(3), 485-494. doi:https://doi.org/10.1016/0010-2180(94)00138-I

References

Boivin, P., Jiménez, C., Sánchez, A. L., & Williams, F. A. (2011). An explicit reduced mechanism for $H_2$–air combustion. *Proc. Combust. Inst., 33*(1), 517-523.

Bokhon, Y. A., Gal'burt, V., & Gostintsev, Y. (1998). Explosion initiation in a gaseous mixture behind shock wave, Report No. 2-416, Inst. High Temp. Phys. , Moscow.

Borghi, R. (1985). On the structure and morphology of turbulent premixed flames. In *Recent advances in the Aerospace Sciences* (pp. 117-138): Springer.

Bradley, D. (2008). Fundamentals of lean combustion. In *Lean Combustion* (pp. 19-II): Elsevier.

Bradley, D. (2012). Autoignitions and detonations in engines and ducts. *Phil. Trans. R. Soc. A, 370*(1960), 689-714.

Bradley, D., Gaskell, P., & Gu, X. (1996). Burning velocities, Markstein lengths, and flame quenching for spherical methane-air flames: a computational study. *Combust. Flame, 104*(1-2), 176-198.

Bradley, D., Gaskell, P., & Gu, X. (1998a). The mathematical modeling of liftoff and blowoff of turbulent non-premixed methane jet flames at high strain rates. *Symp. (Int.) Combust., 27*(1), 1199-1206.

Bradley, D., Gaskell, P., Gu, X., Lawes, M., & Scott, M. (1998b). Premixed turbulent flame instability and NO formation in a lean-burn swirl burner. *Combust. Flame, 115*(4), 515-538.

Bradley, D., Gaskell, P., Gu, X., & Sedaghat, A. (2005). Premixed flamelet modelling: Factors influencing the turbulent heat release rate source term and the turbulent burning velocity. *Combust. Flame, 143*(3), 227-245.

Bradley, D., Gaskell, P., Sedaghat, A., & Gu, X. (2003a). Generation of PDFS for flame curvature and for flame stretch rate in premixed turbulent combustion. *Combust. Flame, 135*(4), 503-523.

Bradley, D., Haq, M., Hicks, R., Kitagawa, T., Lawes, M., Sheppard, C., & Woolley, R. (2003b). Turbulent burning velocity, burned gas distribution, and associated flame surface definition. *Combust. Flame, 133*(4), 415-430.

Bradley, D., Hicks, R., Lawes, M., Sheppard, C., & Woolley, R. (1998c). The measurement of laminar burning velocities and Markstein numbers for iso-octane–air and iso-octane–n-heptane–air mixtures at elevated temperatures and pressures in an explosion bomb. *Combust. Flame, 115*(1-2), 126-144.

Bradley, D., & Kalghatgi, G. T. (2009). Influence of autoignition delay time characteristics of different fuels on pressure waves and knock in reciprocating engines. *Combust. Flame, 156*(12), 2307-2318. doi:http://dx.doi.org/10.1016/j.combustflame.2009.08.003

Bradley, D., Lau, A., & Lawes, M. (1992). Flame stretch rate as a determinant of turbulent burning velocity. *Phil. Trans. R. Soc. Lond. A, 338*(1650), 359-387.

Bradley, D., Lawes, M., & Liu, K. (2008). Turbulent flame speeds in ducts and the deflagration/detonation transition. *Combust. Flame, 154*(1), 96-108.

Bradley, D., Lawes, M., Liu, K., & Mansour, M. S. (2013). Measurements and correlations of turbulent burning velocities over wide ranges of fuels and elevated pressures. *Proc. Combust. Inst., 34*(1), 1519-1526.

Bradley, D., Lawes, M., Liu, K., Verhelst, S., & Woolley, R. (2007a). Laminar burning velocities of lean hydrogen–air mixtures at pressures up to 1.0 MPa. *Combustion and Flame, 149*(1), 162-172.

Bradley, D., Lawes, M., Liu, K., & Woolley, R. (2007b). The quenching of premixed turbulent flames of iso-octane, methane and hydrogen at high pressures. *Proc. Combust. Inst., 31*(1), 1393-1400.

Bradley, D., Lawes, M., & Mansour, M. (2009a). Explosion bomb measurements of ethanol–air laminar gaseous flame characteristics at pressures up to 1.4 MPa. *Combust. Flame, 156*(7), 1462-1470.

Bradley, D., Lawes, M., & Mansour, M. (2012). Turbulent deflagrations, autoignitions, and detonations. *Combust Explos Shock Waves, 48*(5), 526-535. doi:10.1134/s0010508212050048

Bradley, D., Lawes, M., & Mansour, M. S. (2009b). Flame surface densities during spherical turbulent flame explosions. *Proc. Combust. Inst., 32*(1), 1587-1593. doi:https://doi.org/10.1016/j.proci.2008.06.020

Bradley, D., Lawes, M., & Mansour, M. S. (2011). Correlation of turbulent burning velocities of ethanol–air, measured in a fan-stirred bomb up to 1.2MPa. *Combust. Flame, 158*(1), 123-138. doi:https://doi.org/10.1016/j.combustflame.2010.08.001

Bradley, D., Lawes, M., Mumby, R., & Ahmed, P. (2018). The stability of laminar explosion flames. *Proc. Combust. Inst.*

Bradley, D., & Shehata, M. (2018). Acceleration of laminar hydrogen/oxygen flames in a tube and the possible onset of detonation. *Int. J. Hydrogen Energy, 43*(13), 6734-6744.

Bradley, D., Shehata, M., Lawes, M., & Ahmed, P. (2019). Flame Extinctions: Critical Stretch Rates and Sizes. *submitted to journal of Combustion and Flame*.

Bray, K. (1980). Topics in Applied Physics, PA Libby and FA Williams ed. In: Springer Verlag.

Bray, K. (1990). Studies of the turbulent burning velocity. *Proc. R. Soc. Lond. A, 431*(1882), 315-335.

Bray, K. (1996). The challenge of turbulent combustion. *Symp. (Int.) Combust., 26*(1), 1-26.

# References

Bychkov, V., Akkerman, V. y., Fru, G., Petchenko, A., & Eriksson, L.-E. (2007). Flame acceleration in the early stages of burning in tubes. *Combust. Flame, 150*(4), 263-276.

Cai, W., de la Piscina, P. R., & Homs, N. (2012). Hydrogen production from the steam reforming of bio-butanol over novel supported Co-based bimetallic catalysts. *Bioresource technology, 107*, 482-486.

Candel, S. M., & Poinsot, T. J. (1990). Flame stretch and the balance equation for the flame area. *Combust. Sci. Technol., 70*(1-3), 1-15.

Chapman, W. R., & Wheeler, R. V. (1926). The propagation of flame in mixtures of methane and air. Part IV. The effect of restrictions in the path of the flame. *J. Chem. Soc., 129*, 2139-2147.

Chomiak, J., & Jarosiński, J. (1982). Flame quenching by turbulence. *Combust. Flame, 48*, 241-249.

Ciccarelli, G., & Dorofeev, S. (2008). Flame acceleration and transition to detonation in ducts. *Prog. Energy Combust. Sci., 34*(4), 499-550. doi:https://doi.org/10.1016/j.pecs.2007.11.002

Ciccarelli, G., Fowler, C., & Bardon, M. (2005). Effect of obstacle size and spacing on the initial stage of flame acceleration in a rough tube. *ShockWaves, 14*(3), 161-166.

Ciezki, H. K., & Adomeit, G. (1993). Shock-tube investigation of self-ignition of n-heptane-air mixtures under engine relevant conditions. *Combust. Flame, 93*(4), 421-433. doi:https://doi.org/10.1016/0010-2180(93)90142-P

Clavin, P. (1985). Dynamic behavior of premixed flame fronts in laminar and turbulent flows. *Prog. Energy Combust. Sci., 11*(1), 1-59.

Dakshina Murty, V. (2018). *Turbomachinery*: Boca Raton: CRC Press, https://doi.org/10.1201/b22106.

Damköhler, G. (1940). The effect of turbulence on the combustion rate in gas compounds. *Z. Elektrochem. Angew. Phys. Chem, 46*, 601-626.

de Groot, W., Arrington, L., McElroy, J., Mitlitsky, F., Weisberg, A., Carter, I., Preston, Myers, B., Reed, B., de Groot, W., & Arrington, L. (1997). *Electrolysis propulsion for spacecraft applications.* Paper presented at the 33rd Joint Propulsion Conference and Exhibit.

Design Reaction, CHEMKIN  (2013). *Reaction Des.*

Dixon-Lewis, G. (1988). Structure and extinction limits of some strained premixed flames. *Dynamics of reactive systems. Part I. Flames Kuhl AL, Bowen JR, Leyer J.-C, Borisov A Prog. Astronaut. Aeronaut, 113*, 166-183.

Donbar, J. M., Driscoll, J. F., & Carter, C. D. (2001). Strain rates measured along the wrinkled flame contour within turbulent non-premixed jet flames. *Combust. Flame, 125*(4), 1239-1257.

Dong, Y., Holley, A. T., Andac, M. G., Egolfopoulos, F. N., Davis, S. G., Middha, P., & Wang, H. (2005). Extinction of premixed $H_2$/air flames: chemical kinetics and molecular diffusion effects. *Combust. Flame, 142*(4), 374-387.

Dorofeev, S., Sidorov, V., Dvoinishnikov, A., & Breitung, W. (1996). Deflagration to detonation transition in large confined volume of lean hydrogen-air mixtures. *Combust. Flame, 104*(1-2), 95-110.

Driscoll, J. F. (2008). Turbulent premixed combustion: Flamelet structure and its effect on turbulent burning velocities. *Prog. Energy Combust. Sci., 34*(1), 91-134. doi:https://doi.org/10.1016/j.pecs.2007.04.002

Driscoll, J. F., Skiba, A. W., Wabel, T. M., & Carter, A. (2017). Turbulent Flames at High Reyolds Number, 1st near limit flames Workshop  (NSF Project CBET-1703543, AFOSR Project FA9550-16-1-0028).

Dziemińska, E., & Hayashi, A. K. (2013). Auto-ignition and DDT driven by shock wave – Boundary layer interaction in oxyhydrogen mixture. *Int. J. Hydrogen Energy, 38*(10), 4185-4193. doi:https://doi.org/10.1016/j.ijhydene.2013.01.111

Edse, R., & Lawrence, L. (1969). Detonation induction phenomena and flame propagation rates in low temperature hydrogen-oxygen mixtures. *Combust. Flame, 13*(5), 479-486.

Edwards, A. L. (1984). *An introduction to linear regression and correlation*: (No. 04; QA278. 2, E3 1984.).

Egolfopoulos, F. (1994). Geometric and radiation effects on steady and unsteady strained laminar flames. *Symp. (Int.) Combust., 25*(1), 1375-1381.

Egolfopoulos, F., & Law, C. (1991). An experimental and computational study of the burning rates of ultra-lean to moderately-rich $H_2/O_2/N_2$ laminar flames with pressure variations. *Symp. (Int.) Combust., 23*(1), 333-340.

Egolfopoulos, F. N., & Campbell, C. S. (1996). Unsteady counterflowing strained diffusion flames: diffusion-limited frequency response. *J. Fluid Mech., 318*, 1-29.

Fukuda, M., Dzieminska, E., Hayashi, A. K., Yamada, E., & Tsuboi, N. (2013). Effect of wall conditions on DDT in hydrogen-oxygen mixtures. *Shock Waves, 23*(3), 191-200.

Gal'burt, V., Ivanov, M., & Petukhov, V. (2007). Mathematical modeling of different combustion regimes. *Chem Phys, 26*, 46-59.

Gamezo, V. N., & Oran, E. S. (2006). Flame acceleration in narrow channels: applications for micropropulsion in low-gravity environments. *AIAA J., 44*(2), 329.

Gardiner, W., & Wakefield, C. (1969). Influence of gasdynamic processes on the chemical kinetics of the hydrogen-oxygen explosion at temperatures near 1000 K and pressures of several atmospheres(Gas dynamic processes effects on hydrogen-oxygen explosion chemical kinetics, calculating ignition delays under steady conditions behind plane reflected shock waves). *Acta Astronaut., 15*, 399-409.

# References

Gavrikov, A., Bezmelnitsyn, A., Leliakin, A., & Dorofeev, S. (2001). Extraction of basic flame properties from laminar flame speed calculations. *Proceedings of the 18th International Colloquium on the Dynamics of Explosions and Reactive Systems (ICDERS),* , paper 114.

Gelfand, B. E., Silnikov, M. V., Medvedev, S. P., & Khomik, S. V. (2012). Laminar and Cellular Combustion of Hydrogenous Gaseous Mixtures. In *Thermo-Gas Dynamics of Hydrogen Combustion and Explosion* (pp. 15-51): Springer.

Gibbs, G., & Calcote, H. (1959). Effect of molecular structure on burning velocity. *J. Chem. Eng. Data, 4*(3), 226-237.

Gillespie, L., Lawes, M., Sheppard, C., & Woolley, R. (2000). Aspects of laminar and turbulent burning velocity relevant to SI engines. *SAE transactions*.

Goodwin, D. (2005). Cantera: Object-oriented software for reacting flows. *California Institute for Technology (Caltech). Available: (accessed October, 2016)* http://www.cantera.org .

Göttgens, J., Mauss, F., & Peters, N. (1992). Analytic approximations of burning velocities and flame thicknesses of lean hydrogen, methane, ethylene, ethane, acetylene, and propane flames. *Symp. (Int.) Combust., 24*(1), 129-135. doi:https://doi.org/10.1016/S0082-0784(06)80020-2

Griffiths, J., Halford-Maw, P., & Rose, D. (1993). Fundamental features of hydrocarbon autoignition in a rapid compression machine. *Combust. Flame, 95*(3), 291-306.

Griffiths, J. F., & Barnard, J. A. (1995). *Flame and combustion*: CRC Press.

Gu, X., Emerson, D., & Bradley, D. (2003). Modes of reaction front propagation from hot spots. *Combust. Flame, 133*(1), 63-74.

Gu, X. J., Haq, M. Z., Lawes, M., & Woolley, R. (2000). Laminar burning velocity and Markstein lengths of methane–air mixtures. *Combust. Flame, 121*(1-2), 41-58.

Gülder, Ö. L. (1991). Turbulent premixed flame propagation models for different combustion regimes. *Symp. (Int.) Combust., 23*(1), 743-750.

Han, W., Gao, Y., & Law, C. K. (2017). Flame acceleration and deflagration-to-detonation transition in micro-and macro-channels: An integrated mechanistic study. *Combust. Flame, 176*, 285-298.

Harker, M., Hattrell, T., Lawes, M., Sheppard, C., Tripathi, N., & Woolley, R. (2012). Measurements of the three-dimensional structure of flames at low turbulence. *Combust. Sci. Technol., 184*(10-11), 1818-1837.

Holley, A., Dong, Y., Andac, M., & Egolfopoulos, F. (2006). Extinction of premixed flames of practical liquid fuels: Experiments and simulations. *Combust. Flame, 144*(3), 448-460.

Holley, A., Dong, Y., Andac, M., Egolfopoulos, F., & Edwards, T. (2007). Ignition and extinction of non-premixed flames of single-component liquid hydrocarbons, jet fuels, and their surrogates. *Proc. Combust. Inst., 31*(1), 1205-1213.

Hui, X., Das, A. K., Kumar, K., Sung, C.-J., Dooley, S., & Dryer, F. L. (2012). Laminar flame speeds and extinction stretch rates of selected aromatic hydrocarbons. *Fuel, 97*, 695-702.

Ingram, G. (2009). *Basic concepts in turbomachinery*: Bookboon.

Ivanov, M., Kiverin, A., & Liberman, M. (2011a). Hydrogen-oxygen flame acceleration and transition to detonation in channels with no-slip walls for a detailed chemical reaction model. *Phys. Rev. E, 83*(5), 1-16.

Ivanov, M., Kiverin, A., & Liberman, M. A. (2011b). Flame acceleration and DDT of hydrogen-oxygen gaseous mixtures in channels with no-slip walls. *Int. J. Hydrogen Energy, 36*(13), 7714-7727.

Ivanov, M., Kiverin, A., Yakovenko, I., & Liberman, M. A. (2013). Hydrogen-oxygen flame acceleration and deflagration-to-detonation transition in three-dimensional rectangular channels with no-slip walls. *Int. J. Hydrogen Energy, 38*(36), 16427-16440.

Jericha, H., Hacker, V., Sanz, W., & Zotter, G. (2010). *Thermal steam power plant fired by hydrogen and oxygen in stoichiometric ratio, using fuel cells and gas turbine cycle components.* Paper presented at the ASME Turbo Expo 2010: Power for Land, Sea, and Air.

Ji, C., Dames, E., Wang, Y. L., Wang, H., & Egolfopoulos, F. N. (2010). Propagation and extinction of premixed $C_5$–$C_{12}$ n-alkane flames. *Combust. Flame, 157*(2), 277-287.

Karlovitz, B., Denniston Jr, D., Knapschaefer, D., & Wells, F. (1953). Studies on Turbulent flames: A. Flame Propagation Across velocity gradients B. turbulence Measurement in flames. *Symp. (Int.) Combust., 4*(1), 613-620.

Kee, R. J., Miller, J. A., Evans, G. H., & Dixon-Lewis, G. (1989). A computational model of the structure and extinction of strained, opposed flow, premixed methane-air flames. *Symp. (Int.) Combust., 22*(1), 1479-1494. doi:https://doi.org/10.1016/S0082-0784(89)80158-4

Kerampran, S., Desbordes, D., Veyssière, B., & Bauwens, L. (2001). Flame propagation in a tube from closed to open end. *39th Aerospace Sciences Meeting and Exhibit*, , paper 1082.

Kéromnès, A., Metcalfe, W. K., Heufer, K. A., Donohoe, N., Das, A. K., Sung, C.-J., Herzler, J., Naumann, C., Griebel, P., & Mathieu, O. (2013). An experimental and detailed chemical kinetic modeling study of hydrogen and syngas mixture oxidation at elevated pressures. *Combust. Flame, 160*(6), 995-1011.

Kessler, D., Gamezo, V., & Oran, E. (2010). Simulations of flame acceleration and deflagration-to-detonation transitions in methane-air systems. *Combust. Flame, 157*(11), 2063-2077.

Khokhlov, A., Oran, E., & Thomas, G. (1999). Numerical simulation of deflagration-to-detonation transition: the role of shock–flame interactions in turbulent flames. *Combust. Flame, 117*(1-2), 323-339.

Kiverin, A. D., Kassoy, D. R., Ivanov, M. F., & Liberman, M. A. (2013). Mechanisms of ignition by transient energy deposition: Regimes of combustion wave propagation. *Phys. Rev. E, 87*(3), 1-10.

Kobayashi, H., Seyama, K., Hagiwara, H., & Ogami, Y. (2005). Burning velocity correlation of methane/air turbulent premixed flames at high pressure and high temperature. *Proc. Combust. Inst., 30*(1), 827-834.

Kolmogorov, A. (1991). The local structure of turbulence in incompressible viscous fluid for very large Reynolds numbers. *Proc. R. Soc. Lond. A, 434*(1890), 9-13.

Kolmogorov, A. N. (1941). The local structure of turbulence in incompressible viscous fluid for very large Reynolds numbers. *Cr Acad. Sci. URSS, 30*(4), 299-303.

Koroll, G., Kumar, R., & Bowles, E. (1993). Burning velocities of hydrogen-air mixtures. *Combust. Flame, 94*(3), 330-340.

Koroll, G., & Mulpuru, S. (1988). The effect of dilution with steam on the burning velocity and structure of premixed hydrogen flames. *Symp. (Int.) Combust., 21*(1), 1811-1819.

Kumar, K., & Sung, C.-J. (2007). Laminar flame speeds and extinction limits of preheated n-decane/$O_2$/$N_2$ and n-dodecane/$O_2$/$N_2$ mixtures. *Combust. Flame, 151*(1-2), 209-224.

Kusharin, A. Y., Popov, O., & Agafonov, G. (1995). Normal flame velocities in mixtures of oxyhydrogen gas with water steam. *Himicheskaya Fizika, 14*(4), 179-189.

Kuznetsov, M., Alekseev, V., Bezmelnitsyn, A., Breitung, W., Dorofeev, S., Matsukov, I., & Yankin, Y. (1999). Effect of obstacle geometry on

behaviour of turbulent flames. *Report FZKA-6328, Karlsruhe, Forschungszentrum Karlsruhe GmBH, Karlsruhe*.

Kuznetsov, M., Alekseev, V., Matsukov, I., & Dorofeev, S. (2005a). DDT in a smooth tube filled with a hydrogen–oxygen mixture. *Shock Waves, 14*(3), 205-215. doi:10.1007/s00193-005-0265-6

Kuznetsov, M., Alekseev, V., Matsukov, I., & Dorofeev, S. (2005b). DDT in a smooth tube filled with a hydrogen–oxygen mixture. *Shock Waves, 14*(3), 205-215.

Kuznetsov, M., Ciccarelli, G., Dorofeev, S., Alekseev, V., Yankin, Y., & Kim, T. (2002). DDT in methane-air mixtures. *Shock Waves, 12*(3), 215-220.

Kuznetsov, M., Liberman, M., & Matsukov, I. (2010). Experimental study of the preheat zone formation and deflagration to detonation transition. *Combust. Sci. Technol., 182*(11-12), 1628-1644.

Kuznetsov, M., Redlinger, R., Breitung, W., Grune, J., Friedrich, A., & Ichikawa, N. (2011). Laminar burning velocities of hydrogen-oxygen-steam mixtures at elevated temperatures and pressures. *Proc. Combust. Inst., 33*(1), 895-903.

Kuznetsov, V. (1982). Limiting laws of propagation of a turbulent flame. *Combust. Explos. Shock Waves, 18*(2), 172-179.

Kwon, O. C., & Faeth, G. M. (2001). Flame/stretch interactions of premixed hydrogen-fueled flames: measurements and predictions. *Combust. Flame, 124*(4), 590-610. doi:https://doi.org/10.1016/S0010-2180(00)00229-7

Laufer, J. (1951). Investigation of turbulent flow in a two-dimensional channel, NACA Technical Report 1053.

Law, C., Zhu, D., & Yu, G. (1988). Propagation and extinction of stretched premixed flames. *Symp. (Int.) Combust., 21*(1), 1419-1426.

## References

Law, C. K., Ishizuka, S., & Mizomoto, M. (1981). Lean-limit extinction of propane/air mixtures in the stagnation-point flow. *Symp. (Int.) Combust., 18*(1), 1791-1798.

Lawes, M., Ormsby, M. P., Sheppard, C. G. W., & Woolley, R. (2012). The turbulent burning velocity of iso-octane/air mixtures. *Combust. Flame, 159*(5), 1949-1959. doi:http://dx.doi.org/10.1016/j.combustflame.2011.12.023

Lee, J., Knystautas, R., & Chan, C. (1985). Turbulent flame propagation in obstacle-filled tubes. *Symp. (Int.) Combust., 20*(1), 1663-1672.

Lee, J. H. (1977). Initiation of gaseous detonation. *Annu. Rev. Phys. Chem., 28*(1), 75-104.

Lefebvre, A. H., Freeman, W. G., & Cowell, L. H. (1986). Spontaneous ignition delay characteristics of hydrocarbon fuel-air mixtures. *NASA Contractor, Report 175064. National Aeronautics and Space*.

Liang, Z., Browne, S., Deiterding, R., & Shepherd, J. (2007). Detonation front structure and the competition for radicals. *Proc. Combust. Inst., 31*(2), 2445-2453.

Liberman, M., Ivanov, M., Kiverin, A., Kuznetsov, M., Chukalovsky, A., & Rakhimova, T. (2010a). Deflagration-to-detonation transition in highly reactive combustible mixtures. *Acta Astronaut., 67*(7), 688-701.

Liberman, M., Ivanov, M., Kiverin, A., Kuznetsov, M., Rakhimova, T., & Chukalovskii, A. (2010b). On the mechanism of the deflagration-to-detonation transition in a hydrogen-oxygen mixture. *J. Exp. Theor. Phys., 111*(4), 684-698.

Liberman, M. A., Kiverin, A., & Ivanov, M. (2012). Regimes of chemical reaction waves initiated by nonuniform initial conditions for detailed chemical reaction models. *Phys. Rev. E, 85*(5), 1-16.

Lifshitz, A., Scheller, K., Burcat, A., & Skinner, G. B. (1971). Shock-tube investigation of ignition in methane-oxygen-argon mixtures. *Combust.*

*Flame, 16*(3), 311-321. doi:https://doi.org/10.1016/S0010-2180(71)80102-5

Lutz, A. E. (1988). A numerical study of thermal ignition, Report No. SAND88-8228, Sandia National Laboratories, CA, USA.

Maas, U., & Warnatz, J. (1988). Ignition processes in hydrogen-oxygen mixtures. *Combust. Flame, 74*(1), 53-69.

Mansour, M. S. (2010). *Fundamental Study of Premixed Combustion Rates at Elevated Pressure and Temperature*: PhD Thesis, University of Leeds (School of Mechanical Engineering).

Mari, R., Cuenot, B., Rocchi, J.-P., Selle, L., & Duchaine, F. (2016). Effect of pressure on hydrogen/oxygen coupled flame–wall interaction. *Combust. Flame, 168*, 409-419.

Markstein, G. (1964). In *Theory of flame propagation* (Vol. 75, pp. 5-14): Elsevier.

Massey, B. S. (1989). *Mechanics of fluids, 6th ed. Van Nostrand Reinhold (International)*. US: CRC Press.

Matalon, M., & Matkowsky, B. (1982). Flames as gasdynamic discontinuities. *J. Fluid Mech., 124*, 239-259.

McComb, W. (1990). The Physics of Fluid Turbulence Oxford University Press. In: Oxford.

Melling, A. (1997). Tracer particles and seeding for particle image velocimetry. *Meas. Sci. Technol., 8*(12), 1406.

Meneveau, C., & Poinsot, T. (1991). Stretching and quenching of flamelets in premixed turbulent combustion. *Combust. Flame, 86*(4), 311-332.

Meyer, J., & Oppenheim, A. (1971). On the shock-induced ignition of explosive gases. *Symp. (Int.) Combust., 13*(1), 1153-1164.

## References

Mittal, G., Sung, C. J., & Yetter, R. A. (2006). Autoignition of $H_2$/CO at elevated pressures in a rapid compression machine. *Int. J. Chem. Kinet., 38*(8), 516-529.

Morley, C. (2005). Gaseq: a chemical equilibrium program for Windows. Available from: http://www.gaseq.co.uk .

Müller, U., Bollig, M., & Peters, N. (1997). Approximations for burning velocities and Markstein numbers for lean hydrocarbon and methanol flames. *Combust. Flame, 108*(3), 349-356.

Muppala, S. R., Aluri, N. K., Dinkelacker, F., & Leipertz, A. (2005). Development of an algebraic reaction rate closure for the numerical calculation of turbulent premixed methane, ethylene, and propane/air flames for pressures up to 1.0 MPa. *Combust. Flame, 140*(4), 257-266.

Musmar, S. e. A., & Al-Rousan, A. A. (2011). Effect of HHO gas on combustion emissions in gasoline engines. *Fuel, 90*(10), 3066-3070.

Nagai, K., Okabe, T., Kim, K., Yoshihashi, T., Obara, T., & Ohyagi, S. (2009). A study on DDT processes in a narrow channel. *Shock Waves*, 203-208.

Nwagwe, I. K., Weller, H. G., Tabor, G. R., Gosman, A. D., Lawes, M., Sheppard, C. G. W., & Wooley, R. (2000). Measurements and large eddy simulations of turbulent premixed flame kernel growth. *Proc. Combust. Inst., 28*(1), 59-65. doi:http://dx.doi.org/10.1016/S0082-0784(00)80195-2

Obara, T., Yajima, S., Yoshihashi, T., & Ohyagi, S. (1996). A high-speed photographic study of the transition from deflagration to detonation wave. *Shock Waves, 6*(4), 205-210.

Olm, C., Zsély, I. G., Pálvölgyi, R., Varga, T., Nagy, T., Curran, H. J., & Turányi, T. (2014). Comparison of the performance of several recent hydrogen combustion mechanisms. *Combust. Flame, 161*(9), 2219-2234.

References

Palacios, A., & Bradley, D. (2017). Generalised correlations of blow-off and flame quenching for sub-sonic and choked jet flames. *Combust. Flame, 185*, 309-318. doi:https://doi.org/10.1016/j.combustflame.2017.07.019

Pang, G., Davidson, D., & Hanson, R. (2009). Experimental study and modeling of shock tube ignition delay times for hydrogen–oxygen–argon mixtures at low temperatures. *Proc. Combust. Inst., 32*(1), 181-188.

Park, O., Veloo, P. S., Liu, N., & Egolfopoulos, F. N. (2011). Combustion characteristics of alternative gaseous fuels. *Proc. Combust. Inst., 33*(1), 887-894.

Peters, N. (1988). *Laminar flamelet concepts in turbulent combustion.* Paper presented at the Symp. (Int.) Combust.

Peters, N. (1999). The turbulent burning velocity for large-scale and small-scale turbulence. *J. Fluid Mech., 384*, 107-132.

Peters, N. (2000). *Turbulent Combustion*: Cambridge University Press.

Poinsot, T., Veynante, D., & Candel, S. (1991). Quenching processes and premixed turbulent combustion diagrams. *J. Fluid Mech., 228*, 561-606.

Popov, N. A. (2007). The effect of nonequilibrium excitation on the ignition of hydrogen-oxygen mixtures. *Teplofizika vysokikh temperatur, 45*(2), 296-315.

Qiao, L., Kim, C. H., & Faeth, G. M. (2005). Suppression effects of diluents on laminar premixed hydrogen/oxygen/nitrogen flames. *Combust. Flame, 143*(1–2), 79-96. doi:http://dx.doi.org/10.1016/j.combustflame.2005.05.004

Ravi, K., Mathew, S., Bhasker, J. P., & Porpatham, E. (2016). Gaseous alternative fuels for ci engines—a technical review. *Int. J. Pharm. Technol., 8*, 5257-5268.

Röhl, O., Jerzembeck, S., Beeckmann, J., & Peters, N. (2009). Numerical investigation of laminar burning velocities of high octane fuel blends containing ethanol. *SAE paper,*.

Sarathy, S. M., Thomson, M. J., Togbé, C., Dagaut, P., Halter, F., & Mounaim-Rousselle, C. (2009). An experimental and kinetic modeling study of n-butanol combustion. *Combust. Flame, 156*(4), 852-864.

Schmidt, E. H., Steinicke, H., & Neubert, U. (1953). Flame and schlieren photographs of combustion waves in tubes. *Symp. (Int.) Combust., 4*(1), 658-666.

Scott, M. (1992). Distributions of strain rate and temperature in turbulent combustion. *PhD Dissertation, The University of Leeds*.

Sharpe, G. (2011). Private Communications, cited in Mumby (2016).

Shatalov, O., Ibraguimova, L., Pavlov, V., Smekhov, G., & Tunik, Y. V. (2009). Analysis of the kinetic data described oxygen-hydrogen mixtures combustion. *4th European Combustion Meeting*, paper 222.

Shchelkin, K. (1940). Influence of tube roughness on the formation and detonation propagation in gas. *J. Exp. Theor. Phys., 10*, 823-829.

Shchelkin, K. (1947). Occurance of detonation in gases in rough-walled tubes. *Sov. J. Tech. Phys., 17*(5), 613.

Short, M., & Sharpe, G. J. (2003). Pulsating instability of detonations with a two-step chain-branching reaction model: theory and numerics. *Combust. Theory Model., 7*(2), 401-416.

Shy, S., Lin, W., & Peng, K. (2000). High-intensity turbulent premixed combustion: General correlations of turbulent burning velocities in a new cruciform burner. *Proc. Combust. Inst., 28*(1), 561-568.

Sidey, J., Mastorakos, E., & Gordon, R. (2014). Simulations of autoignition and laminar premixed flames in methane/air mixtures diluted with hot products. *Combust. Sci. Technol., 186*(4-5), 453-465.

Sirmas, N., & Radulescu, M. I. (2017). Thermal ignition revisited with two-dimensional molecular dynamics: Role of fluctuations in activated collisions. *Combust. Flame, 177*, 79-88.

Sivashinsky, G. I. (2002). Some developments in premixed combustion modeling. *Proc. Combust. Inst., 29*(2), 1737-1761.

Skiba, A. W., Wabel, T., Temme, J., & Driscoll, J. F. (2015). Measurements to determine the regimes of turbulent premixed flames. *51st AIAA/SAE/ASEE Joint Propulsion Conference*, 4089.

Skinner, G. B., & Ringrose, G. H. (1965). Ignition Delays of a Hydrogen-Oxygen-Argon Mixture at Relatively Low Temperatures. *J. Chem. Phys, 42*(6), 2190-2192.

Smirnov, N. N., Nikitin, V. F., & Phylippov, Y. G. (2013). Hydrogen engines numerical modeling. *Proceedings of XLI International Summer School-Conference APM, Russia, St. Petersburg.*

Smith, G. P., Golden, D. M., Frenklach, M., Moriarty, N. W., Eiteneer, B., Goldenberg, M., Bowman, C. T., Hanson, R. K., Song, S., & Gardiner Jr, W. (1999). GRI-Mech 3.0. Available: http://www.me.berkeley.edu/gri_mech

Spadaccini, L., & Colket Iii, M. (1994). Ignition delay characteristics of methane fuels. *Prog. Energy Combust. Sci., 20*(5), 431-460.

Stahl, G., & Warnatz, J. (1991). Numerical investigation of time-dependent properties and extinction of strained methane and propane-air flamelets. *Combust. Flame, 85*(3-4), 285-299.

Stahl, G. R., B. & Warnatz, J. (1988). Dynamics of reactive systems. Part 1. *Flames. Prog. Astronaut. Aeronaut, 113*(195).

Starik, A., & Titova, N. (2003). Kinetics of detonation initiation in the supersonic flow of the $H_2 + O_2$ (air) mixture in $O_2$ molecule excitation by resonance laser radiation. *Kinet. Catal., 44*(1), 28-39.

References

Strozzi, C., Mura, A., Sotton, J., & Bellenoue, M. (2012). Experimental analysis of propagation regimes during the autoignition of a fully premixed methane–air mixture in the presence of temperature inhomogeneities. *Combust. Flame, 159*(11), 3323-3341. doi:https://doi.org/10.1016/j.combustflame.2012.06.011

Tamadonfar, P., & Gülder, Ö. L. (2014). Flame brush characteristics and burning velocities of premixed turbulent methane/air Bunsen flames. *Combust. Flame, 161*(12), 3154-3165.

Taylor, G. I. (1935). Statistical theory of turbulence. IV. Diffusion in a turbulent air stream. *Proc. R. Soc. Lond. A*.

Thibault, P., Liu, Y., Chan, C., Lee, J., Knystautas, R., Gurap, C., & Fuhre, K. (1982). Transmission of an explosion through an orifice. *NASA STI/Recon Technical Report N, 83*.

Thorne, B. (2017). *Development of a 3D Laser Imaging System and its Application in Studies of Turbulent Flame Structure.* PhD Thesis, University of Leeds,

Tripathi, N. (2012). *Dynamics of confined premixed laminar explosion flames.* PhD Thesis, University of Leeds,

UNEP. (2018). The emissions gap report 2018. *UN Environment Programme*.

Urtiew, P., & Oppenheim, A. (1966). Experimental observations of the transition to detonation in an explosive gas. *Proc. R. Soc. A, 295*(1440), 13-28.

UTA. (2011). Pulsed detonation engines, University of Texas *http://arc.uta.edu/research/pde.htm*.

Vancoillie, J., Sharpe, G., Lawes, M., & Verhelst, S. (2014). The turbulent burning velocity of methanol–air mixtures. *Fuel, 130*, 76-91. doi:http://dx.doi.org/10.1016/j.fuel.2014.04.003

Varga, T., Nagy, T., Olm, C., Zsély, I. G., Pálvölgyi, R., Valkó, É., Vincze, G., Cserháti, M., Curran, H., & Turányi, T. (2015). Optimization of a

hydrogen combustion mechanism using both direct and indirect measurements. *Proc. Combust. Inst., 35*(1), 589-596.

Veloo, P. S., Wang, Y. L., Egolfopoulos, F. N., & Westbrook, C. K. (2010). A comparative experimental and computational study of methanol, ethanol, and n-butanol flames. *Combust. Flame, 157*(10), 1989-2004.

Voevodsky, V., & Soloukhin, R. (1965). On the mechanism and explosion limits of hydrogen-oxygen chain self-ignition in shock waves. *Symp. (Int.) Combust., 10*(1), 279-283.

Wabel, T. M., Skiba, A. W., & Driscoll, J. F. (2017). Turbulent burning velocity measurements: Extended to extreme levels of turbulence. *Proc. Combust. Inst., 36*(2), 1801-1808.

Wang, Y., Holley, A., Ji, C., Egolfopoulos, F., Tsotsis, T., & Curran, H. (2009). Propagation and extinction of premixed dimethyl-ether/air flames. *Proc. Combust. Inst., 32*(1), 1035-1042.

Wang, Y. L., Veloo, P. S., Egolfopoulos, F. N., & Tsotsis, T. T. (2011). A comparative study on the extinction characteristics of non-premixed dimethyl ether and ethanol flames. *Proc. Combust. Inst., 33*(1), 1003-1010. doi:https://doi.org/10.1016/j.proci.2010.06.157

Westbrook, C. K., Pitz, W. J., Westmoreland, P. R., Dryer, F. L., Chaos, M., Oßwald, P., Kohse-Höinghaus, K., Cool, T. A., Wang, J., & Yang, B. (2009). A detailed chemical kinetic reaction mechanism for oxidation of four small alkyl esters in laminar premixed flames. *Proc. Combust. Inst., 32*(1), 221-228.

Williams, F. (1985). Combustion Theory 2nd. In: The Benjamin/Cummings.

Wu, M., Wang, M., Liu, J., & Huo, H. (2008). Assessment of potential life-cycle energy and greenhouse gas emission effects from using corn-based butanol as a transportation fuel. *Biotechnology progress, 24*(6), 1204-1214.

Wu, M. H., Burke, M. P., Son, S. F., & Yetter, R. A. (2007). Flame acceleration and the transition to detonation of stoichiometric ethylene/oxygen in microscale tubes. *Proc. Combust. Inst., 31*(2), 2429-2436.

Xue, C., Zhao, X.-Q., Liu, C.-G., Chen, L.-J., & Bai, F.-W. (2013). Prospective and development of butanol as an advanced biofuel. *Biotechnology advances, 31*(8), 1575-1584.

Yang, S., & Shy, S. (2002). Global quenching of premixed $CH_4$/air flames: Effects of turbulent straining, equivalence ratio, and radiative heat loss. *Proc. Combust. Inst., 29*(2), 1841-1847.

Yeung, P., Girimaji, S., & Pope, S. (1990). Straining and scalar dissipation on material surfaces in turbulence: implications for flamelets. *Combust. Flame, 79*(3-4), 340-365.

Zabetakis, M. G. (1965). *Flammability characteristics of combustible gases and vapors*. Retrieved from

Zel'dovich, Y. B., Librovich, V., Mahviladze, G., & Sivashinsky, G. (1970). On the detonation formation in a non-uniformly preheated gas. *J. Appl. Mech. Tech. Ph., 2*, 76-84.

Zhang, Y., Huang, Z., Wei, L., Zhang, J., & Law, C. K. (2012). Experimental and modeling study on ignition delays of lean mixtures of methane, hydrogen, oxygen, and argon at elevated pressures. *Combust. Flame, 159*(3), 918-931.

Zimont, V. L. (2000). Gas premixed combustion at high turbulence. Turbulent flame closure combustion model. *Exp. Therm. Fluid Sci., 21*(1-3), 179-186.

Zipf, R. K., Gamezo, V., Sapko, M., Marchewka, W., Mohamed, K., Oran, E., & Karnack, F. (2013). Methane-air detonation experiments at NIOSH Lake Lynn Laboratory. *J. Loss Prevent. Process Ind., 26*(2), 295-301.